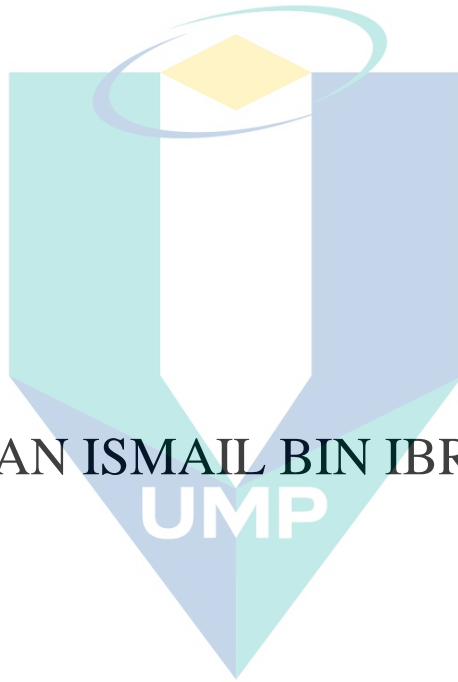


MODELLING AND CONTROL STRATEGIES  
FOR HYDROKINETIC ENERGY HARNESSING



WAN ISMAIL BIN IBRAHIM  
UMP

اونيورسيتي ملايسيا قهغ

UNIVERSITI MALAYSIA PAHANG

DOCTOR OF PHILOSOPHY

UNIVERSITI MALAYSIA PAHANG

## UNIVERSITI MALAYSIA PAHANG

### DECLARATION OF THESIS AND COPYRIGHT

Author's Full Name : WAN ISMAIL BIN IBRAHIM

Date of Birth : 30 APRIL 1984

Title : MODELLING OF RIVER CURRENT TURBINE AND  
CONTROL STRATEGIES FOR HYDROKINETIC ENERGY  
HARNESSING

Academic Session : SEMESTER I 2020/2021

I declare that this thesis is classified as:

- CONFIDENTIAL (Contains confidential information under the Official Secret Act 1997)\*
- RESTRICTED (Contains restricted information as specified by the organization where research was done)\*
- OPEN ACCESS I agree that my thesis to be published as online open access (Full Text)

I acknowledge that Universiti Malaysia Pahang reserves the following rights:

1. The Thesis is the Property of Universiti Malaysia Pahang
2. The Library of Universiti Malaysia Pahang has the right to make copies of the thesis for the purpose of research only.
3. The Library has the right to make copies of the thesis for academic exchange.

Certified by:

\_\_\_\_\_  
(Student's Signature)

840430-03-5345

\_\_\_\_\_  
New IC/Passport Number

Date:

\_\_\_\_\_  
(Supervisor's Signature)

PROF. MADYA TS. DR. MOHD  
RUSLLIM MOHAMED

\_\_\_\_\_  
Name of Supervisor

Date:

NOTE : \* If the thesis is CONFIDENTIAL or RESTRICTED, please attach a thesis declaration letter.

## SUPERVISOR'S DECLARATION

We hereby declare that we have checked this thesis and in our opinion, this thesis is adequate in terms of scope and quality for the award of the degree of Doctor of Philosophy.



---

(Supervisor's Signature)

Full Name : ASSOC. PROF. Ts. DR. MOHD. RUSLLIM BIN MOHAMED

Position : ASSOCIATE PROFESSOR

Date :



---

(Co-supervisor's Signature)

Full Name : DR. RAJA MOHD TAUFIKA BIN RAJA ISMAIL

Position : SENIOR LECTURER

Date :

## STUDENT'S DECLARATION

I hereby declare that the work in this thesis is based on my original work except for quotations and citations which have been duly acknowledged. I also declare that it has not been previously or concurrently submitted for any other degree at Universiti Malaysia Pahang or any other institutions.



(Student's Signature)

Full Name : WAN ISMAIL BIN IBRAHIM

ID Number : PEE 17002

Date :

UMP

اونيورسيتي ملايسيا قهغ

UNIVERSITI MALAYSIA PAHANG

MODELLING AND CONTROL STRATEGIES FOR HYDROKINETIC ENERGY  
HARNESSING



WAN ISMAIL BIN IBRAHIM

UMP

Thesis submitted in fulfillment of the requirements

for the award of the degree of

Doctor of Philosophy

اونيورسيتي مليسيا قهغ

UNIVERSITI MALAYSIA PAHANG

College of Engineering

UNIVERSITI MALAYSIA PAHANG

DECEMBER 2020

## ACKNOWLEDGEMENTS

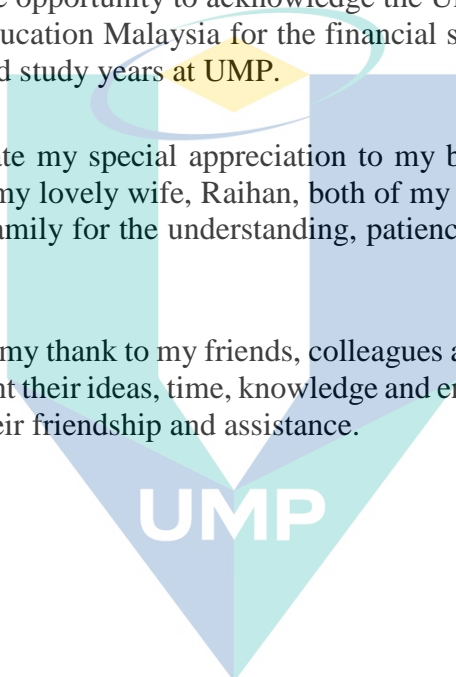
Alhamdulillah, I am grateful to Almighty Allah s.w.t for the good health, His blessing, merciful and rahmah in guiding me throughout all this tenure years in completing this research.

I would like to express my sincere appreciation to my supervisors, Associate Professor Ts. Dr Mohd Rusllim Bin Mohamed and Dr Raja Taufika Bin Raja Ismail for the continuous support, motivations and immense knowledge. Their guidance is invaluable.

I would like to take the opportunity to acknowledge the Universiti Malaysia Pahang and Ministry of Higher Education Malaysia for the financial support and scholarship award during my research and study years at UMP.

I would like to dedicate my special appreciation to my beloved mother, Wan Mariam Binti Wan Sulaiman, my lovely wife, Raihan, both of my hero, Darwisy & al-Fateh and as well as my entire family for the understanding, patience, support and doa during my PhD journey.

I would also to extend my thank to my friends, colleagues and everyone who directly and indirectly who have lent their ideas, time, knowledge and energy during my difficult time. I greatly appreciate their friendship and assistance.



اونيورسيتي مليسيا قهغ

UNIVERSITI MALAYSIA PAHANG

## ABSTRAK

Harga yang tinggi dan kekurangan sumber tenaga konvensional di samping kesedaran tentang alam sekitar kerana kadar pelepasan gas CO<sub>2</sub> yang tinggi telah menggalakkan ramai penyelidik di seluruh dunia untuk menerokai bidang baru dalam sumber tenaga yang boleh diperbaharui. Tenaga hidrokinetik terhasil daripada sungai adalah salah satu tenaga yang berpotensi untuk memastikan kesinambungan tenaga yang bersih, boleh dipercayai dan lestari. Sistem penjanaan konvensional hidroelektrik memerlukan turbin khas, kawasan tadahan air yang luas dan isu berkaitan alam sekitar. Sebaliknya, sistem hidrokinetik berdasarkan pengaliran air berterusan adalah salah satu pilihan yang terbaik untuk menyediakan tenaga elektrik terutamanya untuk kawasan luar bandar dan tenaga berskala kecil. Walaubagaimanapun, terdapat isu dan cabaran yang perlu diberikan perhatian seperti pilihan turbin, turbin model dan juga strategi kawalan untuk sambungan grid dan bukan grid. Sekarang, usaha memanfaatkan tenaga berdasarkan teknologi hidrokinetik muncul dengan ketara. Walaupun begitu, beberapa cabaran dan masalah perlu dipertimbangkan, seperti pemilihan turbin, strategi kawalan untuk sambungan grid dan bukan grid. Sehingga kini, tidak ada maklumat terperinci mengenai turbin dan turbine model yang paling sesuai dengan ciri sungai di Malaysia untuk di aplikasikan. Selain itu, ayunan besar turut berlaku pada keluaran arus dan kuasa semasa dalam keadaan mantap disebabkan oleh variasi pengaliran air sungai yang turun naik. Disebabkan itu, tenaga yang terhasil dan kecekapan pengawal untuk sistem yang bersendirian dan bersambung dengan grid menjadi kurang. Oleh itu, kajian ini bertujuan untuk menganalisa beberapa reka bentuk turbin, menentukan model turbin dan mengkaji strategi kawalan yang berpotensi untuk tenaga hidrokinetik yang bersendirian dan bersambung dengan grid. Dalam kajian ini, tiga jenis turbin paksi menegak, iaitu H-Darrieus, Darrieus, dan Gorlov dengan dua belas hidrofil NACA dan NREL, masing-masing dianalisa menggunakan perisian QBlade dan Matlab. Kesan profil geometri simetri dan tidak simetri, ketebalan hidrofoil, dan kepejalan turbin telah dianalisa untuk memilih turbin yang terbaik berdasarkan pekali kuasa ( $C_P$ ) dan pekali tork ( $C_M$ ) yang tertinggi. Selepas itu, model turbin telah dicadangkan berdasarkan karekter turbin menggunakan persamaan anggaran polinomial. Sementara itu, kaedah tanpa sensor telah di gunakan untuk system sendirian sebagai strategi kawalan MPPT. Litar topologi berdasarkan penerus tidak terkawal dan DC penukar rangsangan telah di gunakan untuk mengawal voltan keluaran dari penerus melalui kitar tugas. Seterusnya, kaedah metaheuristik berdasarkan gabungan algoritma Hill-Climbing Search (HCS) dan Fuzzy Logic Controller telah dicadangkan untuk menghasilkan ukuran saiz yang berubah-ubah berbanding dengan ukuran saiz tetap dalam konvensional algoritma HCS. Tambahan pula, dinamik model untuk system bersambung grid telah dilinearisasi untuk analisa kestabilan isyarat kecil. Pendekatan berdasarkan analisa nilai eigen telah diterapkan untuk menilai kestabilan sistem disebabkan gangguan kecil. Pengawal PI dengan kaedah penelusuran nilai eigen telah dicadangkan untuk meningkatkan kestabilan sistem dengan mengurangkan frekuensi ayunan. Hasil penyelidikan menunjukkan bahawa H-Darrieus dengan NACA 0018 adalah turbin terbaik untuk mendapatkan tenaga elektik di sungai. Selain itu, HCS-Fuzzy MPPT algoritma dapat meningkatkan tenaga yang terhasil sehingga 88.30% dan juga mengurangkan 74.47% ayunan berbanding dengan SS-HCS MPPT. Manakala, kestabilan system tenaga hidrokinetik yang bersambungkan dengan grid dapat dipertingkatkan sehingga 63.63% dengan mengurangkan frekuensi ayunan pada nilai  $\lambda_{8,9,10,11}$  serta mengurangkan ayunan 40.1% arus stator penjana pada pengawal sisi pemutar (RSC).



## ABSTRACT

The high prices and depletion of conventional energy resources and the environmental concern due to the high emission of CO<sub>2</sub> gases have encouraged many researchers worldwide to explore a new field in renewable energy resources. The hydrokinetic energy harnessing in the river is one of the potential energies to ensure the continuity of clean, reliable, and sustainable energy for the future generation. The conventional hydropower required a special head, lots of coverage area, and some environmental issues. Conversely, the hydrokinetic system based on free stream flowing is one of the best options to provide the decentralised energy for rural and small-scale energy production. Lately, the effort of energy harnessing based on hydrokinetic technology is emerging significantly. Nevertheless, several challenges and issues need to be considered, such as turbine selection for energy conversion, generalised turbine model and control strategies for the grid and non-grid connection. To date, no detailed information on which turbines and turbine model are most suited to be implemented that match Malaysia's river characteristics. Besides, a large oscillation has occurred on the output current and power during dynamic steady state due to the water variation and fluctuation in the river. Hence, reducing the energy extraction and controller efficiency for stand-alone and grid-connected systems, respectively. Therefore, the study aims to analyse the different turbine's design, proposed the turbine model, and propose the potential control strategies for stand-alone and grid-connected hydrokinetic energy harnessing in the river. In this work, three types of vertical axis turbines, including the H-Darrieus, Darrieus, and Gorlov with twelve different NACA and NREL hydrofoils, were analysed using the QBlade and MATLAB software, respectively. The effect of symmetrical and non-symmetrical geometry profiles, hydrofoils thicknesses, and turbine solidities have been compared to choose one of the best option turbines based on the highest power coefficient ( $C_P$ ) and a torque coefficient ( $C_M$ ), respectively. Subsequently, the turbine power model generalised equation has been proposed to represent the hydrokinetic turbine characteristic using a polynomial estimation equation. On the other hand, the MPPT control strategy is employed for the off-grid system using the sensorless method. The circuit topology based on an uncontrolled rectifier with the DC boost converter is implemented to regulate the rectifier output voltage through duty ratio. Subsequently, the metaheuristic method based on the combination of the Hill-Climbing Search (HCS) MPPT algorithm and the Fuzzy Logic Controller has been proposed to produce a variable step size compared to the fixed step size in conventional HCS algorithm. On the contrary, the dynamic model of the grid-connected hydrokinetic system has been linearised for small-signal stability analysis. The eigenvalues analysis-based approach has been applied to evaluate the system stability due to the small disturbance. The PI controller with the eigenvalues tracing method has been proposed to improve the system stability by reducing the oscillation frequency. The research outcomes indicated that the H-Darrieus with NACA 0018 was the best turbine for energy conversion in the river. Besides, the HCS-Fuzzy MPPT algorithm improved the energy extraction up to 88.30 % as well as reduced 74.47 % the oscillation compared to the SS-HCS MPPT. The stability of grid-connected hydrokinetic energy harnessing was improved up to 63.63 % by removing the oscillation frequency at states of  $\lambda_{8,9,10,11}$  as well as reducing 40.1 % oscillation of the generator stator current at the rotor side controller (RSC).



## TABLE OF CONTENT

**DECLARATION**

**TITLE PAGE**

**ACKNOWLEDGEMENTS** **ii**

**ABSTRAK** **iii**

**ABSTRACT** **iv**

**TABLE OF CONTENT** **v**

**LIST OF TABLES** **xi**

**LIST OF FIGURES** **xiii**

**LIST OF SYMBOLS** **xvii**

**LIST OF ABBREVIATIONS** **xviii**

**LIST OF APPENDICES** **xx**

**CHAPTER 1 INTRODUCTION** **1**

1.1 Chapter Overview 1

1.2 Backgrounds 1

1.3 Problem Statements 3

1.4 Research Objectives 5

1.5 Scopes and Limitations 6

1.6 Statement of Contribution 8

1.7 Thesis Outlines 9

**CHAPTER 2 LITERATURE REVIEW** **11**

2.1 Chapter Overview 11

2.2 Introduction 11

2.3 An Overview of River Current Energy Conversion System (RCECS) 14

2.4	Hydrokinetic Energy Conversion System (HECS)	16
2.4.1	The structure of Hydrokinetic System	16
2.4.2	Concept and Operation of the Hydrokinetic System	17
2.5	Hydrokinetic Turbine Classification	19
2.5.1	Horizontal Axis Hydrokinetic Turbines	20
2.5.2	Vertical Axis Hydrokinetic Turbine	21
2.5.3	Cross-flow Hydrokinetic Turbine	24
2.5.4	Non-Turbine Hydrokinetic System	25
2.6	Turbines Hydrofoils Selection	27
2.6.1	Hydrofoils Profiles Geometry	27
2.6.2	National Advisory Committee for Aeronautics (NACA) Airfoils	29
2.7	Power Turbine Modelling	30
2.7.1	Modelling of General $C_P$ Equation in WECS	30
2.7.2	Modelling of General $C_P$ Equation in Hydrokinetic	33
2.8	Comparison of Hydrokinetic System with other Technology	34
2.8.1	Hydrokinetic Versus Conventional Hydropower	34
2.8.2	Hydrokinetic Versus Wind Energy Conversion System	36
2.9	Variable Speed Hydrokinetic System	37
2.9.1	Operating Region and Control Strategy	39
2.10	Maximum Power Point Tracking (MPPT) Algorithm for Off-Grid Hydrokinetic Energy Harnessing	41
2.10.1	MPPT Algorithm Classification	42
2.10.2	Tip Speed Ratio (TSR) MPPT	43
2.10.3	Optimal Torque (OT) MPPT	44
2.10.4	Power Signal Feedback (PSF) MPPT	45
2.10.5	Hill Climbing Search (HCS) MPPT	46

2.10.6	Incremental Conductance (INC) MPPT	46
2.10.7	Optimal Related Based (ORB) MPPT	47
2.10.8	Fuzzy Logic MPPT	48
2.10.9	Performance Comparison between MPPT Algorithm	49
2.11	Control Strategies for Grid-Connected Hydrokinetic Energy Harnessing	52
2.11.1	Pitch Control Strategies	52
2.11.2	Robust Control Strategies in Hydrokinetic Technology	54
2.11.3	Conventional PI Controller with Parameter Tuning	60
2.11.4	Small Signal Stability Analysis (SSSA) and Eigenvalues Tracing Method	63
2.12	Summary	64
<b>CHAPTER 3 METHODOLOGY</b>		<b>67</b>
3.1	Chapter Overview	67
3.2	Research Implementations	67
3.3	Assessment on Hydrokinetic Resources	71
3.3.1	Hydrology Measurement and Observation	71
3.3.2	Case Studies 1: River Assessment at Pasir Kubur River Sg. Lembing, Kuantan	73
3.3.3	Evaluation Method	74
3.3.4	Velocity Measurement	76
3.4	Assessment on Hydrokinetic Resources-Data of Department of Irrigation & Drainage (DID) Malaysia	79
3.4.1	Site Location	80
3.4.2	DID Hydrology Data	81
3.4.3	River Analysis	82
3.5	Summary	86

<b>CHAPTER 4 DESIGN CONSIDERATION &amp; SELECTION OF RIVER CURRENT TURBINE</b>	<b>88</b>
4.1 Chapter Overview	88
4.2 Turbines Design Considerations	89
4.2.1 Principle and Concept of Operation	89
4.2.2 Turbine Simulation and Design Consideration	94
4.2.3 Turbine Sizing	98
4.2.4 Hydrofoil Blade Selection	101
4.3 Results and Discussions	103
4.3.1 XFoils Analysis on Hydrofoils Profiles	103
4.3.2 Hydrofoil Profile Geometry for H-Darrieus Turbine	106
4.3.3 Hydrofoil Profile Geometry for Darrieus Turbine	110
4.3.4 Hydrofoil Profile Geometry for Gorlov Helical Turbine (GHT)	112
4.3.5 Performance Comparison between H-Darrieus, Darrieus and Gorlov Helical Turbines	115
4.3.6 The Effect of Turbine Solidity on H-Darrieus	117
4.3.7 The Modelling of H-Darrieus Turbine	118
4.3.8 Turbine Power and Torque	121
4.4 Summary	124

## UNIVERSITI MALAYSIA PAHANG

<b>CHAPTER 5 MAXIMUM POWER POINT TRACKING (MPPT) CONTROL STRATEGIES FOR STAND-ALONE HYDROKINETIC ENERGY HARNESSING</b>	<b>125</b>
5.1 Introduction	125
5.2 Configuration Establishment of Hydrokinetic Energy Harnessing	126
5.2.1 Variable Speed Hydrokinetic Turbine	126
5.2.2 Hydrokinetic System Topology	127

5.2.3	Model of River Current Turbine	128
5.2.4	Permanent Magnet Synchronous Generator (PMSG) and Rectifier	129
5.2.5	DC-DC Converter	132
5.3	MPPT Control Strategy	134
5.3.1	Conventional Hill-Climbing Search MPPT Algorithm	134
5.3.2	Problem in Conventional HCS MPPT Algorithm	137
5.3.3	Michas MPPT Algorithm	138
5.3.4	Proposed MPPT Algorithm	140
5.4	Results and Discussions	148
5.4.1	Tracking Accuracy	148
5.4.2	Tracking Response Time	152
5.4.3	MPPT Oscillation	152
5.4.4	MPPT Overshoot	154
5.4.5	MPPT Performance Comparison	155
5.5	Summary	157

## **CHAPTER 6 CONTROL STRATEGY FOR GRID-CONNECTED HYDROKINETIC SYSTEM** 158

6.1	Introduction	158
6.2	Modelling of Grid-Connected Hydrokinetic Energy Harnessing	159
6.2.1	Hydrokinetic System Topology	159
6.2.2	Turbine Model	161
6.2.3	Model of Permanent Magnet Synchronous Generator (PMSG)	161
6.2.4	Model of Drive Train	163
6.2.5	Model of the Converter	163
6.2.6	Model of Power Grid	165

6.3	Control Strategies for Grid-Connected Hydrokinetic System	166
6.3.1	Proposed PI Controller with Eigenvalues Trajectory Tracing Method	166
6.3.2	Rotor Side Controller (RSC)	169
6.3.3	Grid Side Controller (GSC)	171
6.3.4	Linearising of The Hydrokinetic Model	175
6.4	Results & Discussions	178
6.4.1	Controller Stability Analysis	179
6.4.2	PI Controller Gain by Eigenvalues Tracing Method	181
6.4.3	Matlab Simulink Simulation Model	188
6.5	Summary	191
<b>CHAPTER 7 CONCLUSION</b>		<b>192</b>
7.1	Chapter Overview	192
7.2	Concluding Remarks	192
7.3	Recommendation for the Future Work	193

<b>REFERENCES</b>	<b>195</b>
-------------------	------------

<b>APPENDICES</b>	<b>218</b>
-------------------	------------

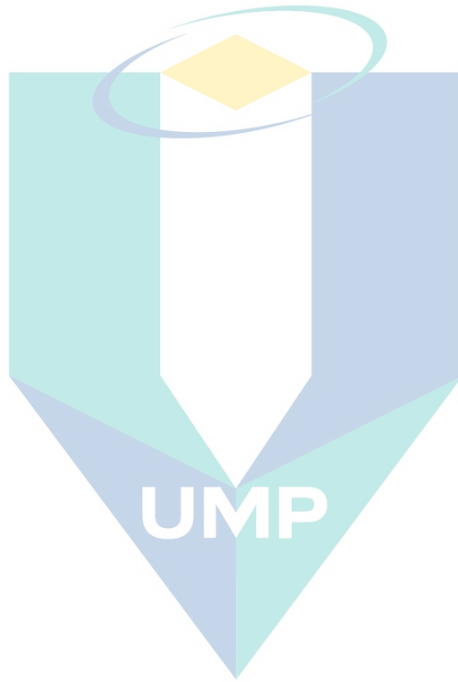
**UNIVERSITI MALAYSIA PAHANG**

## LIST OF TABLES

Table 2.1	Prediction of world renewable energy for electrical generation.	12
Table 2.2	$C_P$ Coefficient $\alpha_{i,j}$ for modelling of turbine power equation	31
Table 2.3	Comparison between conventional hydropower and hydrokinetic technology	35
Table 2.4	Summary comparison between WECS and hydrokinetic technology	37
Table 2.5	Analysis and comparison of different MPPT algorithm.	51
Table 2.6	The potentials of robust control strategies in hydrokinetic research field	55
Table 2.7	The potential of control strategies for hydrokinetic based on PI with parameter tuning	61
Table 3.1	List of telemetry stations under studied.	81
Table 4.1	Summary of sampling measurement at Station 2 Pasir Kubur River, Sungai Lembing, Kuantan in April 2018.	98
Table 4.2	The detailed specification of the turbine under study.	100
Table 4.3	Properties of NREL S-Series hydrofoil profiles	102
Table 4.4	Summary of maximum $C_L/C_D$ at different AoA for higher and lower $Re$ .	106
Table 4.5	A comparison of $C_P$ and $C_M$ between NACA and NREL hydrofoils for the H-Darrieus turbine .	109
Table 4.6	A comparison of $C_P$ and $C_M$ between NACA and NREL hydrofoils for the Darrieus turbine .	112
Table 4.7	A comparison of $C_P$ and $C_M$ between NACA and NREL hydrofoils for the Gorloy Helical Turbine .	115
Table 4.8	Summary of $C_P$ vs. $\lambda$ curve for different number of blades	118
Table 4.9	The H-Darrieus turbine specification details for the turbine model	119
Table 4.10	A comparison of the MSE and RMSE discrepancies for the different polynomial level equations	121
Table 4.11	A summary of peak power and torque vs. turbine rotational speed at different water velocities	123
Table 5.1	The parameter of the permanent magnet synchronous generator (PMSG)	131
Table 5.2	The parameter for DC Boost Converter	133
Table 5.3	Fuzzy logic control rules	146
Table 5.4	The output power and the efficiency of the algorithms at constant water velocity. The algorithm was simulated based on input water variation in Figure 5.11	151



Table 5.5	The oscillation of the output power at different water velocities	153
Table 5.6	The summary of performance comparison between the MPPT algorithm	156
Table 6.1	The Parameter gain and boundary condition	168
Table 6.2	Parameter of hydrokinetic system under study	179
Table 6.3	State variable of Matrix A without the proposed controller	180
Table 6.4	The values of the controller parameter	186
Table 6.5	Eigenvalues of State Matrix A with the proposed controller	187



اونيور سيطي مليسيا قهغ

UNIVERSITI MALAYSIA PAHANG

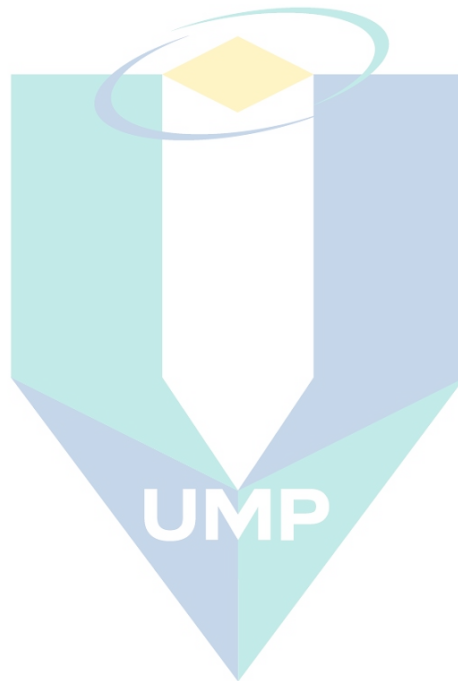
## LIST OF FIGURES

Figure 2.1	Timeline for development of hydrokinetic technology (not limited to)	15
Figure 2.2	The structure of hydrokinetic system. The high-end system can be a stand alone or grid connected system.	17
Figure 2.3	Hydrokinetic configuration under the classification of the energy conversion scheme	20
Figure 2.4	Horizontal axis turbines in the hydrokinetic system.	21
Figure 2.5	Vertical Axis Turbine hydrokinetic turbines	22
Figure 2.6	The RivGen and TidGen produced by ORCP.	25
Figure 2.7	Non-Turbine system for energy conversion in the water.	26
Figure 2.8	Airfoils profile geometry	28
Figure 2.9	NACA four digit series	29
Figure 2.10	Generator power speed curve at various water velocity	38
Figure 2.11	The operating region in the hydrokinetic control strategy.	40
Figure 2.12	The Classification of MPPT algorithm for WECS	42
Figure 2.13	Tip Speed Ratio MPPT Algorithm	43
Figure 2.14	The Optimal torque MPPT Algorithm	44
Figure 2.15	Power signal feedback MPPT algorithm	45
Figure 2.16	Flowchart of modified INC MPPT algorithm.	47
Figure 2.17	The FLC MPPT system	48
Figure 2.18	The pitch control strategies in hydrokinetic system	53
Figure 2.19	Literature map of hydrokinetic system research	66
Figure 3.1	The general methodology for hydrokinetic research	68
Figure 3.2	Prosedure for water velocity measurement	72
Figure 3.3	The Location of Pasir Kubur River, Sungai Lembing Kuantan, Pahang.	73
Figure 3.4	The evaluation step of river energy potential for hydrokinetic energy harnessing.	75
Figure 3.5	Determination of the stream cross-section and discharge computation	78
Figure 3.6	The location of sampling station at Pasir Kubur river Sungai Lembing, Kuantan, Pahang.	79
Figure 3.7	The location of Pahang River basin.	80
Figure 3.8	Mean Annual Discharge at 10 selected gauging stations' location.	82
Figure 3.9	Mean river depth of Pahang River from 2012 to 2017	83

Figure 3.10	The relationship between flowrate and water depth for Pahang River at Lubuk Paku and Temerloh in 2017.	84
Figure 3.11	Mean monthly water velocity between 2012 to 2017 for Pahang River at Lubuk Paku	85
Figure 3.12	The relationship between flowrate and water velocity at Pahang River in 2017	86
Figure 4.1	The force diagram on a typical blade section.	90
Figure 4.2	The hydrofoils flow velocity distribution and force diagram	91
Figure 4.3	The comparison of power coefficient versus tip speed ratio ( $C_p-\lambda$ ) for different types of turbine designs.	94
Figure 4.4	The turbine design consideration process	95
Figure 4.5	The software module in QBade	96
Figure 4.6	Vertical axis hydrokinetic turbine simulated by QBlade	97
Figure 4.7	The dimensions of the straight blade H-Darrieus turbine under study.	100
Figure 4.8	Symmetrical and non-symmetrical hydrofoil blades profiles under study.	103
Figure 4.9	Lift to Drag ratio vs. Angle of Attack (AoA) of NACA and NREL hydrofoils at higher and lower Reynolds number. The XFOIL analysis is applied from $-10^\circ$ to $20^\circ$ AoA.	105
Figure 4.10.	The $C_p$ vs. TSR curve of symmetrical and non-symmetrical hydrofoils for the H-Darrieus turbine.	107
Figure 4.11.	The $C_p$ vs. TSR curve for symmetrical and non-symmetrical hydrofoils of the Darrieus turbine.	110
Figure 4.12	The $C_p$ vs. TSR curve for symmetrical and non-symmetrical hydrofoils of the Gorlov helical turbine.	113
Figure 4.13	The $C_p$ vs. TSR curves of H-Darrieus, Darrieus and Gorlov helical turbines for performance comparison.	116
Figure 4.14.	The $C_p$ vs. TSR curve due to the effect of solidity for different number of blades.	117
Figure 4.15	The hydrokinetic turbine model and the simplified $C_p$ -TSR curve representing the H-Darrieus turbine characteristic (in circle).	120
Figure 4.16	A comparison of the $C_p$ vs. TSR curves at different polynomial equations to represent $C_p$ as a function of $\lambda$ .	120
Figure 4.17	Power and torque vs. turbine rotational speed, respectively, at a different water velocities.	122
Figure 4.18	Power vs. turbine rotational speed at different water velocities	123
Figure 5.1	The hydrokinetic design topology for MPPT control strategy.	128
Figure 5.2	PMSG equivalent circuit in per phase diagram.	129
Figure 5.3	DC Boost converter circuit.	132

Figure 5.4	The basic concept of Hill-Climbing Search MPPT algorithm	134
Figure 5.5	The flow chart of the conventional Hill-Climbing search algorithm.	136
Figure 5.6	The illustration to show the process of climbing the power curve by adding different step-size. (a) HCS with large step-size, (b) HCS with small step-size.	138
Figure 5.7	The circuit topology of the Michas MPPT Algorithm	139
Figure 5.8	The flow chart of the Michas algorithm.	140
Figure 5.9	Flow chart of the proposed algorithm: Fuzzy-HCS MPPT algorithm	142
Figure 5.10	The basic concept of Fuzzy Logic Controller	143
Figure 5.11	Membership functions of the fuzzy logic controller.	145
Figure 5.12	Water velocity to represent the input water variation for MPPT tracking.	149
Figure 5.13	The output power of the hydrokinetic system simulated with four different MPPT algorithms. The small figure shows the water velocity as an input signal.	150
Figure 5.14	The tracking response time of four MPPT algorithm. The small figure shows the tracking dynamic response time for SS-HCS at 67ms to achieve dynamic steady-state.	152
Figure 5.15	The oscillation of the output power for four algorithms at dynamic steady-state. The algorithm was simulated at constant $1\text{ms}^{-1}$ water velocity in five seconds.	153
Figure 5.16	The instant changing of water variation between 2.4 ms and 1.0 ms. The simulation is running for a five-second of duration.	154
Figure 5.17	The settling time and amplitude of SS-HCS due to overshoot for energy loss calculation.	155
Figure 6.1	The complete of hydrokinetic system with the back-to-back converter	160
Figure 6.2	PMSG d-q reference frame modelling	162
Figure 6.3	Model of back-to-back converter for modal analysis	164
Figure 6.4	Model of grid network	165
Figure 6.5	Eigenvalues Trajectory Tracing Method	167
Figure 6.6	The block diagram of rotor side controller	169
Figure 6.7	The vector diagram of GSC in $\alpha\text{-}\beta$ and $d\text{-}q$ reference frame.	171
Figure 6.8	The schematic diagram of the grid side controller	174
Figure 6.9	The eigenvalues placement of the Matrix A without the proposed controller	181
Figure 6.10	The traces of the eigenvalues as a function of $K_P$ and $K_I$ .	185
Figure 6.11	The eigenvalues placement of Matrix A with the proposed controller	187

Figure 6.12	The dynamic response of the direct and quadrature current at the RSC and GSC respectively during Case 1.	189
Figure 6.13	The dynamic response of the direct and quadrature current at the RSC and GSC respectively during the Case 2.	190
Figure 7.1	The water velocity at sampling station. Three sampling stations were setup to measure the water velocity.	220
Figure 7.2	The water variation at Station 2. The River Sampling represent the measurement of river data whereas the Spline-Interpolant represent the mathematical interpolation technique.	220



اونيورسيتي ملايسيا قهغ

UNIVERSITI MALAYSIA PAHANG

## LIST OF SYMBOLS

$\Delta S$	Step-size
$A$	Swept Area of turbine ( $m^2$ )
$C_P$	Power Coefficient of the turbine
$E$	Kinetic Energy
$F$	Thrust Force
$M$	Mass of water
$P$	Power (Watt)
$P_o$	Output Power
$P_T$	Power develop at the rotor (Watt)
$T$	Torque (Nm)
$V$	Water velocity ( $ms^{-1}$ )
$\beta$	Pitch Angle
$\lambda$	Tip Speed Ratio
$\rho$	Water density ( $1000 \text{ kg/m}^3$ )
$\omega$	Angular speed of rotor
$P_m$	Power Developed
$T_m$	Torque Mechanical
$Re$	Reynolds Number
$h$	Height
$N$	Number of Blades
$c$	Chord Length
$C_n$	Converter Efficiency
$K_P$	Proportional Gain
$K_I$	Integral Gain
$\sigma$	Turbine solidity
$Q$	Flowrate

## LIST OF ABBREVIATIONS

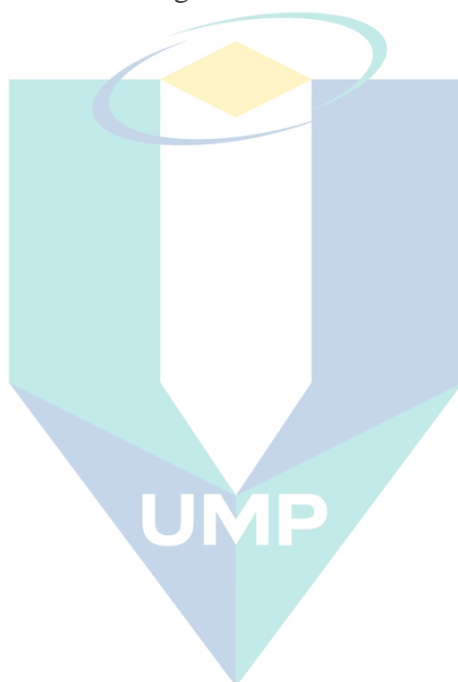
AoA	Angle of Attack
AR	Aspect Ratio
BEM	Blade Element Momentum
CEC	Current Energy Conversion
CFD	Computational Fluid Dynamics
COG	Centre of gravity
$C_P$	Power Coefficient
DC	Direct Current
DFIG	Double-Fed Induction Generator
DID	Department of Irrigation and Drainage
DMS	Double Multiple Streamtube
DPC	Direct Power Control
DPC	Direct Power Control
DTC	Direct Torque Control
DTC	Direct Torque Control
ELM	Extreme Learning Machine
EMEC	European Marine Energy Centre Ltd
ETR	Effective Tracking Range
FGS	Fuzzy Gain Scheduling
FLC	Fuzzy Logic Controller
FOC	Field Oriented Control
FOPI	Fractional Order Proportional Integral
GSC	Grid Side Controller
HCS	Hill-Climbing-Search
HECS	Hydrokinetic Energy Conversion System
HOSM	High Order Sliding Mode
IC	Incremental Conductance
IGBT	Insulated Gate Bipolar Transistor
IPC	Indirect Power Control
IPC	Indirect Power Control
LCOE	Levelized Cost of Energy



LPV	Linear Parameter Varying
LS-HCS	Large-Step Hill-Climbing Search
MCT	Marine Current Turbine
MPP	Maximum Power Point
MPPT	Maximum Power Point Tracking
NACA	National Advisory Committee for Aeronautics
ORB	Optimum Related Based
ORPC	Ocean Renewable Power Company
OT	Optimal Torque
PEC	Power Electronics Converter
PLL	Phase Loop Lock
PMSG	Permanent Magnet Synchronous Generator
PSF	Power Signal Feedback
PV	Photovoltaic
RCECS	River Current energy Conversion System
RE	Renewable Energy
RSC	Rotor Side Controller
SFS	Smart Flow Stream
SS-HCS	Small-Step Hill-Climbing Search
WECS	Small Wind Energy Conversion System
TISEC	Tidal In-Stream Energy Conversion System
TSR	Tip Speed Ratio
UDE	Uncertainty & Disturbance Estimator
USGS	U.S Geological Survey
VAT	Vertical Axis Turbine
VIV	Vortex Induce Vibration
VOC	Voltage Oriented Control
WCT	Water Current Turbine
WEC	Wave Energy Converter
WECS	Wind Energy Conversion System

## LIST OF APPENDICES

Appendix A: Analysis of DID Data	219
Appendix B: Mean Square Error Calculation	225
Appendix C: MPPT Circuit Topology-Uncontrolled Rectifier with DC Boost Converter	229
Appendix D: Derivation of Matrix A for Small-signal Stability Analysis	237
Appendix E: Matlab M-File Code for Small Signal Stability Analysis	241
Appendix F: Matlab/Simulink Program -Back-to-back Converter	243



اونيورسيتي مليسيا قهغ

UNIVERSITI MALAYSIA PAHANG

# CHAPTER 1

## INTRODUCTION

### 1.1 Chapter Overview

This chapter provides an introduction to research work on hydrokinetic energy harnessing. The backgrounds, problem statements, research goals and approaches, scopes, and limitations are presented. The statement of contribution and thesis outlines are also explained in this chapter.

### 1.2 Backgrounds

The energy demand is significantly expanding over the years due to the economic prosperity and increasing of number population worldwide (A. Hussain, Arif, & Aslam, 2017). Conversely, the high price of conventional fossil fuels, limited reserve capacity, and environmental issues due to elevated CO<sub>2</sub> emission are the primary concern nowadays (Hansen, Breyer, & Lund, 2019). Therefore, a clean, safe, and inexhaustible energy resources are required for energy sustainability for future development.

Renewable Energy (RE) resources are one of the best options to provide environmental sustainability, reliable, and decentralised energy for rural and small-scale energy requirements (Baruah & Enweremadu, 2019). Renewable energy resources such as wind energy, solar PV, hydropower, geothermal, and bioenergy have been explored by researchers and private industries worldwide (Erdiwansyah et al., 2019).

Nevertheless, instead of the sustainability function, the RE resources have their demerit too. For instance, wind energy and solar PV are intermittent energy resources (Kumar. K, Ramesh Babu, 2017). This type of energy is not suitable to fulfill the base energy load demand. In addition, hydropower and geothermal required high initial capital

costs and several issues due to environmental concern (Kadier et al., 2018). On the other hand, the bioenergy process required a complex engineering process and advanced technology in the energy conversion scheme (Scarlat & Dallemand, 2018). Therefore, the energy harnessing based on free-flowing of the water stream, i.e., the hydrokinetic system is one of the best options to provide a clean, safe and sustainable energy for the future generation.

As defined by Khan et al. (2008), hydrokinetic system is an electromechanical device that converts the kinetic energy of water flow into electrical energy through the energy conversion scheme and power electronics converter. This type of technology can be implemented in the river, man-made channel, tidal, and marine without using a special head and impoundment (Yuce & Muratoglu, 2015).

According to Othman (2005); Raman, Hussein, and Palanisamy, (2009); Yah, Oumer, and Idris, (2017), Malaysia has the potential to harness electricity from this technology due to an average rainfall of 2540 mm in peninsular Malaysia, 2630 mm in Sabah, and 3850 mm in Sarawak. The yearly rainfall in Malaysia is much higher than the global average (750 mm). As noted by Belhassan (2011), high rainfall will increase the groundwater recharge and increase the flow in the river. Therefore, the high quantity of rainfall will increase the water velocity at the river basin.

Besides that, the combination of highland area and hilly topography in the entire country promise Malaysia a lot of potentials (Kadier et al., 2018; Yah, Oumer, and Idris, 2017). The highland area and hilly topography serve as the water catchment for the upstream rivers and its tributaries. According to Borhanazad et al. (2013), Malaysia is fortunate to possess abundant water sources in its 150 peninsular and 50 Bornean (Sabah and Sarawak) rivers. Furthermore, reconnaissance studies by Hussein and Raman (2010) at 149 sites identified the potential for micro-hydro electrification.

The hydrokinetic system can provide clean and sustainable energy as long as the river is flowing (Kirke, 2019). Besides, the technology only gives a minimal impact on the environment and ecosystem. This is due to the construction of the system can be operated without the reservoir or impoundment (Forbush et al. 2017).

Moreover, the system can be deployed along the riverside by a floating pontoon or fix structure (Anyi & Kirke, 2010). Furthermore, this type of technology is easy to install, transport and relocate to another place due to the small-scale and portable system. Although the hydrokinetic system is relatively for small-scale power production, the system can be installed as multi-unit arrays like wind farms to increase energy extraction (Alvarez et al. 2018; Shafei et al., 2015). Therefore, hydrokinetic energy harnessing can be one of the best choices to provide electricity for off-grid remote communities and small-scale energy needs.

Nevertheless, despite the benefits, enormously researches are expected in order to improve the hydrokinetic technology, especially for energy conversion application. The area of research which requires further attentions among others (not limited to) are the turbine selection and enhancement, maximum power point tracking (MPPT) algorithm and controller strategies to extract the maximum power and reduce the oscillation.

Therefore, this thesis aims to address the fundamental research of the hydrokinetic system through modelling and simulation studies. This includes the selection of the turbines, design of the MPPT algorithm, analysis of small-signal stability, and design of the Proportional and Integral (PI) controller based on traces of eigenvalues. The analysis, data collection, and simulation study will leap the researcher to explore further in the hydrokinetic technology, especially in Malaysia.

### 1.3 Problem Statements

Even though large scale hydroelectric technology has been awhile in Malaysia, relatively, small scale hydrokinetic river-based energy harnessing in Malaysia is still considered as a new venture of research, therefore, several issues need to be properly addressed prior this technology can be used at large.

The first issue that needs to be considered is the design consideration of the turbine based on the river characteristics in Malaysia. To date, the best selection turbines and turbine model for hydrokinetic energy harnessing has not been extensively investigated

by researchers in Malaysia. Hence, there no specific information which turbines and generalised model are most suitable to be implemented that match Malaysia's rivers. Based on current engineering practice in the field, mostly engineers used a ready made turbine available in the market, and made amendment of systems to suit with the whole energy harnessing system design, hence resulted in requirement of large catchment areas, therefore creating further environmental issues to build river-based energy harnessing system, from small up to large scale of hydro technology.

Conversely, to implement the most efficient energy harnessing system, the river characteristics at the resources area needs to be properly evaluated. According to Sarauskiene et al. (2017), the river assessments study is necessary to determine the depth, width, cross-sectional, flow velocity and potential of the river for hydrokinetic energy harnessing. This will lead into properly characterised design of turbines, hence providing efficient design of harnessing system as well as optimising catchment area; reducing stress on environmental issues. To date, there have been a few reseachers published on the river characteristic in Malaysia such as Gasim et al. (2013), Gasim at el. (2006), and Siti Waznah et al.(2010), nevertheless their research are not directly focusing on the hydrokinetics energy harnessing.

The second issue is regarding the river flow pattern and variations. According to Khan et al. (2011), the variation of water flow in a river presents a significant challenge to extract energy. Maximum power point tracking (MPPT) is one of the technology that quite popular and proven to be implemented in Wind Energy Conversion System (WECS) and solar PV. It can also be considered to be implemented to extract the maximum power under the variation and turbulent of water flow. Nevertheless, as far as preliminary surveys on the topic, the application of MPPT algorithms in the hydrokinetic technologies are scarce and limited to be found in the literature. Michas et al. (2019) have proposed the MPPT based on Perturb & Observe algorithm to extract the maximum power on the hydrokinetic system. Nevertheless, the studies concluded the efficiency is still lower as well as an oscillation problems on the output power. Therefore, further attention in this areas are needed for improving the efficiency of the conventional MPPT algorithm by reducing the oscillations on the system.



For better judgement of a technology requires an in depth analysis of a system prior converting into real practice or implementation. Therefore, detail analysis of robustness of the hydrokinetic technology under different circumstances are needed. Since the development of hardware or prototype of the hydrokinetic system is time-consuming and complicated, therefore, a modelling analysis on complete hydrokinetic system with mathematical equations is expected to represent a close-case real system with respect to system requirements, time, cost and errors. As far as author concerns, the equivalent system model to represent the complete hydrokinetic system in the river for the controller design and small signal stability analysis has rarely been discussed by the researcher. This is due to the complicated derivation in the mathematical model and required the linearising of the non-linear equation using Taylor series or Jacobian formulation. Therefore further research is required in this field to design and analyse the system stability in a grid network under different circumstances.

#### 1.4 Research Objectives

The objectives of this study are:

1. To design H-Darrieus turbine based on river characteristic and proposed a generalised power model for the hydrokinetic turbine.
2. To propose the Fuzzy-HCS MPPT algorithm for maximum energy extraction in a fluctuation of river velocity for the stand-alone hydrokinetic system.
3. To formulate the mathematical model of the hydrokinetic system for grid-connected system and proposed PI controller with eigenvalues tracing method.



## 1.5 Scopes and Limitations

The scope and limitations of the study can be outlined as follows:

1. This thesis addresses an investigation and observation at the location of the resources in determining the river characteristics. The sampling process to measure the water velocity is conducted in April 2018 at the Pasir Kubur River, Sungai Lembing, Kuantan Pahang. Three stations have been set up for the data sampling. The distance between each station is 70 m with the total length of the river involved is only 210 m.
2. All the sampling processes used the FP 211 Digital Water Velocity Meter for water velocity and river depth measurement. The water velocity measurement technique is limited to U.S Geological Survey (USGS) Six-Tenth Depth due to accuracy and established method. Besides, the water density ( $\rho$ ), is considered  $1000 \text{ kg m}^{-3}$  approximately, and the value is fixed at all locations of the river .
3. The raw data of river reading are taken from the Department of Irrigation and Drainage (DID) Malaysia for an assessment study. The data at ten gauging stations along Pahang River from January 2012 to December 2017 have been analysed to investigate the potential of hydrokinetic energy harnessing.
4. The turbine has been designed and simulated by the QBlade software v0.96 in determining the Power Coefficient ( $C_p$ )-Tip Speed Ratio (TSR) curve. In this work, three types of turbines which are the H-Darrieus, Darrieus, and Gorlov are considered for design and simulation. The BEM analysis involved using twelve different types of symmetrical and non-symmetrical hydrofoils. The solidity analysis has been limited for the turbine with two, three, four and five blades for the highest power coefficient. Regardless of different topology, turbines arrangement, and control strategy, the turbines with array design are out the scope of this research.
5. The design of the turbine is based on a vertical axis turbine (VAT) with the direct-drive permanent magnet synchronous generator (PMSG). Regardless of different energy conversion and the suitability in the river, the horizontal axis turbine, cross-flow turbine and non-turbine system are out the scope of this study. Besides, the PMSG model is based

on the datasheet specification from DVE Technologies Aps with 300 AC, 5 kW and 28 poles.

6. The 6<sup>th</sup> polynomial equation to represent the  $C_P$  equation as a function of  $(\lambda)$  is suitable and can be applied for the generalised hydrokinetic turbine model. Nevertheless, the generalised model only applicable to the hydrokinetic system and design simulation under 5 m of river depth. Moreover, a 1.0 m minimum depth of the river is required due to the length of the turbine is 0.8 m. Furthermore, the output power is limited to below 5 kW with water velocity is ranging from  $0.5 \text{ ms}^{-1}$  to  $4.0 \text{ ms}^{-1}$ . Another design criteria are not applicable and out of scope.

7. In this work, the circuit topology of MPPT control for the small-scale hydrokinetic system is based on an uncontrol-rectifier with the boost converter. This circuit topology is suitable for the stand-alone system due to a low cost, simple and high reliability with only single switching control of IGBT/MOSFET.

8. In this work, the turbine inertia and generator inertia are neglected and not considered for the off-grid MPPT algorithm using the Simulink model. The reason is due to the system is considered as small-scale with the output power below 5 kW. Nevertheless, for the grid-connected system, the inertia ( $J$ ), which is combined inertia of the turbine and rotor ( $\text{kg.m}^2$ ) is considered for the dynamic modelling of the hydrokinetic system.

9. The back-to-back converter based circuit topology is employed for the grid-connected system to control the rotor side converter (RSC) and grid side converter(GSC). The field-oriented control (FOC) is applied at the RSC to extract the maximum power at the generator. Whereas, the voltage source converter is applied at the GSC to regulate the DC link voltage bus.

10. The research only focusses on the simulation model by Matlab/Simulink using Sim Power System Toolbox. The Matlab/Simulink version R2014a (8.3.0.532), 64-bit (Window 10), has been used in the simulation under the Faculty of Electrical & Electronics Engineering Technology (FTKEE) UMP license.

## 1.6 Statement of Contribution

This thesis presents an investigation and fundamental studies of the state-of-the-art of the hydrokinetic system for application in Malaysia river. In particular, the potentials of hydrokinetic technology harnessing using a sample of Pahang River and the simulation studies of the hydrokinetic turbine design based on the river characteristics. Furthermore, the thesis focuses on the design of the MPPT algorithm and controller stability using simulated data through the Matlab/Simulink toolbox.

The key contributions of the research are summarised as follow:

1. This work proposed the vertical axis H-Darrieus turbine for the energy harnessing conversion devices based on the comparison of simulation studies. Even though the H-Darrieus turbine is widely used as an energy conversion devices, however in this research, the design considerations of the H-Darrieus turbine is based on the Malaysia River's characteristics. The outcome is the  $C_P$  - $TSR$  curve which is simplified into the 6<sup>th</sup> polynomial approximation equation to represent the  $C_P$  as a function of ( $\lambda$ ) for the H-Darrieus turbine model. The turbine model is one part of the completed hydrokinetic system program. The turbine model is used to simulate the MPPT algorithm and small signal stability analysis.

2. This work proposed the MPPT algorithm for maximum energy extraction of the hydrokinetic system under the fluctuation of the water velocity. Since the MPPT algorithm in the hydrokinetic system is considered an emerging technology, hence the MPPT algorithm is inspired by the WECS. The conventional MPPT algorithm required a lot of sensors and the turbine's characteristic, which only provided by the manufacturer.

In this work, the MPPT algorithm is designed by the combination of the fuzzy logic controller (FLC) and the HCS algorithm. The outcome is a new hybrid MPPT algorithm, which is sensor-less and improved the tracking efficiency.

3. This work proposed the linearised equation using the Jacobian formulation for grid-connected hydrokinetic energy harnessing. The complete model of the hydrokinetic system consists of a turbine, PMSG, drive-train, back-to-back converter, and power grid equation have been linearised through the equilibrium point for the small-signal stability

analysis. The eigenvalues analysis has been implemented to determine the stability of the system under small disturbances, such as water fluctuation. The outcome is a new control strategy for the grid-connected hydrokinetic system based on the PI controller with the controller's gains are tuned by the eigenvalues trajectory tracing method.

## 1.7 Thesis Outlines

This thesis consists of seven chapters, including this chapter. The contents of each chapter are outlined as follows:

**Chapter 2** provides an in-depth literature review of the concept and operation of the hydrokinetic system. An overview of renewable energy to bring the hydrokinetic system into perspective as one of the possible applications of energy harnessing for the rural and small-scale is explained. Besides that, the hydrofoil profile geometry, turbine model based on  $C_P$  equation and variable speed operation have also been described. The classification of maximum power point tracking (MPPT) and different control strategies for off-grid and grid-connected have been presented.

**Chapter 3** presents the general methodology of the design and modeling of the hydrokinetic system in the river. In addition, the assessment study on the hydrokinetic energy resources at the selected river and the analysis of river basin data from the Department of Irrigation and Drainage (DID) are explained. As the thesis is writing in the paper-based format, other methods will explain in each chapter accordingly.

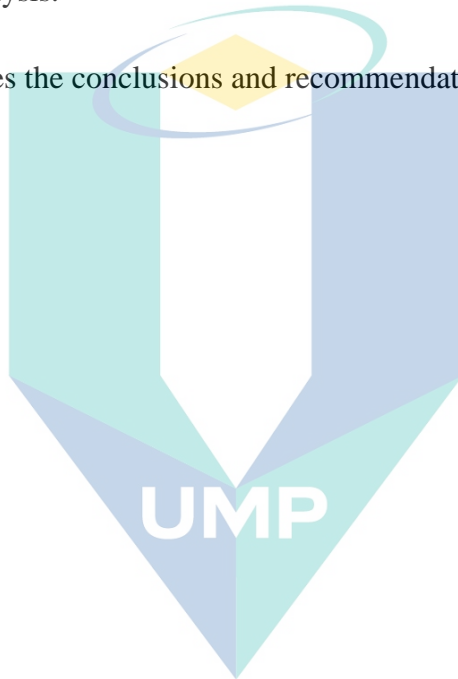
**Chapter 4** presents the design consideration for the hydrokinetic turbines, including the technical knowledge of blades and aerofoils design. The turbine design requirement is given, including the explanation of the blade element momentum (BEM). The effect of hydrofoil thicknesses and camber on the performance of the H-Darrieus, Darrieus, and Gorlov helical turbine are investigated. Besides the effect of the turbine solidity and turbine model based on the  $C_P$  equation are also discussed.

**Chapter 5** presents the maximum power point tracking algorithm used for the hydrokinetic energy harnessing in the river. The MPPT control strategy, including the

established circuit topology and the weakness of the conventional MPPT, is explained. The proposed algorithm is described and implemented in the Matlab/Simulink simulation. The performance of the proposed algorithm is presented.

**Chapter 6** focuses on the mathematical modelling of the grid-connected hydrokinetic system and the derivation of the state-space equation for small stability analysis. In addition, the proposed of the PI controller based on traces of eigenvalues is presented. The eigenvalues analysis and Matlab/Simulink model are evaluated for the validation of the small stability analysis.

**Chapter 7** provides the conclusions and recommendations for future research work.



اونيورسيتي مليسيا قهغ

UNIVERSITI MALAYSIA PAHANG

## CHAPTER 2

### LITERATURE REVIEW

#### 2.1 Chapter Overview

This chapter presents an overview of renewable energy resources and the-state-of-art of the Hydrokinetic Energy Conversion System (HECS) as an emerging technology in renewable energy. Subsequently, in depth-review of the HECS including the concept of operation, energy conversion classification, technology, assessment study, Maximum Power Point Tracking (MPPT) and control strategies are explained.

#### 2.2 Introduction

The depletion of fossil fuels, high CO<sub>2</sub> emission, global warming, and environmental pollution are among the main factors of all initiatives by governments to move forward for a sustainable environment. Renewable Energy (RE) has the potential to play a significant role as a clean and sustainable energy resource for electricity generation in the future. The RE is reliable, key-climate solution and offers climate-safe energy by reduction of CO<sub>2</sub> emission and environmental friendly (Camera, 2019).

Table 2.1 shows the prediction of renewable energy for electrical generation in the world. It is observed that the RE contributed almost 25 % of world energy demand with 6321 TWh electrical generation (IEA, 2018). The primary resources in RE are the hydropower, wind energy, bioenergy, solar PV, and geothermal. The hydropower is widely used as the world's largest clean energy source to generate electricity (Kadier et al., 2018). In 2017, the hydropower produced 4109 TWh of electrical generation, and the capacity will increase up to 6990 TWh in 2040 (IEA, 2018). The hydropower often becomes the catalyst for social-economic development, water irrigation system, flood



mitigation, etc., but embraces overwhelming complex issues such as environmental concern and nature destruction (Foo, 2015).

Table 2.1 Prediction of world renewable energy for electrical generation.

Electrical Generation (TWh)	2017	2025	2040
Bioenergy	623	890	1427
Hydro	4109	4821	6179
Wind	1085	2304	4690
Geothermal	87	129	343
Solar PV	435	1463	3839
Marine	1	3	52
Share of Total Generation	25 %	32 %	41%

The fastest-growing in RE is the WECS with the entire world installed capacity has been increased from 1.29 GW in 1995 to 568.4 GW in 2018 (GWEC, 2019). The installation cost of WECS has been decreased by more than 80 % since 1980 and keep falling (Mathias Maehlum, 2019). Also, the life-time of WECS plant has been increased up to 25 years, hence able to reduce the Levelized Cost of Energy (LCOE) approximately 7 % and 9 % for fixed-bottom offshore and floating offshore respectively (Stehly, Heimiller, & Scott, 2016). Nevertheless, the WECS is intermittent energy and not suitable to fulfil the base energy load demand. Besides, the wind turbine blades are the primary concern due to the noisy operation and a significant threat to wildlife (Frick et al., 2017; Maizi et al., 2018).

Currently, the solar PV is widely installed at the residential, commercial, and industrial park to generate the electricity (Petinrin & Shaaban, 2015). The cost of solar PV is reduced significantly from \$4 per watt in 2007 to \$0.35 per watt in 2017 (Comello, Reichelstein, & Sahoo, 2018). The cost reduction trend is predicted to continue in the future due to cheap material cost, enhanced efficiency and extensive research and



development (R&D) by public and private sector (Hansen et al., 2019). In contrast, the solar PV is also intermittent energy resource because the access to the sunlight is limited at the daylight and particular time. Besides, the solar PV plant requires much space to operate due to the low power density or watt per square meter ( $W/m^2$ ).

On the other hand, the bioenergy contributed 623 TWh of electrical power generation in 2017 (IEA, 2018). The bioenergy is based on organic waste, animals dung, agricultural waste, organic matter of plant and animal origin such as swamp and marshes (Melts, Ivask, Geetha, Takeuchi, & Heinsoo, 2019; Scarlet & Dallemand, 2018). The bioenergy offers flexibility and versatility in generating power through several methods of energy conversion system such as thermal (combustion), thermochemical (gasification, pyrolysis, torrefaction), biochemical (fermentation, anaerobic digestion) and chemical (transesterification) (Kaltschmitt & Thrän, 2019). Nevertheless, the bioenergy required the advanced technology and further technological development will enhance the energy conversion scheme such in the machines and thermal engines (Paredes-Sánchez et al., 2019).

On the contrary, geothermal energy is expected to rise significantly in the next few decades since these resources are abundant all over the world (Zwaan & Longa, 2019). In 2017, the geothermal energy resource contributed 87 TWh electricity generation, and the capacity is predicting to proliferate almost 300 % in 2040 (IEA, 2018). The geothermal is a non-intermittent source and not influence by the weather condition since the geothermal is utilizes the underground heat located from a few hundred meters up to a few kilometre depths (Gupta & Roy, 2008). Despite the enormous potentials, the geothermal energy required high initial capital costs, low efficiency, and risk of geological change due to seismic disturbances and geological alterations (Anderson & Rezaie, 2019).

All the RE resources are providing clean and sustainable energy for the future electrical generation. Although the RE resources are promising, however for the remote community's areas, where grid connection does not exist, not all RE resources are suitable to be implemented. The reasons are due to high initial capital costs, access to sunlight is limited, no head or elevation for micro-hydro power, etc. Therefore, for the off-grid

remote areas, small-scale renewable energy technology is possible to provide the electricity. Hence, the hydrokinetic energy harnessing based on free-flowing water is one of the possible options to supply the power for the remote community located near to the river.

### 2.3 An Overview of River Current Energy Conversion System (RCECS)

The RCECS has utilised the water turbine and conversion devices to extract the kinetic energy of river flow (M. J. Khan et al., 2008). Several terms have been used to represent the RCECS and term is interchangeable. Radkey & Hibbs (1981) has defined the river current turbines as low-pressure run-of-the-river or ultra-low-head turbine due to the technology is able to operate at equal or less than 0.2 m of head/elevation. The term run-of-river also has been applied by Yah, Oumer, & Idris, (2017) to classify the hydropower technology based on natural water flow.

The interchangeable term such as water current turbine (Peter Garman, 1986; Ponta & Dutt, 2000), zero head turbine (Niebuhr, van Dijk, Neary, & Bhagwan, 2019; Yavuz, Kilkis, Akpınar, & Erol, 2011), in-stream turbine by Lalander & Leijon (2009), hydrokinetic turbine (Grabbe, Yuen, Goude, Lalander, & Leijon, 2009; M. J. Khan, Bhuyan, Iqbal, & Quaiçoe, 2009). The hydrokinetic energy conversion system (HECS) are commonly used and employ the same principle of operation. In this thesis, the term RCECS, HECS, and hydrokinetic will be used extensively and identical to each other.

The water stream was used as a source of energy almost for centuries in the world (Tasnier-Gesner et al., 2014). During that era, the watermills or paddle-wheels have been used to drive the mechanical proses such as grinding, rolling, and hammering in the food processing (Elliott, 2013). The time line of hydrokinetic progress and development is shown in Figure 2.1.

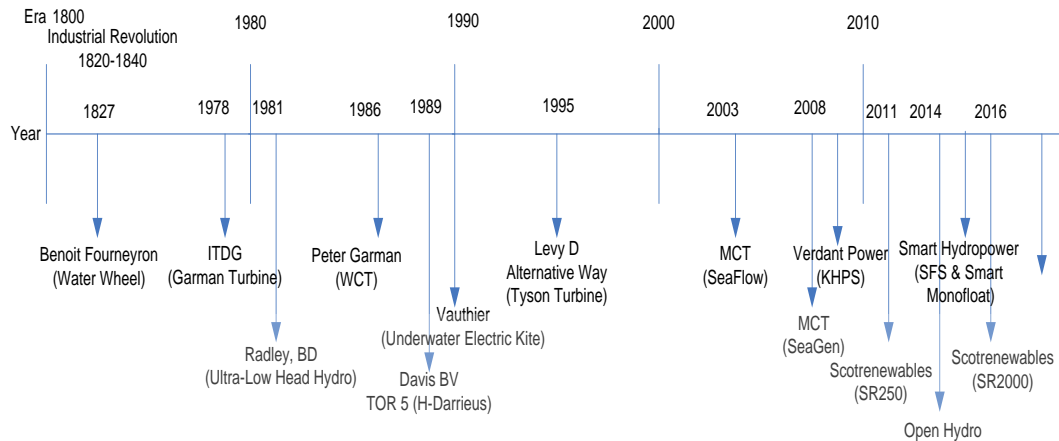


Figure 2.1 Timeline for development of hydrokinetic technology (not limited to)

The first literature regarding the energy harnessing by the flow of water is recorded in 1827 through the development of a Water Wheel (Benoit Fourneyron, 1827). The WCT is used for water pumping and electricity generation in the remote area. In 1978, the Intermediate Technology Development Group (ITDG) was developed the Garman Turbine for water pumping and irrigation system.

During the early 1980s, a free rotor with 15 kW output power at  $3.87 \text{ ms}^{-1}$  water velocity has been installed under US Department of Energy's for ultra-low head hydro energy program as reported in (RL & BD, 1981).

The experiment on using WCT for electricity generation and irrigation has been carried to several countries such as Canada (Davis, 1989), Zaire, Africa (Mukherji, 2010) and Australia (Levy, 1995). Straight blades Darrieus turbine has been used in Canada and Africa with 5 kW and 15 kW output power respectively. Other similar work also has been carried out by Alternative Way, Nimbin in Australia (Ponta & Dutt, 2000). The company has introduced a horizontal axis Tyson Turbine with the generator submerged in the water. In 1990 the idea to manipulate the WCT for the large scale capacity has emerged (Güney & Kaygusuz, 2010).

During early of 2000, the Marine Current Turbine (MCT) Ltd has successfully deployed the Seaflow Project under the finance of UK DTI, European Commission, and the German government (Fraenkel, 2004). Currently, the marine and tidal hydrokinetic

technology is doing the pre-commercial testing under The European Marine Energy Centre Ltd (EMEC) (“Atlantis Resources Corporation,” 2019). On the other hand, the Smart Hydro Power GmbH has produced the Smart Monofloat and Smart Free Stream in the river to enhance the productivity and living standard in the off-grid remote communities. (“Smart Hydro Power,” 2019).

The review found that hydrokinetic technology is not only for generating electricity but also can be applied in the irrigation system and food processing. Even though several terms have been used to represent this kind of technology, the use of hydrokinetic energy conversion is preferable in this field. Based on the timeline for hydrokinetic technology development, starting from years of 2000 and beyond, hydrokinetic technology becomes one of the popular in research and development.

## **2.4 Hydrokinetic Energy Conversion System (HECS)**

The structure of the hydrokinetic system is presented in this section. Subsequently, the brief concept, operation and the comparison between the conventional hydropower and WECS are described at the end of this section.

### **2.4.1 The structure of Hydrokinetic System**

The structure of the hydrokinetic system consists of a hydrokinetic turbine, generator (PMSG), power electronics conversion, and battery or grid-tie connection system, as shown in Figure 2.2. The flowing water able to rotate the turbine at a certain speed of velocity. The Permanent Magnet Synchronous Generator (PMSG) rotor coupled to the turbine shaft directly without a gearing system, and the movement automatically turns the generator rotor to operate. The output power from the PMSG has been controlled and converted by the power electronics conversion system. In the stand-alone system, the variable AC (three-phase) system converted into the variable DC voltage through three-phase rectifiers. Then, the DC-DC converter converted the variable DC voltage into a

constant DC bus voltage. In contrast, the grid-tie connection system, an inverter used to convert the constant DC bus voltage into AC power prior transport it to the grid system.

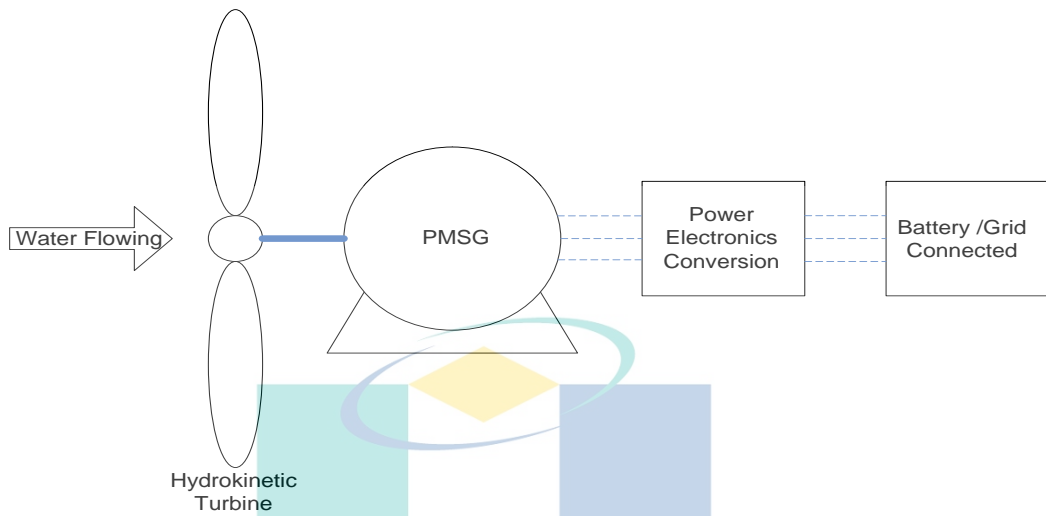


Figure 2.2 The structure of hydrokinetic system. The high-end system can be a stand alone or grid connected system.

#### 2.4.2 Concept and Operation of the Hydrokinetic System

The ability of the hydrokinetic turbines to capture the power depends on the water density ( $\rho$ ), turbine power coefficient ( $C_p$ ), cross-sectional area ( $A$ ), as well as velocity cubed ( $V$ ) (Sornes, 2010; Vermaak, Kusakana, & Koko, 2014). The ideal kinetic energy of the hydrokinetic system is given by Eq.(2.1).

$$E = \frac{1}{2}mV^2 \quad 2.1$$

where  $V$  is the speed of water,  $m$  is the mass of water, which is given by Eq.(2.2).

$$m = \rho v \quad 2.2$$

where  $\rho$  is the water density (approximately  $1022 \text{ kg/m}^3$ ) and  $v$  is the water volume. Consequently, the kinetic energy can be expressed in Eq.(2.3).

$$E = \frac{1}{2} \rho v V^2 \quad 2.3$$

For a mass of water passing through a rotor with a cross-sectional area of  $A$ , the ideal power can be expressed in Eq.(2.4).

$$P = \frac{1}{2} \rho A V^3 \quad 2.4$$

Considering the efficiency of the turbine, the mechanical power can be expressed by Eq.(2.5).

$$P_m = \frac{1}{2} \rho A C_p V^3 \quad 2.5$$

where  $P_m$  is the power developed by the rotor (W), and  $C_p$  is the power coefficient of the turbine.

$C_p$  is the percentage of power that the turbine can extract from the water flowing through the turbine. According to the studies carried out by Betz, the theoretical maximum amount of power that can be extracted from a fluid flow is about 59 %, which is referred to the Betz limit (Vermaak et al., 2014). In addition,  $C_p$  is the function of the Tip Speed Ratio ( $TSR$ ) which is the ratio of the linear speed of the tip of the blade to the water speed given by Eq.(2.6).

$$\lambda = \frac{\omega_m R}{V} \quad 2.6$$

where  $R$  is the turbine radius and  $\omega_m$  is the turbine rotational speed. On the other hand, the mechanical torque ( $T_m$ ) can be determined by Eq.(2.7).



$$T_m = \frac{P_m}{\omega_m}$$

2.7

The review proves that hydrokinetic technology's structure required a turbine for energy conversion, a generator to produce electricity and a power electronics converter to control the output power. On the other hand, the energy capacity depends on the water density, turbine power coefficient and swept area, and water velocity cubed.

## 2.5 Hydrokinetic Turbine Classification

As an emerging technology in renewable energy, the hydrokinetic system can be classified based on the energy conversion scheme and the working principle of the system. M. J. Khan et al. (2009) and Lago et al. (2010) have classified the hydrokinetic technology in two classes based on conversion scheme: first is using a turbine and second is the non-turbine system. Figure 2.3 shows the hydrokinetic configuration under turbines and non- turbine classification.

اونيورسيتي ملايسيا قهغ

UNIVERSITI MALAYSIA PAHANG



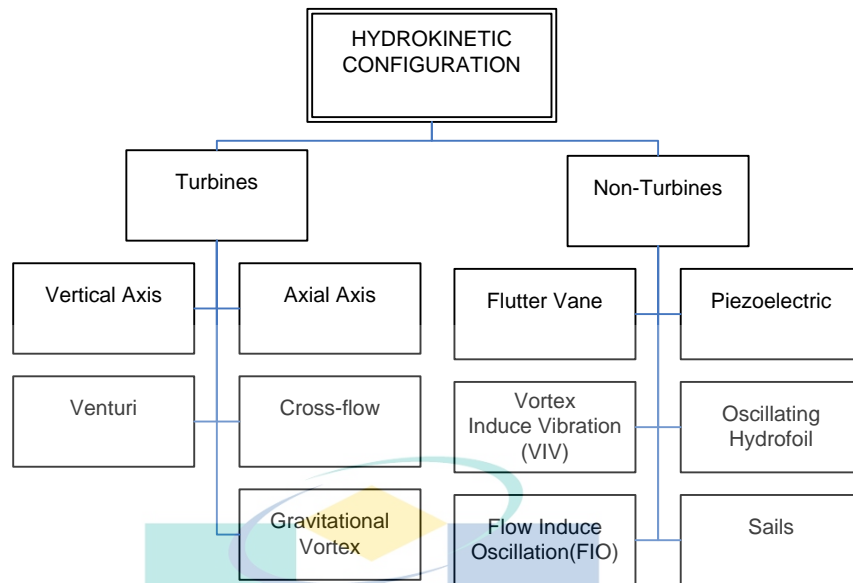


Figure 2.3 Hydrokinetic configuration under the classification of the energy conversion scheme

### 2.5.1 Horizontal Axis Hydrokinetic Turbines

The conversion scheme using the turbines such as horizontal axis, vertical axis, and cross-flow are widely used in HECS as reported by Elbatran et al. (2015). According to Magagna & Uihlein (2015), the horizontal axis turbine has dominated almost 76 % of the research and development in the turbine's design worldwide. The horizontal axis turbine is having the rotational axis parallel or inclined to the direction of flowing water, as shown in Figure 2.4(a)-(d). The advantage of horizontal axis turbine is the turbine has the self-starting capability under slow water current (Sandile Phillip Koko, Kusakana, & Vermaak, 2015). Nevertheless, the turbine is easy to get clogged with debris in the river, and the cost of manufacturing is higher compared to the vertical axis turbine.

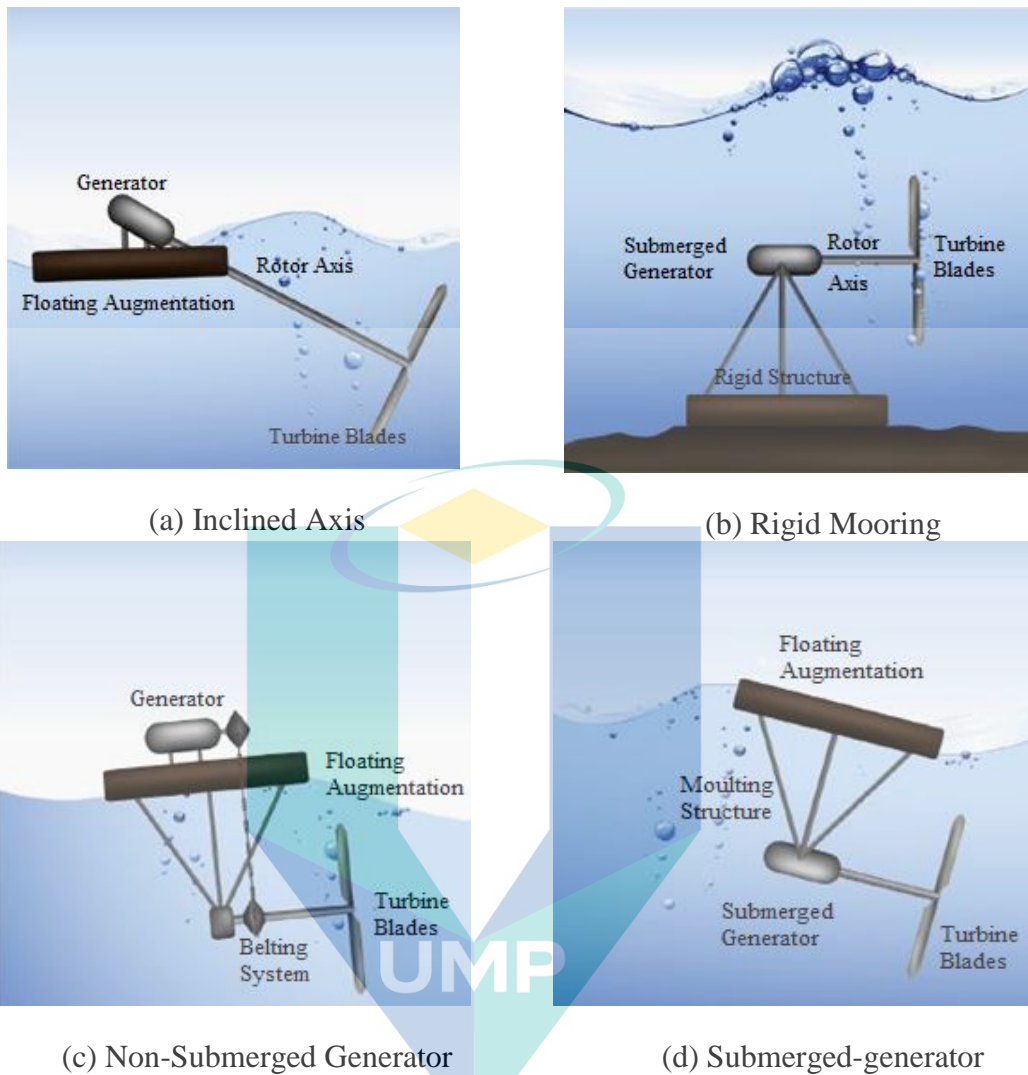


Figure 2.4 Horizontal axis turbines in the hydrokinetic system.

Source: Behrouzi et al., (2016)

### 2.5.2 Vertical Axis Hydrokinetic Turbine

The vertical axis turbine is commonly used to extract the kinetic energy in the rivers (Behrouzi et al., 2016). The vertical-axis turbines as shown in Figure 2.5 (a)-(e) have the rotor's axis of rotation is at a right angle to the surface of the water (Khalid, Liang, & Shah, 2013). This property means that vertical-axis turbines can do without a yawing device since it can handle incoming flows from any direction. Besides, the turbines are quieter in operation, and the mechanical complexity has been reduced. Furthermore, this

type of turbine requires no gearing coupling, and the costs will decrease because of placement above water (Birjandi, Woods, & Bibeau, 2012).

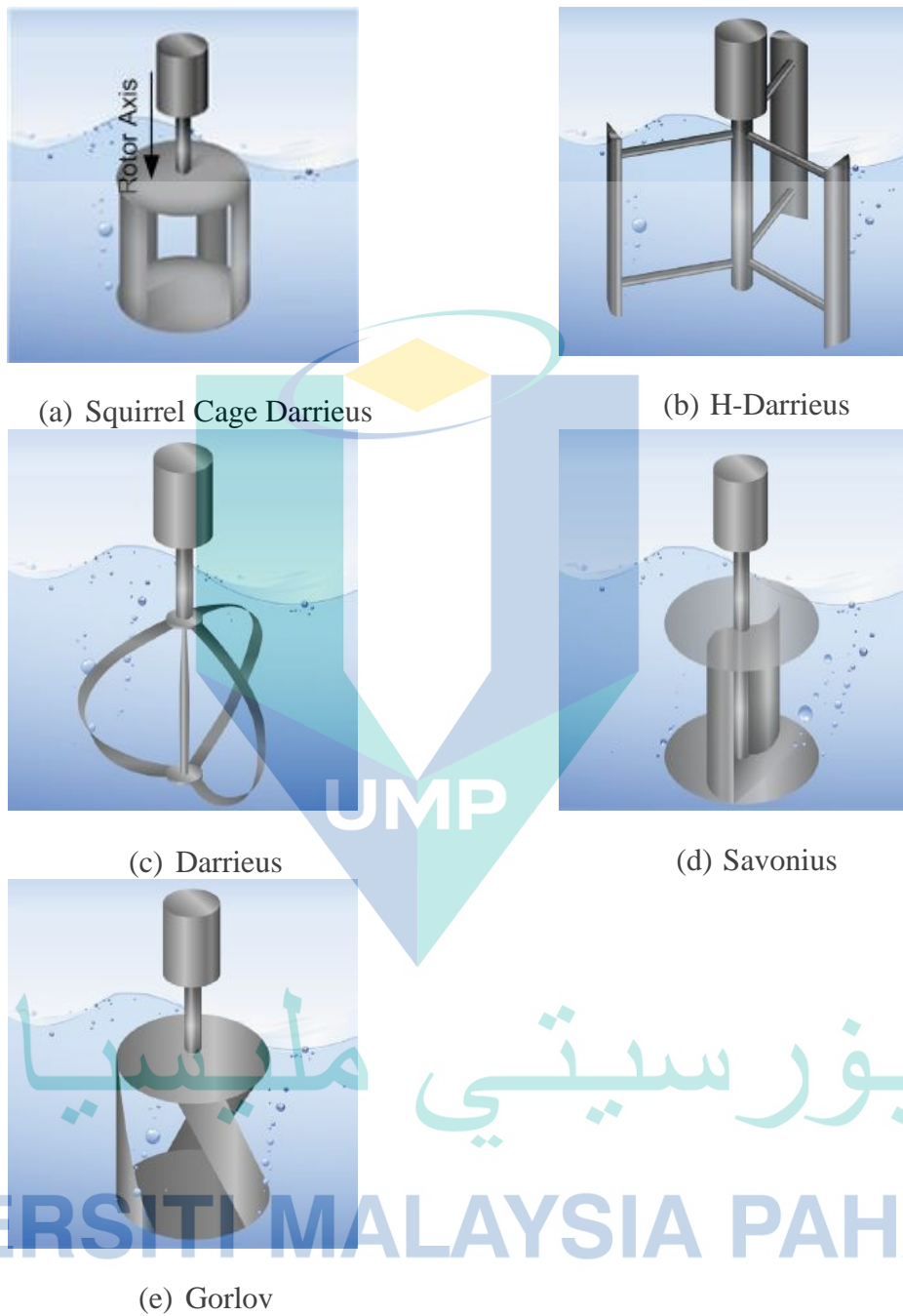


Figure 2.5 Vertical Axis Turbine hydrokinetic turbines

Source:Behrouzi et.al, (2016)

### 2.5.2.1 H-Darrieus Turbine

The Darrieus rotor configuration gained significant attention due to its unique performance, operational and design features. This turbine design was invented by G.J.M Darrieus, who was a French inventor. In 1931, the turbine was patented by the U.S Patent Office (Chong & Lam, 2013). The H-Darrieus turbine had its axis perpendicular to the direction of incoming water as shown in Figure 2.5 (b). This means that the vertical axis can accept incoming flow from any direction and therefore did not require the yaw mechanism (Sornes, 2010).

As noted by Wang et al. (2018), the advantages of the H-Darrieus turbine are light weight, balance proportion, high  $C_p$  and high prospects of application. Moreover, the design of H-Darrieus straight blades was simple and less expensive compared to the horizontal axis turbine (Malipeddi & Chatterjee, 2012; Patel, Eldho, & Prabhu, 2017a). Nevertheless, the mechanical vibration is occurred on the turbine body which can reduce the life time of the turbine and consequently, less of the output power (Karimian & Abdolahifar, 2019).

### 2.5.2.2 Darrieus Turbine

The Darrieus turbine is a curved blades turbine as shown in Figure 2.5 (c). Nevertheless, the Darrieus turbine has lower self-starting capability to rotate. This reason is due to the small bending stress on the turbine blades (Wang et al., 2018).

### 2.5.2.3 Gorlov Helical Turbine (GHT)

The GHT was invented and patented by Professor Alexender M Gorlov from Northeastern University, Boston, USA in 1995 (Bachant & Wosnik, 2015). The GHT was designed based on twisted blades with helical shape as shown in Figure 2.5 (e). The advantages of GHT are can be operated in shallow water depth and easy to install because of simple mechanical coupling (Pongduang et al., 2015). In addition, the Gorlov turbine

is able to reduce the torque ripple during the start-up rotation (Tanier-Gesner et al., 2014). Nevertheless, the helical blades are more complicated, expensive to design and fabricate and produces the lower averages of the output power.

### 2.5.3 Cross-flow Hydrokinetic Turbine

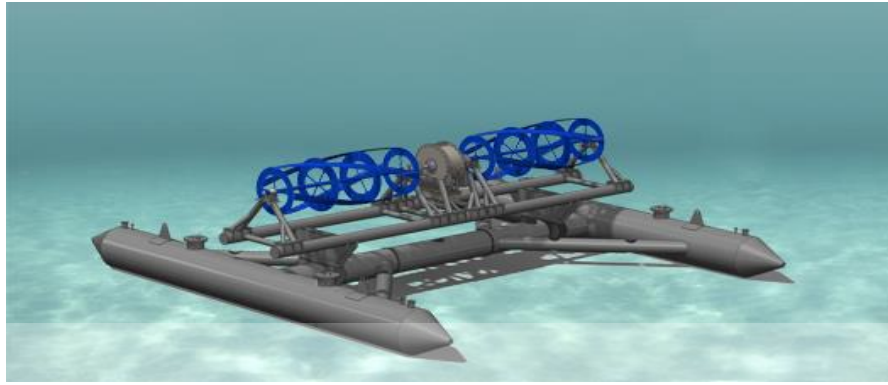
The cross-flow turbine has the orthogonal rotor axis with respect to the flow of water but parallel with reference to the surface of the water (Laws & Epps, 2016). The cross-flow turbine can operate without the yawing mechanism similar to vertical axis turbine (Bachant & Wosnik, 2015). In addition, the cross-flow turbines are preferable to use in hydrokinetic farm or arrays due to more economical in space, and the rectangular swept area will increase the output power (Cavagnaro, 2016). Besides, this turbine also is operated at a lower speed, as a result, will reduce the cavitation, low noise and safe for marine animals (Forbush et al., 2017).

Figure 2.6 shows the example of the cross-flow turbine by Ocean Renewable Power Company (ORPC). The ORPC founder in 2004 at Florida is one of the active companies in marine renewable energy. In 2015, the ORPC successfully installed the RivGen to the remote Alaska village. The company also has installed the first grid-connected hydrokinetic system from the tidal energy system using the TidGen at eastern Maine in 2012 (ORPC, 2019).

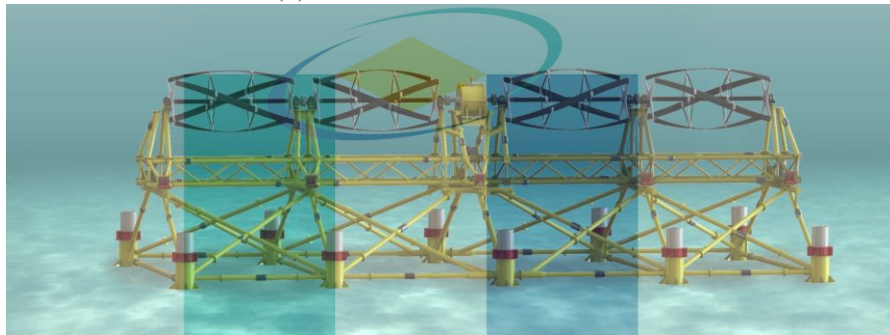
اونيور سيئي مليسيا قهغ

UNIVERSITI MALAYSIA PAHANG





(a) RivGen CrossFlow Turbine



(b) TidGen CrossFlow Turbine

Figure 2.6 The RivGen and TidGen produced by ORCP.

Source: TidGen Power Generation (2017).

#### 2.5.4 Non-Turbine Hydrokinetic System

The non-turbine system is also can be used to extract the power from the free stream velocity in the marine, river, or open channel. The flapping foil, as shown in Figure 2.7 (a) is inspired from the animal's motion due to their aerodynamic manoeuvrability in the water flow (Karbasian et al. 2016). Figure 2.7 (b) depicts the physical design model of sails to extract the energy from the water flow. The model is represented by the series of sails that are connected and rotate in rectangular motion. If the water flows through the device, the sails produce a lift force perpendicular to the water flow that able to turn the generator (Arkel et al., 2011).

On the other hand, the concept of VIVACE converter is utilized from the Vortex-Induced Vibration (VIV), galloping, and Flow-Induced Motions (FIM) as shown in

Figure 2.7 (c). The early model of VIVACE converter is a combination of physical spring, damper, and generator (J. H. Lee, Xiros, & Bernitsas, 2011). Nevertheless, recent VIVACE is more complicated with cylinder, a belt, and pulley transmission, a generator and controller to control the damping and spring force. The flutter flag consists of von Karman hydrodynamic instability and two-layer of piezoelectric polymer PVDF with an electrode in-between, as shown in Figure 2.7 (d) (Pobering & Schwesinger, 2004). As in turbulent water flow, the different pressure around the flag resulting bending occurred. The twist will activate the charge separation inside the piezoelectric materials to produce the energy.

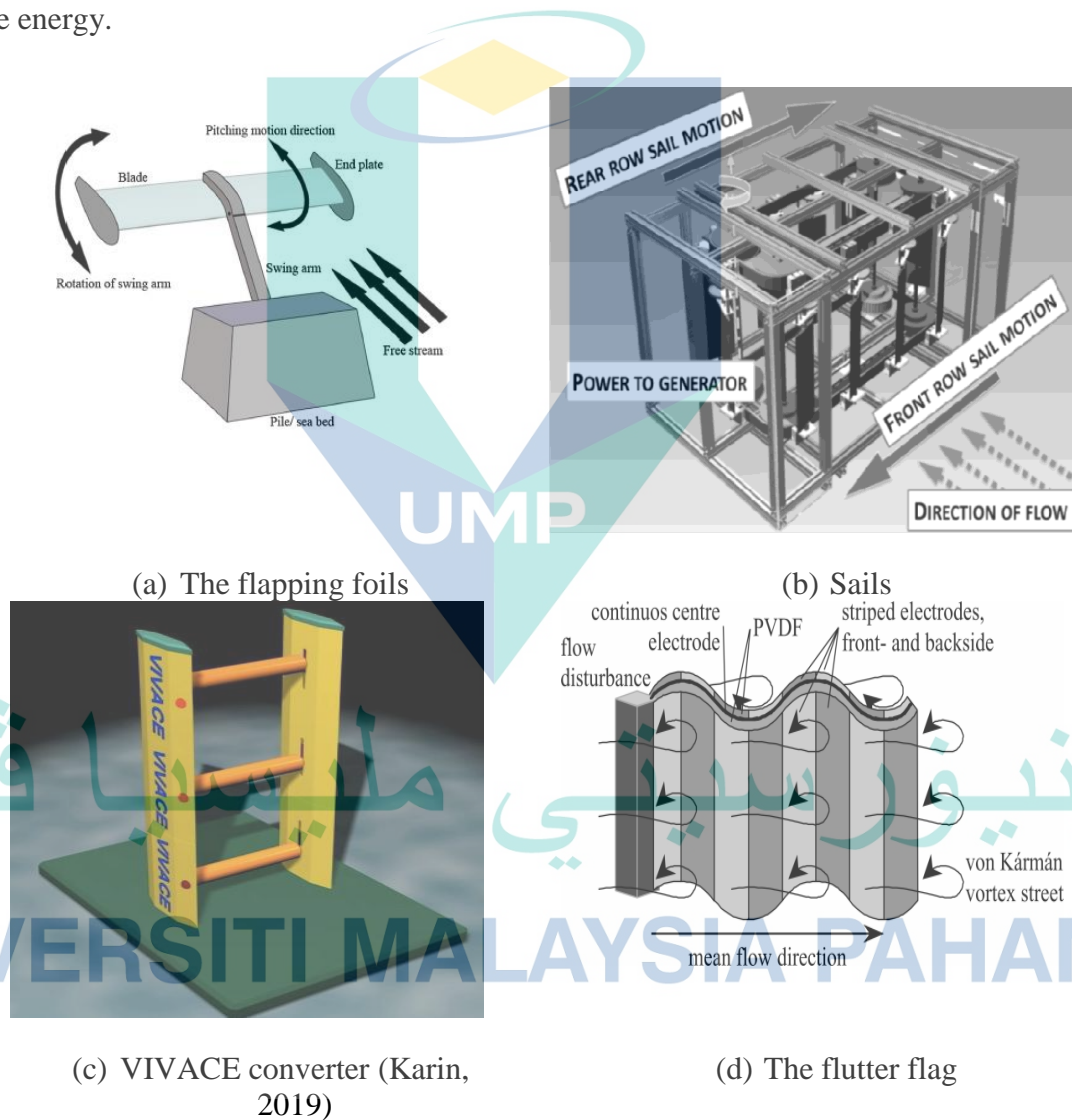


Figure 2.7 Non-Turbine system for energy conversion in the water.



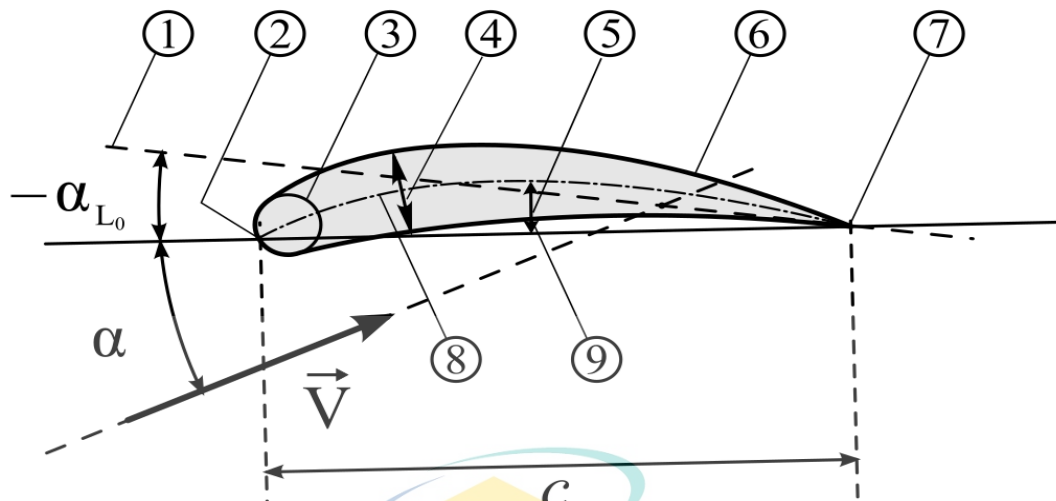
Judging from literature, the hydrokinetic turbine classification can be classified under the turbine and non-turbine system. The review indicates that the energy conversion through the turbine system has dominated the research and development of hydrokinetic technology worldwide. The vertical axis turbine is preferable for the river application due to small capacity, practicality and cost-saving. Nevertheless, the non-turbine system for hydrokinetic technology is still a new research concept that requires many studies to test the reliability and practically for energy harnessing.

## 2.6 Turbines Hydrofoils Selection

In this section the basic hydrofoils geometry for the turbine blades profile is presented. Subsequently, the standardised NACA hydrofoils is discussed at the end of this section.

### 2.6.1 Hydrofoils Profiles Geometry

The selection of blades profile shape is an essential to determine the aerodynamic or hydrodynamic performance. As noted by Heliciel (2020), the lift and drag ratio is important as it provided the quality of the profile by represented the forces around the airfoils. The airfoils which able to generate the maximum  $F_L$  with minimum  $F_D$  is one of the key performance in blades profile selection. On the other hand, the thickness of the airfoils is used to measure the strength of the blades. Figure 2.8 shows the profile geometry of hydrofoils.



where,

- |                                 |                                 |                         |
|---------------------------------|---------------------------------|-------------------------|
| 1. Zero Lift Line               | 2. Leading edge                 | 3. Nose circle          |
| 4. Thickness                    | 5. Camber                       | 6. Upper surface        |
| 7. Trailing edge                | 8. Main camber line             | 9. Lower surface        |
| $\alpha$ is the angle of attack | $\vec{V}$ is the water velocity | $c$ is the chord length |

Figure 2.8 Airfoils profile geometry

Source: McCormick (1998)

According to Mohamed (2012), NACA 00XX, NACA 63XXX, S-series, A-series, and FX-series are commonly used as an airfoil for the wind turbines blades profiles. In his studies, the turbine with the different airfoils has been investigated to find the highest output torque. Nevertheless, the research studied concentrated on large turbines with higher capacity of output power. On the contrary, Islam et al. (2019) investigated a suitable airfoil for a small wind turbine system. Their findings indicate that the NACA airfoils have better average performance compared to the NREL airfoils. Nevertheless, the samples of studies are limited to NACA and NREL-S series airfoils types only.

Several researchers have investigated the effect of airfoils profiles on the aerodynamic performance on the vertical axis wind turbines. Jafari et al. (2018) studied and investigated the effect of airfoils profile at a different height, tip speed ratio, and solidity. Nevertheless, his study only focuses on six asymmetrical airfoils, which are

S809, S814, RISO-A1-24, DU 93-W-210, FFA-W3-241, and FX66-S196-V1. Subramaniam et al. (2017) presented the 3D CFD model to study the effect of the airfoils and solidity on the small scale wind turbines. Nevertheless, the analysis is limited to four different airfoils consists of NACA 0012, NACA 0015, NACA 0030, and AIR 001.

## 2.6.2 National Advisory Committee for Aeronautics (NACA) Airfoils

A standardised airfoil from the NACA was commonly used in designing the airfoils for aircraft, wind turbine and hydrokinetics blades system. The profile of NACA airfoils is described by a series digit as shown in Figure 2.9. For instance, the NACA 2415 has a maximum camber of 2 %, located at 40 % from leading edge with 15 % of maximum thickness.

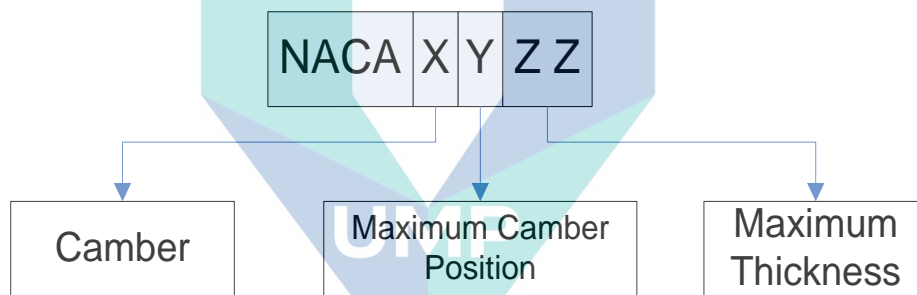


Figure 2.9 NACA four digit series

Source: Wang et al. (2018)

From the review, it is discovered that hydrofoils profiles are classified into symmetrical and non-symmetrical geometry. A standardised airfoil from National Advisory Committee for Aeronautics (NACA) and National Renewable Energy Laboratory (NREL) is commonly used as an airfoil for aircraft and wind turbine systems. Symmetrical hydrofoil profiles such as NACA four series, NACA five series, S-Series, A-Series and FX-series are practically used for hydrokinetic technology as a blades profiles for energy harnessing.

## 2.7 Power Turbine Modelling

This section presents the modelling of the power turbine,  $C_P$ - $TSR$  curve to represent the characteristic of the turbine. At first, the modelling of power turbines in WECS is described and followed by the modelling of power turbines for the hydrokinetic system.

### 2.7.1 Modelling of General $C_P$ Equation in WECS

The turbine characteristic,  $C_P$ - $TSR$  curve, can be modeled through the numerical approximation and curve fitting. According to (Bracke 2014), the relationship  $C_P(\lambda, \beta)$  can be determined by simulation and experimental studied. Some of the manufacturers in wind turbine industries are provided the turbine characteristics curve for their customers. For instance, the General Electric Company USA is provided the wind power model as given in Eq. (2.8) (Miller, Price, & Sanchez-Gasca, 2003).

$$C_P(\lambda, \beta) = \sum_{i=0}^4 \sum_{j=0}^4 \alpha_{i,j} \lambda^i \beta^j \quad 2.8$$

where  $\alpha_{i,j}$  is a turbine coefficient and given in Table 2.2.

As noted by Miller et al. (2003), the curve fitting method is used to obtain the mathematical representation of the  $C_P$  model in Eq. (2.8). Nevertheless, the turbine model is only applicable to the larger wind turbine system with the output power between 1.5 MW and 3.6 MW. A similar turbine power model is also used by Lei Wang (2012) to control the DFIG to achieve the maximum power in WECS. Besides, most of the researchers such as Mousa et al. (2019), Liu et al. (2017) and Nasiri et al. (2014) used the general equation model as given in Eq. (2.9) to represent the dynamic behavior of turbine.

Table 2.2  $C_P$  Coefficient  $\alpha_{i,j}$  for modelling of turbine power equation

Source: Miller et al. (2003),

<b>i</b>	<b>j</b>	<b><math>\alpha_{i,j}</math></b>
4	4	$4.9686e^{-010}$
4	3	$-7.1535e^{-008}$
4	2	$1.6167e^{-006}$
4	1	$-9.4839e^{-006}$
4	0	$1.4787e^{-005}$
3	4	$-8.9194e^{-008}$
3	3	$5.9924e^{-006}$
3	2	$-1.0479e^{-004}$
3	1	$5.7051e^{-004}$
3	0	$-8.6018e^{-004}$
2	4	$2.7937e^{-006}$
2	3	$-1.4855e^{-004}$
2	2	$2.1495e^{-003}$
2	1	$-1.0996e^{-002}$
2	0	$1.5727e^{-002}$
1	4	$-2.3895e^{-005}$
1	3	$1.0683e^{-003}$
1	2	$-1.3934e^{-002}$
1	1	$6.0405e^{-002}$
1	0	$-6.7606e^{-002}$

اونيورسيٲى ملايسيا قهغ

UNIVERSITI MALAYSIA PAHANG

$$C_P(\lambda, \beta) = C_1 \left( \frac{C_2}{\lambda_i} - C_3 \beta - C_4 \right) e^{\frac{-C_5}{\lambda_i}} + C_6$$

2.9

where coefficient  $C_1$ - $C_6$  are given as follows:  $C_1=0.5176$ ,  $C_2=116$ ,  $C_3=0.4$ ,  $C_4=5$ ,  $C_5=21$ ,  $C_6=0.0068$  and  $\lambda_i^{-1} = (\lambda + 0.08\beta)^{-1} - 0.035(1 + \beta^3)^{-1}$ .

According to Sloodweg et al. (2002), the numerical approximation was used to develop the turbine model characteristic such given in Eq.(2.9). The numerical approximation method is based on minimising the error between the simulation and datasheet from the manufacturer. Nevertheless, this general equation model is suitable to be applied for a larger horizontal axis wind turbine with the pitch control system.

On the other hand, a comparison between the turbine model was conducted by Xia et al. (2013). Several different turbine models, as given in Eq. (2.10)-(2.12), were analysed to investigate the turbine model performance. As noted by Xia et al. (2013), all the turbine models have the same curve pattern with the maximum  $C_P$  at  $TSR=8$ . Nevertheless, Eq. (2.12) was recorded with the highest  $C_P$  compared to other models.

$$C_P(\lambda) = (1.12\lambda - 2.8)e^{-0.38\lambda} \quad 2.10$$

$$C_P(\lambda, \beta) = 0.22 \left( \frac{116}{\lambda_i} - 0.4\beta - 5 \right) e^{-\frac{12.5}{\lambda_i}} \quad 2.11$$

$$C_P(\lambda, \beta) = (0.44 - 0.0167\beta) \sin \frac{\pi(\lambda - 2)}{13 - 0.3\beta} - 0.00184(\lambda - 2)\beta \quad 2.12$$

The turbine power model in Eq. (2.10) was proposed by Wai (2007) to develop a novel maximum power tracking algorithm based on the conventional Hill-Climbing Search (HCS) algorithm. Nevertheless, the turbine model is applied for a small wind turbine system without a pitch controller. Whereas, the turbine model for Eq (2.11) is

similar to Eq. (2.9), except the coefficient is different due to the dynamic characteristic of the turbine. Kim & Eung-Sang (2007) proposed the turbine model for Eq. (2.12) to investigate the control performance and dynamic behaviour of variable speed grid-connected wind turbines. Nevertheless, the turbine model is based on the horizontal axis turbine with two blades profiles.

### 2.7.2 Modelling of General $C_P$ Equation in Hydrokinetic

Based on the literature searching in modelling of power turbines for the hydrokinetic system, two researchers were presented the turbine model equation in this field. Odedele et al. (2014), was implemented the turbine model based on an analytical approximation method for tidal energy harnessing. The equation is given by Eq. (2.13).

$$C_P(\lambda, \beta) = C_1(C_2 - C_3\beta - C_4\beta - C_5)e^{-C_6} + C_7 \quad 2.13$$

where  $C_1=0.5$ ,  $C_2=116\lambda$ ,  $C_3=0.4$ ,  $C_4=0$ ,  $C_5=5$ ,  $C_6=21\lambda$ ,  $C_7=0.01\lambda$ , and  $\beta=0$ .

The equation model has been applied to achieve the maximum power for the off-grid system by proposed the passive rectifier control strategy. Nevertheless, the type of turbine is undisclosed, but the turbine model is applicable for a small scale system with a fixed pitch angle for tidal energy harnessing.

Donald et al. (2017) applied the general equation turbine model to study several MPPT algorithms for hydrokinetic energy harnessing. The turbine model is based on polynomial approximation, and the equation was acquired numerically from ANSYS CFX software. The turbine model is given by Eq.(2.14).

$$C_P(\lambda) = -0.0295\lambda^4 + 0.2169\lambda^3 - 0.6754\lambda^2 + 1.0122\lambda - 0.1958 \quad 2.14$$

The turbine model is managed to achieve 0.39 of the power coefficient by optimal torque (OT) MPPT control. Nevertheless, the turbine model is designed based on the



horizontal axis turbine with a fixed pitch angle as well as limited to 10 kW of output power.

Judging from the literature, the modelling of the general  $C_P$  equation to represent the turbine characteristics in the hydrokinetic system is scarce and limited. The turbine model can be determined using simulation or experimental studied to find the relationship between  $C_P$  and  $\lambda$ . The curve fitting method is commonly used to obtain a mathematical representation of the  $C_P$  equation. Several turbines models have been developed in the WECS system; however, the turbine model can be applied for a larger wind system. The turbine model based on the polynomial approximation equation was applied in hydrokinetic technology. Nevertheless, the turbine model is based on the horizontal axis turbine with two blades profiles.

## 2.8 Comparison of Hydrokinetic System with other Technology

This section presents the comparison of the hydrokinetic system between the conventional hydropower and WECS. The advantages and disadvantages of each technologies is described.

### 2.8.1 Hydrokinetic Versus Conventional Hydropower

As one of promising renewable energy, the HECS offers economical and reliable option for the remote area and off-grid system compared to the conventional hydropower. The conventional hydropower required a head ( $H$ ) and the flow rate ( $Q$ ); as the output power is proportional to both parameter (Mishra, Khare, & Agrawal, 2015). On the contrary, the HECS does not required a head, large dam or reservoir to operate but a free stream velocity as low as 0.3 m/s is acceptable to rotate the small turbine (Sarma, Biswas, & Misra, 2014).

The construction of large conventional hydropower gives a negative impact on the environment and ecosystem. Sovacool & Bulan (2012) reported that more than 1600

protected plants and 300 rare and engendered species are threatened due to the development of the Bakun hydropower in Sarawak. In addition, Izadyar et al. (2016) reported that almost 10000 indigenous people need to relocate due to the hydropower plant construction.

In contrast, the HECS give less impact to flora and fauna compared to conventional hydropower (Petrie, Diplas, Gutierrez, & Nam, 2014). According to Güney & Kaygusuz (2010), HECS is environmentally friendly and water-life friendly. For example, several researchers have investigated on impacted of hydrokinetic turbines on fish. Romero-Gomez & Richmond (2014) has reported that the survival rates of fish on the hydrokinetic system due to blade-strike are higher than 96 % and better than conventional hydropower. Besides, Schramm et al. (2017) reported that nothing happened to the behavior of fish due to the turbines sound emission.

Furthermore, even the capacity of power generation for hydrokinetic is small compared to conventional hydropower, however by array system or hydrokinetic farm, the capacity of HECS can be increased up to 100 Megawatt of power (Laws & Epps, 2016). To date, several studies have reported regarding the hydrokinetic array system. For example, Vennell et al (2015) has proposed the design layout for macro-micro array turbines in HECS. The controller and details design for modular hydrokinetic connected to the smart grid has presented by (Alvarez Alvarez et al., 2018). Table 2.3 shows the summarise of comparison between conventional hydropower and hydrokinetic technology.

Table 2.3 Comparison between conventional hydropower and hydrokinetic technology

Conventional Hydropower	Hydrokinetic
Required Head (H) and Flow Rate (Q)	Without Head or reservoir
Negative impact to nature due to construction.	Less impact to nature and environmentally friendly
Fixed Construction	Portable and easy moving
High initial starting cost	Minimal cost
High output power	Low output power

### 2.8.2 Hydrokinetic Versus Wind Energy Conversion System

Most of the researchers, Behrouzi et al. (2016), Kumar et al. (2016a) and Vermaak et al. (2014) have reported that the hydrokinetic system was similar to wind turbine system in term of concept, operation and as well as electrical hardware. In addition, A S Bahaj & Myers (2003) has identified that with the water velocity between 2-3  $\text{ms}^{-1}$ , the hydrokinetic system able to generate four times output power than a similarly rated wind turbine. On other words, the size of the hydrokinetic turbine could be much smaller than WECS but have the same capacity of the output power. This is because of the water density is 800 times greater than air density (Marine Renewables Canada, 2018; Zupone et al., 2015).

The significant difference between the HECS and WECS is the range of Tip Speed Ratio (TSR). Ginter & Pieper (2011) has reported that the HECS has a lower TSR than WECS. The optimal TSR for WECS is typically between 5 to 6. In contrast, the TSR value for HECS is less than 2.5 to avoid the cavitation (Salter, 2005).

Furthermore, Romero-Gomez & Richmond (2014) has reported that the HECS is less dependent on weather condition, unlike WECS. The direction and water velocity are practically fixed and can be predicted during seasonal monsoon compared to WECS (Shahsavari, Bibeau, & Chatoorgoon, 2015). On the contrary, the WECS is highly non-linear system due to the speed and direction of the wind are influenced by the atmospheric changes such as air pressure, air temperature and earth's rotation (Barber, 2018).

Conversely, E. Muljadi et al (2016) has found that the level of turbulence in the air and water are similar for HECS and WECS. The high turbulence flow will affect the efficiency of the system and reducing the output power (Hamta, Birjandi, & Bibeau, 2013). Besides, it will increase the mechanical stress and inducing the more significant fatigue on the physical components of both systems. Therefore, the turbine design and the employment of control strategy such as maximum power point tracking algorithm (MPPT), pitch control and robust controller are required to reduce the mechanical stress and fatigue due to turbulent effect in the harsh marine environment. Table 2.3 shows the

comparison between WECS and hydrokinetic technology in term of turbine size, weather condition, TSR and turbulence.

Table 2.4 Summary comparison between WECS and hydrokinetic technology

<b>WECS</b>	<b>Hydrokinetic Technology</b>
Required a large size of turbine	Small size of turbine
Highly dependent on weather condition	Less dependent on weather condition
Optimal TSR at 5-6	Optimal TSR less than 2.5
High air turbulence	High water turbulence

The review reveals that hydrokinetic technology is preferable for the remote community's area compared to the conventional hydropower. This is because technology is clean, reliable, sustainable and environmentally friendly, especially to flora and fauna. Besides, the concept, operation and hardware components are similar to the WECS is one of the advantages. Moreover, the output capacity is higher than a similar rate of the wind turbine. It is proved the hydrokinetic technology can generate four times output power compared to the wind turbine. Hence, this kind of technology is necessary for future energy growth.

## 2.9 Variable Speed Hydrokinetic System

The variable speed generator is used to maximise the amount of energy extract by the turbine. In different water velocity, the maximum power point (MPP) for the turbine occurs at different turbine rotational speed, as shown in Figure 2.10 (Alireza Khaigh, 2010). It should be noted, the maximum power of the water velocity curve occurs at a particular rotational speed. The optimal line is produced by connecting all the maximum power point at different water velocity. Therefore, the maximum power can be extracted by optimised the turbine rotational speed.

The turbine rotational speed can be optimised through the power of electronic control by different converter topologies and maximum power point tracking (MPPT) algorithm (M. N. I. Khan, 2015). The used of power electronics converter for MPPT control are typical for the small WECS due to advance in converter technology and able to reduce the cost (Aner, 2014). This topology also can be applied to the variable speed of hydrokinetic turbines. The details of the converter topology will describe in the next following section.

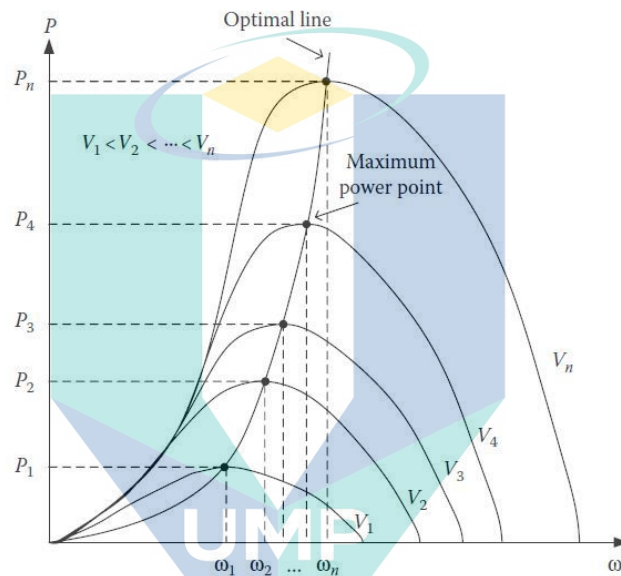


Figure 2.10 Generator power speed curve at various water velocity  
Source: Alireza Khaigh (2010).

The variable-speed turbines can be classified into direct-drive (gearless) and indirect-drive (with gear)(Chowdhury, 2014). The direct-drive turbine is pair to the low speed generator with a higher number of poles. The wound rotor synchronous generator and permanent magnet synchronous generator (PMSG) is suitable for the drive-drive configuration. Meanwhile, the indirect-drive consists of a turbine, mechanical gearbox, and generator. Double-Fed Induction Generator (DFIG) is commonly used for indirect-drive variable speed turbine.

The advantages of variable speed turbines are based on the fact of an increased energy and efficiency were observed due to the maximum energy extraction at the wide range of speed (Prakashkumar & Tamilselvi, 2010). According to Thongam et al. (2009) the variable speed system will reduce mechanical stress, as a result, will increase the lifespan of mechanical components. Moreover, as noted by Bianchi et al. (2007), the variable speed operation is capable to reduce the acoustic noise at low speed operation and power condition, respectively. Furthermore, the system is also suitable to be implemented at remote area off-grid system.

On the other hand, the fixed-speed turbine is designed to achieve maximum efficiency at a particular speed of operation. Hence, the fixed-speed turbine has a lower energy conversion compared to variable speed system due to the turbines only operate at only one speed (Mansour, Mansouri, & Mimouni, 2011). Besides, the fixed speed turbines have several disadvantages compared to variable-speed turbines such as high mechanical stress on turbines blades, low power quality due to fluctuation on output power and low efficiency because unable to implement MPPT (Chowdhury, 2014).

The study discovered that the variable speed hydrokinetic turbine is necessary to maximise the energy extraction. This is due to the maximum power occurs at a particular rotational speed for different water velocity. In addition, the turbine rotational speed can be optimised by the MPPT algorithm to achieve high efficiency in energy conversion. Moreover, hydrokinetic technology can be divided into several operating regions to extract the maximum power and protect the system. Therefore, the MPPT and control strategy can be implemented through a variable speed operation system.

### 2.9.1 Operating Region and Control Strategy

The MPPT has been used to achieve high efficiency in energy conversion system. The MPPT control strategy is commonly used in Region 2, as shown in Figure 2.11 to extract the maximum power at optimal operation. One of the challenges in the hydrokinetic system is due to the fluctuation of the water velocity. Therefore, the development of reliable, efficient and robust techniques is required to track the optimal



operating point of the hydrokinetic system while extracting the maximum energy from the river.

On the other hand, for the large and medium turbines, the pitch control method is applied to optimise the output power and reduce the power variation in high water velocity (Novaes Menezes, Araújo, & Bouchonneau da Silva, 2018; Tiwari & Babu, 2016b; Zhou, 2012). Nevertheless, for the small turbines, the pitch control is unrealistic due to the limitation of the mechanical structure (Zhou, 2012). Therefore, the power converter is commonly used to implement the MPPT control strategy for the small-scale turbines.

The reliable and efficient methods for optimal operating point of the hydrokinetic system is essential to extract the maximum power from the variation and fluctuation of water velocity. According to Ginter & Pieper (2011), the operation of the hydrokinetic system can be divided into several operating regions to extract the maximum power and to protect the system. The regions are describing as follows as shown in Figure 2.11.

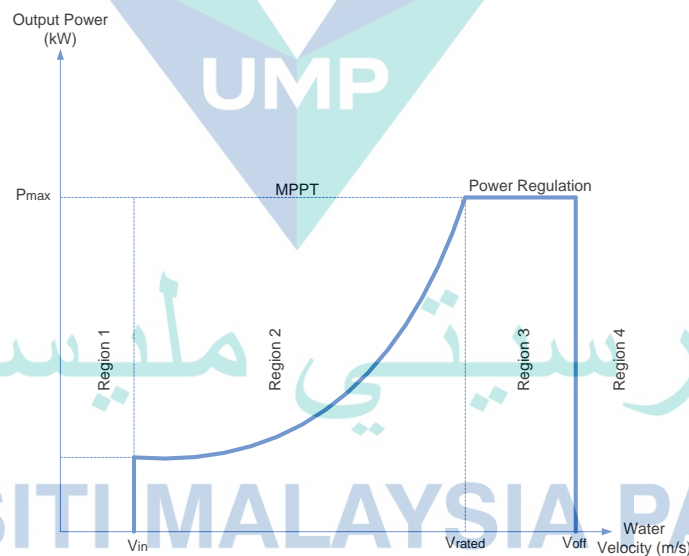


Figure 2.11 The operating region in the hydrokinetic control strategy.

Source: Ginter & Pieper (2011).



a) Region 1: Cut-in Region.

In this region, the water velocity is too low and not sufficient enough to drive the hydrokinetic turbine. In this case, the turbine is shut down and waiting for the water velocity to increase at the  $V_{in}$  or cut-in speed to operate.

b) Region 2: Maximum Power Point Operation.

In this region, the hydrokinetic system will startup, and the turbine will rotate based on flowing water velocity. However, the MPPT is required to maximize the output power during the accelerating and decelerating of flowing water. During this region, the rotor speed controller will operate and determine the optimal speed for the turbine and rotor generator at the particular water velocity to extract the maximum power.

c) Region 3: The Power Regulation

At this region, the hydrokinetic system needs to maintain the output power within generator rated power. Consequently, the rotor speed can be reduced to operate at below than optimal speed. When the actual water velocity passed the rated water velocity of the system, the turbine power must be regulated to maintain the output power at the rated output power. The hydrokinetic system can be running at the optimal operation point while reducing the turbine rotation/minute as the flow increase past the rated flow speed.

d) Region 4: Cut-off speed.

At this region, the turbine is shut down for protection purpose. This is due to high torque ripple, which can cause severe damage to the hydrokinetic system at the higher water velocity.

## 2.10 Maximum Power Point Tracking (MPPT) Algorithm for Off-Grid Hydrokinetic Energy Harnessing

This section presents the different techniques of the MPPT algorithm available in WECS. The concepts, advantages and disadvantages of each technique are discussed.

Subsequently, the performance comparison of the MPPT is described at the end of this section.

### 2.10.1 MPPT Algorithm Classification

The knowledge from wind turbine has been referred to due to the insufficient literature regarding the MPPT and control strategy in the hydrokinetic system. The objective of control is to maximise the harnessing energy, reduce mechanical stress on the turbine and improve the system performance within the safety limit of operation.

As discussed by Kumar & Chatterjee (2016) the MPPT algorithm can be categorized into three groups which are Indirect Power Control (IPC), Direct Power Control (DPC) and soft computing method, as shown in Figure 2.12. The IPC algorithm is based on maximising the mechanical power ( $P_m$ ) while the DPC algorithm directly maximizes the power output ( $P_o$ ). Under IPC groups, three types of MPPT algorithm have been considered, which is Tip Speed Ratio (TSR), Power Signal feedback (PSF) and Optimal Torque (OT). While, under the DPC group, Hill Climbing Search (HCS), Incremental Conductance (INC) and Optimum Related Based (ORB) have been considered.

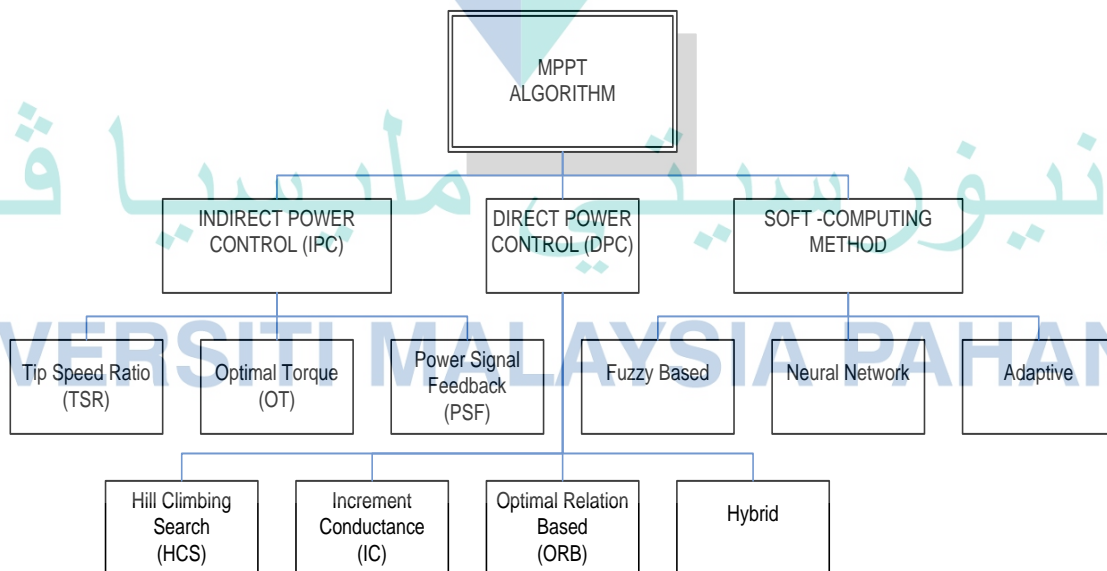


Figure 2.12 The Classification of MPPT algorithm for WECS

### 2.10.2 Tip Speed Ratio (TSR) MPPT

As noted by Abdullah et al. (2011) the TSR MPPT algorithm, is required to keep up the TSR at the optimum value by regulating the rotational speed of the generator. The block diagram in Figure 2.13 shown the TSR algorithm. The optimum rotational speed  $\omega_m^{opt}$  is compared to the actual speed,  $\omega_m$  and the error is given into the controller. According to Nasiri et al. (2014) the TSR algorithm is highly efficient and quick response under high variation of the wind speed. Nevertheless, this algorithm required the accurate sensor for wind speed measurement as a result will increase the system operating cost (K. Kim, Van, Lee, Song, & Kim, 2013) .

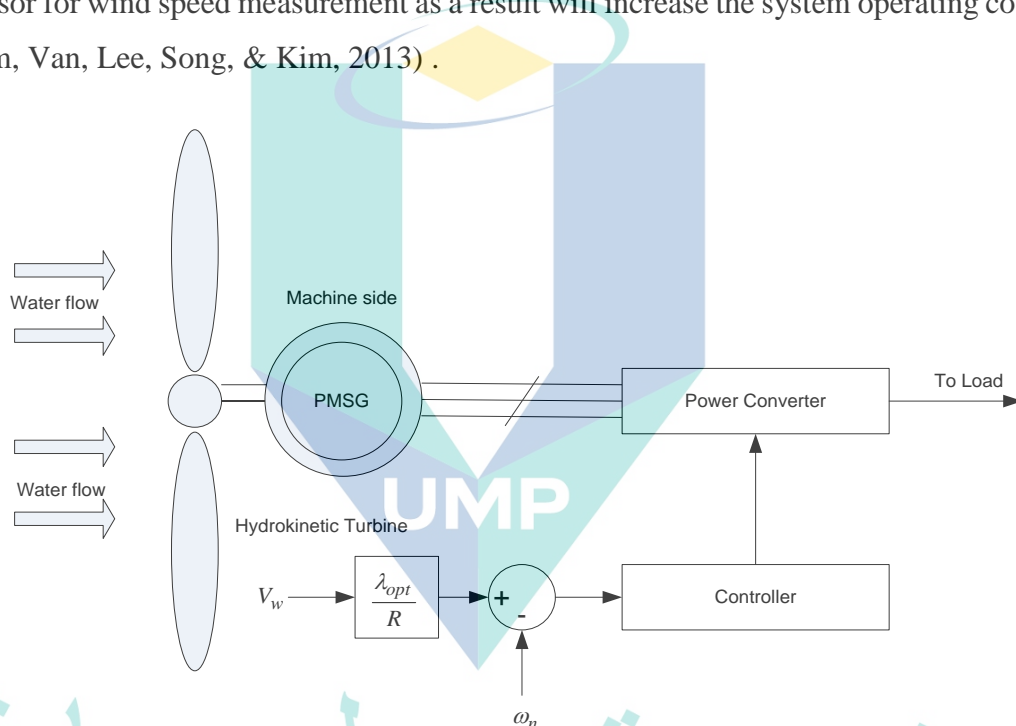


Figure 2.13 Tip Speed Ratio MPPT Algorithm

An improvement of TSR MPPT algorithm has been studied by Ganjefar et al. (2014). The authors proposed the direct and indirect adaptive control structures based on Quantum Nuetral Network (QNN) to improve the power coefficient and maximum power respectively. Nevertheless, the QNN MPPT algorithm required a learning process to train the algorithm specifically.

### 2.10.3 Optimal Torque (OT) MPPT

In the optimal torque algorithm, the torque of the generator is controlling to obtain the optimum torque reference curve according to the maximum power of wind turbine at given wind speed (Lopez, 2007). Figure 2.14 shows the block diagram of the algorithm, which is the difference of  $T_m^{opt}$  and  $T_e$  as the input to the controller.

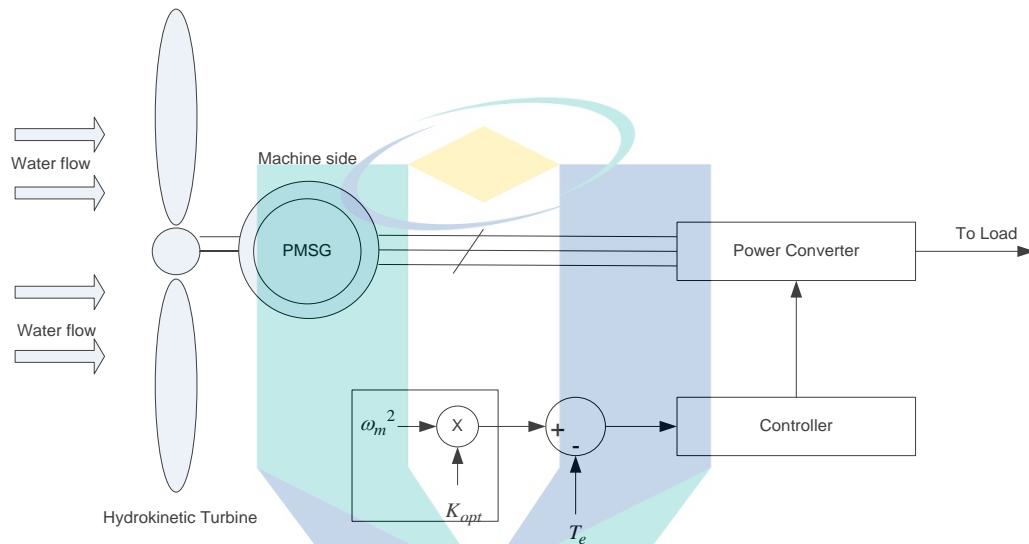


Figure 2.14 The Optimal torque MPPT Algorithm

As stated by Abdullah et al. (2012), the OT algorithm is fast, simple and efficient but the efficiency is lower compared to the TSR algorithm. Several researchers have tried to improve the sluggish response of the WECS due to high initial of large wind turbine. For example, Yin et al. (2017) has proposed the effective tracking range (ETR) with OT to improve stability and efficiency under varying wind conditions. On the other hand, a comparison studied by Nasiri et al. (2014) has proved that OT is highly efficient compared to the TSR in power smoothing techniques in the wind farm grid-connected system.

### 2.10.4 Power Signal Feedback (PSF) MPPT

Power signal feedback (PSF) algorithm shows in Figure 2.15. In this method, the optimum power  $P_m^{opt}$  is generated either using a pre-obtained power-speed curve or using the expression of turbine output power. Where wind speed or turbine speed used as input and the controller reduces the error between the optimum power and actual power

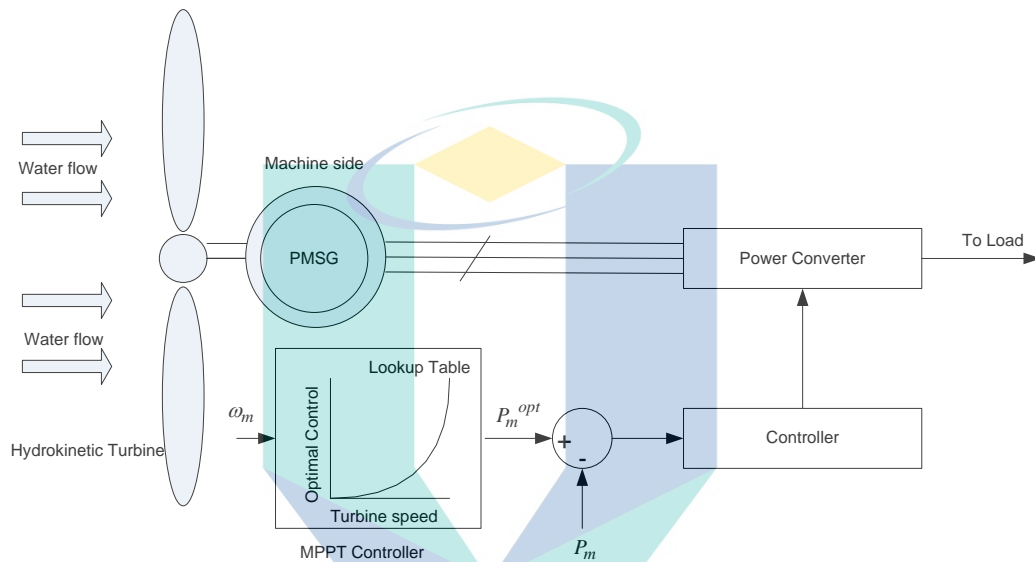


Figure 2.15 Power signal feedback MPPT algorithm

It has been highlighted by Musunuri & Ginn (2011), the PSF required the knowledge of the wind's turbine maximum power curve. Nevertheless, the maximum power curve can be obtained through an experiment or simulation studies (Dipesh Kumar & Chatterjee, 2016). Consequently, the PSF algorithm is one of the difficult and expensive algorithm to apply. Furthermore, the PSF algorithm required the mechanical sensor to measure the turbine speed which are higher cost and less reliable for long term (Yazici & Yaylaci, 2017).

### 2.10.5 Hill Climbing Search (HCS) MPPT

HCS algorithm is a mathematical optimisation strategy to locate the local maximum point of a given function. The algorithm consists of three steps; the first step is to search for a  $k_{opt}$  value to track peak point. Second step is to keep the system at MPP for the constant wind speed. Third step is the online updated  $k_{opt}$  value is implemented under variable wind speed.

As noted by Raza Kazmi et al. (2011), the HCS algorithm does not require any knowledge of the system and independent of the turbine, generator and wind characteristics. Nevertheless, the algorithm has poor performance under rapidly wind speed (He, Li, & Harley, 2013). Due to this weakness, several researchers have apply the improvement on HCS algorithm such as modified HCS algorithm by Zhu et al. (2018), and adaptive HCS by Hussain (2016).

Furthermore, a hybrid HCS algorithm is also become a subject of research. For instance, Whei-Min Lin (2010) has proposed the Wilcoxon radial basic function network (WRBFN) with HCS for the fast tracking speed and minimised the turbine initials. All the discussed algorithm has a similar mission, which is to produce the variable step-size and minimised the oscillate output voltage at a dynamic steady state condition. Nevertheless, the programming structure become a complicated and some algorithm required a training process.

### 2.10.6 Incremental Conductance (INC) MPPT

According to Kumar & Chatterjee (2016) The INC MPPT algorithm does not required a sensor to operate. Hence, the algorithm reduces the cost and improves the liability of the system. The turbine output power can be represented as the function of DC-link Voltage  $V_{dc}$ . The modified INC algorithm will be enhancing the performance of the algorithm by considering the variable step for  $V_{dc}$  as shows in Figure 2.16. The algorithm



is automatically able to adjust the step size to track the MPP in the wind turbine system, which leads to enhance the accuracy and convergence speed.

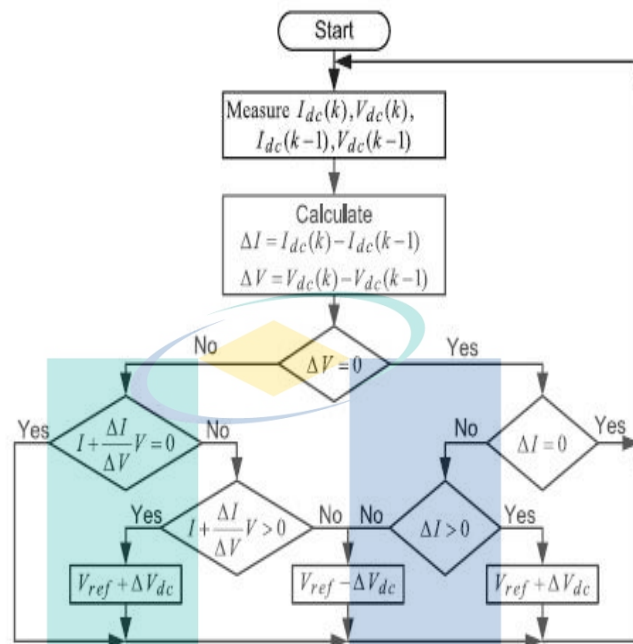


Figure 2.16 Flowchart of modified INC MPPT algorithm.

Source: Kumar (2016)

As noted by Soheil Ahmadzadeh (2017) the INC MPPT algorithm improved the dynamic response compared to the conventional PI controller. Other similar work by Daniel Zammit et al. (2017) explained, the algorithm required less computational time due to simple step without the DC-link power calculation. Nevertheless, the common problem with the INC algorithm is the oscillation occurred around the dynamic steady-state due to the fixed step-size.

### 2.10.7 Optimal Related Based (ORB) MPPT

Optimal Related Based (ORB) algorithm depends on optimum relation between quantities like wind speed, turbine power output, converter DC voltage, current, power, etc. The advantages of this algorithm are sensorless and not required look-up table

because it operates based on the pre-obtained system curve (Dalala et al., 2013). Nevertheless, the weakness of this algorithm is not able to sustain in highly variation wind speed.

### 2.10.8 Fuzzy Logic MPPT

The FLC MPPT algorithm is based on the fuzzy if-then linguistic rules, which resembles the imprecise reasoning process in the human mind (Liu et al., 2017). Hence, the FLC can analyse the non-linearity input signal and provided the fast convergence method (Tiwari & Babu, 2016a). Figure 2.17 shows the basic concepts of the FLC MPPT algorithm in WECS. The rotational speed ( $\omega_m$ ) and mechanical torque ( $T_m$ ) are commonly used as an input parameter. Other parameters such as voltage and current from the generator ( $V_g$  and  $I_g$ ) can be used too as an input parameter to the FLC system (Dipesh Kumar & Chatterjee, 2016).

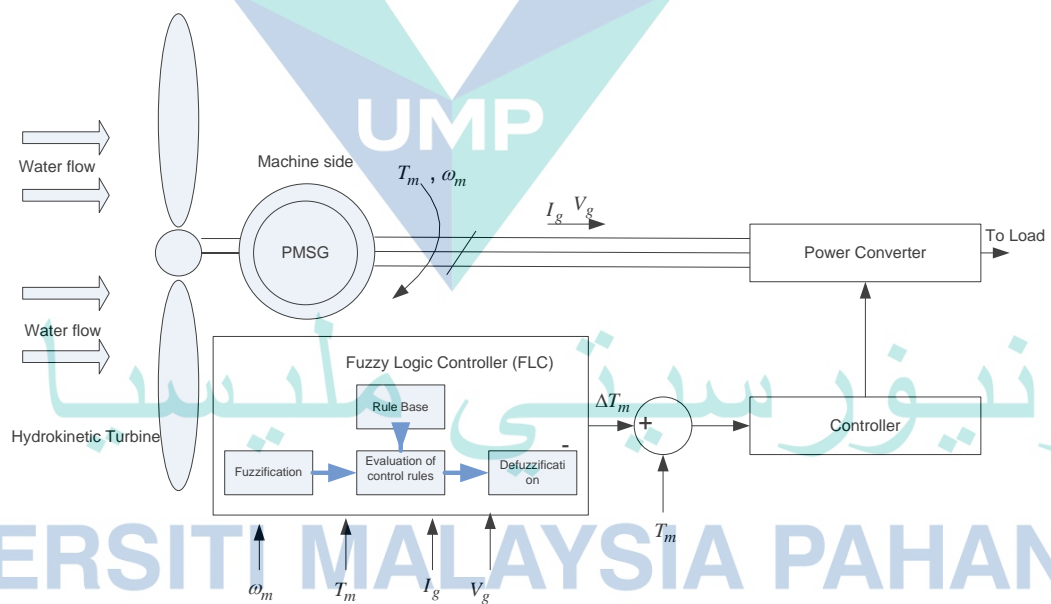


Figure 2.17 The FLC MPPT system

The FLC strategies consist of four steps which are rule base, fuzzification, evaluation of control rules and defuzzification (Abazari, Dozein, & Monsef, 2018; Simões, Bose, &

Spiegel, 1997). A rule base is derived from the system behaviours consists of IF-THEN logic rules. According to Yaakoubi et al. (2016), fuzzification is a process of converting the input parameter into linguistic variables using memberships functions. As noted by Sasi (2017), the FLC output response is influenced by a membership function. Several potentials shape such as triangular, Gaussian, trapezoidal, bell and sigmoid are commonly used to represent the participation level of the input parameter.

On the other hand, the inference system or evaluation of control rules is to determine the output regions. According to Aashoor (2015), the Mamdani and Takagi-Sugeno Kang method are commonly used to perform a fuzzy inference system. Nevertheless, the Mamdani method is familiar due to the most efficient and interpolative properties compared to other methods (Hassan Bevrani & Daneshmand, 2012). The defuzzification is a process of converting the fuzzy output data to real or craps values (Yaakoubi et al., 2016). The centroid of gravity (COG) is commonly used for defuzzification process due to simplicity approach (Sasi, 2017).

The FLC is provided with better outcomes compared to a conventional controller, especially in response and settling time, robustness and fast convergence (A. Z. Mohamed, Eskander, & Ghali, 2001). The FLC MPPT control strategies have been applied by many researchers to improve the energy extraction in WECS for instance (Belmokhtar, Doumbia, & Agbossou, 2014; H Bevrani & Daneshmand, 2012; J. Lee & Kim, 2016; Sefidgar & Asghar Gholamian, 2014).

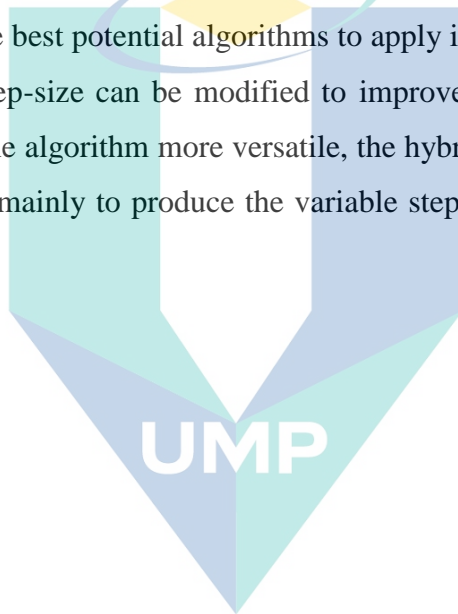
#### **2.10.9 Performance Comparison between MPPT Algorithm**

Choosing an appropriate MPPT technique is a tough task. Table 2.5 shows the comparison of different MPPT algorithm. The analysis and comparison of the MPPT algorithms have been evaluated in term of complexity, convergence speed, memory requirement, wind/ water speed measurement, performance and training.

Judging from the literature, the MPPT algorithm can be classified into three group which are IPC, DPC and soft computing. The IPC-based algorithms such as TSR, OT and

PSF are simple and fast, but it maximizes the captured mechanical wind power instead of output electrical power. TSR control has excellent performance with fast response and high efficiency. Nevertheless, an accurate anemometer is required, due to gust and turbulence, which is expensive and adds extra cost to the system, especially for small-scale WECS.

The DPC techniques such as HCS, INC and ORB are simple, and less memory requirements. The algorithm calculates the optimal electrical power directly without prior training and measurement of wind speed. On the other hand, the soft computing method required learning and complicated programming structures. Therefore, the HCS algorithm is one of the best potential algorithms to apply in the MPPT. The algorithm is sensorless, and the step-size can be modified to improve the performance in tracking response. To make the algorithm more versatile, the hybrid or combination with others algorithm is required mainly to produce the variable step-size as well as improved the algorithm itself.



اونيورسيتي مليسيا قهغ

UNIVERSITI MALAYSIA PAHANG

Table 2.5 Analysis and comparison of different MPPT algorithm.

Algorithm	Complexity	Convergence Speed	Memory Requirement	Wind/Water Speed Measurement	Performance in variation Wind/Water speed	Training/Learning
TSR	Simple	Fast	No	Yes	Moderate	No
OT	Simple	Fast	No	Yes	Moderate	No
PSF	Simple	Fast	Yes	Yes	Moderate	No
HCS	Simple	Low	No	No	Moderate	No
Modified HCS	Medium	Fast	No	No	Very Good	No
INC	Simple	Low	No	No	Moderate	No
Modified INC	Medium	Medium	No	No	Good	No
Hybrid	Medium	Fast	No	No	Good	No
NN-Based	High	Medium	Yes	Depends	Very Good	Required

اونیورسیتی ملیسیا قهق

UNIVERSITI MALAYSIA PAHANG

## 2.11 Control Strategies for Grid-Connected Hydrokinetic Energy Harnessing

In this section, the pitch and robust control strategies for the grid-connected hydrokinetic system are introduced. Subsequently, the conventional PI controller with tuned parameter is presented and followed by small-signal stability analysis.

### 2.11.1 Pitch Control Strategies

The pitch control is commonly used to regulate the power and load reduction in Region 3 as shown in Figure 2.11 for the variable speed operation system (Novaes Menezes et al., 2018). The concept of pitch control strategies is manipulated the angle of attack by changing the turbine blades pitch angle. Hence, the relative water flow will change accordingly and subsequently the aerodynamic efficiency and lift force on the turbine blades is changed (Chen et al. 2015). Furthermore, the power coefficient is also depending on the pitch angle ( $\beta$ ) and consequently the power capture will vary as well.

Figure 2.18 illustrates the pitch controller control strategies with the speed sensor ( $\omega$ ) is used to measure the rotor speed. The output of the speed sensor become the collective of pitch angle controller ( $\beta$ ) and an input to the torque converter ( $\tau_g$ ). The pitch system consists of the motor and electromechanical actuator. The system also can be classified into two groups hydraulic controller and electric pitch controller (Tiwari & Babu, 2016b).



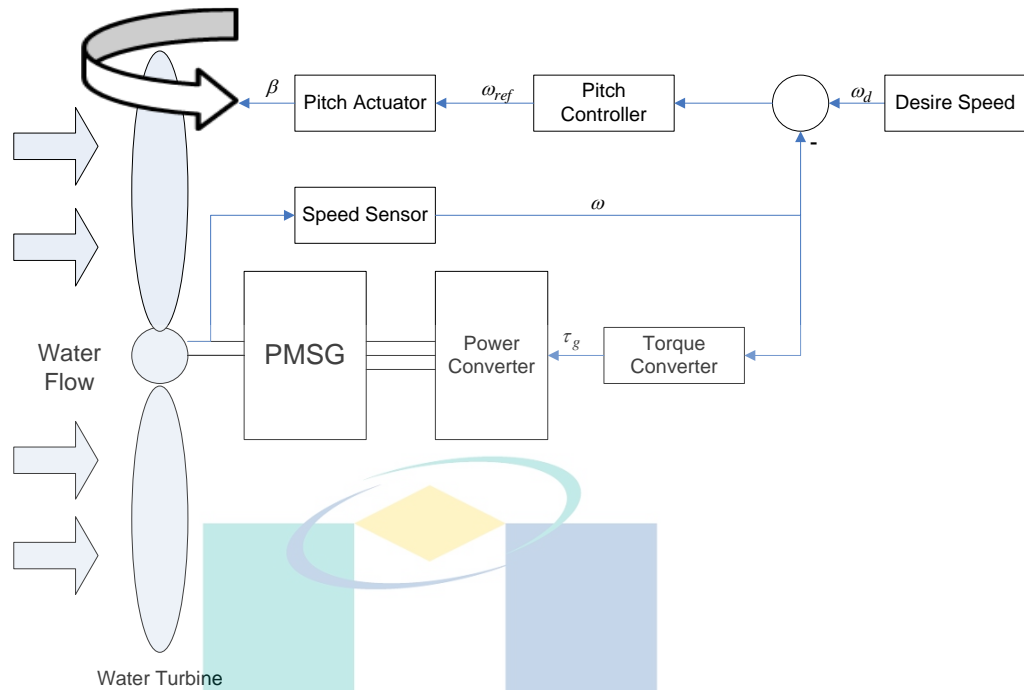


Figure 2.18 The pitch control strategies in hydrokinetic system

The pitch controller has been applied in the marine current turbine and tidal technology to limit the excessive power due to variation of flow and strong tidal current. In an early study conducted by Takagi et al. (2011), the pitch control strategy was applied to the contra rotating turbines. The equation of motion was implemented to reduce the unsteady motion and blades stress due to high waves and disturbances. In a different study by Xue-wei et al. (2012), the free variable pitch control for the vertical axis tidal turbine has been investigated. The finding shows that the free variable pitch has good starting capability and the performance in term of power and structure can be improved by adjusting the range of limit angle. Additionally, as noted by Chen et al. (2018), the variable pitch vertical axis tidal turbine will enhance the power efficiency and output torque almost 33 % compared to the fixed pitch turbine.

In other work, Ghafari et al. (2018) has proposed the firefly algorithm to tune the PI controller parameter for the optimal operating condition. The proposed system is able to maintain the system operation within the limit without overloading. The Incremental PI control algorithm has been applied in pitch regulated system to improve the efficiency (Z. Chen et al., 2015). The turbine blades are regulated by considering the flow and

direction of water current. On the other hand, the individual active pitch control also has been studied for positioning moored ocean current turbine in an array system. VanZwieten et al. (2016) proposed the active pitch control to eliminate the wake effect in an array position. It was noted that the proposed control strategy able to reduce the power losses due to wakes effect from 50 % to 1.5 % of losses.

Nevertheless, the pitch control strategies only practical to be applied to large turbines; however, for the small turbine, this type of control is not feasible due to the higher cost on turbine construction.

### **2.11.2 Robust Control Strategies in Hydrokinetic Technology**

Past researchers have explored a few studies regarding the hydrokinetic control system and strategies. Alvarez et al. (2018) proposed the design and control strategies for a modular hydrokinetic smart grid based on operating zones of electrical generator frequency. Nevertheless, the control strategies used the boost converter circuit, which has a low efficiency compared to active rectifier control. On the contrary, Ashourianjzdani et al. (2017) proposed the control strategy for a fixed-pitch hydrokinetic turbine with PMSG by controlling the duty cycle of the boost converter. Nevertheless, the control system was suitable to be applied for stand-alone and DC microgrid. Table 2.6 shows the summarise of the robust control strategies that have the potential to be implemented on the hydrokinetic energy harnessing.

اونیورسیتی ملیسیا قهق

UNIVERSITI MALAYSIA PAHANG

Table 2.6 The potentials of robust control strategies in hydrokinetic research field

Authors	Research Topic	Notes/Comments	Issues
(X. Yin & Zhao, 2019)	Tidal Turbine Control	<ul style="list-style-type: none"> <li>Proposed a nonlinear observer based on Extreme Learning Machine (ELM) to predict the turbine torque and tidal speed respectively.</li> <li>The ELM is based neural network learning algorithm for better approximation capability and fast learning speed</li> </ul>	Required a complex structure program as well as training algorithm
Ghefiri et al. (2018)	Generator Control for Tidal turbine	<ul style="list-style-type: none"> <li>Proposed Fuzzy Gain Scheduling (FGS) to improve the rotational speed of the tidal turbine at the RSC</li> <li>Used power converter with back-to-back topology connected to the grid</li> </ul>	Complex structure programming Some parameter needs to be trained
(Ren, Wang, & Zhong, 2017)	Control of Variable Speed WECS	<ul style="list-style-type: none"> <li>Proposed Uncertainty and Disturbance Estimator (UDE) through regulation of DC-link Voltage at RSC and GSC</li> <li>The circuit topologies based on back-to-back converter with PMSG                             <ul style="list-style-type: none"> <li>Improved 5 % of the extraction energy</li> </ul> </li> </ul>	Required a lot of sensors to measure the turbine speed, water velocity and generator speed.

اونيفورسيتي ملايسيا قهق

Table 2.6 Continued

Authors	Research Topic	Notes/Comments	Issues
(Michas et al., 2019)	MPPT for hydrokinetic energy conversion	<ul style="list-style-type: none"> <li>• Applied the Perturb and Observe (P&amp;O) method for MPPT algorithm.</li> <li>• The circuit topology based on bridge rectifier, DC-DC converter and an inverter.</li> <li>• To solve the turbines constraint such as in turbulent water flow.</li> </ul>	Oscillation at output power due to fixed step-size
(Eduard Muljadi, Gevorgian, Wright, Donegan, & Marnagh, 2016)	Turbine, Generator Control in river	<ul style="list-style-type: none"> <li>• The small disturbance in the flowing of water will affect the energy harnessing in the river.</li> <li>• Proposed additional K-gain to improve the tracking effect.                             <ul style="list-style-type: none"> <li>• Robust and improve the tracking accuracy.</li> </ul> </li> </ul>	The K-gain need to manually tune.
(Jahangir, Tariq, & Quaiocoe, 2015)	Evaluation of MPPT for hydrokinetic energy conversion	<ul style="list-style-type: none"> <li>• Conventional MPPT algorithm required sensor for speed/torque measurement. Hence increase cost, inaccuracy due to turbulent/ complex flow.</li> <li>• Proposed Extremum Seeking Control (ESC) for sensor-less control, good tracking and reduce the transient.</li> </ul>	Complicated programming and some parameter need to be fixed.

اونيور سيني مليسيا قهغ

Table 2.6 Continued

Authors	Research Topic	Notes/Comments	Issues
(Abdul, Shafei, Ibrahim, & El-Zahab, 2014)	PI controller with Biogeography based Optimisation (BBO) technique for MPPT	<ul style="list-style-type: none"> <li>• The non-linear characteristics of water velocity required optimal controller for high efficiency energy extraction.</li> <li>• Proposed the PI controller with the controller's parameter is tuned by BBO optimisation.</li> <li>• Able to maintain the power coefficient and TSR at optimum value under the stochastic of water velocity.</li> </ul>	Complicated programming and long convergence time
(Ahmed, Shoyam, & Dousoky, 2012)	Marine & Tidal Converter with DC-DC Boost Converter	<ul style="list-style-type: none"> <li>• Design to overcome the drawback of the mechanical system such as gearbox.</li> <li>• Proposed AC-DC-AC conventional system with the DC Boost converter.</li> <li>• Able to regulate the output power and harness the electricity at low speed of water.</li> </ul>	Oscillation at the output power due to the boost converter switching

اونيور سيبي مليسيا قهع

Table 2.6 Continued

Authors	Research Topic	Notes/Comments	Issues
(Zhang, Fletcher, Greeves, Finney, & Williams, 2011)	Variable speed wind/tidal stream turbines with synchronous generator.	<ul style="list-style-type: none"> <li>• Design to reduce the complex control algorithm and extra hardware cost due to requirement of torque and speed control reference.</li> <li>• Proposed one-power point (OPP) operating scheme on maximum power curve.</li> </ul>	Required turbine characteristics
(Ginter & Pieper, 2011)	Robust Gain scheduled to control the hydrokinetic turbine.	<ul style="list-style-type: none"> <li>• Design to control the highly non-linear plant with wide operating range.</li> <li>• Proposed the <math>H_{\infty}</math> Linear Parameter Varying (LPV).</li> <li>• Able to maintain the stability and performance over large range of operating condition.</li> <li>• However, used sensor to measure the speed and torque.</li> </ul>	Reliability issues regarding the usage of sensors

اونیورسیتی ملیسیا قهق

UNIVERSITI MALAYSIA PAHANG



Table 2.6 Continued

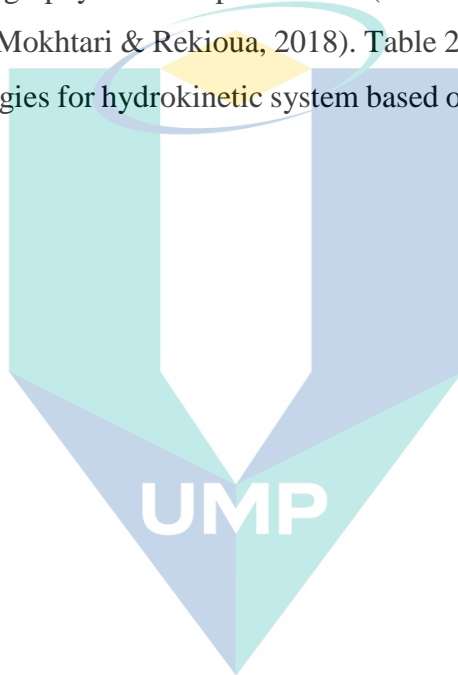
Authors	Research Topic	Notes/Comments	Issues
(Eddine, Seif Elghali, El, Mohamed Benbouzid, Ahmed-ali, & Charpentier, 2010)	Higher Order Sliding Mode (HOSM) to control Marine Current Turbine	<ul style="list-style-type: none"> <li>• Design to handle the turbulence and swell effect due to harsh environment effect in the sea.</li> <li>• Proposed High order sliding mode (HOSM) control, robust nonlinear control strategy</li> <li>• Good tracking</li> </ul>	Produce the ripple at the output power

اونيورسيتي ملايسيا قهق

UNIVERSITI MALAYSIA PAHANG

### 2.11.3 Conventional PI Controller with Parameter Tuning

Another control strategies that suitable to be implemented for hydrokinetic energy harnessing is the conventional PI controller. The PI controller is commonly used because of the robustness and ability to improve the system stability by shifting the poles towards the left s-plane (Aly & El-Hawary, 2011; Omkar et al., 2019). In addition, the PI controller is the universal controller, and the gains ( $K_P$  and  $K_I$ ) can be tuned with available optimisation techniques such as Gravitational Search Algorithm (GSA), (Assareh & Biglari, 2015), Biogeography-Based-Optimisation (Abdul et al., 2014) and Ant Colony Optimisation (ACO) (Mokhtari & Rekioua, 2018). Table 2.3 shows the summarise of the potential control strategies for hydrokinetic system based on PI controller with parameter tuning.



اونيورسيتي مليسيا قهغ

UNIVERSITI MALAYSIA PAHANG

Table 2.7 The potential of control strategies for hydrokinetic based on PI with parameter tuning

Author	Research Topic	Notes	Issues
(Mokhtari & Rekioua, 2018)	Energy extraction using metaheuristic method	<ul style="list-style-type: none"> <li>Proposed the Ant Colony Optimisation to determine optimal PI controller parameter.</li> <li>Applied on 15 kW DFIG through simulation studied.</li> </ul>	<p>Focus on speed control at rotor side controller only.</p> <p>Complex programming</p>
(Beddar, Bouzekri, Babes, & Afghoul, 2016)	Variable speed WECS	<ul style="list-style-type: none"> <li>Proposed Fuzzy Fractional Order PI Controller (FFOPI+I) for grid connected WECS.</li> <li>Implemented on PMSG with back-to-back converter.</li> </ul>	<p>Complex programming as well as increased convergence time due to PSO and Fuzzy.</p>
(Assareh & Biglari, 2015)	Variable speed WECS with hybrid control	<ul style="list-style-type: none"> <li>Proposed generator torque control using PI controller tuned by radial basic function (RBF).</li> <li>Applied the Gravitational Search Algorithm to determine the optimal dataset to train the RBF.</li> </ul>	<p>Focus on generator control at rotor side controller only.</p> <p>Required learning to train the ANN</p>

اونيور سيئي مليسيا قهع

UNIVERSITI MALAYSIA PAHANG

Table 2.7 Continued.

Authors	Research Topic	Notes/Comments	Issues
(H. Chen, Chen, & Xie, 2018)	Torque speed control of DFIG MCT	<ul style="list-style-type: none"> <li>Proposed Fractional Order PI (FOPI) controller for marine current turbine under harsh environment</li> <li>Able to integrate with parameter tuning algorithm such as PSO, Differential Evolution (DE), RBF</li> </ul>	<p>Focus on generator speed control at RSC only.</p> <p>Required strong mathematical foundation to derive fractional calculus.</p>

UMP

اونيورسيتي ملايسيا قهق

UNIVERSITI MALAYSIA PAHANG

#### 2.11.4 Small Signal Stability Analysis (SSSA) and Eigenvalues Tracing Method

Small-signal analysis has been presented by many researchers in WECS either to design the controller and analysed the system stability in the grid network (Arani & Mohamed, 2015; Hu, et al.,2015; Hu et al., 2017; 2012; Wei et al., 2014). In addition, SSSA is also implemented in the power system network to identify oscillatory instability in the system (Wen & Ajarapu, 2006).

According to Kani et al. (2014), the small-signal analysis can be executed by linearising the dynamic model around steady-state values or equilibrium operating point. By linearising differential equation to the steady-state value, the dynamic model can be obtained through the state space equation. Subsequently, the system stability can be assessed through several method such as eigenvalues analysis, pole-zero maps, and frequency response (Mcgrath, 2018).

Several reseacher have studied the SSSA for WECS, for instance, Ugalde-loo et al. (2013) has derived the mathematical model for a variable speed wind turbine system into the state-space equation for transient and SSSA. Nevertheless, their case studied is limited to the disturbances due to the voltage sags. Rahimi (2017) presented the linearised model and controller design for stability analysis of the grid-connected WECS. Nevertheless, the circuit topology and linearised model of the grid-connected system is based on the diode bridge and a boost converter circuit.

On the other hand, in the power system research, Chabane & Hellal (2013), has analysed the system oscillation under small disturbances to maintain synchronism and sufficient damping for the generator system. Nevertheless, the studies focused on a large network system and tested for The New England New York 39-bus and IEEE-145 bus, respectively. Paduani et al. (2019), has investigated the stability issues of distributed generation (DG) for islanded-mode due to intermittent power supply and inertia when disconnected from micro-grid. Nevertheless, their research focused on the stability on DC side dynamic inverter with saturation current controller.

On the contrary, the eigenvalues analysis method is commonly used to investigate the stability of the system (Chouket & Krichen, 2015). Several paper were published by Wen

& Ajarapu (2004), (2006) and Yang & Ajarapu (2005) regarding to this method. Nevertheless, the method was applied in the power system network to investigate oscillatory stability due to line tripping disturbance. Besides, Mao & Wang (2012), has determined the parameter of  $K_P$  and  $K_I$  using the traces of eigenvalues. Nevertheless, their research limited to investigate the influence of the controller's parameter on the wind turbine system performance.

The review indicates that the pitch and robust control strategies are commonly used to regulate the output power and load reduction for grid-connected hydrokinetic technology. Nevertheless, the pitch control strategy is applicable for a large turbine system with high output capacity. On the other hand, the robust control strategies required complex structure programs, and some parameters need to be trained. Hence, PI Controller is one of the potentials to improve the stability of hydrokinetic energy harnessing for the grid-connected system. The PI controller has been proposed because of robustness, able to improve the system stability, universal and their gain ( $K_P$  and  $K_I$ ) can be tuned with other optimisation techniques. Therefore with the proper controller design, the system is stabilised if it can suppress the oscillation due to the small disturbance.

## 2.12 Summary

This chapter presents the state-of-the-art of the hydrokinetic system in marine and river applications. The relevant literature, such as the energy conversion classifications, MPPT, control strategies, and variables speed operation of the hydrokinetic system, have been studied to identify the research gaps. Figure 2.19 shows the literature map on hydrokinetic system research.

Compared to the other renewable energy, the hydrokinetic energy harnessing is very promising for clean and sustainable energy resources. The hydrokinetic system is not depending on the weathers condition such as solar and WECS. Besides, the initial capital cost is lower compared to the conventional hydropower, solar PV, WECS, and others RE.



Therefore, the hydrokinetic system is one of the best options for clean energy, especially for remote communities areas and small-scale needs.

Judging from the literature, to date, most of the literature studies in hydrokinetic energy harnessing have been focusing on energy conversion schemes, such as turbines design and improvement, non-turbines system, maximum energy extraction, and control strategies. There is almost no known report in the literature regarding the modeling of the  $C_P$  equation for vertical axis turbine and small-signal stability analysis for the grid-connection hydrokinetic turbine.

While several MPPT control strategies for off-grid connection systems have been proposed, such as DPC, IPC, and soft-computing methods, however, the issues and problems need to be catered to improve the energy extraction and reduce the oscillation. Moreover, several control strategies for the grid-connected system have been suggested, such as pitch, robust, and adaptive control. Nevertheless, the controller's suitability needs to be evaluated before it can be executed on the hydrokinetic to improve the system stability and reduce the frequency oscillation.

Although, there are still issues on the hydrokinetic technology that need to be explored, such as modelling of turbine placement and arrays arrangement, control strategies for turbine arrays, and transient analysis for micro-grid connection hydrokinetic energy harnessing.

اونيورسيتي ملايسيا قهغ

UNIVERSITI MALAYSIA PAHANG

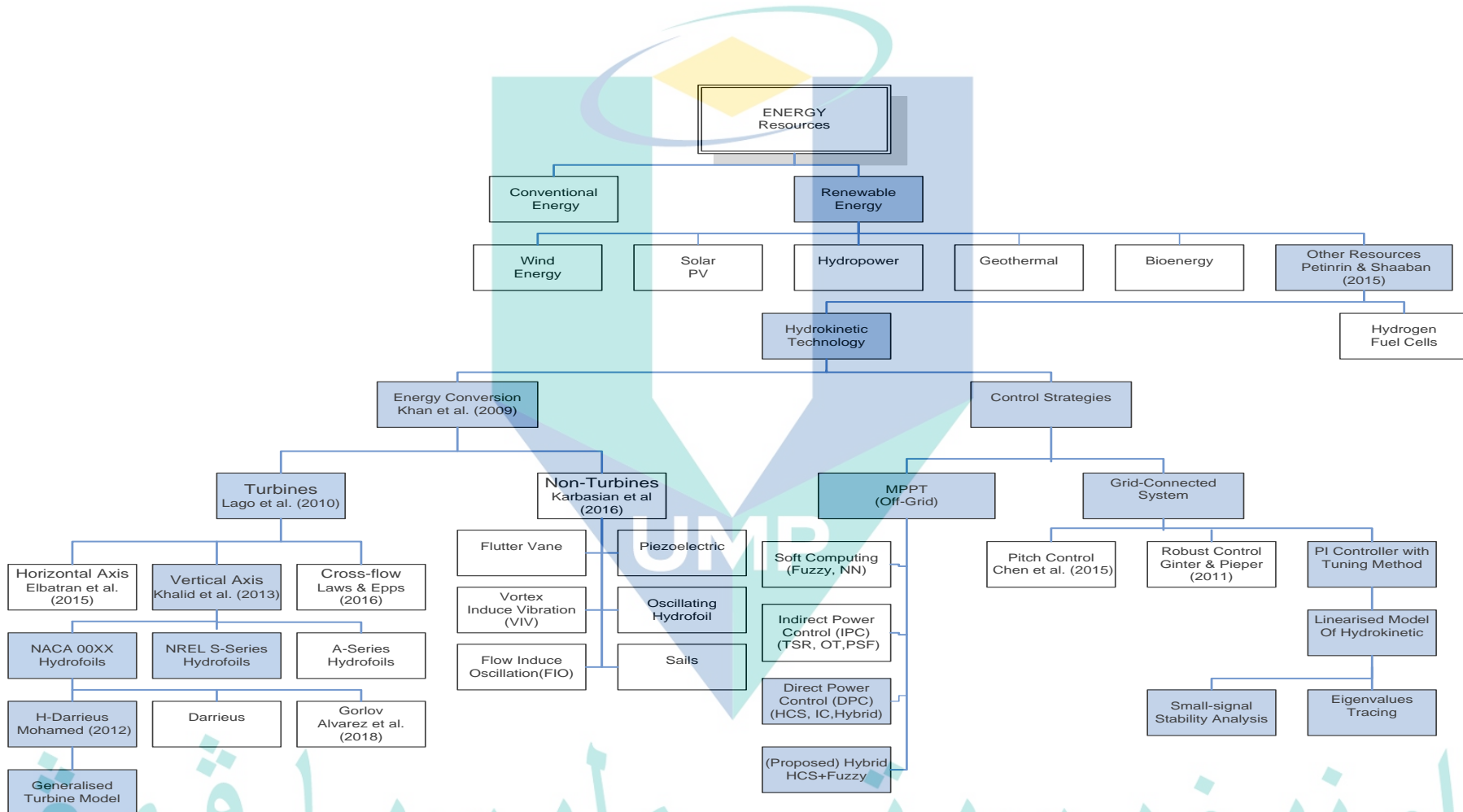


Figure 2.19 Literature map of hydrokinetic system research

## CHAPTER 3

### METHODOLOGY

#### 3.1 Chapter Overview

This chapter presents a brief methodology of the modelling and simulation of the river current energy conversion for hydrokinetic energy harnessing. Subsequently, the assessment studies on hydrokinetic energy harnessing at the Pasir Kubur River and Pahang River basin are discussed. As the thesis is written in the paper-based format. Therefore, the following chapters are presented by the recollection of published or submitted technical papers related to the study. Other methodologies are self-standing and described in each chapter accordingly.

#### 3.2 Research Implementations

This research intends to investigate a proper design for the complete structures of the hydrokinetic energy harnessing through simulation studies, including the turbines design considerations, MPPT algorithms, converter topologies, small-signal stability analysis and design of PI controller. This research has been divided into five stages, as shown in Figure 3.1.

UNIVERSITI MALAYSIA PAHANG

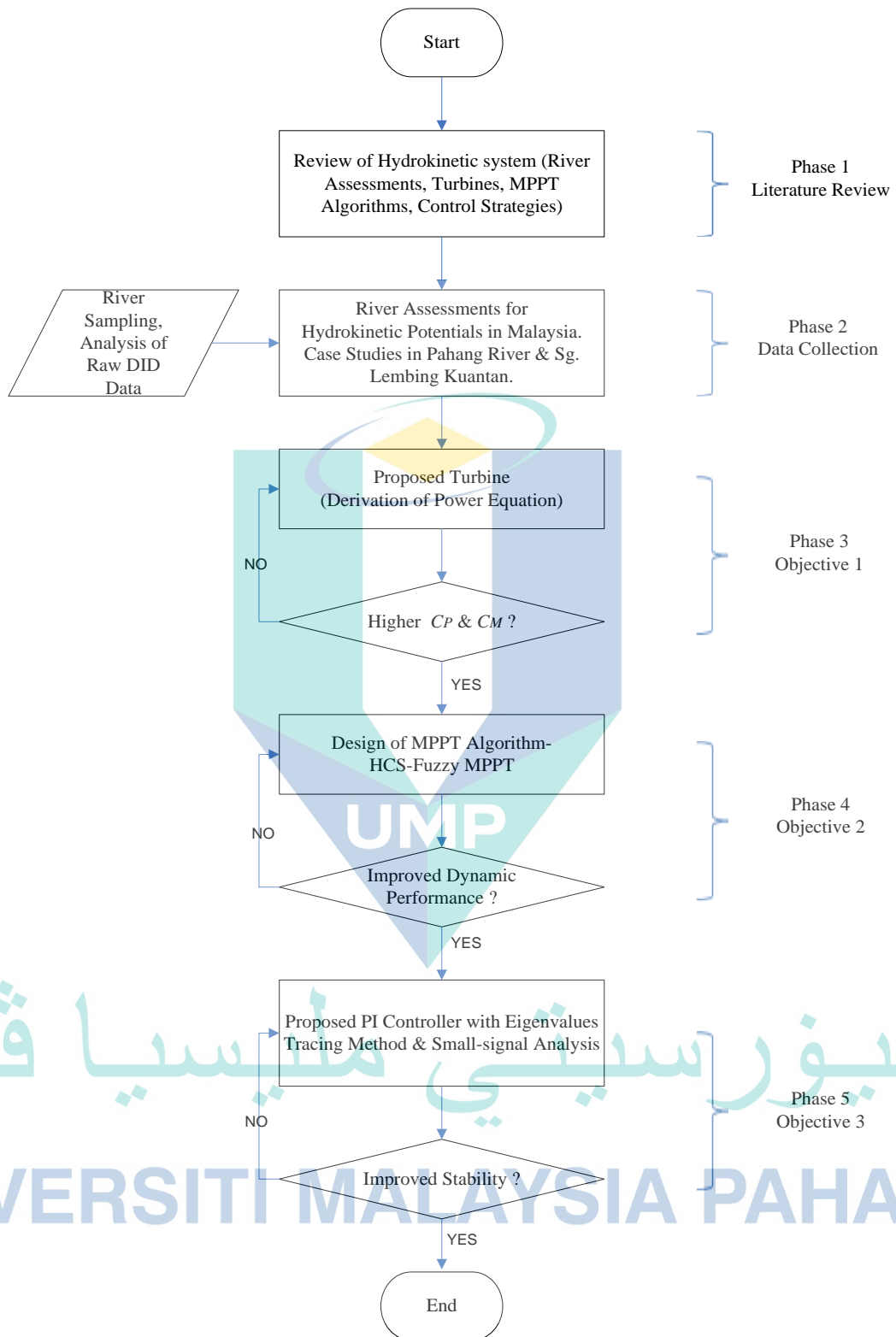


Figure 3.1 The general methodology for hydrokinetic research

The research implementation can be outlined as follows:

### **Phase I: Know-how Knowledge**

The first parts of the research are concentrated on the in-depth knowledge of the hydrokinetic system, such as the concept of operation, advantages, and disadvantages, the technology, and developments, which focus on the turbine's parameter design, the maximum power point tracking, modelling, and control strategies. Notably, the hydrokinetic technology is a new field of research in Malaysia. Therefore, the fundamental study regarding this technology is necessary to speed-up the learning process.

### **Phase II: Data Collection**

The second phase is to identify a suitable location for hydrokinetic energy harnessing. The assessment studies are necessary to determine and evaluate the potentials of the resources area. The primary requirement for river assessment is the river flow velocity and channel geometry, such as river bed, depth, and width (Sarauskiene, 2017). The sampling measurement at the Pasir Kubur River, Sg. Lembing Kuantan shows the location has the potential, and the river characteristics are required in designing the hydrokinetic turbines. Besides, the Pahang River hydrological data between 2012 and 2017 produced by the Department of Irrigation and Drainage (DID) has been analysed in this work to investigate the potentials of implementation of the hydrokinetic system.

### **Phase III: Proposed Turbine and Derivation of Generalised Equation**

The third stage is to select the turbine with proper hydrofoils for energy conversion in the water. Three types of vertical axes for hydrokinetic turbines have been considered for turbine performance analysis. The H-Darrieus, Darrieus, and Gorlov helical turbine with twelve quantity of NACA and NREL S-Series hydrofoil have been analysed using the QBlade and Matlab software. The turbine's performances have been analysed in terms of power coefficient ( $C_P$ ) and torque coefficient ( $C_M$ ). The turbine with suitable hydrofoil, highest of  $C_P$  and  $C_M$  has been selected as the best option turbine based on river characteristics in Malaysia. Subsequently, the  $C_P$  equation has been simplified into the

polynomial approximation to represent the turbine power model based on the  $C_P$ -TSR curve. This  $C_P$  approximation equation will be applied for designing the MPPT algorithm and small-signal stability analysis in controller design.

#### **Phase IV: Design of MPPT Algorithm**

The next phase in this research is to propose the Maximum Power Point Tracking algorithm (MPPT) to extract the maximum output power for the off grid-connected system. The combination of Hill-Climbing Search (HCS) and Fuzzy Logic Controller (FLC) has been proposed in this work. The conventional HCS algorithm has a limitation due to the oscillation of the output power. Besides, a fixed step-size in conventional HCS algorithm needs to compromise between the fast-tracking and accuracy of the output power. The FLC has been implemented in this work to provide the variable step-size on the HCS algorithm. The FLC has been applied because of the fast convergence, able to analyse imprecise input and adaptive (Eltamaly & Farh, 2013). Therefore, the combination of this algorithm has been chosen due to the sensorless technique, establish algorithm, and easier for verification and validation.

#### **Phase V: Proposed PI Controller with Eigenvalues Tracing Method**

The final stage is the mathematical modelling of the turbine, permanent magnet synchronous generator (PMSG) and back-to-back converter for the grid-connected hydrokinetic system. In this work, the PI controller parameters have been determined based on traces of eigenvalues. The PI controller has been chosen because of the robustness and ability to improve the system stability by shifting the poles towards the left s-plane (Aly & El-Hawary, 2011; Omkar et al., 2019). The state-space equation has been derived for small-signal stability analysis. A trace of eigenvalues can investigate the stability of the system. Therefore, the dynamic stability of the hydrokinetic system can be improved and reduced oscillation frequency.



### 3.3 Assessment on Hydrokinetic Resources

This section presents the assessment study to investigate the river characteristics for the hydrokinetic energy harnessing in Malaysia. The sampling measurement was conducted at the Pasir Kubur river, Sungai Lembing, Kuantan, as a sample of assessment studies to observe the water velocity and river depth. Subsequently, the evaluation method, velocity measurement and results & discussions are also explained at the end of this section.

#### 3.3.1 Hydrology Measurement and Observation

Based on the hydrology study, several steps are required to conduct the river velocity measurement, as shown in Figure 3.2. The first step is site selection, where several characteristics need to be considered. For example, the site selection for streamflow measurement is reasonable straight and free from swirls, vortices and backward flow. In addition, the selection of the site must be avoided if the cross-section is immediately from sharp bends or obstructions. Moreover, the cross-section area with the turbulent flow is not suggested.

The second step is to measure the cross-section width by stretching a measuring tape across the river stream. Secure the tape on the river edge using pins or stakes and prevent the tape from touching the water surfaces. It is recommended to lay out the tape 0.3 m above the water surface. Then calculate the distance on the tape corresponding to the left and right position of the riverbank.

The third step is to determine the number and spacing of vertical for velocity and depth measurement. The spacing and number of verticals are crucial for the accurate measurement of the river discharge. It is recommended to have between 20 and 30 sub-section of spacing if applicable.

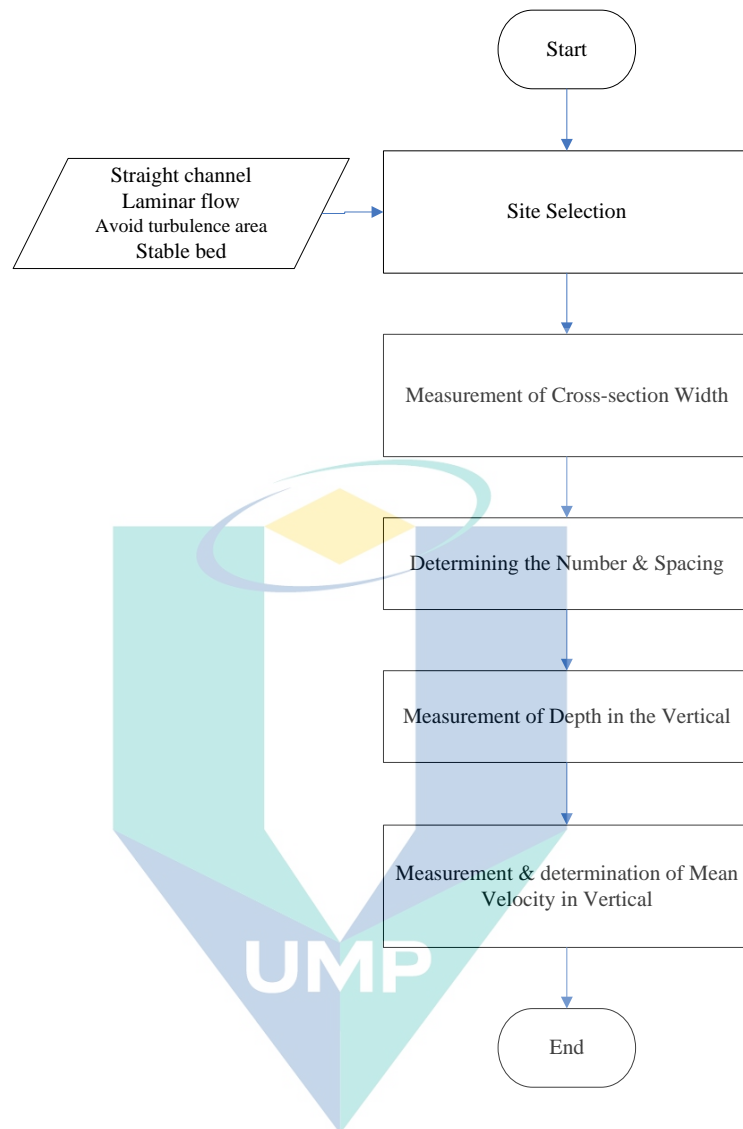


Figure 3.2 Procedure for water velocity measurement

The next step is to determine the river depth using the marks on the current meter rod.

It is desirable to take at least two readings at each vertical. The inaccuracy of reading can occur at the sand-bottom stream or soft muck due to the rod sinking into the riverbed. The final step is to measure the mean velocity. The mean velocity can be obtained by measuring the velocity at each vertical section and calculated the mean. This method will provide a reliable estimation mean velocity closed to actual velocity profiles.

### 3.3.2 Case Studies 1: River Assessment at Pasir Kubur River Sg. Lembing, Kuantan

Sungai Lembing is located in the district of Kuantan, Pahang, in the east coast of Peninsular Malaysia, almost 35 kilometres from Kuantan town. Figure 3.3 shows the location of the study area which is located at Kampung Seberang Kuala Kenau about 4 km from the main town of Sungai Lembing. The exact location of Sungai Pasir Kubur is between latitude  $3^{\circ} 56' 24.4''$  N and longitude  $103^{\circ} 3' 3.1''$  E. This area was selected due to its easy access and the river's condition such as suitable depth, width and water velocity. Besides, the river has a shallow water depth, low current speed and floating debris and can represent common characteristics of the river in Malaysia.

The Pasir Kubur River is well-known as the recreation area among Kuantan's people, especially during the weekend. While keeping place as a recreation area, the function of the river can be expanded as a renewable energy source. Half of the river's cross-section can be used to produce electricity by installing hydrokinetic energy harnessing. Nevertheless, several factors need to be considered while selecting the resources area such as the channel geometrics, slope and roughness, and the climate's condition (Canadian Hydraulics Centre, National Research Council of Canada, 2010). Therefore, the assesment study is necessary to observe the potential and evaluate the best design based on the river characteristics.



Figure 3.3 The Location of Pasir Kubur River, Sungai Lembing Kuantan, Pahang. Source: Google Map (2019).

The river was chosen as a sample of assessment study to represent the typical characteristics of rivers in Malaysia, which has floating debris such as leaves, grass, and trees. Besides, several segments of the river have a shallow water depth and low water velocity.

### 3.3.3 Evaluation Method

The investigation on the potential of hydrokinetic energy harnessing at Pasir Kubur River Sungai Lembing required the evaluation method, simulation and flow velocity measurement. The evaluation method was developed for river assessment to determine the energy capacity and to locate the highest potential resources sites. The technique covers several steps, including flow measurement and data validation.

The evaluation method for hydrokinetic energy harnessing can be applied to any river to investigate the resource's potential. Figure 3.4 shows the flow chart of the evaluation method before the installation of the hydrokinetic turbines. The first step is the pre-reconnaissance study, which involves desk studies and maps analysis to determine and narrow down the suitable locations. The second step is the reconnaissance study. This step requires site visits to observe the physical location of the resources area. Proper observation at the sites will influence the operation for optimal performance and cost viability of the project.

اونيورسيتي ملايسيا قهغ

UNIVERSITI MALAYSIA PAHANG

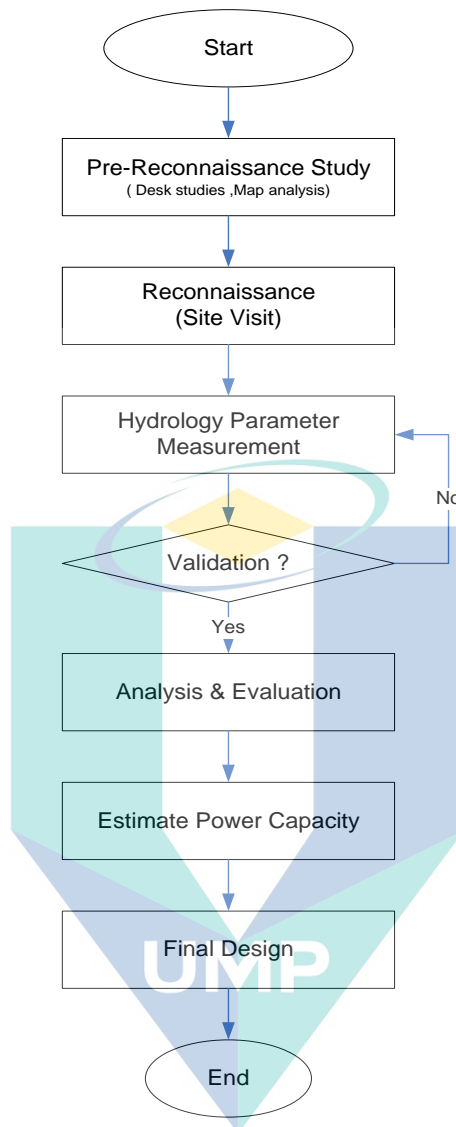


Figure 3.4 The evaluation step of river energy potential for hydrokinetic energy harnessing.

The third step is the hydrology study which requires sampling measurement activities. The river velocity, depth, cross-sectional area, and discharge rate need to be measured to investigate the potential of the resource area. Conversely, the primary requirement for hydrokinetic energy harnessing in the river is sufficient water velocity with suitable depth (Sarauskiene, 2017). The validation data could be fulfilled if the river basin is near the gauging station. In Malaysia, the Department of Irrigation and Drainage (DID) is responsible to manage the river basin, water resources, hydrology, flood and coastal zone (Official Page: Department of Irrigation & Drainage, 2018). The data regarding the water

discharge, water level, rainfall, flood, and water quality can be requested and bought at DID Ampang.

The analysis and evaluation step is required to locate the river segments with the highest potential either for single turbine placement or array turbines arrangement. The average bed depth and cross-section width with suitable flow velocity could be considered. Moreover, the analysis such as mean water velocity, flow duration curve and frequency distribution will provide a strong justification in determine the river potentials for energy harnessing.

The next step is to calculate the amount of power that can be harnessed in the river. The annual energy yield can be estimated by Eq. (3.1) (Ani, Polinder, and Ferreira, 2013; Papathanassiou and Boulaxis, 2006).

$$E = T \int_0^{\infty} f(v) \frac{1}{2} \rho A V^3 C_p dv = T \bar{P}_w \quad 3.1$$

where  $T$  is the integral time interval (8760 hours for a time period of 1 year),  $\rho$  is the water density,  $A$  is the turbine swept area,  $f(v)$  is the function of mean water speed,  $C_p$  is the turbine power coefficient, and  $\bar{P}_w$  is the average output power over the interval  $T$ .

The final design is the last step in the evaluation method. At this level, the hydrokinetic system is suitable for ultimate deployment in the river after a very high confidence analysis. This stage requires a much greater effort and time commitment, especially in simulation and test rig hardware.

## UNIVERSITI MALAYSIA PAHANG

### 3.3.4 Velocity Measurement

The water velocity was measured using the Current Meter (FP211) produced by Global Water. The probe is a rugged and highly accurate water velocity instrument and is ideal for measuring flows in rivers and streams (Water, 2009). Three methods can be used to determine the average water velocity in the river using the FP211. The first method is suitable for small streams. The probe can be placed in the flow and then moved



slowly and smoothly from the top to the bottom of the flow during average velocity measurement. The probe must be kept moving for 20-40 seconds to obtain the accurate average value.

The second method is well-known as the velocity-area method and is suitable for larger streams and rivers. The measurement is collected by subdividing a stream cross-section into segments, as shown in Figure 3.5. The flow velocity and depth for each segment are measured to obtain the average velocity in the cross-section. The probe needs to move vertically from top to bottom smoothly for 20-40 seconds to obtain a good average. The total discharge can be calculated by the summation of all the segments and is expressed by the Eq. (3.2)

$$Q = \sum_{i=1}^n a_i v_i \quad 3.2$$

where  $Q$  is the total discharge in cubic m<sup>3</sup>/s,  $a_i$  is the area of cross section at  $i^{\text{th}}$  segment (m<sup>2</sup>) and  $v_i$  is velocity at  $i^{\text{th}}$  segment (m<sup>2</sup>/s).

The third method is by the the U.S Geological Survey (USGS) Six-Tenth Depth method. Based on the theory, the observation of velocity is made at 60 % of the depth below the water surface as a mean velocity for the vertical segment (D. Phil Turnipseed and Vernon B. Saue, 2010). The Flow Probe is placed at the center of the subsection at a depth from the surface of 60 % of the total depth. The Flow Probe is held in place, and the average velocity is obtained over a period of 40 seconds.

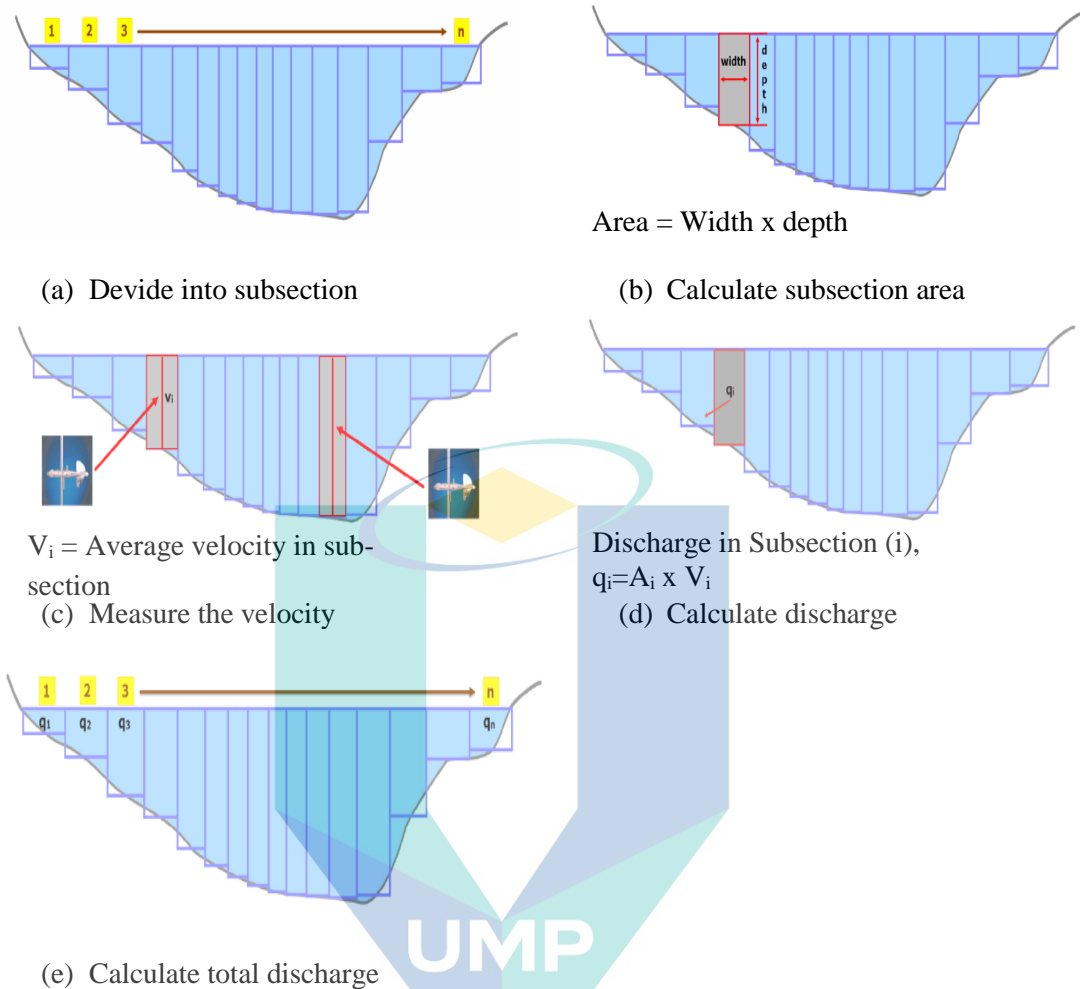


Figure 3.5 Determination of the stream cross-section and discharge computation

The sampling measurement was carried out at three stations along the Pasir Kubur River, as shown in Figure 3.6 (a)-(c). All the measurements were taken using the USGS Six-Tenth Depth method because of the accuracy measurement. The distance between sampling station to another is around 70 m with a total length of almost 250 m. Based on observation and analysis, the depth of the stream at Station 1 ranges between 0.4 m to 0.7 m with the width around 30 m. Station 2 is quite narrow and has the highest velocity among the stations. However, several areas at Station 2 have a turbulent flow and a restricted area for swimming due to past drowning cases (Kamsani, 2018). Station 3 can be classified as a shallow stream with a depth of around 0.2-0.45 m. Figure 3.6 (d) shows the river bank pebbles, which is suitable as a recreation and picnic area.



(a) Location of Station 1



(b) Location of Station 2



(c) Location of Station 3



(d) Recreation and picnic area

Figure 3.6 The location of sampling station at Pasir Kubur river Sungai Lembing, Kuantan, Pahang.

### 3.4 Assessment on Hydrokinetic Resources-Data of Department of Irrigation & Drainage (DID) Malaysia

This section presents the data produced by the Department of Irrigation & Drainage (DID) Malaysia from 2012 to 2017 at the ten selected rivers along the Pahang River. The raw data has been analysed to determine the river characteristics and hydrokinetic potentials. The methods of data analysis include the mean annual discharge, flow duration curve (FDC), frequency distributions, mean river depth, mean monthly water velocity, and annual energy yield. The mean annual discharge, river depth, and water velocity at the selected river are presented.

### 3.4.1 Site Location

The Pahang River basin is located at Peninsular Malaysia between latitude  $2^{\circ} 48' 45''$  –  $3^{\circ} 40' 24''$  N and longitude  $101^{\circ} 16' 31''$  -  $103^{\circ} 29' 34''$  E. The total area of the basin is  $27000\text{km}^2$  with the upstream located at the main range of Titiwangsa (Tekolla, 2010). The length of the Pahang River is estimated to be 440 km, and it is the longest river in Peninsular Malaysia. The main tributaries of the Pahang River are the Jelai River ( $7320\text{ km}^2$ ) and Tembeling River ( $5050\text{ km}^2$ ). Both rivers meet at a confluence of Kuala Tembeling which is 300 km away from the river mouth at Kuala Pahang, Pekan.

The Pahang River meanders through several townships such as Jerantut, Temerloh, Maran, Bera, and lastly Pekan before flowing into the South China Sea (Muhamad Barzani Gasim et al., 2013). Ten hydrological sampling stations along the Pahang River were selected in this investigation. Among the hydrology, stations are located at Sungai Yap (upstream), Temerloh (middle) and Lubuk Paku (downstream). The Pahang River basin has an annual rainfall range from 1609 mm at Temerloh to 2132.36 mm at Lubuk Paku. High rainfall occurs during the northeast monsoon between November to March every year. Figure 3.7 shows the location of the Pahang River basin.

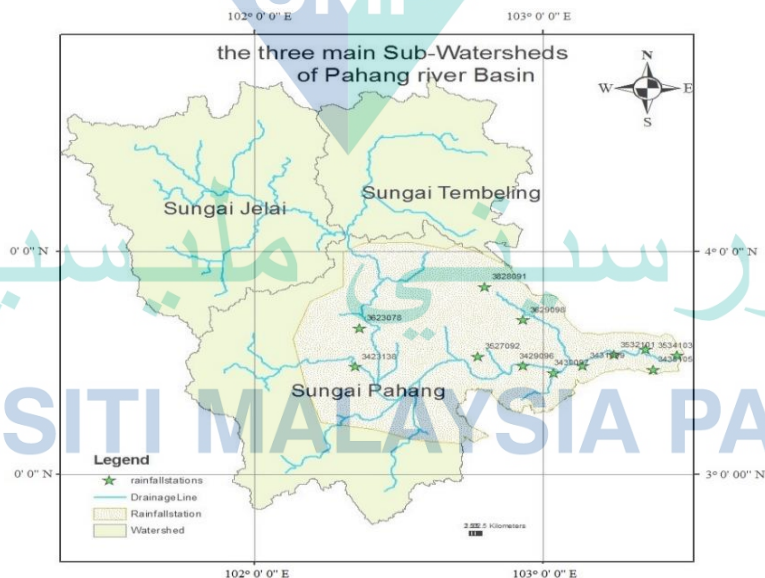


Figure 3.7 The location of Pahang River basin.

Source: Tekolla (2010).



### 3.4.2 DID Hydrology Data

The hydrological data from 2012-2017 at ten selected gauging stations along the Pahang River were used in this study. The raw data were produced by the Department of Irrigation and Drainage Malaysia (DID), Jalan Ampang, Kuala Lumpur. Seven years of data such as river flow and water level were used in this analysis to determine the potential for hydrokinetic technology. The telemetry station number and the name of the site location are listed in Table 3.1.

Table 3.1 List of telemetry stations under studied.

Station Number	Name of Station
Site 3329401	Sungai Mentiga at Jam. Chini 1
Site 3930401	Sungai Kuantan at Bukit Kenau
Site 3527410	Sungai Pahang at Lubuk Paku
Site 3424411	Sungai Pahang at Temerloh
Site 4023412	Sungai Pahang at Sg. Yap
Site 3519426	Sungai Bentong at Jam. Kuala Marong
Site 4019462	Sungai Lipis at Benta
Site 4218416	Sungai Jelai at Kuala Medang
Site 4223450	Sungai Tembeling at Kg. Merting
Site 4224454	Sungai Tembeling at Kuala Tahan

Several techniques of data analysis were undertaken to analyse the raw data of river discharge. The techniques included the mean annual discharge, flow duration curve and frequency distribution. In addition, the river depth and monthly water velocity were analysed based on raw data.

### 3.4.3 River Analysis

In this section, the mean annual discharge, Pahang River depth and water velocity are presented. The flow duration curve and frequency distribution are attached in Appendix A1 and A2 respectively.

#### 3.4.3.1 Mean Annual Discharge

Figure 3.8 shows the mean annual discharge of the ten selected gauging stations along the Pahang River, starting from 2012 to 2017. As can be seen, the highest water discharge that occurred at Lubuk Paku was 733.08 m<sup>3</sup>/s, followed by Sg. Pahang (Temerloh) and Sg. Pahang (Sungai Yap) with 594 m<sup>3</sup>/s and 518.4 m<sup>3</sup>/s respectively. Other rivers shows below 200 m<sup>3</sup>/s with Sg. Mentiga (Jam. Chini) being the lowest at 2.16 m<sup>3</sup>/s. The previous data shows that Sg. Pahang at Lubuk Paku achieved 596 m<sup>3</sup>/s during 1973-2002 and 1184.46 m<sup>3</sup>/s during 1980-2009 (Muhamad Barzani Gasim et al., 2013; Tekolla, 2010).

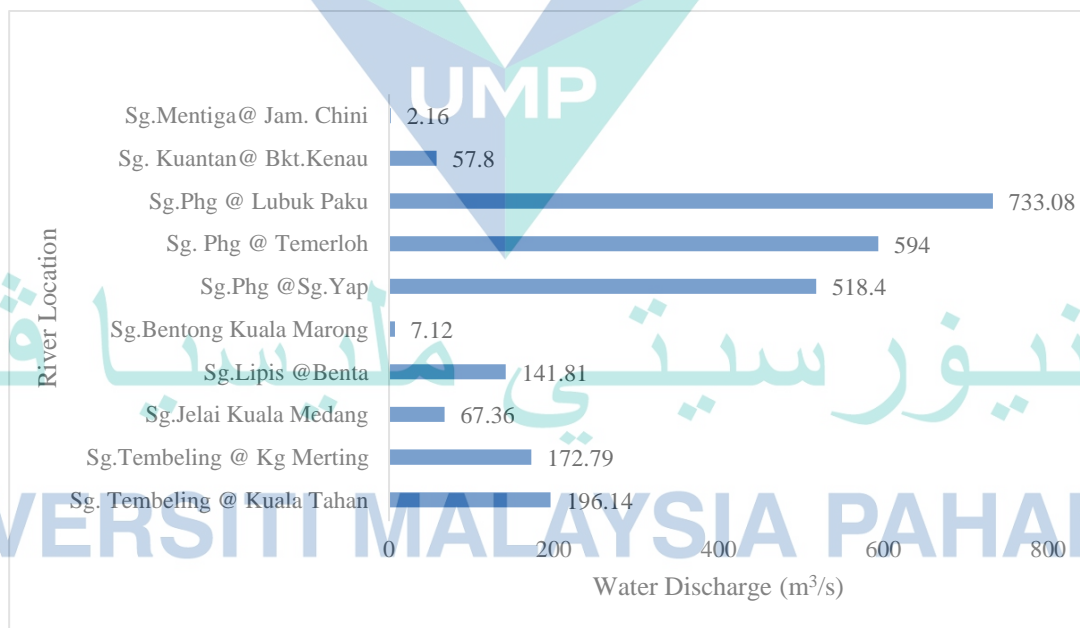


Figure 3.8 Mean Annual Discharge at 10 selected gauging stations' location.

Higher water discharge happens due to higher rainfall at the Pahang River basin, as discussed by Muhammad Barzani Gasim et al. (2011). The higher total rainfall is



triggered by the northeast monsoon which occurs from November to March every year. The highest discharge rate shows that three rivers along the Pahang River (Sg. Yap, Temerloh and Lubuk Paku) have the potential for hydrokinetic energy harnessing.

### 3.4.3.2 Pahang River Depth

Figure 3.9 shows the mean river depth during 2012-2017 at ten selected gauging stations. In the hydrokinetic energy harnessing, river depth is necessary to be considered due to turbine placement (Johnson and Pride, 2010). If the river depth is too shallow, the turbine is unable to rotate and ultimately can reduce the amount of energy harnessing. With a suitable river depth, the hydrokinetic system can use different sized turbines, and the amount of energy harnessing can be increased because the output power depends on the swept area of the turbine as shown in Eq. (2.5). It is observed, the river depth increased at the upstream resources of the Pahang River, which is Sg. Jelai and Sg Tembeling, Kuala Tahan with 75.89 m and 55.6 m, respectively. Nevertheless, at the downstream site such as Sg. Pahang at Lubuk Paku, the depth slightly decreased to 13.7 m.

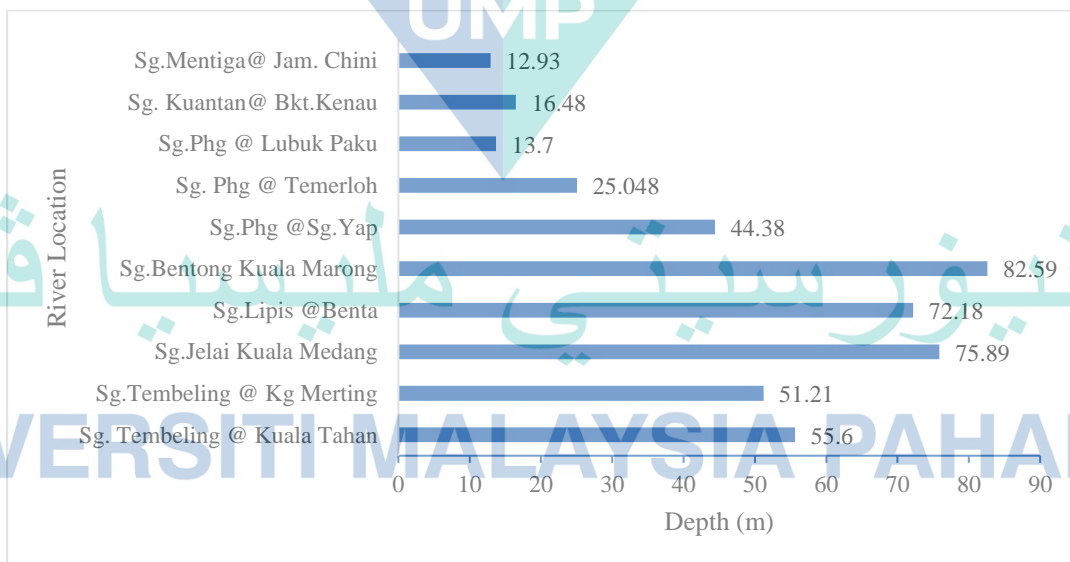
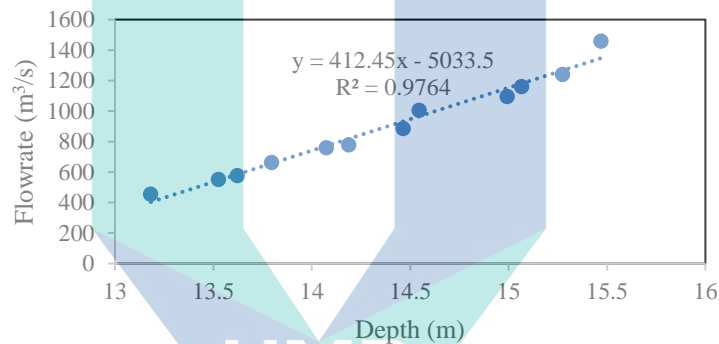
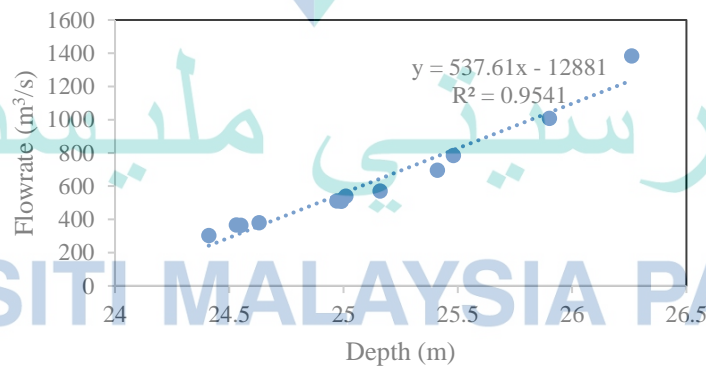


Figure 3.9 Mean river depth of Pahang River from 2012 to 2017

The flowrate vs water velocity was plotted to identify the relationship between both parameters. In this case, Pahang River at Lubuk Paku and Temerloh were chosen for investigation based on flow duration curve and frequency distribution data. It is observed, the water depth is proportional to the flowrate, as shown in Figure 3.10 (a) and (b). These relationships can be considered as linear through  $R^2= 0.986$  and  $R^2=0.9918$  for Pahang River at Lubuk Paku and Temerloh, respectively. The discharge quantity and water depth are dependent on the total rainfall during the monsoon season. The discharge quantity increased during the northeast monsoon between October to January each year. Both discharge and depth will reduce significantly during the southwest monsoon, which occurs between March to September every year.



(a) Flowrate vs Depth for Pahang River at Lubuk Paku in 2017



(b) Flowrate vs Depth for Pahang River at Temerloh.in 2017

Figure 3.10 The relationship between flowrate and water depth for Pahang River at Lubuk Paku and Temerloh in 2017.

### 3.4.3.3 Water Velocity

The Pahang River at Lubuk Paku was chosen for the monthly mean velocity analysed due to the location of the river at the downstream of Pahang River. Figure 3.11 shows the monthly mean velocity of the Pahang River at Lubuk Paku between 2012 and 2017. It is observed, the water velocity at Lubuk Paku is mostly higher than  $1.0 \text{ ms}^{-1}$ . Instead, the velocity slightly increased from  $1.0 \text{ ms}^{-1}$  to  $2.0 \text{ ms}^{-1}$  during the northeast monsoon between October to January each year. The data in 2015 are unrecorded after the biggest flood occurred in 2014 that destroyed the system at the telemetry station (Kamarudin et al., 2019).

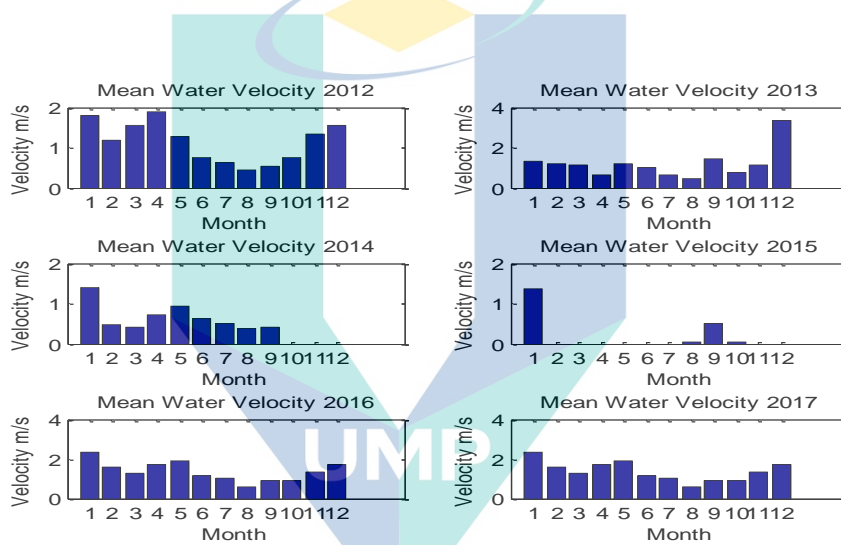
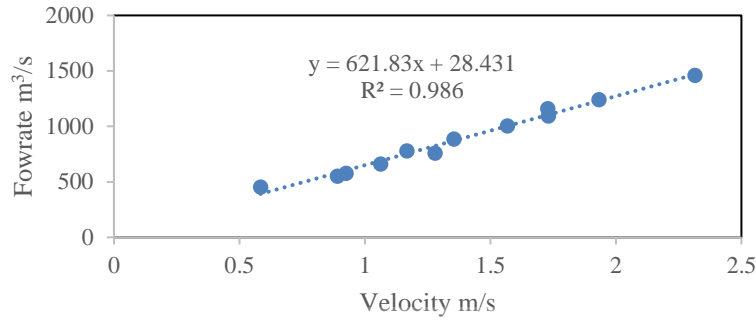
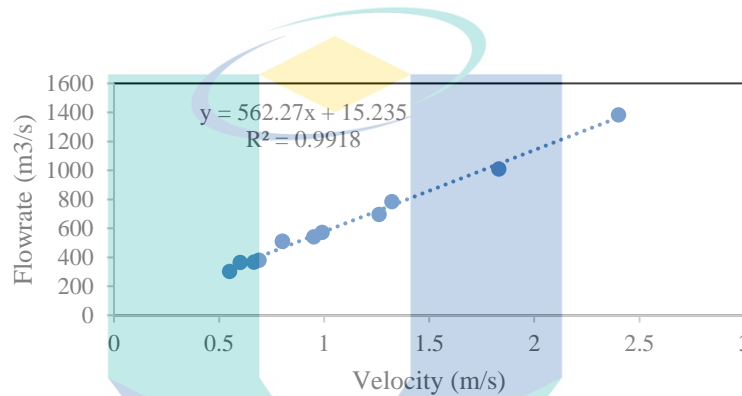


Figure 3.11 Mean monthly water velocity between 2012 to 2017 for Pahang River at Lubuk Paku

The relationship between the flowrate and water velocity of Pahang River at Lubuk Paku and Temerloh were analysed as shown in Figure 3.12 (a) and (b). Both river were chosen due to higher potential on the hydrokinetic energy harnessing compared to other rivers. It is observed that, the water velocity is proportional to the flowrate. These relationships can be considered as linear through  $R^2= 0.9860$  and  $R^2=0.9918$  for the Pahang River at Lubuk Paku and Temerloh respectively.



(a) Flowrate vs Velocity for Pahang River at Lubuk Paku in 2017



(b) Flowrate vs Velocity for Pahang River at Temerloh in 2017

Figure 3.12 The relationship between flowrate and water velocity at Pahang River in 2017

### 3.5 Summary

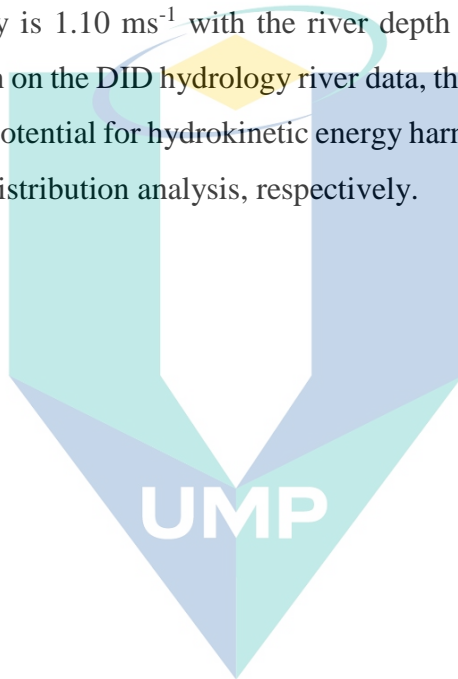
In this chapter, the general methodology and justification for the implementation method used in hydrokinetic energy harnessing are explained briefly. The research work has been divided into five stages to accomplish. At first, the literature survey then follows by river assessment studies to investigate the river characteristics. Next, is the modelling of the power turbine equation based on Malaysian river characteristics and, lastly, control strategies for stand-alone and grid-connected of hydrokinetic system.

As the thesis is written in a paper-based format, therefore, the other methodologies will explain in each chapter accordingly. Nevertheless, the assessment studies of the

hydrokinetic system at the Pasir Kubur River, Sungai Lembing, Kuantan, and the data analysed of ten selected rivers along the Pahang River basin are also presented.

The findings of the assessment studied at Pasir Kubur River and along the Pahang River basin were employed to design the turbine based on the Malaysian river characteristics. Two parameters, water velocities and water depth, are the main components to determine the design consideration of the selected turbine.

Moreover, the sampling measurement at Pasir Kubur River was indicated that the average water velocity is  $1.10 \text{ ms}^{-1}$  with the river depth range from 0.55 m to 5.0 m. Whereas, investigation on the DID hydrology river data, the Pahang River at Lubuk Paku and Temerloh have a potential for hydrokinetic energy harnessing based on flow duration curve and frequency distribution analysis, respectively.



اونيورسيتي ملايسيا قهغ

UNIVERSITI MALAYSIA PAHANG

## CHAPTER 4

### DESIGN CONSIDERATION & SELECTION OF RIVER CURRENT TURBINE

#### 4.1 Chapter Overview

The necessity of new energy sources has received considerable interest due to concerns with CO<sub>2</sub> gas emissions, greenhouse gas effects, and environmental problems. Nevertheless, the increase in energy demand and scarcity in fossil fuel reserves are significant factors. Sustainable energy sources and environmentally friendly methods for electricity generation have been considered.

An example of a sustainable energy resource is the kinetic energy stored in moving water, such as rivers and tidal currents. The hydrokinetic energy conversion system (HECS) is an electromechanical device that converts the kinetic energy of river streams, tidal currents, man-made water channels, or waves into electricity (A. Kumar & Saini, 2017). The HECS does not require a particular head and impoundment to operate (Lago et al., 2010; Yuce & Muratoglu, 2015).

Since hydrokinetic energy harnessing in the river is a new field of research in Malaysia, there are no specific data that indicate which turbines are most suitable to be implemented. Turbine sizing, hydrofoil geometric profiles, and turbine solidity, which are based on river characteristics in Malaysia are scarce in the literature. In addition, the development of hardware or prototype for a hydrokinetic system is time-consuming and complicated. Hence, by modelling the turbine into an equivalent mathematical equation, researchers can provide a better analysis of the system requirement and reduce the time, cost, and errors. As far as the author is concerned, an equivalent model to represent the hydrokinetic turbine in the river is rarely presented in the literature.

In this chapter, three types of vertical axes for hydrokinetic turbines were considered for turbine performance analysis. The H-Darrieus, Darrieus, and Gorlov Helical turbines with 12 NACA and NREL S-Series hydrofoils were analysed using QBlade and Matlab



software. The turbines' performances were analysed in terms of power coefficient ( $C_P$ ) and torque coefficient ( $C_M$ ). The turbine with a suitable hydrofoil, and highest  $C_P$  and  $C_M$  was selected as the best option based on river characteristics in Malaysia. Subsequently, the turbine power model was derived based on a polynomial approximation equation.

This chapter presents the design consideration and selection of a river current turbine for hydrokinetic energy harnessing. Firstly, the principle and concept of operation of the rotating turbine, followed by turbine sizing and types of hydrofoils for blade profiles, are presented. Secondly, the QBlade simulation including the blade element momentum (BEM), double multiple streamtube (DMS) analysis for H-Darrieus, Darrieus, and Gorlov helical turbines with 12 NACA and NREL S-Series hydrofoils are discussed. Finally, the results and discussion regarding the best selection of hydrofoils and turbines for the hydrokinetic system in the river are presented. A turbine model based on the  $C_P$ - $TSR$  curve to represent the H-Darrieus turbine characteristic is also determined using the polynomial approximation equation.

## 4.2 Turbines Design Considerations

This section presents the requirement and consideration of the turbine design. The basic theory and related formula in turbine design are discussed. The different types of hydrofoil profiles for hydrokinetic energy harnessing are described. The blade element momentum and double multiple streamtube analysis for the H-Darrieus, Darrieus, and Gorlov helical turbines are considered using QBlade software.

### 4.2.1 Principle and Concept of Operation

The main principles used to model the rotating hydrokinetic turbines were blade element momentum (BEM) and the double multiple streamtube (DMS) algorithm (Albernaz et al., 2015; Pierre et al., 2015). The BEM and DMS algorithms provide a detailed turbine design procedure, and it was used to determine the lift and drag forces

over the different angles of attack (AoA), torque ( $C_M$ ) and power coefficients ( $C_P$ ) (Yuce & Muratoglu, 2015).

Figure 4.1 shows the resultant loads on the blade section (hydrofoil). As can be seen, each blade section has an optimum angle of attack (AoA), which is the angle between the relative velocity and the blade section's chord line. According to Kumar (2016a), the AoA should be kept to a minimum to avoid stalling and separation of the turbine.

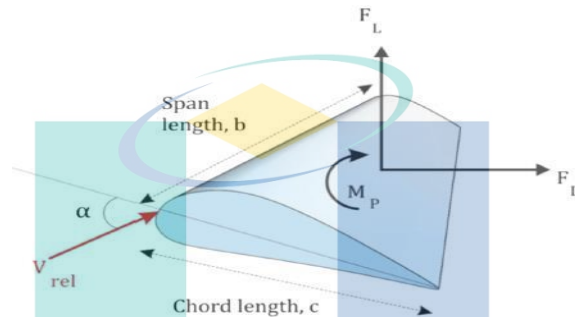


Figure 4.1 The force diagram on a typical blade section.

Source: Yuce & Muratoglu( 2015).

$F_L$  and  $F_D$  represent the lift and drag force of the hydrofoil blade. These two parameters depend solely on the blade shape and Reynolds number ( $R_e$ ) under a given operating condition. The  $R_e$  is an index of turbulence created by a body placed in a fluid (M. J. Khan, Iqbal, & Quaicoe, 2006). This can be expressed in Eq. (4.1).

$$R_e = \frac{Vd}{\nu} \quad 4.1$$

where,  $\nu = 1.1 \times 10^{-6}$  is the kinematic viscosity of water, the rotor diameter ( $d$ ), and water velocity ( $V$ ), an estimate of  $R_e$  can be found. The value of  $R_e$  must be big enough to reduce the cavitation. The Aspect Ratio (AR) of the blade is a measure of its length and slenderness. The AR can be expressed by Eq. (4.2).

$$AR = \frac{h}{c} \quad 4.2$$

where;  $h$  = height and  $c$  = chord length. The dimensions of the rotor, number of blades ( $N$ ), and blade chord length ( $c$ ) are interrelated through solidity information. The solidity,  $\sigma$ , can be expressed by Eq. (4.3).

$$\sigma = \frac{Nc}{d} \quad 4.3$$

Water turbines have higher solidity than wind turbines, and solidity values may range from 0.15 to 1.6. Lower solidity implies excellent hydrodynamic performance, and higher values generally allow for a more durable mechanical structure while improving the power coefficient and turbine performance (Jafari et al., 2018). Figure 4.2 shows the flow velocity distribution and forces of turbine hydrofoils. It is observed that the relationship between AoA ( $\alpha$ ) and the azimuth angle ( $\theta$ ) can be derived from the velocity triangle, as given in Eq. (4.4)–Eq. (4.6).

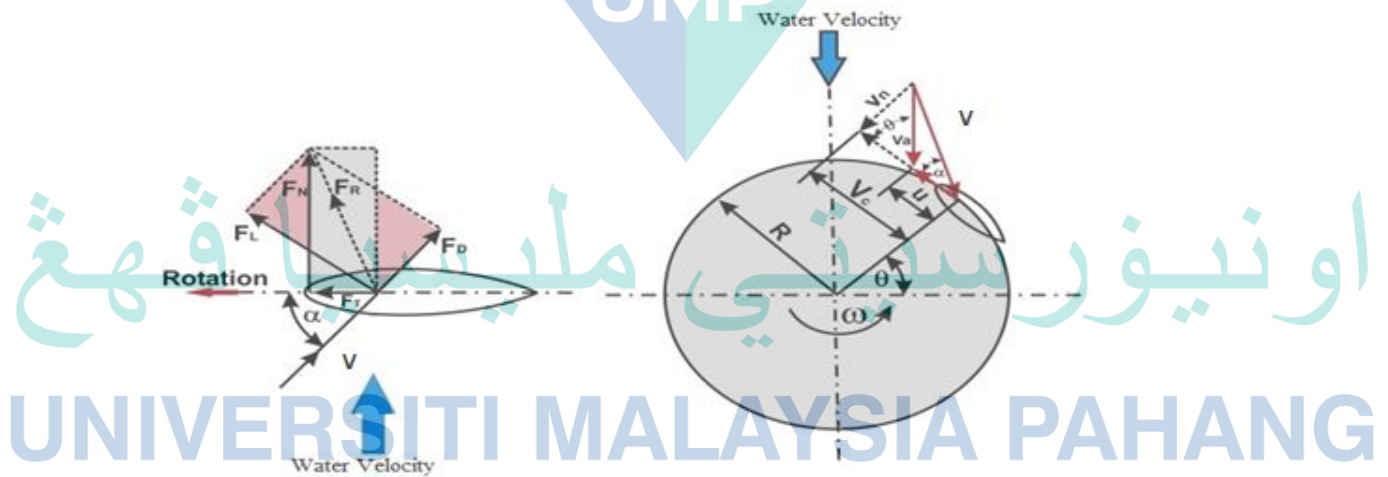


Figure 4.2 The hydrofoils flow velocity distribution and force diagram

Source: M.H. Mohamed, Dessoky & Alqurashi (2019)

$$W = \sqrt{V_n^2 + V_c^2} \quad 4.4$$

where  $W$  is the relative velocity of water.  $V_n$  is the normal component of the relative velocity perpendicular to the chord line.  $V_c$  is the tangential component of the relative velocity parallel to the chord line. Subsequently,  $V_n$  and  $V_c$  are given in Eq. (4.5) and (4.6), respectively. (Patel, Eldho, & Prabhu, 2017b)

$$V_n = V_a \sin \theta \quad 4.5$$

$$V_c = R\omega + V_a \cos \theta \quad 4.6$$

where,  $V_a$  is Maskell's corrected velocity. According to Mohamed et al. (2019), the AoA can be determined by Eq (4.7).

$$\alpha = \tan^{-1} \left[ \frac{\sin \theta}{\lambda + \cos \theta} \right] \quad 4.7$$

where  $\alpha$  is the AoA,  $\theta$  is the azimuth angle, and  $\lambda$  is the tip speed ratio as given in Eq. (4.8).

$$\lambda = \frac{\omega R}{V} \quad 4.8$$

where  $\omega$  and  $R$  are the turbine rotational speed and turbine radius, respectively.  $V$  is the water velocity. The torque coefficient ( $C_M$ ) and power coefficient ( $C_P$ ) can be written as in Eq. (4.9) and (4.10), respectively.

$$C_M = \frac{T}{0.5\rho ARV^2} \quad 4.9$$

$$C_P = \frac{P}{0.5\rho AV^3} \quad 4.10$$

As noted by Mohamed (2012), the lift force,  $F_L$ , and drag force,  $F_D$  can be generated when the aerofoils are set at an angle of attack in a fluid flow. It is observed that  $F_L$  and  $F_D$  can be resolved to get the tangential force  $F_T$  and axial force  $F_N$ , as shown in Figure 4.2.

According to Khan et al. (2006), the maximum efficiency that an ideal turbine can reach is known as the Betz limit. Betz's law proposes that the theoretical maximum power coefficient ( $C_P$ ) for a rotating turbine in a fluid stream is 0.59 (Schleicher, Riglin, & Oztekin, 2015; Shamsavarifard, Bibeau, & Birjandi, 2013). The Betz limit can be applied to hydrokinetic turbines working in a free stream such as tidal and river currents without augmentation or ducts. The use of augmentation channels or ducts around a turbine may increase this theoretical limit of  $C_P$  by concentrating the incoming stream velocity toward the rotor (García et al., 2014). Figure 4.3 shows the standardised  $C_P$  for different types of turbines.

اونيور سیتی ملیسیا فہق

UNIVERSITI MALAYSIA PAHANG

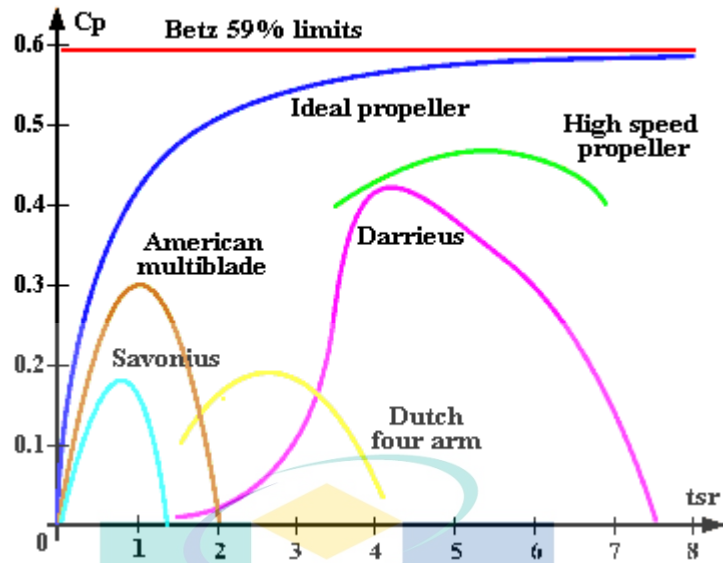


Figure 4.3 The comparison of power coefficient versus tip speed ratio ( $C_p-\lambda$ ) for different types of turbine designs.

Source: Karbasian (2019).

#### 4.2.2 Turbine Simulation and Design Consideration

Figure 4.4 shows the flow chart of the turbine design consideration process. The design constraints include the desired rated power of the turbine, the water velocity, and the river characteristics at the resource location. The parameters which need to be considered are the river depth, cross-section and river current velocity.

اونيورسيتي مليسيا قهغ

UNIVERSITI MALAYSIA PAHANG



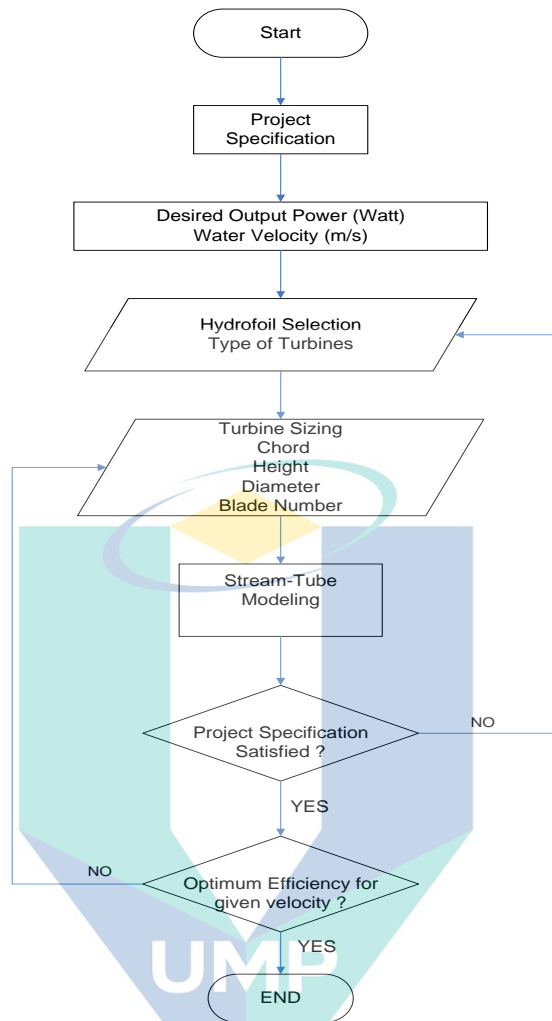


Figure 4.4 The turbine design consideration process

QBlade software version 0.93 was used to simulate the turbine design. The software offered flexibility and user-friendly platform for designing the turbine blades. Besides, the software provided the extrapolation of XFOIL and pressure distribution around a 360° angle of attack (AoA) on the turbine blades. Furthermore, the software was provided for computation of rotor performance over tip speed ratio (TSR) range

The streamtube modelling determined the pressure distribution on the hydrofoils. Figure 4.5 shows the software module in QBlade that consists of XFOIL, polar extrapolation blade design, and turbine analysis. The XFOIL analysis was used to acquire the lift and drag coefficients over different angles of attack (AoA).

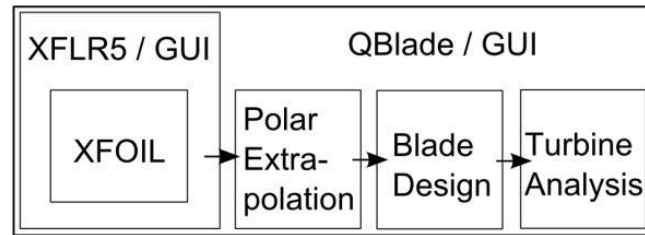
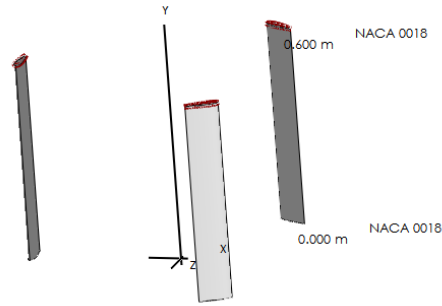


Figure 4.5 The software module in QBade

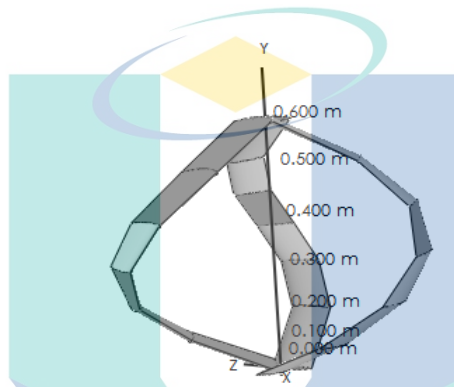
Source: Marten (2013)

The polar extrapolation module was used to ensure the smooth operation of the Blade Element Momentum (BEM) and DMS algorithms. This module can generate or import aerofoil database that needs to be extrapolated to the full range of a  $360^\circ$  angle of attack (AoA). The aerodynamic simulation module for a vertical axis wind turbine in QBlade was based on the DMS algorithm, as developed by Paraschivoiu (Marten & Wendler, 2013). In the DMS analysis, a series of equal streamtubes was assumed to pass through the rotor. For each tube, the momentum equation was computed, and the effects of all the streamtubes were integrated to determine the forces acting on the rotor blade (Pierre et al., 2015).

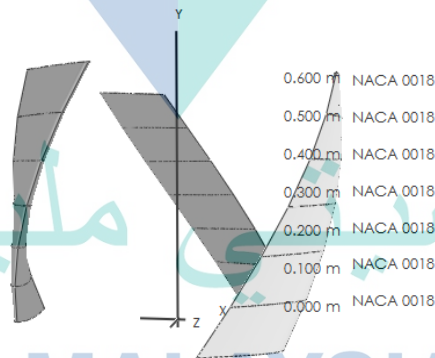
In this work, three types of turbines were applied and simulated for the highest power and torque coefficient, as shown in Figure 4.6. The H-Darrieus, Darrieus, and Gorlov Helical turbines with 12 different NACA and NREL S-Series hydrofoils were analysed using QBlade and Matlab software. The turbines' performances were analysed in terms of power coefficient ( $C_P$ ) and torque coefficient ( $C_M$ ). The turbine with the highest  $C_P$  and  $C_M$  was selected as the best turbine option based on river characteristics in Malaysia.



(a) H-Darrieus Turbine



(b) Darrieus Turbine



(c) Gorlov Helical Turbine

اونیورسیتی ملیسیا قهغ  
 UNIVERSITI MALAYSIA PAHANG

Figure 4.6 Vertical axis hydrokinetic turbine simulated by QBlade

### 4.2.3 Turbine Sizing

The hydrokinetic turbine can be designed by considering river characteristics such as depth, water velocity, cross - section, sedimentation, and riverbed. The assessment study in Chapter 3 investigated the characteristics of several rivers in Pahang. A river with high velocity is necessary as the turbine's output power is increased proportionally to the cube of water velocity. In this work, the turbine sizing was based on the sampling data at Pasir Kubur River, Sungai Lembing, Kuantan, and several selected rivers along the Pahang River basin.

Two parameters need to be considered for the river current turbine in this work. First is water velocity, and the second is river depth. Table 4.1 shows the sampling measurement data and river characteristics at one of the assessment sites in Pahang. The minimum depth and velocity of the river are 1.15 m and  $1.0 \text{ ms}^{-1}$ , respectively. Hence, one of the design criteria is that the turbine dimension must not exceed the minimum level of river depth.

Table 4.1 Summary of sampling measurement at Station 2 Pasir Kubur River, Sungai Lembing, Kuantan in April 2018.

Parameter	Measurement Values
Min-Depth	1.15 m
Max-Depth	5.0 m
Min-Velocity	$1.0 \text{ ms}^{-1}$
Max-Velocity	$1.3 \text{ ms}^{-1}$
Width	9.14 m

The turbine sizing is initiated by estimating the power required by homes in the remote communities. In this work, the output power is set to 200 W for the stand-alone system. According to Anyi and Kirke (2011), 200 W of AC power is sufficient to supply a single remote community home. The power output of the hydrokinetic system can be determined by Eq. (4.11).

$$P_o = \frac{1}{2} \rho A V^3 C_p \quad 4.11$$

where,  $P_o$  is the output power in Watt,  $A$  is the cross-section area and  $C_p$  is the power coefficient. On the other hand,  $\rho$  is the water density and the value is considered constants ( $1000 \text{ kg/m}^3$ ) at all locations of the river.

The power coefficient ( $C_p$ ) is a non-linear function of the Tip Speed Ratio ( $TSR$ ) and pitch angle ( $\beta$ ). Nevertheless, for a hydrokinetic turbine with a fixed pitch angle, the  $C_p$  is only determined by the  $TSR$  (Vermaak et al., 2014). The  $TSR$  is expressed by Eq. (4.8). Therefore, the turbine sizing can be calculated by re-arranging Eq. (4.11) to Eq. (4.12).

$$A = \frac{P_o}{0.5 \rho V^3 C_p} \quad 4.12$$

where,  $\rho$ ,  $V$ , and  $C_p$  are equal to  $1000 \text{ kg/m}^3$ ,  $1.3 \text{ ms}^{-1}$ , and  $0.46$ , respectively. Based on the calculation, the value of  $A$  is equal to  $0.4947 \text{ m}^2$ . The effective area encountered by the vertical axis turbine is essentially a rectangle. Therefore the diameter ( $d$ ) and height ( $h$ ) of the turbine can be calculated as given by Eq. (4.13).

$$A = hd \quad 4.13$$

where,  $A$  is the swept area,  $h$  is the height, and  $d$  is the diameter of the turbine. The height and diameter are set at  $0.8 \text{ m}$  and  $0.6 \text{ m}$ , respectively, for a more straightforward measurement. Figure 4.7 shows an isometric drawing of the H-Darrieus turbine. The full specification of the turbine is given in Table 4.2.

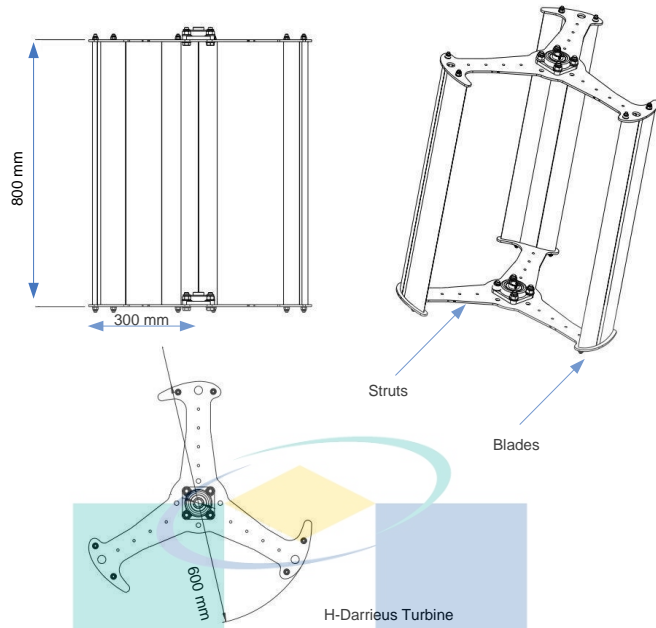


Figure 4.7 The dimensions of the straight blade H-Darrieus turbine under study.

Table 4.2 The detailed specification of the turbine under study.

Parameter	Details
Hydrofoils	NACA
Number of Blades	3
Radius (R)	0.3m
Height	0.8m
Swept Area (A)	0.48m <sup>2</sup>
$R_e$	1.0X10 <sup>6</sup>
Solidity	0.5
Water Density ( $\rho$ )	1000kg/m <sup>3</sup>
Pitch Angle( $\beta$ )	Fixed



#### 4.2.4 Hydrofoil Blade Selection

The selection of blade profile shape is essential to determine the aerodynamic or hydrodynamic performance of a turbine. As noted by Heliciel (2020), the lift and drag ratio is crucial as it determines the quality of the profile by representing the forces around the hydrofoils. A standardised aerofoil from the National Advisory Committee for Aeronautics (NACA) is commonly used in designing aerofoils for aircraft, wind turbines, as well as for hydrokinetic blade systems.

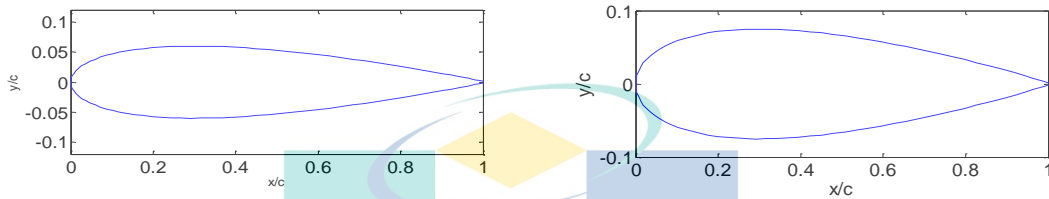
According to Mohamed (2012), NACA 00XX, NACA 63XXX, S-Series, A-Series, and FX-Series are commonly used as aerofoils for vertical axis wind turbine blade profiles. Nevertheless, at present, there is no information regarding which hydrofoil profiles are suitable for hydrokinetic energy harnessing. Therefore, a study to investigate which hydrofoils are suitable for the hydrokinetic system is necessary to improve the efficiency of the system. In this work, the NACA and NREL S-Series hydrofoil profiles were employed on the H-Darrieus, Darrieus, and Gorlov turbines to determine which hydrofoils are the best option for the water turbine.

Figure 4.8 shows symmetrical and non-symmetrical hydrofoil geometric profiles. Figure 4.8 (a)–(d) is a symmetrical geometric profile represented by NACA 0012, NACA 0015, NACA 0018, and NACA 0021. The symmetrical hydrofoils are employed to investigate the effect of different thickness profiles on turbine performance. The non-symmetrical or camber hydrofoils are represented by NACA 2415, NACA 4415, and NACA 6415, as shown in Figure 4.8 (e)–(f). The hydrofoils profiles have a similar thickness but different camber percentages. This type of profile is used to investigate the effect of the camber hydrofoils on turbine performance.

NACA 4412, NACA 4415, and NACA 4418 as shown in Figure 4.8 (f)–(i), are used to investigate the effect of thickness on camber hydrofoils. The hydrofoils have similar camber percentages but have different thicknesses. The National Renewable Energy Laboratory (NREL) S-Series 833, 834, and 835 hydrofoils are shown in Figure 4.8 (j)–(l). These NREL S-Series hydrofoils have different camber percentages and thicknesses. Table 4.3 shows the properties of NREL S-Series hydrofoils. The performance of the NREL hydrofoils has been compared to the NACA hydrofoils.

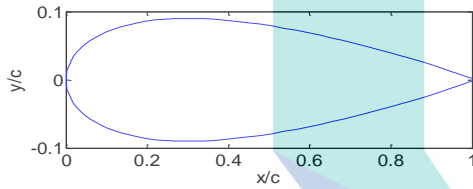
Table 4.3 Properties of NREL S-Series hydrofoil profiles

NREL S-Series	Camber	Thickness
833	2.52 °	18.00 %
834	1.63 °	15.00 %
835	2.44 °	21.05 %

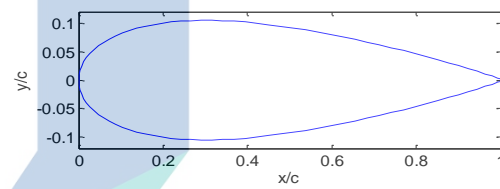


(a) NACA 0012

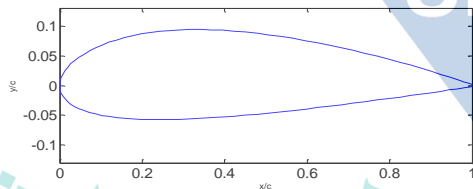
(b) NACA 0015



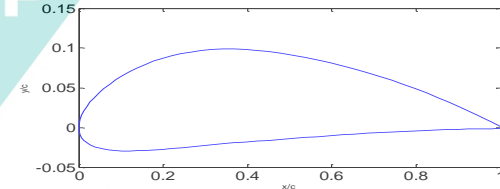
(c) NACA0018



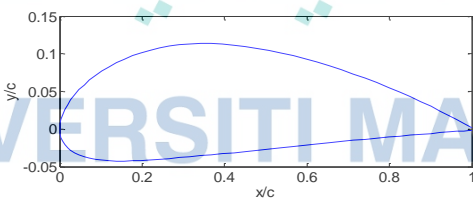
(d) NACA 0021



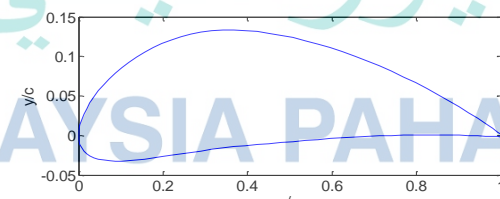
(e) NACA2415



(f) NACA 4412



(g) NACA4415



(h) NACA6415

اونیورسیتی ملیسیا قهق  
UNIVERSITI MALAYSIA PAHANG

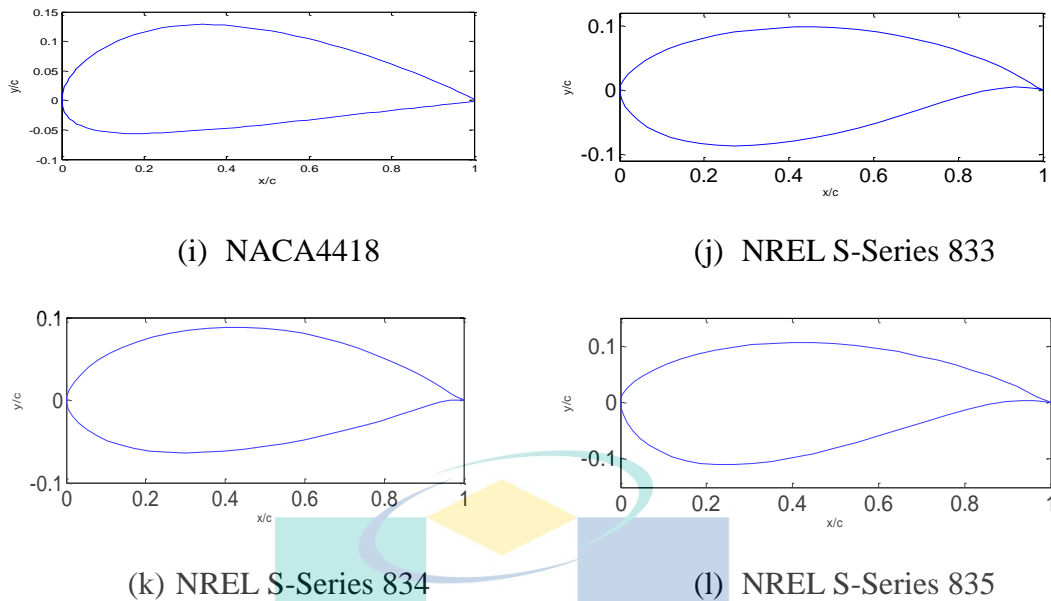


Figure 4.8 Symmetrical and non-symmetrical hydrofoil blades profiles under study.

### 4.3 Results and Discussions

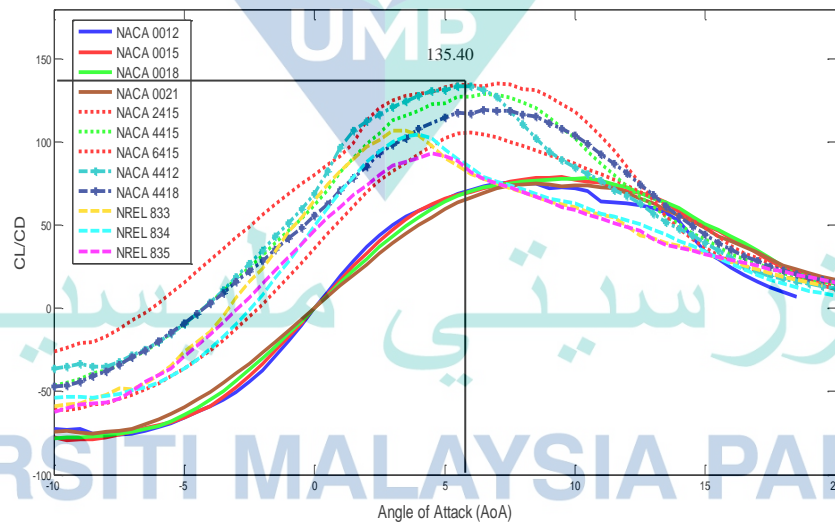
This section presents the results and discussion on XFOils analysis on different Reynolds number, hydrofoil profile geometry analysis for H-Darrieus, Darrieus, and Gorlov Helical turbines, and performance comparison between the turbines. Subsequently, the turbine solidity is discussed and a modelling of the H-Darrieus turbines is based on the  $C_P$ - $TSR$  curve. Finally, the turbine power and torque curve characteristics of the H-Darrieus turbine are discussed.

#### 4.3.1 XFOils Analysis on Hydrofoils Profiles

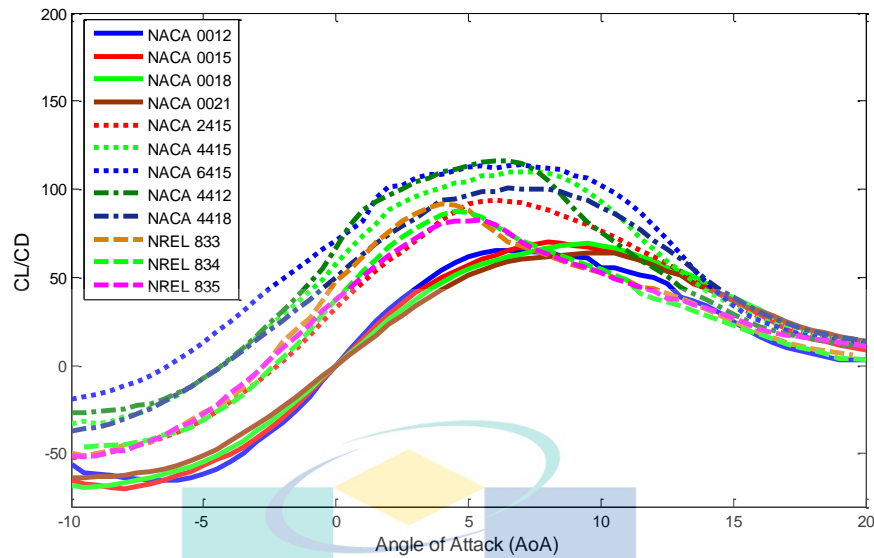
The XFOil analysis was used to acquire the lift ( $C_L$ ) and drag ( $C_D$ ) coefficients, respectively, of the hydrofoils over different angles of attack (AoA). The performance of the NACA and NREL hydrofoils can be compared through the lift to drag ratio ( $C_L/C_D$ ). The  $C_L/C_D$  ratio or glide ratio is expected to be higher, hence it will raise the turbine torque and decrease the bending moment on the turbine blade for higher turbine rotation (Islam et al.,2019).

In this analysis, the hydrofoil performance was evaluated based on the  $C_L/C_D$  ratio at lower and higher Reynolds number ( $R_e$ ) and the difference in AoA in percentage between the higher and lower  $R_e$ . The higher  $R_e$  is set to  $1.0 \times 10^6$ , whereas the lower  $R_e$  is set to  $6.0 \times 10^5$ . The different  $R_e$  numbers are used to investigate the non-dimensional indicator of the inertial forcing in a flow due to the viscous fluid and to analyse the performance of lifting surface on hydrofoils (Cavagnaro, 2016).

Figure 4.9 (a) and (b) show the  $C_L/C_D$  ratio for the 12 NACA and NREL S-Series hydrofoils from  $-15^\circ$  to  $20^\circ$  AoA at  $R_e$  equal to  $1.0 \times 10^6$  and  $6.0 \times 10^5$ , respectively. It can be observed that the camber hydrofoils (non-symmetrical) produced higher  $C_L/C_D$  compared to the NACA symmetrical and NREL S-Series hydrofoils. The higher  $C_L/C_D$  is achieved by NACA 6415 with value of 135.4. The  $C_L/C_D$  ratio is also proportional to the  $R_e$ . As can be seen, the higher  $R_e$  provided the highest  $C_L/C_D$  ratio compared to the lower  $R_e$  and subsequently improved the peak value of power generation for the hydrokinetic energy harnessing. Hence, the higher  $R_e$  is preferable in this design consideration.



(a)  $C_L/C_D$  vs. AoA at  $R_e = 1.0 \times 10^6$



(b)  $C_L/C_D$  vs. AoA at  $R_e=6.0 \times 10^5$

Figure 4.9 Lift to Drag ratio vs. Angle of Attack (AoA) of NACA and NREL hydrofoils at higher and lower Reynolds number. The Xfoil analysis is applied from  $-10^\circ$  to  $20^\circ$  AoA.

According to Kinsey (2017), higher  $R_e$  value can reduce the cavitation in the harsh marine environment. The cavitation occurs on the blade profiles due to the local pressure partially falling below the vapour pressure of water and reducing the turbine speed (H. Chen, Tang, et al., 2018). Therefore, the selection of hydrofoils on the blade profiles and turbine materials is required to reduce the cavitation effect (Silva et al., 2015).

Table 4.4 shows a summary of the Xfoil analysis for NACA and NREL hydrofoils at different  $R_e$ . It can be observed that the AoA of the camber hydrofoils such as NACA 2415, NACA 4415, and NACA 6415 are kept constant at higher and lower  $R_e$ . According to Islam et al. (2019), as the percentage difference in AoA is small between higher and lower  $R_e$ , the hydrofoil profile stability will increase. Therefore, these findings show that the types of hydrofoils, such as NACA 2414, 4415, 6415, 0018, 4418, and 4412 are stable in operation due to the AoA being constant and having lower percentage difference in AoA at higher and lower  $R_e$ , respectively. Nevertheless, all the hydrofoil profiles have the potential to be applied in the turbine design consideration as the XFoils analysis

provided the pressure distribution and lift to drag ratio. The actual hydrofoil selection is based on the turbine's performance in the streamtube analysis for each turbine configuration.

Table 4.4 Summary of maximum  $C_L/C_D$  at different AoA for higher and lower  $Re$ .

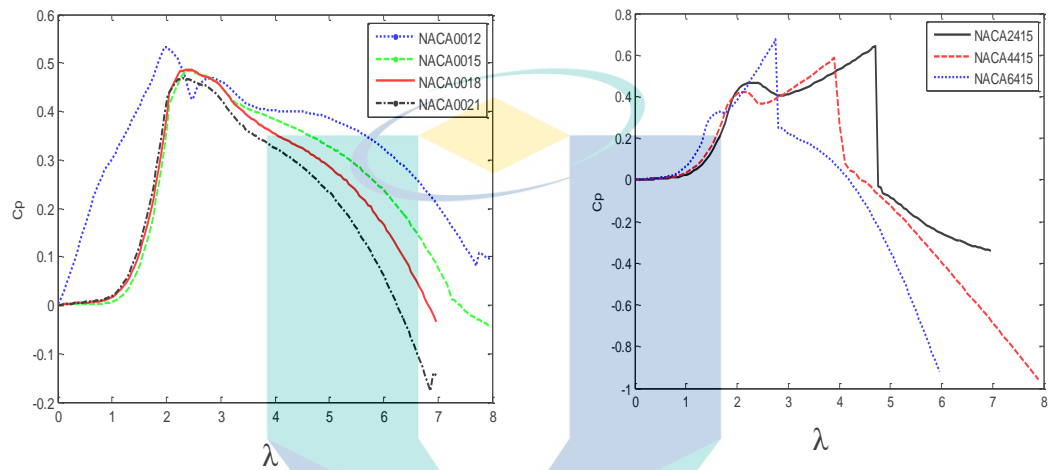
No.	Hydrofoils Profiles	$Re=1.0 \times 10^6$		$Re=6.0 \times 10^5$		% Different of AoA
		$C_L/C_D$	AoA	$C_L/C_D$	AoA	
1	NACA0012	75.86	7.50°	65.07	6.50°	13.33
2	NACA0015	77.34	9.50°	69.86	8.00°	15.79
3	NACA0018	78.20	10.00°	69.25	9.50°	5.00
4	NACA0021	74.81	9.00°	62.14	8.00°	11.11
5	NACA2415	105.7	6.00°	93.47	6.00°	0
6	NACA4415	129.10	6.50°	109.90	6.50°	0
7	NACA6415	135.40	7.00°	114.00	7.00°	0
8	NACA4412	133.60	5.50°	115.80	6.00°	8.33
9	NACA4418	119.30	6.50°	100.30	7.00°	7.14
10	NREL833	107.00	3.50°	91.61	4.00°	12.50
11	NREL834	104.90	4.00°	87.46	4.50°	11.11
12	NREL835	93.90	4.50°	82.72	5.50°	27.27

#### 4.3.2 Hydrofoil Profile Geometry for H-Darrieus Turbine

Figure 4.10 (a) shows a H-Darrieus turbine with symmetrical blade hydrofoils. The symmetrical foil refers to hydrofoils without camber. In this case, NACA 0012, NACA 0015, NACA 0018, and NACA 0021 have been implemented to investigate the effect of hydrofoil thickness on turbine performance. It can be seen that the  $C_P$  increases along with the tip speed ratio ( $\lambda$ ) for all hydrofoil profiles and decreases when achieving maximum value. At  $\lambda < 2.00$ , NACA 0012 shows the highest  $C_P$  across the hydrofoil profiles. Nevertheless, after  $\lambda > 2.00$ , this profile shows inappropriate curve characteristics. Hence, NACA 0012 (less thick) is not suitable for higher tip ratio speed.

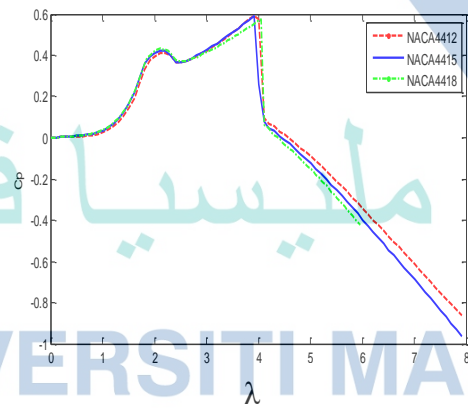


NACA 0021 (thickest) also has a low  $C_P$  compared to NACA 0018 and NACA 0015 at low tip speed ratio ( $\lambda < 2.50$ ). At a higher tip speed ratio ( $\lambda > 6.00$ ), NACA 0021 rotates in the reverse direction due to negative  $C_P$ . Therefore, NACA 0021 (thickest) is not suitable to be used on the H-Darrieus turbine. These findings show as the thickness of the symmetrical hydrofoils increases, turbine performance is reduced significantly due to lower  $C_P$ .

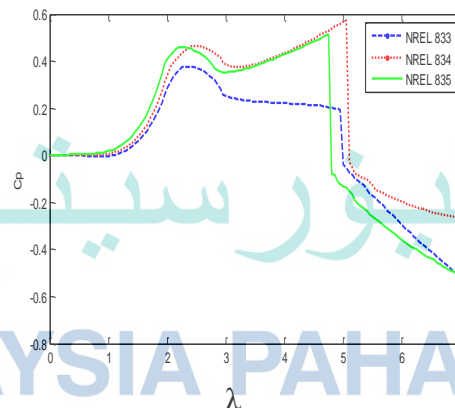


(a) Symmetrical hydrofoils

(b) Non-symmetrical hydrofoils with different camber percentages



(c) Non-symmetrical hydrofoils with a different chord thickness



(d) NREL S-Series Hydrofoils

Figure 4.10. The  $C_P$  vs. TSR curve of symmetrical and non-symmetrical hydrofoils for the H-Darrieus turbine.

The effect of non-symmetrical hydrofoils on the H-Darrieus turbine is shown in Figure 4.10 (b). Non-symmetrical hydrofoils are referred to as foils with camber. In this case, NACA 2415, NACA 4415, and NACA 6415 with the same 15% thickness have been investigated. It is observed that as the percent of the camber is increased, the TSR is reduced significantly. NACA 6415, for instance, has a low operating range with  $\lambda$  dropping significantly when reaching 3.00. In addition, all the  $C_P$  exceed the Betz limit (0.59 maximum) with a narrow TSR. Therefore, a hydrofoil with a large camber is not suitable to be implemented for the H-Darrieus turbine.

The effect of hydrofoils with camber at different thicknesses have been investigated for NACA 4412, NACA 4415, and NACA 4418, as shown in Figure 4.10 (c). It is observed that hydrofoils with camber are not suitable for high-speed ratio turbines as the  $C_P$  will decrease rapidly after reaching the maximum peak at  $\lambda > 4.00$ . Besides, the turbine will rotate in the reverse direction as the  $C_P$  reaches negative values. The finding is in line with the investigation conducted by Mohamed et al. (2019). In this case, the thickness does not have any significant effect on hydrofoils with camber as their  $C_P$  is equivalent to each other at a low tip speed ratio ( $\lambda < 3.00$ ).

The NREL S-Series hydrofoil profiles for H-Darrieus turbines are shown in Figure 4.10 (d). NREL 833, NREL 834, and NREL 835 have camber with different hydrofoil thicknesses. It is observed that the  $C_P$ -TSR curve for the NREL S-Series is similar to the non-symmetrical NACA turbines. The finding is acceptable as the NREL S-Series are hydrofoils with camber. Nevertheless, these hydrofoils have the most significant tip speed ratio at higher operating speeds, and the  $C_P$  will rapidly decrease when  $\lambda > 5.00$ .

Table 4.5 shows the summary of the performance of the H-Darrieus turbine for all hydrofoil profiles. The turbine performance has been evaluated in terms of power coefficient ( $C_P$ ) and torque coefficient ( $C_M$ ). The symmetrical hydrofoil is the best hydrofoil profile option for the H-Darrieus turbine. In this case, both NACA 0015 and NACA 0018 are suitable for the H-Darrieus turbine. Nevertheless, NACA 0018 has been chosen as the best option due to its higher  $C_P$  and  $C_M$  compared to NACA 0015 for the specification given in Table 4.2.

Table 4.5 A comparison of  $C_P$  and  $C_M$  between NACA and NREL hydrofoils for the H-Darrieus turbine .

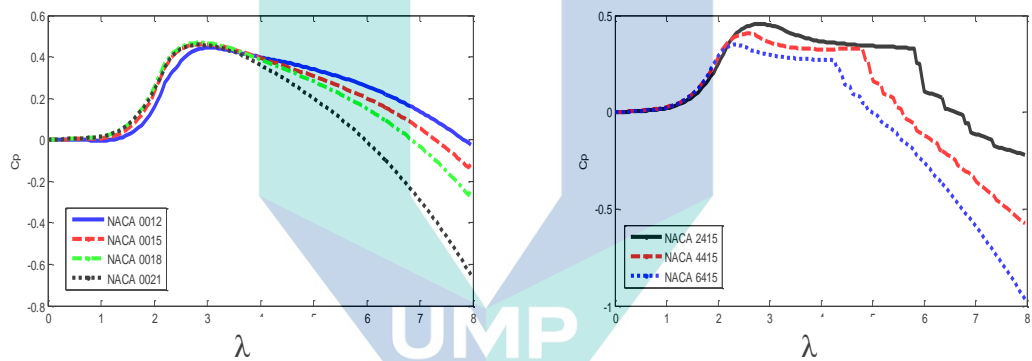
No.	Hydrofoils	$C_{P-max}$	$\lambda$	$C_{M-max}$	$\lambda$
1	NACA0012	0.533	1.96	0.335	0.61
2	NACA0015	0.484	2.46	0.206	2.21
3	NACA0018	0.485	2.36	0.215	2.16
4	NACA0021	0.468	2.31	0.213	2.06
5	NACA2415	0.645	4.71	0.215	2.06
6	NACA4415	0.589	3.91	0.207	1.91
7	NACA6415	0.676	2.76	0.245	2.76
8	NACA4412	0.593	3.91	0.197	2.01
9	NACA4418	0.575	4.06	0.210	1.96
10	NREL833	0.377	2.36	0.164	2.21
11	NREL834	0.574	5.06	0.193	2.31
12	NREL835	0.513	4.76	2.090	2.11

It is observed that hydrofoils with camber are not suitable for implementation in the H-Darrieus turbine. Most hydrofoils with camber exceed the Betz limit and have a low range of operating points. Furthermore, the turbine performance will decrease until it reaches negative  $C_P$  when  $\lambda > 4.00$ . Therefore, a hydrofoil with camber is not a suitable choice for the H-Darrieus turbine based on the design consideration and specification given in Table 4.2.

The NREL S-Series hydrofoils are also not suitable for implementation in the H-Darrieus turbine. The NREL S-Series hydrofoils have similar characteristics to the NACA hydrofoil with camber. However, the NREL S-Series hydrofoils are suitable for high-speed turbines due to their maximum  $C_P$  at high tip speed ratio. These simulation studies show that the symmetrical NACA hydrofoils have a better performance compared to the non-symmetrical and NREL hydrofoils. The findings are in line with the simulation by Mohamed et al. (2019).

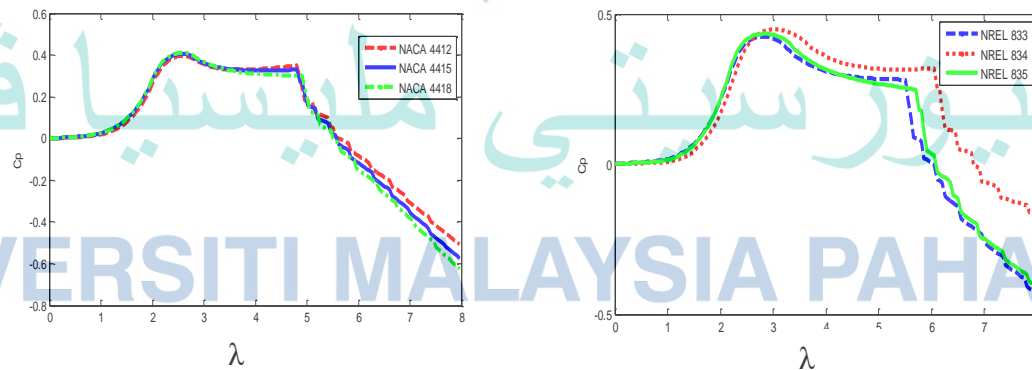
### 4.3.3 Hydrofoil Profile Geometry for Darrieus Turbine

Similar configurations have been applied for the Darrieus turbine. In this case, symmetrical hydrofoils such as NACA 0012, NACA 0015, NACA 0018, and NACA 0021 have been implemented to investigate the effect of hydrofoil thickness on the Darrieus turbine. Figure 4.11 (a) shows the  $C_P$ - $\lambda$  characteristic of the Darrieus turbine with symmetrical hydrofoil profiles. It can be seen that the thickness is inversely proportional to the tip speed ratio ( $\lambda$ ).  $\lambda$  is reduced as the hydrofoil thickness is increased. For instance, NACA 0021 (thickest hydrofoil) has negative  $C_P$  and operates in the reverse rotation when  $\lambda > 5.50$ . In contrast, the optimum operating range of  $\lambda$  for the thinner hydrofoil (NACA 0012) has slightly shifted forward compared to the thicker hydrofoils.



(a) Symmetrical hydrofoils

(b) Non-symmetrical hydrofoils with different camber percentages



(c) Non-symmetrical hydrofoils with different chord thicknesses

(d) NREL S-Series hydrofoils

Figure 4.11. The  $C_P$  vs. TSR curve for symmetrical and non-symmetrical hydrofoils of the Darrieus turbine.

The effect of non-symmetrical hydrofoils on the Darrieus turbine is shown in Figure 4.11 (b). It is observed that the  $C_P$ -TSR curve characteristic is similar to the H-Darrieus turbine where as the percent of the camber is increased, the operating range of  $\lambda$  is reduced. In addition, when  $\lambda > 4.34$ , the  $C_P$  will decrease to negative. Hence, hydrofoils with camber are not suitable to be used in a Darrieus turbine with the specifications given in Table 4.2.

The effect of thickness on camber hydrofoils is shown in Figure 4.11 (c). It is observed that the thickest hydrofoils have the highest  $C_P$  but the lowest range of operating points. At  $\lambda > 5.00$ , the  $C_P$  begins to drop significantly until it reaches negative. Nevertheless, the turbine performance for NACA 4412, NACA 4415, and NACA 4418 are similar to each other. The finding indicates that the thickness of the camber hydrofoils has no significant effect on the Darrieus turbine.

Figure 4.11 (d) shows the performance of NREL S-Series hydrofoil profiles for the Darrieus turbine. NREL 833, NREL 834, and NREL 835 represent the camber hydrofoils with different thicknesses. It is observed that the  $C_P$ -TSR curve for the NREL S-Series is similar to the non-symmetrical NACA turbines. Nevertheless, NREL 834 has a broad range of operating  $\lambda$  compared to NREL 833 and NREL 835. The  $C_P$  of NREL 834 begins to decrease when  $\lambda > 6.16$  after reaching  $C_{P-\max}$  at 0.47.

Table 4.6 shows the performance of the Darrieus turbine in terms of  $C_P$  and  $C_M$ . As can be seen, the symmetrical hydrofoils offer the best performance compared to non-symmetrical hydrofoils. Based on the analysis, NACA 0018 has been chosen as the best hydrofoil for the Darrieus turbine due to its higher  $C_P$  and  $C_M$  compared to the other types of hydrofoils.

Table 4.6 A comparison of  $C_P$  and  $C_M$  between NACA and NREL hydrofoils for the Darrieus turbine .

No.	Hydrofoils	$C_{Pmax}$	$\lambda$	$C_{Mmax}$	$\lambda$
1	NACA0012	0.443	3.01	0.156	2.71
2	NACA0015	0.462	2.91	0.175	2.51
3	NACA0018	0.467	2.81	0.179	2.46
4	NACA0021	0.457	2.76	0.175	2.51
5	NACA2415	0.454	2.76	0.174	2.46
6	NACA4415	0.405	2.56	0.165	2.41
7	NACA6415	0.348	2.31	0.153	2.26
8	NACA4412	0.397	2.61	0.160	2.36
9	NACA4418	0.410	2.51	0.167	2.41
10	NREL833	0.425	2.76	0.168	2.36
11	NREL834	0.447	2.96	0.159	2.71
12	NREL835	0.434	2.81	0.164	2.56

This simulation study has indicated that the performance of non-symmetrical and NREL S-Series hydrofoils for the Darrieus turbine are similar to the typical H-Darrieus turbine. Both types of hydrofoils are not suitable due to the low operating range of TSR. Nevertheless, the performance of the non-symmetrical hydrofoils for the Darrieus turbine is much better than the performance of the non-symmetrical hydrofoil for the H-Darrieus turbine. Moreover, the  $C_P$  has not exceeded the Betz limit compared to the H-Darrieus turbine.

## UNIVERSITI MALAYSIA PAHANG

### 4.3.4 Hydrofoil Profile Geometry for Gorlov Helical Turbine (GHT)

The symmetrical hydrofoils of NACA 0012, NACA 0015, NACA 0018, and NACA 0021 with different thicknesses have been investigated to examine the performance of GHT, as shown in Figure 4.12 (a). It is observed that the  $C_P$  is proportional to the hydrofoil thickness. In addition, the  $C_P$  for the thickest hydrofoils will reach negative



faster than thinner hydrofoils. For instance, the  $C_P$  of NACA 0021 turns negative when  $\lambda > 6.00$ . Conversely, the optimum operating point for the thinner hydrofoils, NACA 0012, shifts forward at  $\lambda = 3.00$  with  $C_P$  equal to 0.456. NACA 0015 and NACA 0018 have an optimum  $C_P$  at  $\lambda$  between 2.00 and 2.50, respectively.

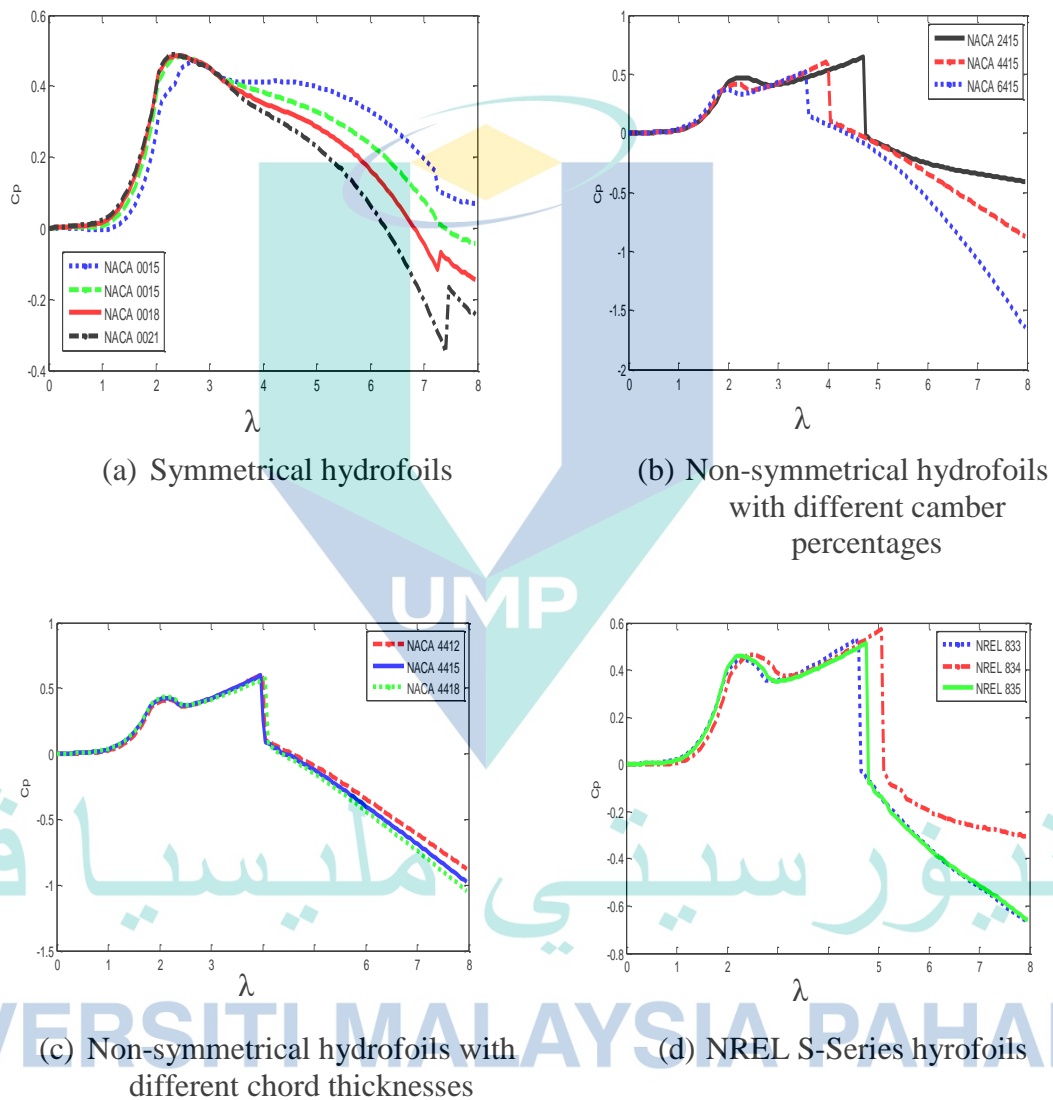


Figure 4.12 The  $C_P$  vs. TSR curve for symmetrical and non-symmetrical hydrofoils of the Gorlov helical turbine.

The effect of hydrofoils with camber for the GHT is shown in Figure 4.12 (b). It is observed that the percent of camber is inversely proportional to the operating range of  $\lambda$ . The performance of NACA 6415, for instance, has been reduced significantly after  $\lambda > 3.50$ . Meanwhile, the  $C_P$  of NACA 2415 and NACA 4414 exceed the Betz limit. These findings show that a hydrofoil with camber is not suitable for the GHT based on the specification given in Table 4.2.

The effect of thickness for a camber hydrofoil is shown in Figure 4.12 (c). It can be seen that the thickness is inversely proportional to the  $\lambda$ . As the thickness is increased, the operating range of  $\lambda$  is reduced until it reaches negative  $C_P$ . However, the performance of camber hydrofoils with different thicknesses for the GHT are similar to each other at  $\lambda < 4.00$ . This finding shows that the thickness has no effect on the GHT with camber if  $\lambda$  is below 4.00.

The NREL S-Series 833,834 and 835 hydrofoils for the GHT is shown in Figure 4.12 (d). It is observed that the  $C_P$ -TSR curve characteristics for the NREL hydrofoils are similar to the NACA hydrofoils with camber. Nevertheless, the maximum  $C_P$  for NREL hydrofoil is ranging between 4.50 and 5.10 at tip speed ratio. This finding shows that the NREL S-Series hydrofoils are not suitable to be implemented on the GHT due to a large operating tip speed ratio.

Table 4.7 shows a summary of GHT performance for all hydrofoil profiles. The turbine's performance has been evaluated in terms of power coefficient ( $C_P$ ) and torque coefficient ( $C_M$ ). The summary shows that the NACA 0015 and NACA 0018 symmetrical hydrofoils are the best hydrofoil profiles for the GHT. Nevertheless, NACA 0018 has been chosen as the best option due to its higher  $C_P$  and  $C_M$  at low tip speed ratio compared to NACA 0015.

Table 4.7 A comparison of  $C_P$  and  $C_M$  between NACA and NREL hydrofoils for the Gorlov Helical Turbine .

No.	Hydrofoils	$C_{Pmax}$	$\lambda$	$C_{Mmax}$	$\lambda$
1	NACA0012	0.470	2.71	0.181	2.51
2	NACA0015	0.482	2.51	0.206	2.21
3	NACA0018	0.484	2.46	0.212	2.19
4	NACA0021	0.489	2.31	0.217	2.16
5	NACA2415	0.631	4.66	0.215	2.06
6	NACA4415	0.597	3.96	0.207	1.96
7	NACA6415	0.522	3.56	0.190	1.86
8	NACA4412	0.605	3.96	0.197	1.96
9	NACA4418	0.575	4.06	0.210	1.96
10	NREL833	0.5313	4.56	0.20	2.16
11	NREL834	0.574	5.06	0.193	2.31
12	NREL835	0.513	4.76	0.210	2.16

#### 4.3.5 Performance Comparison between H-Darrieus, Darrieus and Gorlov Helical Turbines

Three types of turbines have been compared in terms of  $C_P$  and  $C_M$  to select the most suitable turbine for hydrokinetic energy harnessing based on river characteristics at the Pahang River. The H-Darrieus, Darrieus, and Gorlov turbines with the best hydrofoil options are selected for the comparison. Based on the hydrofoil performance comparison for each turbine from Sections 4.4.2 to 4.4.5 , the symmetrical NACA 0018 shows the outstanding performance with higher  $C_P$  and  $C_M$  at the optimum operating point with  $\lambda$  varying between 2.00 and 3.00.

Moreover, NACA 0018 has a high operating point up to  $\lambda = 6$ , which is suitable for high-speed rotation turbines. Furthermore, its  $C_P$  and  $C_M$  never reached negative values and caused the turbine to stall. Therefore, NACA 0018 has been chosen as hydrofoils for the H-Darrieus, Darrieus, and Gorlov turbines.

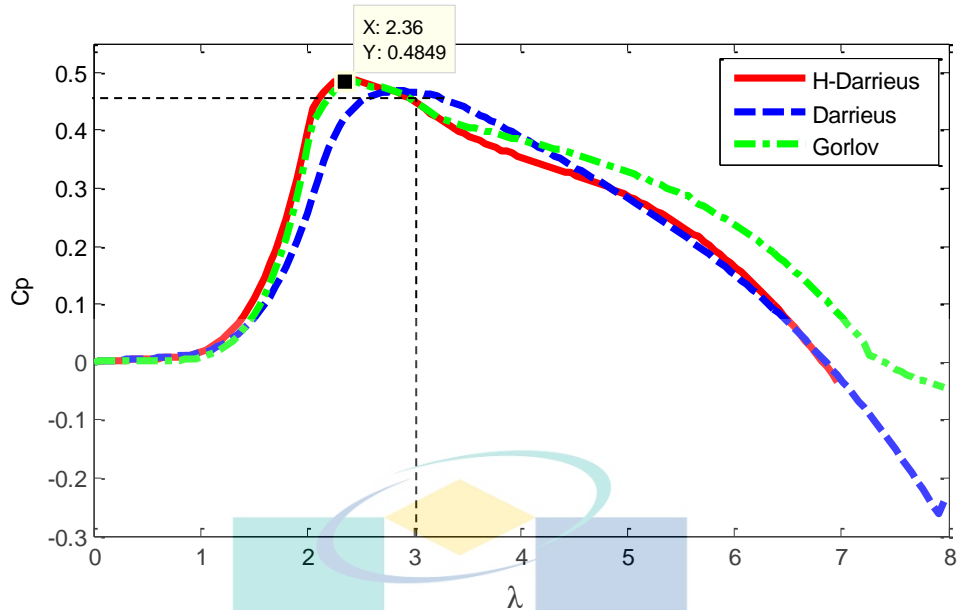


Figure 4.13 The  $C_P$  vs. TSR curves of H-Darrieus, Darrieus and Gorlov helical turbines for performance comparison.

Figure 4.13 shows the  $C_P$ -TSR curves for all turbines with NACA 0018 as the hydrofoil. The curves show that the H-Darrieus turbine and Gorlov helical turbine have an optimum  $C_P$  between  $\lambda = 2.00$  and  $2.40$ . In contrast, the  $C_P$  of the Darrieus turbine has shifted to  $\lambda = 3.00$  and decreases to negative when  $\lambda > 7.00$ . The performance of the H-Darrieus and Gorlov turbines are similar to each other when  $\lambda < 2.00$ . However, when  $\lambda > 2.20$ , the H-Darrieus performs better than the GHT. The H-Darrieus turbine has an optimum  $C_P = 0.485$  at  $\lambda = 2.36$ , while the  $C_P$  of the Gorlov turbine is equal to  $0.482$  at  $\lambda = 2.46$ .

The  $C_M$  of the H-Darrieus turbine is  $0.215$  at  $\lambda = 2.16$ . Comparatively, the  $C_M$  of the Gorlov turbine is  $0.212$  at  $\lambda = 2.19$ . Based on the findings, the vertical axis H-Darrieus turbine has been chosen as the best turbine option for hydrokinetic energy harnessing. Furthermore, in terms of construction, cost, and complexity, the H-Darrieus turbine has an advantage compared to the GHT.

#### 4.3.6 The Effect of Turbine Solidity on H-Darrieus

Turbine solidity is related to the number of blades based on Eq.(4.3). The effect of the number of blades on turbine performance can be investigated by referring to the  $C_P$ -TSR curve. In this case, the chord length ( $c$ ) and turbine diameter ( $d$ ) are kept constant at 0.1 m and 0.6 m, respectively. Figure 4.14 shows the  $C_P$ -TSR curve of the H-Darrieus turbine with NACA 0018 profile for different number of blades.

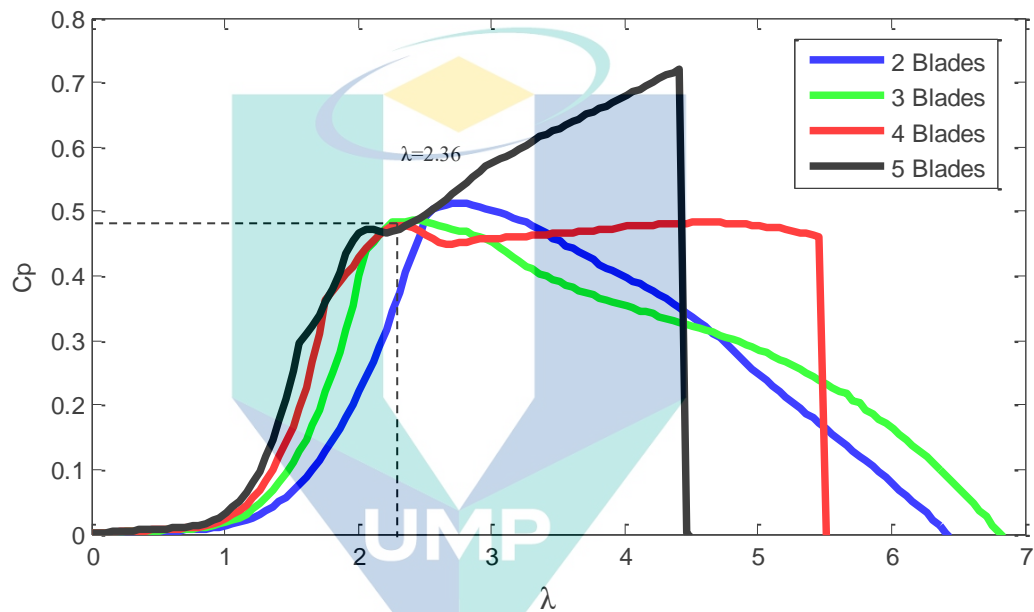


Figure 4.14. The  $C_P$  vs. TSR curve due to the effect of solidity for different number of blades.

The figure shows that the H-Darrieus turbine performs well with two and three blades. Nevertheless, the maximum  $C_P$  of the turbine with two blades is a shift forward at  $\lambda = 2.73$  compared to the turbine with three blades at  $\lambda = 2.36$ . This finding shows that the turbine with three blades is able to extract maximum power at low-speed rotation due to the maximum  $C_P$  at TSR = 2.36. Hence, the three blade H-Darrieus turbine is better than two blades.

Turbines with four and five blades are not fit to be implemented on the H-Darrieus turbine. The reason is the low operating range of TSR for both turbines. The  $C_P$  will drop significantly after reaching the maximum values at TSR = 5.5 and 4.5, respectively.

Furthermore, the  $C_{Pmax}$  for the five blade turbine exceeds the Betz limit from  $TSR = 3.50$  to 4.50 and drastically drops to zero when reaching  $\lambda > 4.50$ .

Table 4.8 shows the solidity at different number of blades and their performance. The results show that the solidity is proportional to the number of blades when the chord and diameter are kept constant. According to Khan et al. (2006), solidity values may range from 0.16 to 1.6.

The trade-off between the cost and  $C_P$  needs to be considered in determining the solidity value. This is because both weight and manufacturing costs will increase with greater solidity. Higher solidity causes the  $TSR$  range to be lower and leads to a decrease in the power coefficient. Lower solidity implies excellent hydrodynamic performance, and higher values generally allow for a more durable mechanical structure and increased induced torque. Therefore, a solidity value of 0.5 is one of the best options in this research.

Table 4.8 Summary of  $C_P$  vs.  $\lambda$  curve for different number of blades

Number of Blades	Solidity	$C_P$	$\lambda$
2	0.33	0.513	2.76
3	0.50	0.485	2.36
4	0.67	0.478	2.31
5	0.83	0.721	4.41

\*Note: Chord and diameter are constant at 0.1m and 0.6 m respectively.

#### 4.3.7 The Modelling of H-Darrieus Turbine

The H-Darrieus turbine with the NACA 0018 hydrofoil profile has been selected as the best turbine option based on river characteristics in Malaysia. The H-Darrieus  $C_P$ - $TSR$  curve can be converted into a mathematical equation to represent the turbine model. The equation can be employed into Matlab/Simulink for simulation purposes especially in MPPT and control strategies. Table 4.9 shows a detailed specification of the H-



Darrieus turbine as the best turbine option for hydrokinetic energy harnessing in river application.

Table 4.9 The H-Darrieus turbine specification details for the turbine model

Parameter	Details
Hydrofoils	NACA 0018
Number of Blades	3
Radius (R)	0.3m
Height	0.8m
Swept Area (A)	0.48m <sup>2</sup>
Re	1.0X10 <sup>6</sup>
Solidity	0.5
Chord	0.1 m
Water Density ( $\rho$ )	1000kg/m <sup>3</sup>
Pitch Angle( $\beta$ )	Fixed

The turbine model, as a function of  $\lambda$ , can be derived based on the  $C_P$ - $TSR$  curve of the H-Darrieus turbine. Figure 4.15 shows the modelling of a hydrokinetic system for energy harnessing. As can be seen, the circle is  $C_P$  as a function of  $\lambda$  to represent the characteristics of the H-Darrieus turbine.

اونيور سیتی ملیسیا فہق

UNIVERSITI MALAYSIA PAHANG

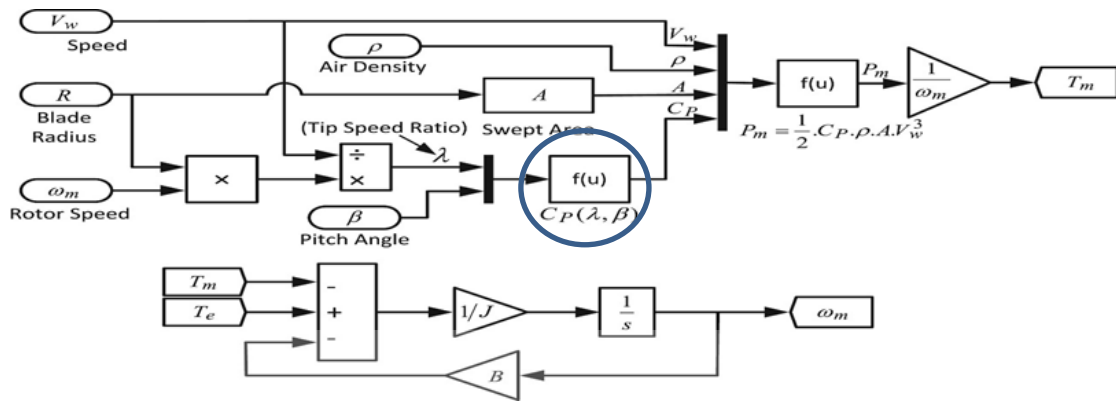


Figure 4.15 The hydrokinetic turbine model and the simplified  $C_p$ -TSR curve representing the H-Darrieus turbine characteristic (in circle).

Figure 4.16 shows the  $C_p$ -TSR curve of the H-Darrieus turbine with polynomial approximation equations. The polynomial equation can be generated using the basic fitting in Matlab tool software. It can be observed that the 4<sup>th</sup> and 7<sup>th</sup> polynomial estimation equation curves oscillate and swing to the positive region when  $\lambda > 7.00$ . Contrastingly, the 5<sup>th</sup> and 6<sup>th</sup> polynomial estimation equation curves drop to the negative region when reaching  $\lambda > 7.00$ .

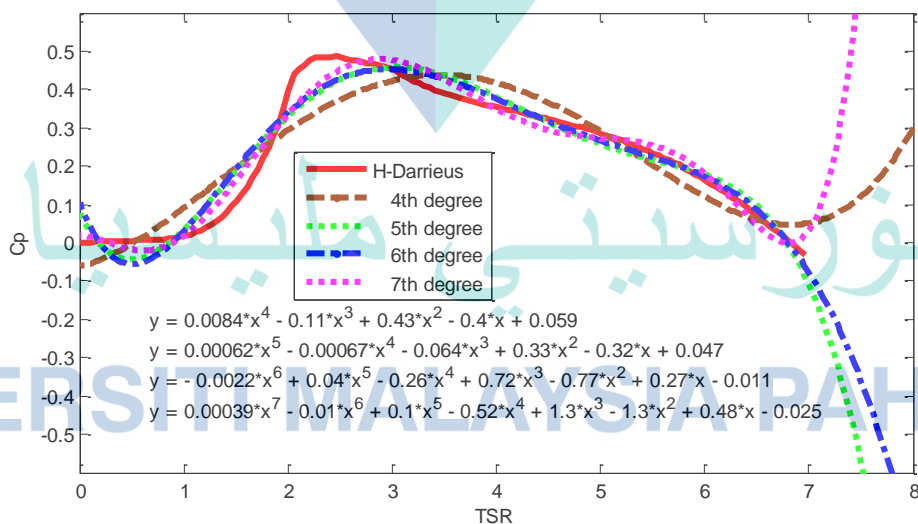


Figure 4.16 A comparison of the  $C_p$  vs. TSR curves at different polynomial equations to represent  $C_p$  as a function of  $\lambda$ .

In this case, the Mean Square Error (MSE) and Root Mean Square Error (RMSE) methods are implemented to find the most suitable polynomial approximation equation to represent the H-Darrieus turbine model. The RMSE provides a useful method to measure the performance of estimators. The estimation method is efficient if the values of the MSE and RMSE are smaller compared to the other.

Table 4.10 shows the MSE and RMSE with the list of polynomial estimation equations. The table shows that the 6<sup>th</sup> polynomial estimation equation has the least MSE and RMSE with 0.0135 and 0.1165, respectively. Therefore, the 6<sup>th</sup> polynomial estimation equation has been chosen as a model for the H-Darrieus turbine as given in Eq. (4.14). The detailed calculation for the polynomial estimation equation can be referred to Appendix B.

Table 4.10 A comparison of the MSE and RMSE discrepancies for the different polynomial level equations

Polynomial	MSE	RMSE
4 <sup>th</sup>	0.0301	0.1735
5 <sup>th</sup>	0.0656	0.2561
6 <sup>th</sup>	0.0135	0.1165
7 <sup>th</sup>	0.0847	0.2911

$$C_p(\lambda) = -0.022\lambda^6 + 0.04\lambda^5 - 0.26\lambda^4 + 0.72\lambda^3 - 0.77\lambda^2 + 0.27\lambda - 0.011 \quad 4.14$$

## UNIVERSITI MALAYSIA PAHANG

### 4.3.8 Turbine Power and Torque

The turbine power in a hydrokinetic system is influenced by the turbine swept area ( $A$ ), power coefficient ( $C_p$ ), and water velocity ( $V$ ). The parameters of  $A$  and  $C_p$  are dependent on the turbine design consideration, while  $V$  is dependent on the resource location in the assessment study. Figure 4.17 shows the power and torque curve of the H-Darrieus turbine with NACA 0018 at different water velocities. As shown in Figure 4.17

(a), the power-curve characteristic is similar to the  $C_P$ - $TSR$  curve. This similar characteristic is due to the curve being influenced by the  $C_P$  curve, since the water density and rotor swept area ( $A$ ) are constants. It can also be observed that the maximum power for each water velocity occurs at different points of the turbine's rotational speed.

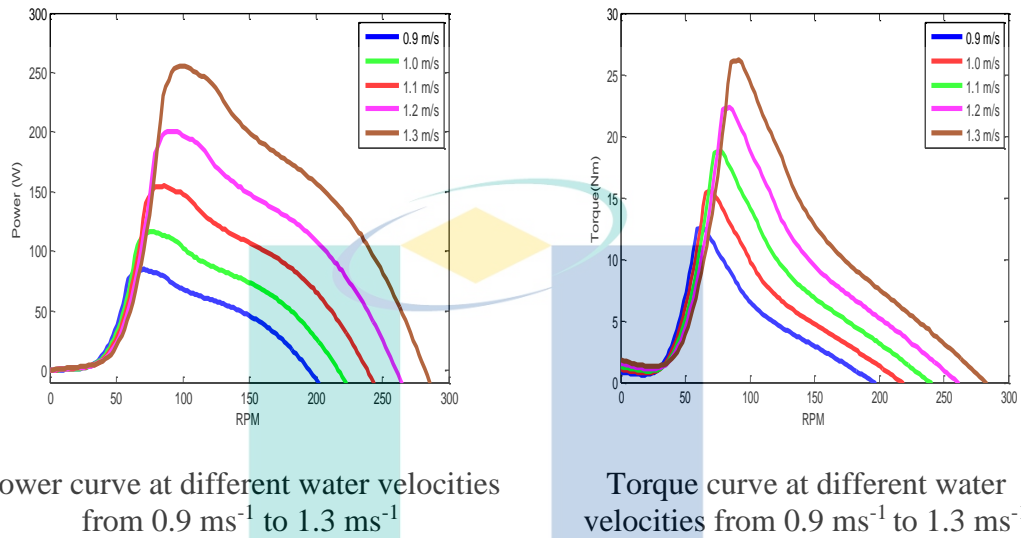


Figure 4.17 Power and torque vs. turbine rotational speed, respectively, at a different water velocities.

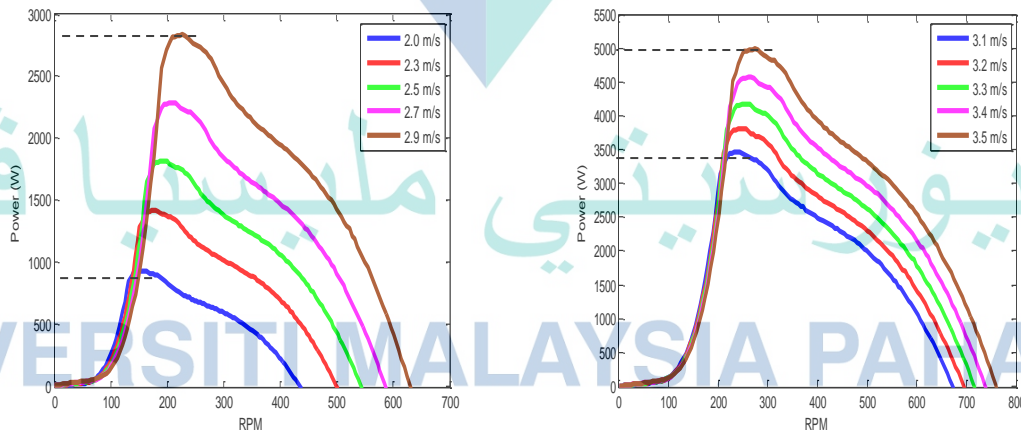
Figure 4.17 (b) shows the torque curve of the H-Darrieus turbine with the NACA 0018 profile at different water velocities. It is observed that the  $C_M$ - $TSR$  curve is also influenced by the  $C_P$  curve characteristic. The peak torque occurs at a particular turbine rotational speed for each water velocity. The shape of the curve is also similar to the turbine power curve characteristic as the torque is mechanical power divided by the angular speed of the turbine. Nevertheless, both maximum power and maximum torque do not occur at the same rotational speed, as shown in

Table 4.11.

Table 4.11 A summary of peak power and torque vs. turbine rotational speed at different water velocities

Velocity ( $\text{ms}^{-1}$ )	Power (W)	Turbine speed (RPM)	Torque (Nm)	Turbine Speed (RPM)
0.9	84.6	68.0	12.4	59.0
1.0	116.0	75.0	15.4	67.0
1.1	154.8	86.0	18.7	76.0
1.2	200.5	90.0	22.2	81.0
1.3	255.2	99.0	26.1	89.0

Figure 4.18 (a) and (b) show the power curve of the H-Darrieus turbine for different water velocities. The figure shows that the turbine is capable of producing an output power of between 900 W and 2.85 kW at water velocities ranging from  $2.0 \text{ ms}^{-1}$  to  $2.9 \text{ ms}^{-1}$ . The power will increase proportionally as the power increases with the cube of the water velocity. At water velocities from  $3.1 \text{ ms}^{-1}$  to  $3.5 \text{ ms}^{-1}$ , the output power of the turbine is ranging between 3.5 kW and 5.0 kW, as shown in Figure 4.18 (b).



The power curve at water velocities from  $2.0 \text{ ms}^{-1}$  to  $2.9 \text{ ms}^{-1}$

The power curve at water velocities from  $3.1 \text{ ms}^{-1}$  to  $3.5 \text{ ms}^{-1}$

Figure 4.18 Power vs. turbine rotational speed at different water velocities

Figure 4.18 shows that maximum power for a particular water velocity occurs at a particular rotational speed. The reason for this is the dynamic performance of the turbines, which is influenced by the  $C_P$ - $TSR$  curve. In contrast, the turbine's rotational speed depends on the generator loading and water fluctuations. Therefore, a variable speed operation of the hydrokinetic system is required to allow for the speed variation on the turbine and extract the maximum energy (J. Hui, 2008).

The turbine's rotational speed can be controlled through the power electronics control. The goal of this control can be achieved by different power electronics converter topologies and maximum power point tracking algorithm (Zhu et al., 2018).

#### 4.4 Summary

This chapter presented the design consideration and turbine selection as well as the turbine model for the hydrokinetic energy harnessing in a river. Three types of vertical axis hydrokinetic turbines; H-Darrieus, Darrieus, and Gorlov with 12 NACA and NREL hydrofoils, respectively, were compared in terms of turbine performance. NACA 0018 was chosen as the best hydrofoil profile for all types of turbines based on the lift to drag ratio and the highest power and torque coefficient. In a comparison of the  $C_P$ - $TSR$  curve between the three types of turbines, H-Darrieus showed the outstanding performance with  $C_P = 0.485$  and  $C_M = 0.215$ . Therefore, H-Darrieus with NACA 0018 was chosen as the best turbine option for hydrokinetic energy harnessing in the river. The turbine was designed at 0.5 solidity with three blades, and 0.48 m<sup>2</sup> swept area with a fixed angle. The turbine achieved a  $C_P$  of 0.485 at 2.36 TSR based on the simulation studies. Moreover, the  $C_P$ - $TSR$  curve characteristic has been modelled by a polynomial approximation equation to represent the H-Darrieus turbine characteristic based on the Pahang River. The 6<sup>th</sup> polynomial approximation equation has been chosen to represent the  $C_P$  as a function of  $\lambda$  due to the minimum values of MSE and RMSE at 0.0135 and 0.1165, respectively.



## CHAPTER 5

### MAXIMUM POWER POINT TRACKING (MPPT) CONTROL STRATEGIES FOR STAND-ALONE HYDROKINETIC ENERGY HARNESSING

#### 5.1 Introduction

The energy harvesting through renewable energy sources has received significant interest due to the environmental concerns and exhaustion of fossil fuels. Instead of the solar photovoltaic (PV) and wind energy conversion system (WECS), the hydrokinetic energy harnessing system has been investigated for clean and future energy sustainability.

Hydrokinetic energy harnessing is an electromechanical device which leverages on water flow to generate energy. The system produces the electricity without the requirement of dams and the associated infrastructure when compared to the conventional hydropower generation (Vermaak et al., 2014). The system can be applied in the river, tailwater, water sewage treatment, or man-made channel (Ladokun, Sule, Ajao, & Adeogun, 2018).

The output power obtained from the hydrokinetic energy harnessing is varied since the power generation is affected by the fluctuation in the water speed. Therefore, maximizing energy output at the minimum cost is a big challenge in this field. Hence, the usage of maximum power point tracking (MPPT) algorithm is necessary to be implemented in the controller design.

The MPPT algorithm for the hydrokinetic system has been used widely in solar PV and WECS. Besides, the concepts underlying the variable-speed feature, operations, as well as electrical components of the generator are similar to WECS (S. P. Koko, Kusakana, & Vermaak, 2017). Therefore, the MPPT algorithm from the WECS is treated as the primary reference for detailed research in this field.

This chapter presents the maximum power point tracking (MPPT) algorithm for the small-scale hydrokinetic stand-alone system in river application. The configurations establishment for simulation of the MPPT algorithm, including the circuit topology, turbine model, permanent magnet synchronous generator, rectifier, and DC-DC converter are described. Subsequently, the MPPT control strategies such as the conventional Hill-Climbing Search (HCS) algorithm and proposed algorithm are explained. Finally, the performance of the proposed MPPT algorithm has been compared with the LS-HCS, SS-HCS, and Michas MPPT algorithm in terms of tracking accuracy, response time, oscillation, and overshoot.

## 5.2 Configuration Establishment of Hydrokinetic Energy Harnessing

In this section, the configuration of stand-alone hydrokinetic technology such as circuit topologies, turbine model, PMSG, passive rectifier, and DC-DC converter has been established for MPPT simulation. This including the explanation of variable speed hydrokinetic, concepts, operation, and parameter design of each component.

### 5.2.1 Variable Speed Hydrokinetic Turbine

The variable speed generator is used to maximise the amount of energy extracted by the turbine. The maximum power of the turbine occurs at different turbine rotational speeds due to the variation of the water velocities, as shown in Figure 4.18 in previous chapter. Since the turbine is connected directly to the PMSG without the gearbox, hence the turbine speed is equal to the generator speed by considering any losses are equal to zero.

The optimal line is produced by connecting all the maximum power point at different water velocity. It should be noted that, the maximum power of the water velocity curve occurs at a particular rotational speed. Therefore, the maximum power can be extracted by optimising the turbine speed.

Nevertheless, the turbine's rotational speed depends on the generator loading and water fluctuations. Hence, the variable speed operation of the hydrokinetic system is required to allow the speed variation on the turbine and extract the maximum energy (J. Hui, 2008). The turbine's rotational speed can be controlled through the power electronics control. The goal of this control can be achieved by different power electronics converter topologies and maximum power point tracking algorithm (Zhu et al., 2018).

### 5.2.2 Hydrokinetic System Topology

The hydrokinetic energy harnessing setup consists of a water turbine, PMSG, and power electronic converters such as a rectifier and DC boost-converter, as shown in Figure 5.1. The circuit topology and physical hardware are similar and commonly used by a small wind turbine energy conversion system (SWECS) as well as in a tidal energy system (J. C. Y. Hui, Bakhshai, & Jain, 2016; M. J. Khan, Iqbal, & Quaicoe, 2010). Although the circuit topology has been adapted from SWECS, nevertheless, the water turbine is based on vertical axis H-Darrieus turbine consideration. Furthermore, the  $C_P$ -TSR curve is based on the 6<sup>th</sup> polynomial approximation equation to represent the H-Darrieus turbine model.

Concerning the current topology, the direct coupling of PMSG with a river turbine (without a gearbox) gives rise to a high-efficiency system (J. Hussain, 2016). The output power is transferred through the rectifier bridge and a boost converter. The uncontrolled diode rectifier bridge is preferable due to high reliability and low cost. Meanwhile, the DC boost-converter regulates the output voltage from the rectifier and to tracks the maximum power point (MPP) through an adjustable duty ratio (Xia et al., 2013).

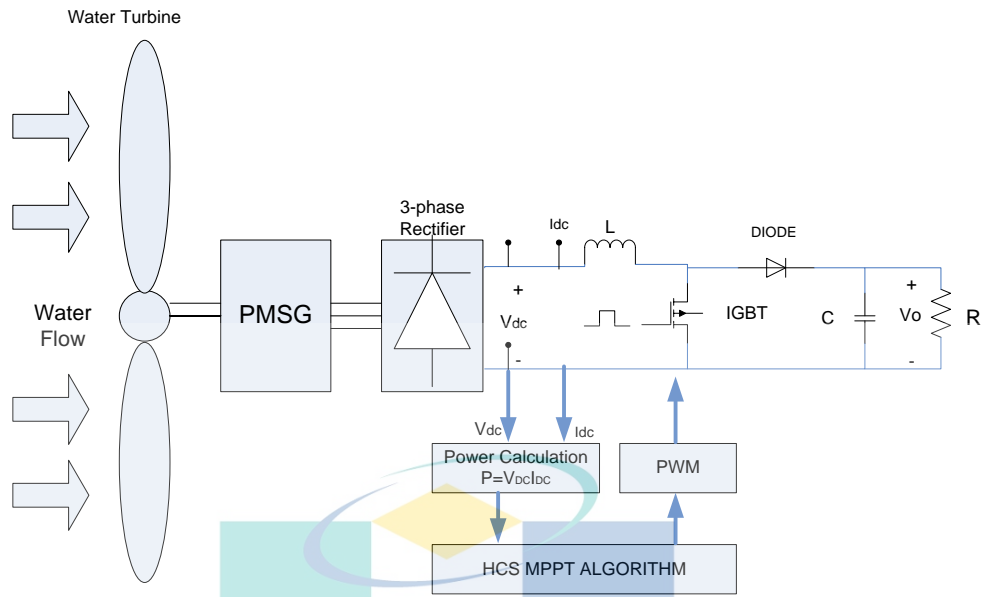


Figure 5.1 The hydrokinetic design topology for MPPT control strategy.

On the other hand, the efficiency of the hydrokinetic system can be evaluated using the following equation, as given in Eq. (5.1).

$$\eta = \frac{P_{out}}{0.5\rho AC_p C_n} \quad 5.1$$

where,  $P_{out}$  is the output power from the MPPT algorithm, while  $n_c$  is the combination of coupling losses, generator losses, and converter losses. In this study, the Matlab/Simulink version R2014a has been used to simulate the complete hydrokinetic system. In addition, the Sim Power System Toolbox in Matlab/Simulink was employed as part of the programming components. The comprehensive Simulink program is attached in Appendix C.

### 5.2.3 Model of River Current Turbine

The vertical axis H-Darrieus turbine with NACA 0018 hydrofoil was chosen as the best option for the river-current turbine based on Pahang River characteristics. The  $C_P$ -

$TSR$  curve has been converted using the 6<sup>th</sup> polynomial estimation equation to represent the characteristics of the H-Darrieus as a turbine model for MPPT simulation. The details modelling of the H-Darrieus turbine was described in Section 4.3.7. The  $C_P$  as a function of  $\lambda$  is to represent the H-Darrieus turbine model is given in Eq. (5.2).

$$C_P(\lambda) = -0.022\lambda^6 + 0.04\lambda^5 - 0.26\lambda^4 + 0.72\lambda^3 - 0.77\lambda^2 + 0.27\lambda - 0.011 \quad 5.2$$

#### 5.2.4 Permanent Magnet Synchronous Generator (PMSG) and Rectifier

The turbine shaft is equipped with a PMSG to convert the rotation of turbine blades into electrical power. Evidently, PMSGs are favoured in small turbines design because of its high efficiency since it does not require excitation current, is lightweight, and possess a gearless design (Baroudi, Dinavahi, & Knight, 2007). According to Chen et al. (2016), for the analysis of PMSG with constant flux, the back electromotive force ( $E$ ) has a linear function of generator rotor speed and given by Eq. (5.3).

$$E = k\omega_m \quad 5.3$$

where  $k$  is the constant coefficient of PMSG while  $\omega_m$  is the generator rotor speed (rad/s). Figure 5.2 shows the equivalent circuit of PMSG for the per phase analysis. By doing the KVL, the terminal phase voltage ( $V_s$ ) of PMSG is derived and given by Eq. (5.3).

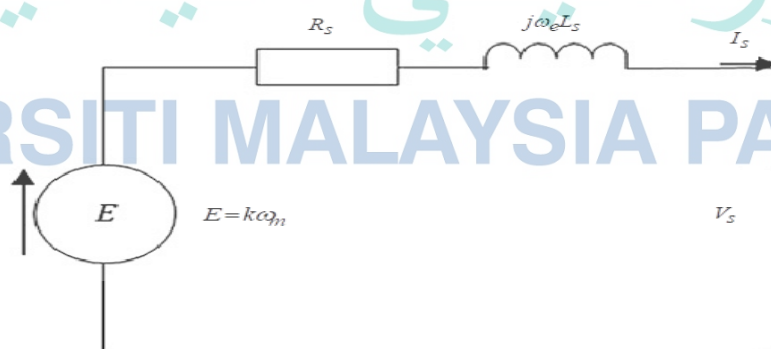


Figure 5.2 PMSG equivalent circuit in per phase diagram.

$$V_s = E - I_s (R_s + j\omega_e L_s) \quad 5.4$$

where  $I_s$  is the stator current,  $R_s$  is the stator resistance, and  $L_s$  is the stator inductance while  $\omega_e$  is the electrical frequency. The relationship between the mechanical frequency  $\omega_m$  and electrical frequency  $\omega_e$  is given by Eq. (5.4)

$$\omega_e = p\omega_m \quad 5.5$$

where  $p$  denotes the number of PMSG poles. Since  $R_s$  is usually small, it is neglected for this analysis. In terms of magnitude, Eq. (5.3) can be simplified as given by Eq.(5.5).

$$V_s^2 = E^2 - (I_s \omega_e L_s)^2 \quad 5.6$$

Table 5.1 shows the details specification of the PMSG used in MPPT simulation. The specification is based on model PMGI-3K-1200 produced by DVE Technologies ApS, Denmark. On the other hand, the bridge rectifier converts the PMSG-generated voltage from an AC to a DC. According to Dalala et al. (2013) and De Freitas et al. (2016), a three-phase passive rectifier with a DC boost-converter helps reduce cost and simplifies the control system. In this topology, only one active switch is required to control compared to six switches required in an active rectifier converter (Daili, Gaubert, & Rahmani, 2015).



Table 5.1 The parameter of the permanent magnet synchronous generator (PMSG)

Parameter	Value
Rated power	3000 W
Stator Resistance ( $R_s$ )	1.76 $\Omega$
Inductance ( $L_s$ )	28.5 mH
Poles	12
Flux Density	0.175 Wb
Rated Speed	1200 RPM

By assuming the commutating inductance and angle can be ignored, the relationship of the rectifier's output voltage,  $V_{DC}$  with the PMSG's phase voltage is presented (J. Hussain, 2016). Therefore, this relationship is given by Eq. (5.6).

$$V_{DC} = \frac{3\sqrt{6}}{\pi} V_S \quad 5.7$$

As noted by Ashourianjozdani et al. (2017) and Muljadi et al. (2016), the resulting DC voltage varies proportionally with regards to the rotor's speed of rotation with a passive diode bridge. Therefore, the approximate relationship between  $V_{DC}$  and  $\omega_m$  can be expressed from Eq. (5.2) to Eq. (5.6) as given by Eq. (5.7).

$$V_{DC} \approx \omega_m \quad 5.8$$

By considering the output power conversion from PMSG into DC power through the rectification process is at a unity power factor with no losses, the output power ( $P_g$ ) can be expressed in Eq. (5.8).

$$P_g = 3V_s I_s = V_{DC} I_{DC} \quad 5.9$$

Upon substituting Eq. (5.7) into Eq. (5.7), the relation between  $I_s$  and  $I_{DC}$  can be expressed by Eq. (5.9).

$$I_s = I_{DC} \frac{\sqrt{6}}{\pi} \quad 5.10$$

### 5.2.5 DC-DC Converter

As noted by Zammit et al. (2017), a DC-DC boost converter helps regulate the amplitude voltage from the PMSG in order to maximize power transfer. According to Abdullah et al. (2012) and Koutroulis & Kalaitzakis (2006), this can be fulfilled by varying the converter's duty cycle so that the generator can adjust the resulting voltage as well as the speed of the rotor speed based on the apparent load. Figure 5.3 shows the topology of the boost converter governed by an insulated-gate bipolar transistor (IGBT). The power switch (S) is driven by the periodic pulse width modulator (PWM); hence it is able to control the amount of power transferred to the load.

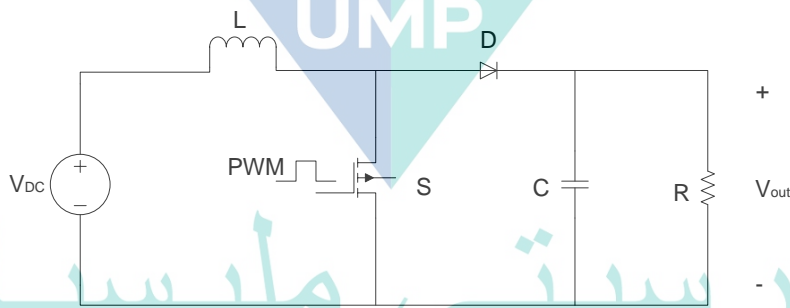


Figure 5.3 DC Boost converter circuit.

As noted by Sira-Ramireza (2006) the voltage conversion ratio of the output voltage ( $V_{out}$ ) to the input voltage for the boost converter is given by Eq. (5.10).

$$\frac{V_{out}}{V_{DC}} = \frac{1}{1-D} \quad 5.11$$

where,  $D$  is the duty cycle of the PWM signal while  $V_{DC}$  is the output voltage from the rectifier or input voltage to boost converter.

The duty cycle-output voltage association has been presented in Eq. (5.10). If  $D$  increases, then the output voltage ( $V_{out}$ ) increases as well. Besides that, the change in  $D$  takes effect on the boost converter's input as well as output currents. For the continuous conduction mode (CCM), the value of the capacitor and inductor can be given by Eq. (5.11). (Kamal, Arifoğlu, & Hassan, 2018)

$$L = \frac{V_{DC} D}{2 \Delta I_L f_s} \quad 5.12$$

where,  $\Delta I_L$  is the desired inductor current peak ripple while  $f_s$  is boost converter switching frequency. On the other hand, the value of the capacitor ( $C$ ) can be determined by Eq. (5.12) (Wai et al., 2007)

$$C = \frac{V_{out} D}{2 \Delta v_o R f_s} \quad 5.13$$

where,  $\Delta v_o$  is the desired output voltage peak ripple while  $R$  is the load resistance. Table 5.2 shows the parameter design of the DC boost converter under studies.

Table 5.2 The parameter for DC Boost Converter

Parameter	Values
Input Capacitor, $C_{in}$ ( $\mu F$ )	100
Output Capacitor, $C_{out}$ ( $\mu F$ )	245
Inductance, $L$ (mH)	1.85
Load Resistance $R_{Load}$ ( $\Omega$ )	10.0
Switching Frequency, $f_s$ (kHz)	20

### 5.3 MPPT Control Strategy

In this section, the concepts and problems of the conventional Hill-Climbing Search algorithm are presented. Subsequently, the proposed MPPT algorithm, which is the Fuzzy-HCS algorithm, is described. On the other hand, the Michas MPPT is presented for performance comparison between the MPPT algorithms.

#### 5.3.1 Conventional Hill-Climbing Search MPPT Algorithm

The hill-climbing search (HCS) method locates the local peak upon climbing the curve by adding the fixed step-size ( $\Delta S$ ). The HCS algorithm is based on the perturb and observe concepts that are employed in the climbing of the turbine's power curve. The algorithm monitors any changes in the rotor speed and output power based on the water velocity. The maximum power (MPP) can be generated from the PMSG when the variation of power over the variation of rotor speed equals zero, Eq. (5.14), as shown in Figure 5.4.

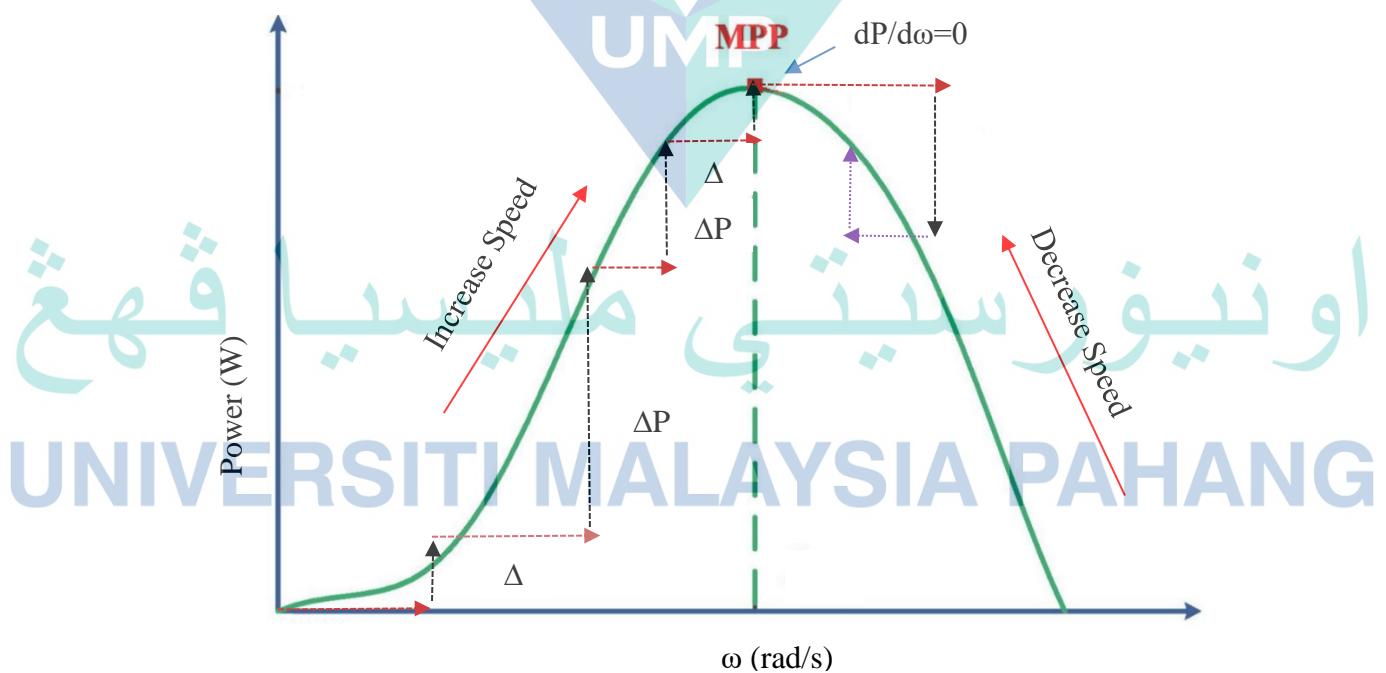


Figure 5.4 The basic concept of Hill-Climbing Search MPPT algorithm

$$\frac{dP}{d\omega} = 0 \quad 5.14$$

where,  $dP$  and  $d\omega$  are the change of power and rotor speed, respectively. According to Koutroulis (2006), by applying the chain rule, the Eq. (5.14) can be represented as Eq.(5.15).

$$\frac{dP}{d\omega} = \frac{dP}{dD} \frac{dD}{dV_{DC}} \frac{dV_{DC}}{d\omega} = 0 \quad 5.15$$

where,  $dD$  is the change of duty cycle of the converter, and  $dV_{DC}$  is the change of rectifier output voltage. For the boost converter, the duty cycle,  $D$  can be expressed in the form of output and input voltage as given in Eq. (5.16).

$$D = \frac{V_{out} - V_{DC}}{V_{out}} \quad 5.16$$

Subsequently, the duty cycle of the converter can be differentiated by the converter input voltage  $V_{DC}$  as given in Eq. (5.17).

$$\frac{dD}{dV_{DC}} = -\frac{1}{V_{out}} \neq 0 \quad 5.17$$

From Eq. (5.14) the converter input voltage is equal to the rectifier output voltage; hence the variation of generator speed is greater than zero as given in Eq. (5.18).

$$\frac{dV_{DC}}{d\omega} > 0 \quad 5.18$$

By considering Eq. (5.15) to Eq. (5.18), hence, the relation of generator power ( $P$ ) to the rotation speed can be transformed into the relation of the generator speed to the duty cycle of the converter as given in Eq. (5.19)

$$\frac{dP}{dD} = 0$$

5.19

Therefore, the MPPT control of the hydrokinetic system can be achieved through the regulation of duty ratio. Figure 5.5 shows the flow-chart of the HCS MPPT algorithm. To elaborate, if the MPP is located to the right of the point of operation, then the controller will need to shift the latter rightwards by climbing the curve to the nearest maximum point. Accordingly,  $\Delta S$  must be added, and the generator must increase the speed to achieve the MPP. On the other hand, should the MPP be situated towards the left of the point of operation, the latter needs to be shifted to the left by reducing the step size ( $\Delta S$ ). Therefore, the generator must reduce the speed to achieve the MPP.

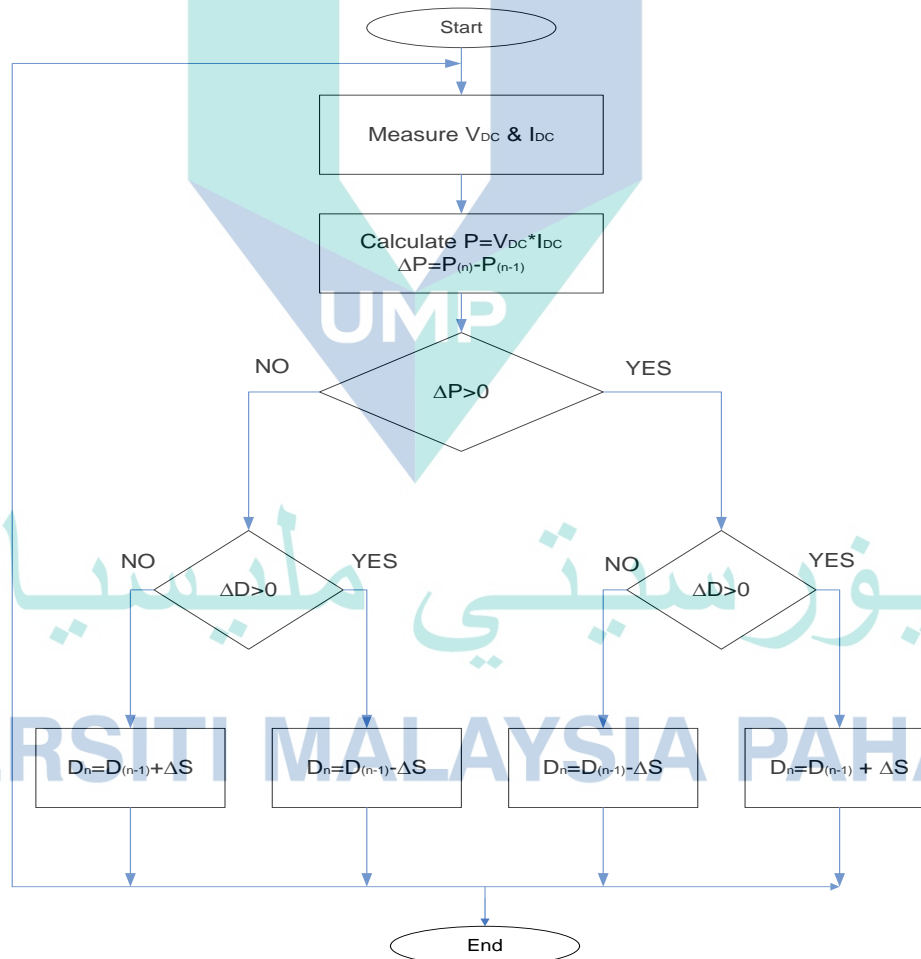


Figure 5.5 The flow chart of the conventional Hill-Climbing search algorithm.



The HCS method is widely applied since its usage is simple and flexible, especially for small-scale WECS. The algorithm is also independent, and the user does not need to know the characteristics of its turbine curves. However, the fixed step-size HCS algorithm needs to compromise between the oscillation at the steady-state and the rapid-dynamic response. If  $\Delta S$  is a large number, the MPP needs to be attained via a quicker response, but this will increase the oscillation around MPP and yield a lower power efficiency.

Conversely, a small  $\Delta S$  makes the system more efficient, even though it reduces the convergence speed. Therefore, to choose the step-size of the HCS algorithm has been very critical because it can significantly affect the performance of the algorithm. Therefore, the fixed- $\Delta S$  HCS algorithm fails to give rise to an acceptable compromise between steady-state oscillation as well as fast dynamic response. Hence, the proposed modified HCS with variable step size will improve the dynamic speed and reduces the steady-state oscillations.

### 5.3.2 Problem in Conventional HCS MPPT Algorithm

The HCS algorithm of fixed  $\Delta S$  performed well at the constant wind and fixed water velocity. Nevertheless, when the wind speed changes rapidly, the aforementioned algorithm fails to reach the maximum power point and detects the wrong direction. Besides, the algorithm needs to compromise between the tracking speed and accuracy. The large step-size, as shown in Figure 5.6 (a), will improve the tracking speed but increases the oscillation during the steady-state, which makes the setup less efficient. Conversely, small step-size in Figure 5.6 (b) reduces the oscillation during dynamic steady-state and becomes slow in convergence speed but high-efficiency output power.

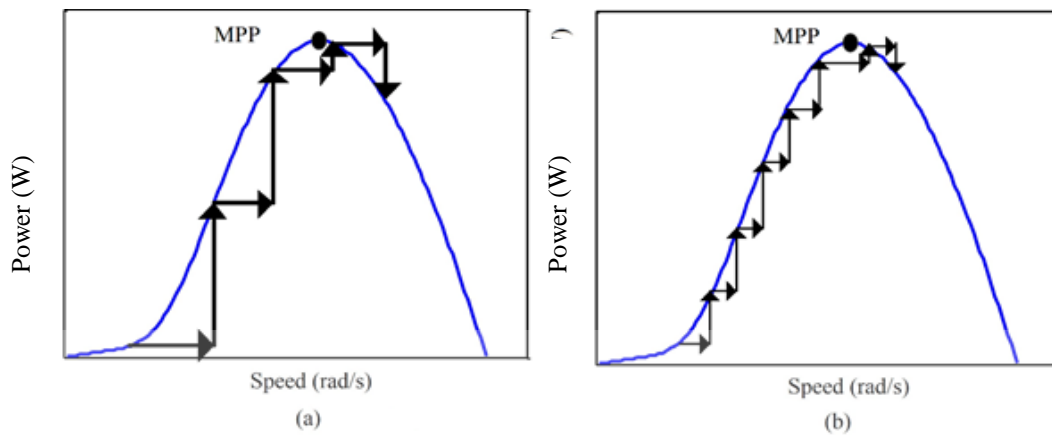


Figure 5.6 The illustration to show the process of climbing the power curve by adding different step-size. (a) HCS with large step-size, (b) HCS with small step-size.

To make the system more efficient as well as reduce the conventional HCS algorithm's drawbacks, Messalti et al. (2017) and Mousa et al. (2019) have proposed a modified variable- $\Delta S$  method. The modified step-size HCS is able to solve the wrong directionality during the rapid changes in the wind turbine and achieve a tracking speed-control efficiency compromise. Besides, the adaptive step size is another best option to eradicate the conventional HCS limitation. Several adaptive algorithms based on conventional HCS are explained by Hui et al. (2015) and Belhadji et al. (2013).

### 5.3.3 Michas MPPT Algorithm

The Michas algorithm is used for the performance benchmarking and comparison with respect to the proposed algorithm. The algorithm is formed based on Perturb and Observe (P&O) with the PI controller. Figure 5.7 shows the circuit topology and control scheme implemented for the Michas algorithm.

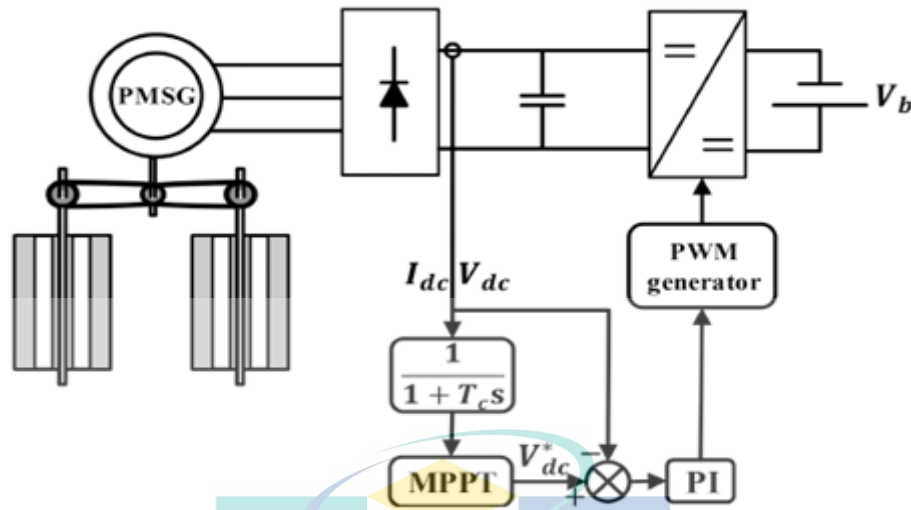


Figure 5.7 The circuit topology of the Michas MPPT Algorithm  
Source: Michas et al. (2019)

As noted by Michas et al. (2019) the  $V_{dc}^*$  is generated at the MPPT stage, and the difference between the  $V_{dc}$  measured and  $V_{dc}^*$  is fed into the PI controller. Consequently, the PI controller will generate the input signal for PWM to control the DC-DC converter. It should be noted, the proportional (P) and integral (I) gains of the controller respectively are chosen based on heuristic technique with the aim to minimise the oscillation and overshoot of the output power.

Figure 5.8 illustrates the flow chart of the Michas algorithm based on the P&O algorithm. First, the output voltage ( $V_{dc}$ ) and output current ( $I_{dc}$ ) are measured to calculate the output power ( $P$ ). Second, the corresponding output power,  $P(k-1)$  is compared to the previous output power  $P(k)$  due to the specific perturbation on the output voltage. Lastly, if the  $P(k-1)-P(k)$  is greater than zero due to the increase of the  $V_{dc}$ , the perturbation should maintain the same direction. Otherwise, the direction of perturbation is changed in the opposite way. The process of perturbation is repeated until reach the maximum value.

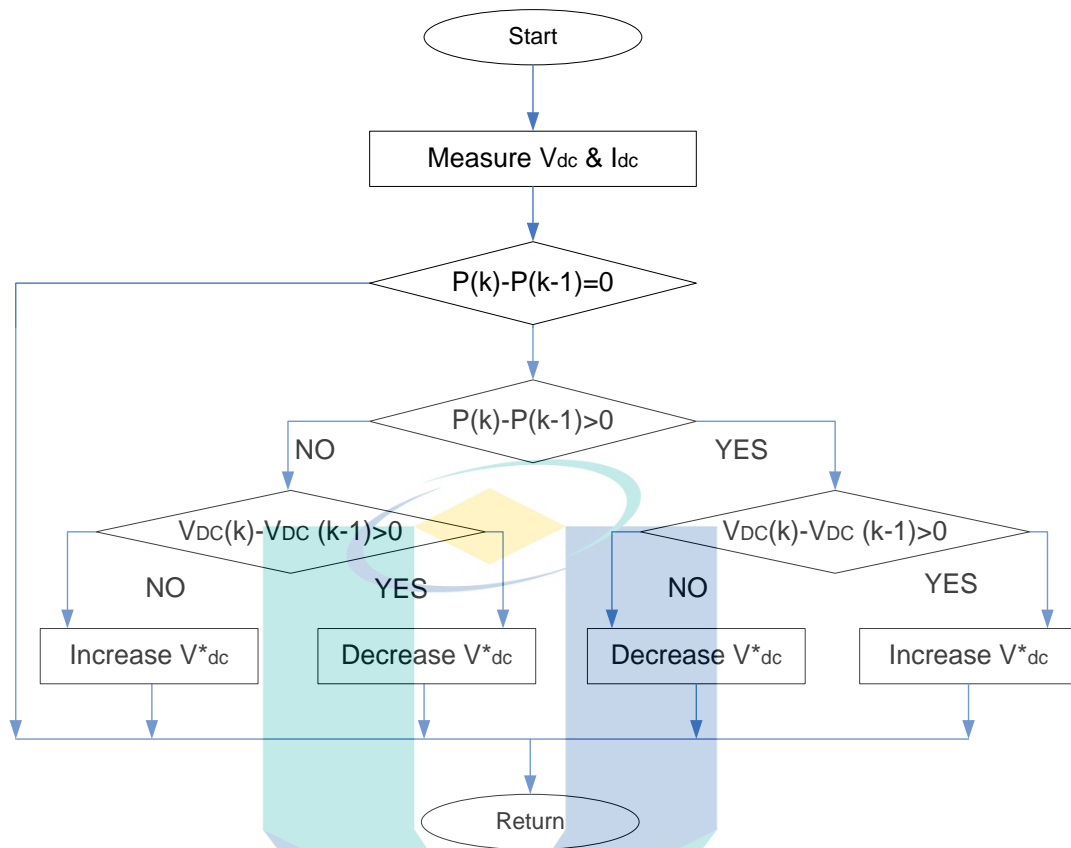


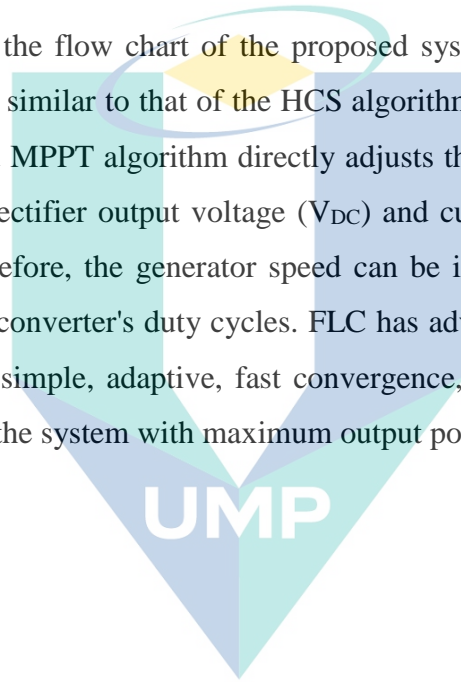
Figure 5.8 The flow chart of the Michas algorithm.

### 5.3.4 Proposed MPPT Algorithm

An algorithm is proposed with reference to the conventional HCS algorithm as well as the fuzzy logic controller (FLC) to provide the variable step size ( $\Delta S$ ). In this strategy, power and voltage changes ( $\Delta P$  and  $\Delta V$ , respectively) were the inputs of the FLC block. On the other hand,  $\Delta S$  serves as the output variable of the FLC, which can be applied as a variable step size in the HCS algorithm. The FLC rules will determine the suitable step size according to the changes in the water speed with respect to the operating point's position. Should there be a huge distance between this point and the MPP, the FLC will set  $\Delta S$  as a large value and vice-versa. The process remains until the MPP is achieved, hence reduces the oscillation around the MPP during the steady-state operation and improves the dynamic response of the system.

The conventional HCS algorithm has a limitation due to the oscillation on the output power. Besides, a fixed step-size in conventional HCS algorithm need to compromise between the fast-tracking and accuracy of the output power. The FLC has been implemented in this work to provide the variable step-size on the HCS algorithm. The FLC has been applied because of the fast convergence, able to analyse imprecise input and adaptive (Eltamaly & Farh, 2013). Therefore, the combination of this algorithm has been chosen due to the sensorless technique, establish HCS and FLC algorithm and easier for verification and validation.

Figure 5.9 shows the flow chart of the proposed system, whereby the operational concept of the FLC is similar to that of the HCS algorithm (i.e., MPP-tracking via duty cycles). The proposed MPPT algorithm directly adjusts the duty cycle according to the measurement of the rectifier output voltage ( $V_{DC}$ ) and current ( $I_{DC}$ ) as an input in the boost converter. Therefore, the generator speed can be increased or decreased by the function of the boost converter's duty cycles. FLC has advantages against conventional PI-controller such as simple, adaptive, fast convergence, imprecise input, and able to track non-linearity in the system with maximum output power.



اونيورسيتي مليسيا قهغ

UNIVERSITI MALAYSIA PAHANG

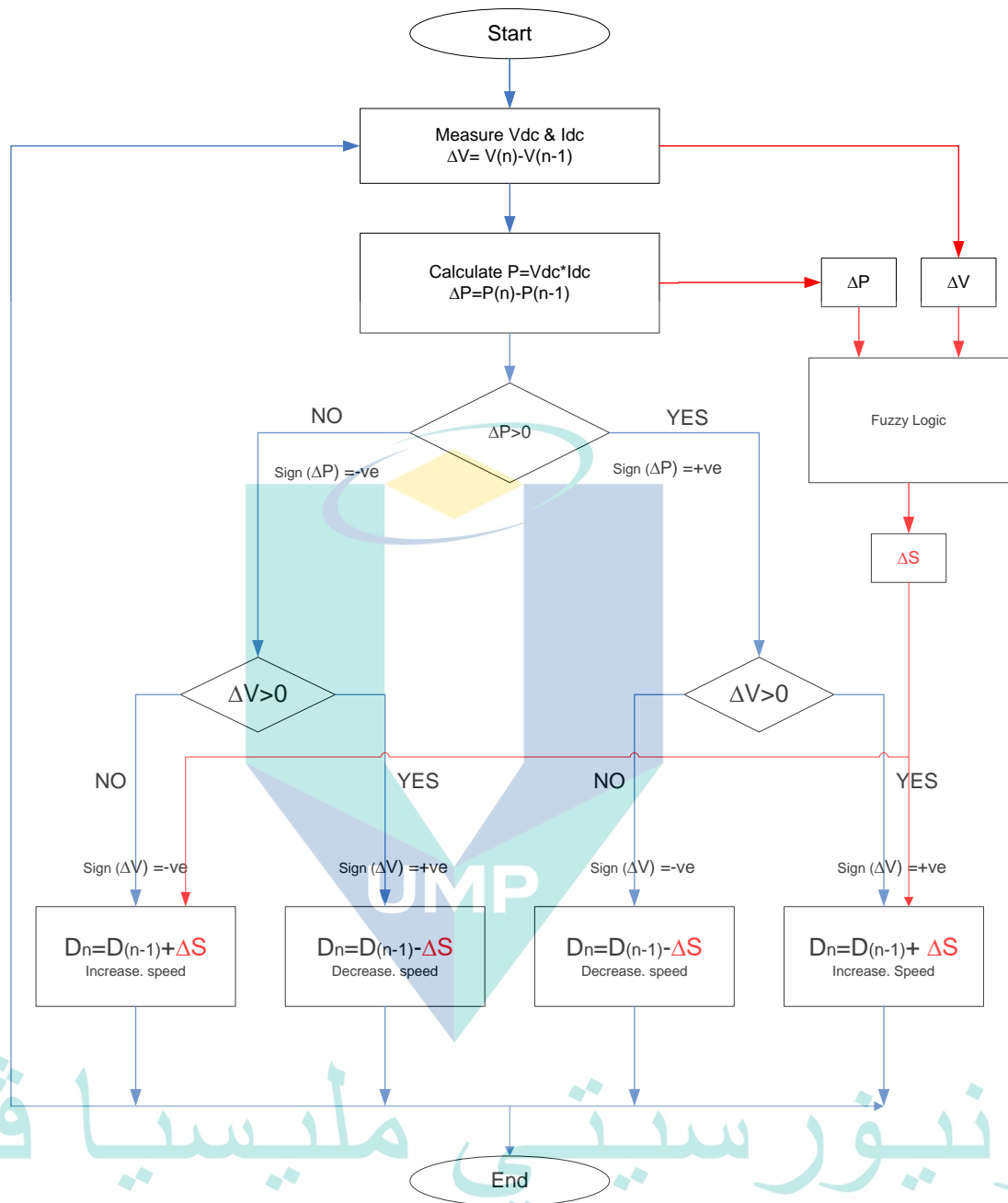


Figure 5.9 Flow chart of the proposed algorithm: Fuzzy-HCS MPPT algorithm

The design of the variable step size HCS begins with an understanding of the basic FLC. The FLC comprises four sections, as shown in Figure 5.10. The fuzzification is the process of making crisp quantity into fuzzy. In this proposed design, the fuzzy input can be measured from the voltage ( $V_{dc}$ ) and current ( $I_{dc}$ ) of the rectifier's output voltage.



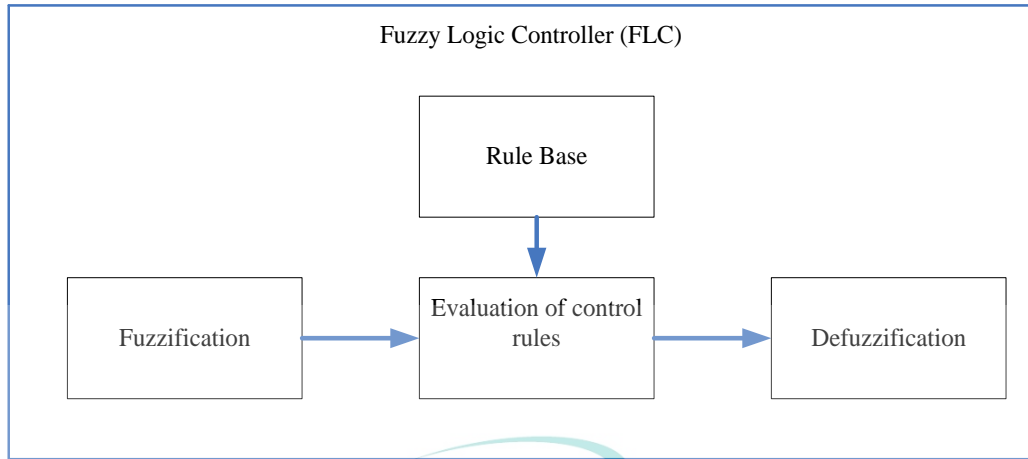


Figure 5.10 The basic concept of Fuzzy Logic Controller

The formulae to calculate the inputs of the proposed variables step-size FLC are given by Eq. (5.19)- Eq. (5.21).

$$P(n) = V_{dc} I_{dc} \quad 5.20$$

$$\Delta P(n) = G_P [P(n) - P(n-1)] \quad 5.21$$

$$\Delta V(n) = G_V [V(n) - V(n-1)] \quad 5.22$$

اونیورسیتی ملیسیا قهق

UNIVERSITI MALAYSIA PAHANG

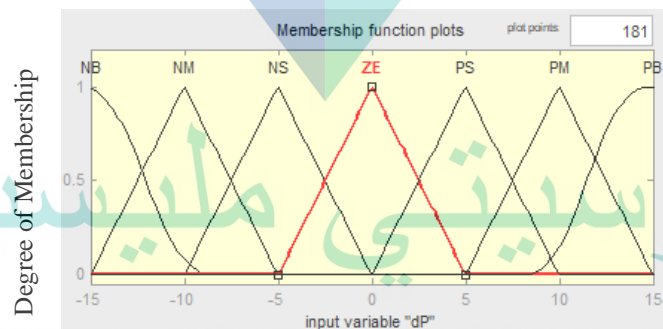
where,  $\Delta P(n)$  is the output power variation,  $P(n)$  is the current output power,  $P(n-1)$  is the previous output power,  $\Delta V$  is the output voltage variation,  $V(n)$  is the current output voltage while  $V(n-1)$  is the previous output voltage.

Notably, the scaling factor is implemented to simplify the control calculation for the output variation of  $\Delta P$  and  $\Delta V$ . The  $G_P$  and  $G_V$  are represented the scaling factor for the

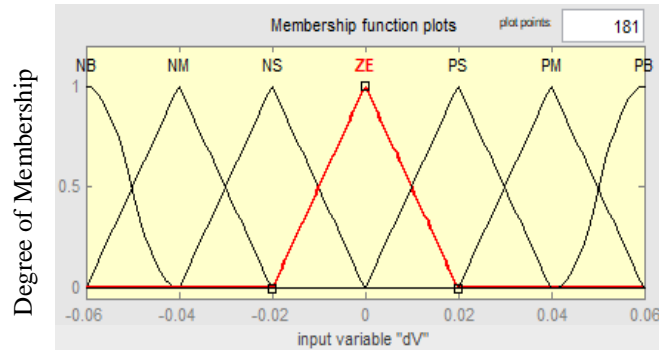
normalisation before the fuzzification process in fuzzy logic control. Therefore, the output variation of  $\Delta P$  and  $\Delta V$  will maintain between 0 and 1.

Subsequently, the process continues by creating the membership function to represent the fuzzy set. As to simplify the calculations, the fuzzy membership functions shape are nominated by triangular and Gaussian. The reason is due to this type of membership function is more sensitive when variables approach the zero value (J. Hussain, 2016; Liu et al., 2017). Moreover, as noted by Sadollah (2018), the triangular and Gaussian membership function are widely applied due to simplicity, well performed and better performance compared to other shape of membership functions.

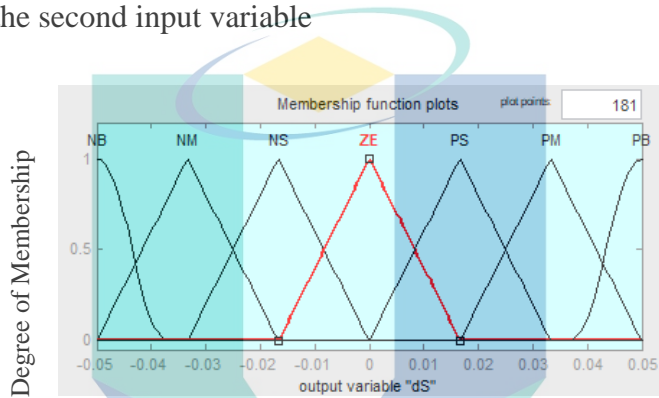
Figure 5.11 shows the FLC system's input as well as output variables' membership functions. As can be seen, the membership functions consist of seven fuzzy subsets as following which consists of NB (negative big), NM (negative medium), NS (negative small), ZE (zero), PS (positive small), PM (positive medium) and PB (positive bigger). The NB and PB are represented by Gaussian membership functions, whereas NM, NS, ZE, PS and PM are expressed by triangular membership functions. A similar combination of triangle and Gaussian shape membership functions was also applied by Zammit et al. (2017).



(a)  $\Delta P$  as the first input variable



(b)  $\Delta V$  as the second input variable



(c)  $\Delta S$  as the output variable

Figure 5.11 Membership functions of the fuzzy logic controller.

The next process is the evaluation of control rules. Table 5.3 shows the input/output variables' control rules for use in the fuzzy inference engine. Following from there, the output variables from these rules were utilized in the determination of the variable step size in the proposed algorithm to track the MPP.

Table 5.3 Fuzzy logic control rules

$\Delta P \backslash \Delta V$	NB	NM	NS	ZE	PS	PM	PB
NB	NB	NB	NB	NM	NS	NS	ZE
NM	NB	NM	NM	NM	NS	ZE	PS
NS	NB	NM	NS	NS	ZE	PS	PM
ZE	NM	NS	ZE	ZE	PS	PM	PB
PS	NM	NS	ZE	PS	PS	PM	PB
PM	NS	ZE	PS	PS	PM	PM	PB
PB	ZE	PS	PS	PM	PM	PB	PB

The FLC rule base is a collection of “IF-THEN” rules with AND logical operator to convert the fuzzy input into the fuzzy output. By referring to Table 5.3, since the membership function for each input variable is seven, hence the fuzzy inference rules will consist of 49 rules for the controlled parameter as follows:

- Rule 1: **IF**  $\Delta P$  is NB **AND**  $\Delta V$  is NB **THEN**  $\Delta S$  is NB
- Rule 2: **IF**  $\Delta P$  is NB **AND**  $\Delta V$  is NM **THEN**  $\Delta S$  is NB
- Rule 3: **IF**  $\Delta P$  is NB **AND**  $\Delta V$  is NS **THEN**  $\Delta S$  is NB
- Rule 4: **IF**  $\Delta P$  is NB **AND**  $\Delta V$  is ZE **THEN**  $\Delta S$  is NM
- Rule 5: **IF**  $\Delta P$  is NB **AND**  $\Delta V$  is PS **THEN**  $\Delta S$  is NM
- Rule 6: **IF**  $\Delta P$  is NB **AND**  $\Delta V$  is PM **THEN**  $\Delta S$  is NS
- Rule 7: **IF**  $\Delta P$  is NB **AND**  $\Delta V$  is PB **THEN**  $\Delta S$  is ZE
- Rule 8: **IF**  $\Delta P$  is NM **AND**  $\Delta V$  is NB **THEN**  $\Delta S$  is NB
- Rule 9: **IF**  $\Delta P$  is NM **AND**  $\Delta V$  is NM **THEN**  $\Delta S$  is NM
- Rule 10: **IF**  $\Delta P$  is NM **AND**  $\Delta V$  is NS **THEN**  $\Delta S$  is NM
- Rule 11: **IF**  $\Delta P$  is NM **AND**  $\Delta V$  is ZE **THEN**  $\Delta S$  is NS
- Rule 12: **IF**  $\Delta P$  is NM **AND**  $\Delta V$  is PS **THEN**  $\Delta S$  is NS
- Rule 13: **IF**  $\Delta P$  is NM **AND**  $\Delta V$  is PM **THEN**  $\Delta S$  is ZE
- Rule 14: **IF**  $\Delta P$  is NM **AND**  $\Delta V$  is PB **THEN**  $\Delta S$  is PS
- Rule 15: **IF**  $\Delta P$  is NS **AND**  $\Delta V$  is NB **THEN**  $\Delta S$  is NB

Rule 16:	<b>IF</b>	$\Delta P$ is	NS	AND	$\Delta V$ is	NB	<b>THEN</b>	$\Delta S$ is	NM
Rule 17:	<b>IF</b>	$\Delta P$ is	NS	AND	$\Delta V$ is	NB	<b>THEN</b>	$\Delta S$ is	NS
Rule 18:	<b>IF</b>	$\Delta P$ is	NS	AND	$\Delta V$ is	NB	<b>THEN</b>	$\Delta S$ is	ZE
Rule 19:	<b>IF</b>	$\Delta P$ is	NS	AND	$\Delta V$ is	NB	<b>THEN</b>	$\Delta S$ is	ZE
Rule 20:	<b>IF</b>	$\Delta P$ is	NS	AND	$\Delta V$ is	NB	<b>THEN</b>	$\Delta S$ is	PS
Rule 21:	<b>IF</b>	$\Delta P$ is	NS	AND	$\Delta V$ is	NB	<b>THEN</b>	$\Delta S$ is	PS
Rule 22:	<b>IF</b>	$\Delta P$ is	ZE	AND	$\Delta V$ is	NB	<b>THEN</b>	$\Delta S$ is	NM
Rule 23:	<b>IF</b>	$\Delta P$ is	ZE	AND	$\Delta V$ is	NM	<b>THEN</b>	$\Delta S$ is	NM
Rule 24:	<b>IF</b>	$\Delta P$ is	ZE	AND	$\Delta V$ is	NS	<b>THEN</b>	$\Delta S$ is	NS
Rule 25:	<b>IF</b>	$\Delta P$ is	ZE	AND	$\Delta V$ is	ZE	<b>THEN</b>	$\Delta S$ is	ZE
Rule 26:	<b>IF</b>	$\Delta P$ is	ZE	AND	$\Delta V$ is	PS	<b>THEN</b>	$\Delta S$ is	ZE
Rule 27:	<b>IF</b>	$\Delta P$ is	ZE	AND	$\Delta V$ is	PM	<b>THEN</b>	$\Delta S$ is	PS
Rule 28:	<b>IF</b>	$\Delta P$ is	ZE	AND	$\Delta V$ is	PB	<b>THEN</b>	$\Delta S$ is	PS
Rule 29:	<b>IF</b>	$\Delta P$ is	PS	AND	$\Delta V$ is	NB	<b>THEN</b>	$\Delta S$ is	NS
Rule 30:	<b>IF</b>	$\Delta P$ is	PS	AND	$\Delta V$ is	NM	<b>THEN</b>	$\Delta S$ is	NS
Rule 31:	<b>IF</b>	$\Delta P$ is	PS	AND	$\Delta V$ is	NS	<b>THEN</b>	$\Delta S$ is	ZE
Rule 32:	<b>IF</b>	$\Delta P$ is	PS	AND	$\Delta V$ is	ZE	<b>THEN</b>	$\Delta S$ is	PS
Rule 33:	<b>IF</b>	$\Delta P$ is	PS	AND	$\Delta V$ is	PS	<b>THEN</b>	$\Delta S$ is	PS
Rule 34:	<b>IF</b>	$\Delta P$ is	PS	AND	$\Delta V$ is	PM	<b>THEN</b>	$\Delta S$ is	PM
Rule 35:	<b>IF</b>	$\Delta P$ is	PS	AND	$\Delta V$ is	PB	<b>THEN</b>	$\Delta S$ is	PM
Rule 36:	<b>IF</b>	$\Delta P$ is	PM	AND	$\Delta V$ is	NB	<b>THEN</b>	$\Delta S$ is	NS
Rule 37:	<b>IF</b>	$\Delta P$ is	PM	AND	$\Delta V$ is	NM	<b>THEN</b>	$\Delta S$ is	ZE
Rule 38:	<b>IF</b>	$\Delta P$ is	PM	AND	$\Delta V$ is	NS	<b>THEN</b>	$\Delta S$ is	PS
Rule 39:	<b>IF</b>	$\Delta P$ is	PM	AND	$\Delta V$ is	ZE	<b>THEN</b>	$\Delta S$ is	PM
Rule 40:	<b>IF</b>	$\Delta P$ is	PM	AND	$\Delta V$ is	PS	<b>THEN</b>	$\Delta S$ is	PM
Rule 41:	<b>IF</b>	$\Delta P$ is	PM	AND	$\Delta V$ is	PM	<b>THEN</b>	$\Delta S$ is	PM
Rule 42:	<b>IF</b>	$\Delta P$ is	PM	AND	$\Delta V$ is	PB	<b>THEN</b>	$\Delta S$ is	PB
Rule 43:	<b>IF</b>	$\Delta P$ is	PB	AND	$\Delta V$ is	NB	<b>THEN</b>	$\Delta S$ is	ZE
Rule 44:	<b>IF</b>	$\Delta P$ is	PB	AND	$\Delta V$ is	NM	<b>THEN</b>	$\Delta S$ is	PS
Rule 45:	<b>IF</b>	$\Delta P$ is	PB	AND	$\Delta V$ is	NS	<b>THEN</b>	$\Delta S$ is	PM
Rule 46:	<b>IF</b>	$\Delta P$ is	PB	AND	$\Delta V$ is	ZE	<b>THEN</b>	$\Delta S$ is	PB
Rule 47:	<b>IF</b>	$\Delta P$ is	PB	AND	$\Delta V$ is	PS	<b>THEN</b>	$\Delta S$ is	PB

Rule 48:     **IF**  $\Delta P$  is   PB     AND  $\Delta V$  is   PM     **THEN**  $\Delta S$  is   PB

Rule 49:     **IF**  $\Delta P$  is   PB     AND  $\Delta V$  is   PB     **THEN**  $\Delta S$  is   PB

The last process is the defuzzification which is the fuzzy set's output will be converted to non-fuzzy value. The centre-of-gravity (COG) method is applied to calculate the  $\Delta S$  for defuzzification process. Subsequently, the output from the defuzzification process will be implemented in the algorithm as an input to variable step-size HCS MPPT algorithm.

## 5.4 Results and Discussions

In this section, the simulative performances of the four different algorithms for the stand-alone hydrokinetic are presented. The simulation was carried out under different variations of water velocity between  $1.0 \text{ ms}^{-1}$  to  $3.5 \text{ ms}^{-1}$  constant speed with 0.5 and 0.3 positive and negative slope, respectively. Subsequently, the algorithm was also tested under rapidly changing water velocity to evaluate the algorithm performance where the performances were assessed based on the tracking accuracy, tracking response time, oscillation and overshoot.

### 5.4.1 Tracking Accuracy

The proposed variable step-size (Fuzzy-HCS) algorithm has been compared with the small step-size (SS-HCS), large step-size (LS-HCS), and the P&O + PI controller by Michas. The tracking ability of the algorithm was evaluated by the output power accuracy. The output power efficiency is also calculated through the comparison between the theoretical maximum value and the output power from each algorithm. The theoretical value was calculated based on Eq. (5.1) by considering that the efficiency of the hydrokinetic system was 60 %, including the coupling losses, generator losses, and converter losses.



The input water velocity from  $1.0 \text{ ms}^{-1}$  to  $3.5 \text{ ms}^{-1}$  for thirty seconds of duration is shown in Figure 5.12 to represent the water variation. According to Koko et al. (2017) and Muljadi et al. (2016), the input variation in water resources is slower and steadier than wind or solar irradiation. As noted by Petrie et al. (2014) and Shahsavarifard et al. (2015), the water resources and the variation also can be predicted based on seasonal or monsoon statistics. Although the input variation does not represent the actual input of water velocity, it offers the worst-case scenario for the tracking algorithm.

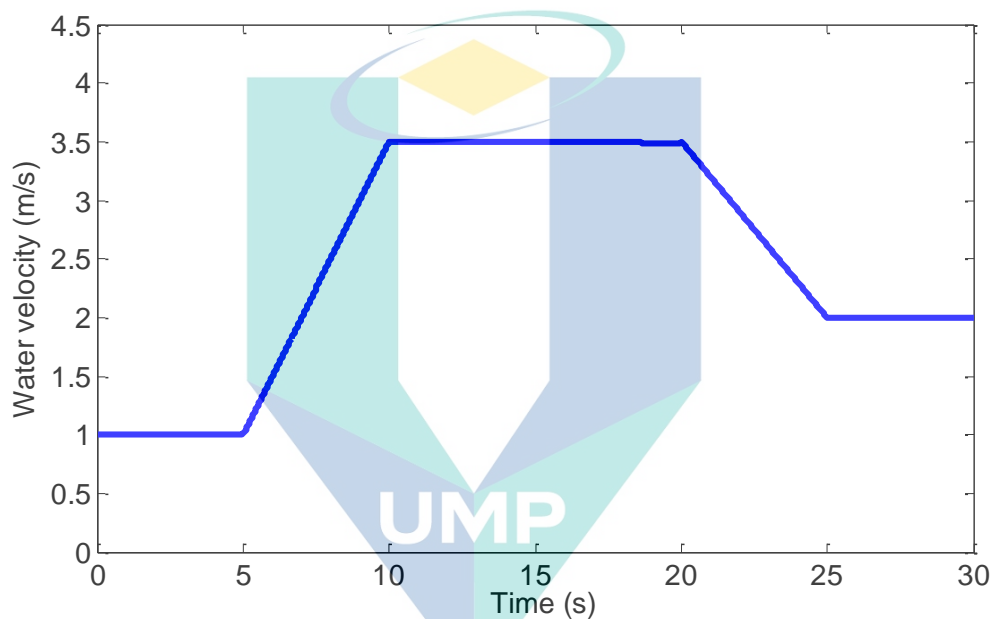


Figure 5.12 Water velocity to represent the input water variation for MPPT tracking.

The dynamic tracking accuracies were evaluated in terms of the output power of four MPPT algorithms, as shown in Figure 5.13. It is observed that all the algorithms are able to track the input water variation; however, the value of output power for each algorithm are different. It can be observed too that the Fuzzy-HCS algorithm has the highest output power compared to other algorithms. On the other hand, the LS-HCS has the lowest output power due to the higher oscillation around the MPP, hence resulting in the loss of energy.

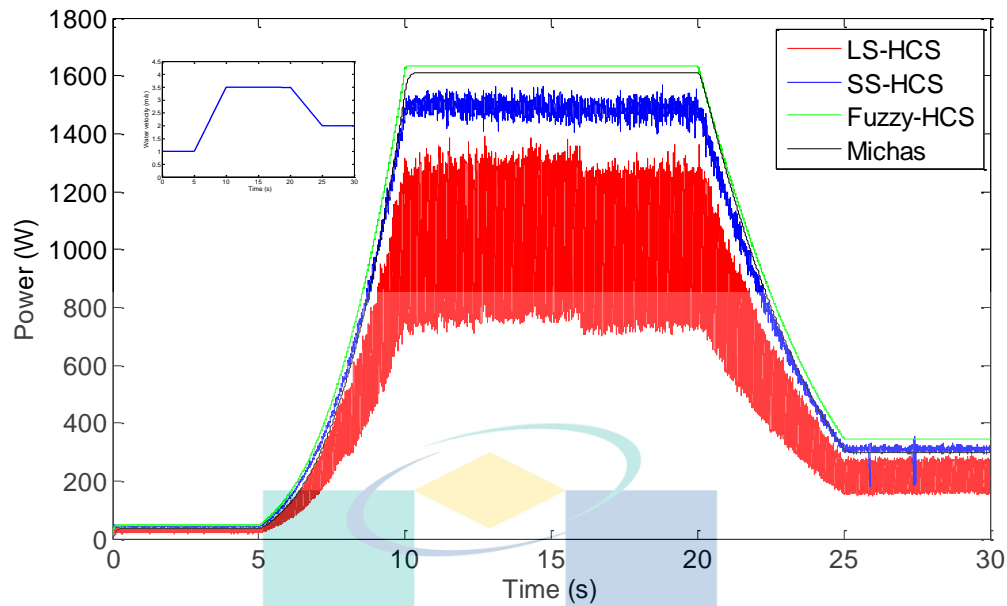


Figure 5.13 The output power of the hydrokinetic system simulated with four different MPPT algorithms. The small figure shows the water velocity as an input signal.

The output powers and the efficiencies of the algorithms are displayed in Table 5.4. The performance of the algorithm was evaluated based on the constant speed from  $1.0 \text{ ms}^{-1}$  to  $3.5 \text{ ms}^{-1}$  with a  $0.5 \text{ ms}^{-1}$  interval. It should be noted that the performance of the Fuzzy-HCS algorithm is the highest, with 88.30 % average efficiency. The output power of Fuzzy-HCS is ranging between 46.5 W and 1635 W. The second highest of the efficiency is SS-HCS MPPT algorithm with 80.41 %, then followed by the Michas algorithm with 74.85 %. On the other hand, the output power of the LS-HCS algorithm is the lowest, which ranges between 30 W to 1007 W due to large oscillation with 55.56 % average efficiency.

Table 5.4 The output power and the efficiency of the algorithms at constant water velocity. The algorithm was simulated based on input water variation in Figure 5.11

Water velocity (m/s)	Theoretical (W)	Output Power (W)				Efficiency (%)			
		SS-HCS	LS-HCS	Michas	Fuzzy-HCS	SS-HCS	LS-HCS	Michas	Fuzzy - HCS
1.0	47.5	42	30	37.5	46.5	88.42	63.16	78.95	97.89
1.5	160.4	136.5	92.4	112	149.7	85.01	57.61	69.82	93.33
2.0	380.2	308.1	225.6	276.2	340.8	81.04	59.34	72.65	89.63
2.5	742.5	581.8	400.3	550.4	640.8	78.36	53.91	74.13	86.30
3.0	1283.0	974.8	640.3	957.3	1057.4	75.98	49.91	74.61	82.41
3.5	2037.4	1500	1007	1608	1635	73.62	49.42	78.92	80.25
Average						80.41	55.56	74.85	88.30

اونیورسیتی ملیسیا قهق

UNIVERSITI MALAYSIA PAHANG

### 5.4.2 Tracking Response Time

Figure 5.14 shows the tracking response times. All dynamic responses and steady-state powers are below 500 ms. The dynamic response for LS-HCS is desirable (within 99 ms); however, the steady-state oscillation is large, which critically affects the captured mechanical power and creates noise and vibration (Harrag & Messalti, 2015). The proposed MPPT, Fuzzy-HCS, is at the second-fastest with 112 ms, followed by SS-HCS at 138 ms. On the other hand, the Michas algorithm took almost 460 ms and had a slower response time among the algorithm due to the effect of proportional controller gain.

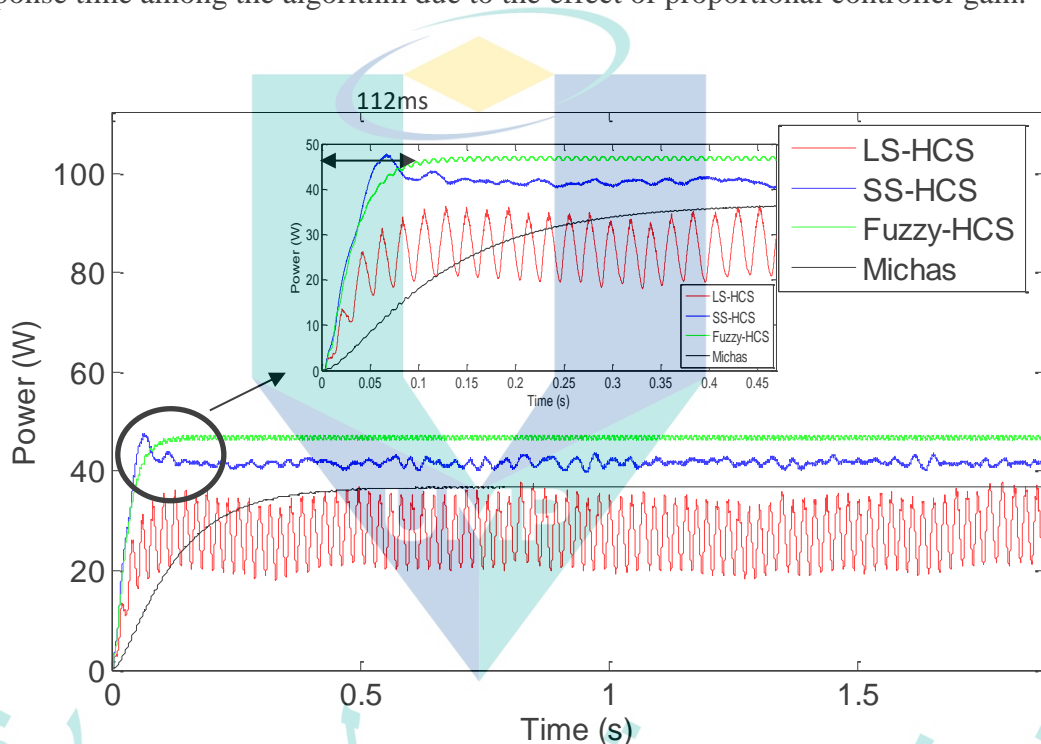
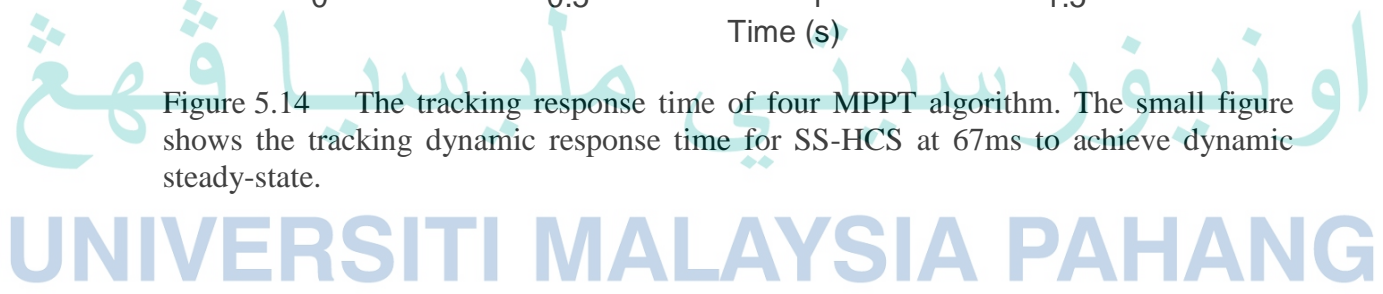


Figure 5.14 The tracking response time of four MPPT algorithm. The small figure shows the tracking dynamic response time for SS-HCS at 67ms to achieve dynamic steady-state.



### 5.4.3 MPPT Oscillation

The oscillation of the output power of the four algorithms is shown in Figure 5.15. It is observed that the LS-HCS possesses a huge oscillation during the dynamic steady-state, which ranges between 20 W and 35 W. In contrast, the SS-HCS has a better performance than the LS-HCS with 2 W amplitude of oscillations. It should be noted that

large oscillation reduces the performance of the MPPT algorithm, specifically the output power. The Michas MPPT algorithm shows the best performance among the algorithm with 0.2 W of attenuation. The less oscillation of the Michas algorithm is attributed to the integral gain in the PI controller. On the other hand, the Fuzzy-HCS algorithm has recorded about 1 W of oscillation at 1.0 ms<sup>-1</sup> of water velocity.

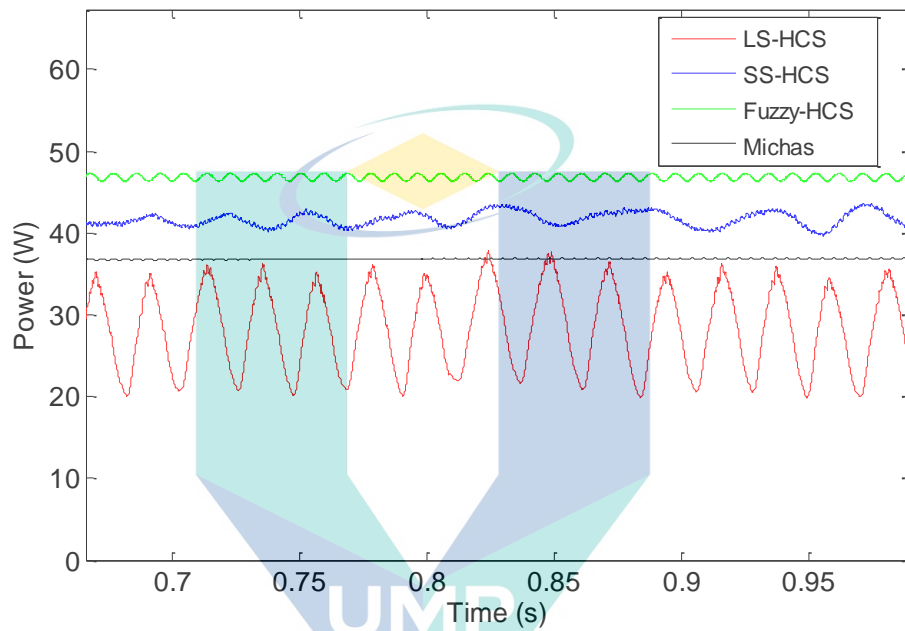


Figure 5.15 The oscillation of the output power for four algorithms at dynamic steady-state. The algorithm was simulated at constant 1ms<sup>-1</sup> water velocity in five seconds.

Table 5.5 The oscillation of the output power at different water velocities

Water Velocities	LS-HCS	SS-HCS	Fuzzy-HCS	Michas
1.0 ms <sup>-1</sup>	15.00 W	2.00 W	1.00 W	0.20 W
1.2 ms <sup>-1</sup>	26.70 W	2.23 W	1.44 W	0.25 W
1.4 ms <sup>-1</sup>	37.56 W	2.45 W	0.72 W	0.23 W
1.6 ms <sup>-1</sup>	50.63 W	3.07 W	0.53 W	0.15 W
1.8 ms <sup>-1</sup>	80.97 W	3.31 W	0.31 W	0.12 W
2.0 ms <sup>-1</sup>	123.14W	3.88 W	0.29 W	0.10 W
Mean Oscillation	55.67 W	2.82 W	0.72 W	0.18 W

Table 5.5 shows the oscillation of the output power at different water velocities. It is observed that the oscillation of LS-HCS and SS-HCS are proportional to the increase of the water velocities. Whereas, the Michas and proposed algorithm are inversely proportional to the increase of the water velocities. This finding indicates the Fuzzy-HCS algorithm is reliable and stable due to less oscillation with 0.72 W mean oscillation, as well as improving the efficiency of the energy extraction.

#### 5.4.4 MPPT Overshoot

The effect of overshoot on the output power can be investigated by changing the input water velocity in a short time. In this case, the unit step function has been used to represent the instant change on water variation from 2.4 ms<sup>-1</sup> to 1.0 ms<sup>-1</sup>, as shown in Figure 5.16. It is observed that the SS-HCS has the most significant overshoot, with 30 % of energy loss. On the other hand, the LS-HCS is not considered in the analysis due to high oscillation on the output power.

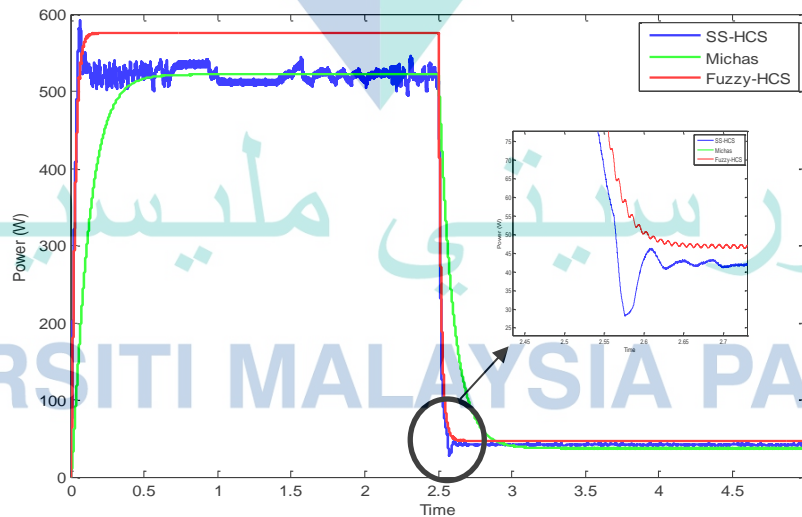


Figure 5.16 The instant changing of water variation between 2.4 ms and 1.0 ms. The simulation is running for a five-second of duration.



Figure 5.17 shows the settling time and energy loss calculation due to overshoot. It is observed that the settling time and amplitude of overshoot for SS-HCS are 0.12 s and 30 W, respectively. Based on the calculation, the energy loss is for SS-HCS is considered as much as 30 %. On the other hand, the energy loss for Fuzzy-HCS and Michas algorithm is only at 1.0 % and 0.41 %, respectively. Nevertheless, the settling time for the Michas algorithm is longest with 0.4 s before reach a dynamic steady state.

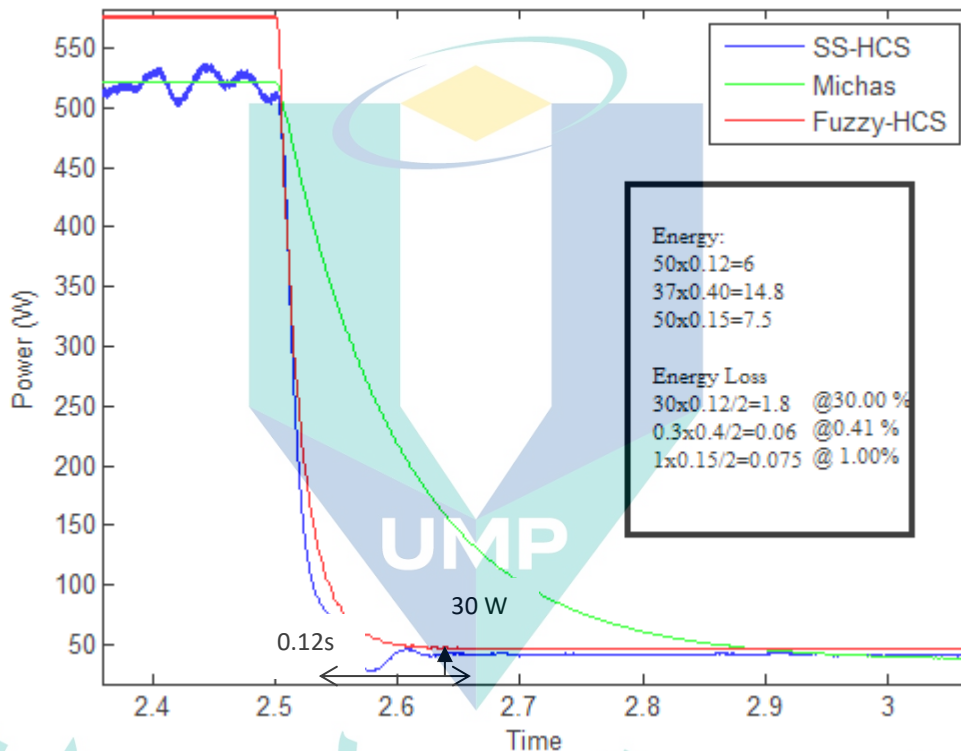


Figure 5.17 The settling time and amplitude of SS-HCS due to overshoot for energy loss calculation.

#### 5.4.5 MPPT Performance Comparison

The proposed algorithm (Fuzzy-HCS) algorithm has an excellent performance in terms of energy extraction, with 88.30 % of tracking efficiency compared to other conventional MPPT algorithms. Nevertheless, the tracking response is slow compared to the LS-HCS due to the complex structure programming that required much time to converge. On the other hand, the oscillation is small due to a low magnitude of attenuation

during the dynamic steady-state. Moreover, the overshoot is also less with 1.0 % of energy loss during the instant changing of water velocities.

As for benchmarking, the Fuzzy-HCS has an outstanding performance in terms of tracking accuracy and energy efficiency with more than 17.96 % energy extraction compared to the Michas algorithm. Besides, the response time is four times faster than the Michas algorithm. Both algorithms are comparable in terms of less oscillation, which can be classified into a small group of oscillation. Moreover, both algorithms are stable from higher overshoot if the water variation occurred. The Michas algorithm has recorded less energy losses due to overshoot with 0.41 % of energy losses compared to 1.0 % for Fuzzy-HCS. The fewer energy losses of the Michas algorithm is due to prolonged recovery time during the dynamic steady state.

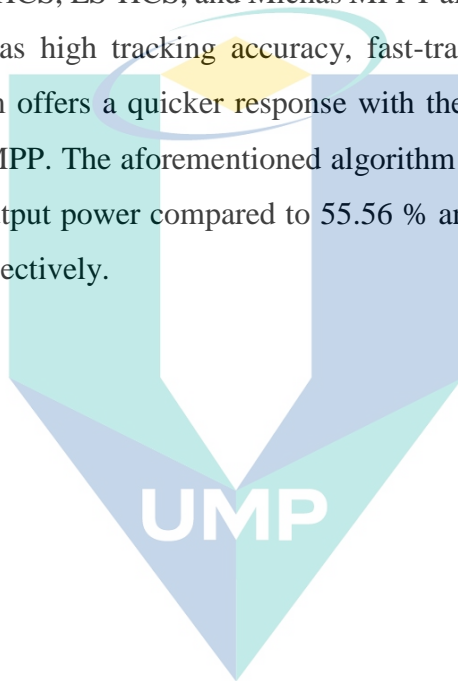
The proposed algorithm needs to compromise between the tracking response time and tracking accuracy due to the structure of the programming is based on HCS. The combination of the FLC algorithm, which provides the variable step-size, is an advantage, and as a result, the response time is 18.84 % reduced compared to the SS-HCS. Besides, the tracking efficiency is 9.81 % higher than SS-HCS. Moreover, the oscillation amplitude is also reduced with a clean and smooth output power. Table 5.6 shows the performance comparison between the MPPT algorithm.

Table 5.6 The summary of performance comparison between the MPPT algorithm

Parameter	LS-HCS	SS-HCS	Michas	Fuzzy-HCS
Tracking Efficiency (%)	55.56	80.41	74.85	88.30
Response Time (ms)	99	138	460	112
Oscillation	Very Large	Large	Small	Small
Energy loss (overshoot) (%)	-	30	0.41	1.00

## 5.5 Summary

In this chapter, the MPPT for the hydrokinetic energy harnessing has been proposed to solve the limitations that exist in the conventional HCS. The proposed algorithm is underpinned by a combination of FLC and conventional HCS (Fuzzy-HCS) to provide the variable  $\Delta S$ . The algorithm's concept is such that, once there is a huge discrepancy between output power and MPP, the  $\Delta S$  increases in the event that the output power moves towards MPP, and vice versa. The efficacy of the proposed algorithm has been validated with the SS-HCS, LS-HCS, and Michas MPPT algorithms. In further detail, the proposed algorithm has high tracking accuracy, fast-tracking, and higher efficiency. Besides, the algorithm offers a quicker response with the lowest dynamic steady-state oscillations near the MPP. The aforementioned algorithm is capable of achieving 88.30 % efficiency in the output power compared to 55.56 % and 74.85 % efficiency for LS-HCS and Michas, respectively.



اونيور سيطي ملايسيا قهغ

UNIVERSITI MALAYSIA PAHANG

## CHAPTER 6

### CONTROL STRATEGY FOR GRID-CONNECTED HYDROKINETIC SYSTEM

#### 6.1 Introduction

The depletion of fossil fuels and severe environmental issues are the primary concern in electrical power generation nowadays. As noted in BP Energy Outlook (2018), the demand for energy is predicted to increase by almost 30 % due to the rising prosperity and fast emerging economics in the evolving transition scenario by 2040.

Renewable energy (RE) is one of the best option to fulfil the energy demand globally due to a lot of resources and potentials such as hydropower, PV solar, wind, geothermal and biomass. Besides, RE is predicted as the most growing energy sources and will be approaching 25 % of global energy supplies by 2040 (EIA, 2018; Exxon Mobil, 2018).

Hydrokinetic energy harnessing is a renewable energy potential that has been explored widely by many researchers (Domenech, Eveleigh, & Tanju, 2018; Els & Junior, 2015; Kilcher & Kilcher, 2016; Nordqvist, 2016). Nevertheless, as the water velocity is always fluctuating and not in constant flow, the hydrokinetic system requires a sophisticated control strategy to extract output power and enhance efficiency. To date, as well as author is aware, there has been no investigation regarding the small signal analysis and stability control on the hydrokinetic system in the literature.

Small-signal analysis has been presented by many researchers in WECS to either design the controller or analyse the system stability in a grid network (Arani & Mohamed, 2015; Hu et al., 2015, 2017; Knüppel et al., 2012; Wei et al., 2014). For example, Ugalde-loo et al. (2013), derived the state-space mathematical modelling of wind turbine for the transient and small-signal analysis study in a weak network. Rahimi (2017) presented the stability analysis and controller design of grid-connected based diode bridge and boost converter. On the other hand, the analysis of the eigenvalues was used to study the small-

signal analysis and the controller's parameter was designed based on traces of eigenvalues (Mao & Wang, 2012). Furthermore the analysis of the eigenvalues was also studied to evaluate the stability problem and improve the system stability under small disturbances (Chouket & Krichen, 2015; Kani et al., 2014).

This chapter presents a mathematical model of the hydrokinetic system with direct drive PMSG and a full-scale back-to-back converter for the grid-connected system. First, the modelling of the turbine, PMSG, drive train, and power electronics converter for hydrokinetic energy harnessing are described. Second, the control strategies for the grid-connected system, such as Rotor Side Controller (RSC) and Grid Side Controller (GSC), are presented. Subsequently, by linearising the equation to the dynamic state, the state space equation is derived. Finally, the small-signal stability analysis and PI controller parameter gain are determined.

## 6.2 Modelling of Grid-Connected Hydrokinetic Energy Harnessing

In this section, the system topology for hydrokinetic energy harnessing is described. Subsequently, the modelling of each component consists of a turbine, PMSG, drive train, converter as well as grid network are presented.

### 6.2.1 Hydrokinetic System Topology

Figure 6.1 depicts the schematic diagram of the hydrokinetic system. The complete system consists of the mechanical part, electrical part and controller part. For the mechanical part, the rotation of the turbine blades will transfer the kinetic energy to the generator rotor shaft. The turbine is immersed in water and connected to the generator rotor shaft through direct coupling without the gearbox. In electrical parts, the PMSG is attached to the back-to-back power electronics converter and connected to the grid system. The controller part is composed of the rotor side controller (RSC) and the grid side controller (GSC).

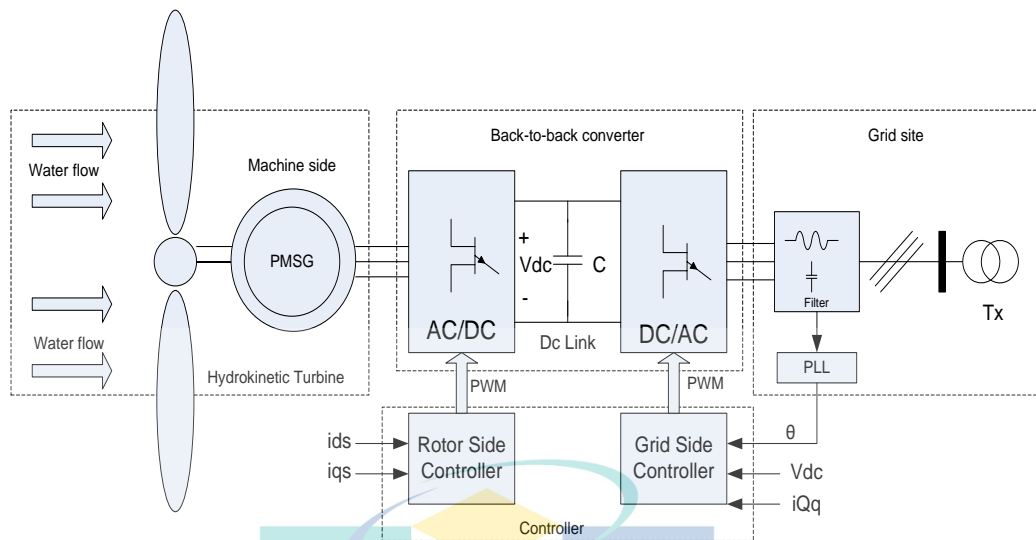


Figure 6.1 The complete of hydrokinetic system with the back-to-back converter

The circuit topology based on back-to-back converter has been considered in this work as part of the control strategy for grid-connected hydrokinetic energy harnessing. The converter has been employed due to full control ability at the rotor side controller (RSC) and the grid side controller (GSC). The function of the RSC is to track the maximum power generated from the turbine. The RSC can gain maximum output power by controlling the rotational speed of the generator via the torque control method. This control method was achieved by controlling the quadrature current  $I_{qs}$ .

Whereas the objectives of GSC are to control, synchronise, maintain the DC-link voltage and supply high-quality power to the grid with the compliance standard code (Jain, Jain, & Nema, 2015). Therefore, the back-to-back converter is one of the best options to regulate the generator speed, improve power factor, reduce the current distortion, and provide the isolation between the generator and the grid (De Freitas et al., 2016). On the other hand, the phase-locked loop (PLL) has been used to match the frequency and phase of the grid-connected system.



## 6.2.2 Turbine Model

The turbine model was based on the vertical axis straight blade H-Darrieus turbine. This type of turbine was preferable due to its capability to accept incoming water flow in any direction. In addition, the vertical axis turbine was quiet and suitable for shallow water depth (Behrouzi et al., 2016). As noted by Hong et al. (2013), the mechanical torque of the turbine is given by Eq. (6.1).

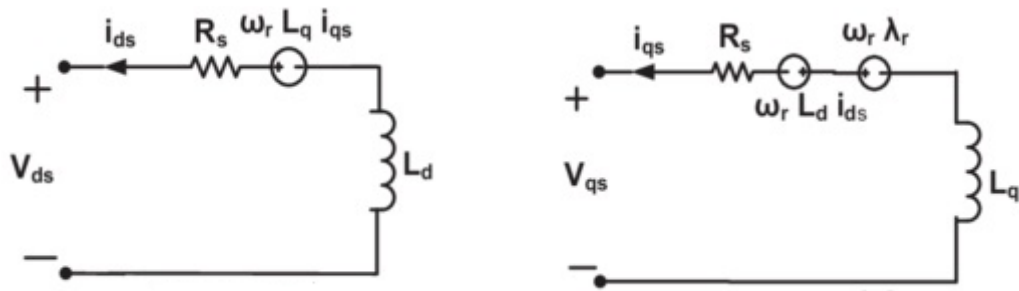
$$T_m = \frac{P_m}{\omega_r} = \frac{0.5\rho AV^3 C_p}{\omega_r} \quad 6.1$$

where,  $A$  was the area of the blade,  $\rho$  was the water density ( $1000 \text{ kg/m}^3$ ),  $C_p$  was the turbine power coefficient,  $V$  was the water velocity ( $\text{ms}^{-1}$ ) and  $\omega$  was the rotational speed of the turbine. The  $C_p$  was represented as the power extraction efficiency at a different rotational speed of the turbine. It has a non-linear function of tip speed ratio ( $TSR$ ) and the blade pitch angle,  $\beta$ . The model of the water turbine was designed in (Ibrahim, Ismail, & Mohamed, 2018) with a fixed pitch angle ( $\beta=0$ ). The turbine was operated at an optimal operating point at  $C_p=0.48$  and  $TSR=2.4$ . Therefore, the  $C_p$  is given by Eq. (6.2).

$$C_p(\lambda) = -0.022\lambda^6 + 0.04\lambda^5 - 0.26\lambda^4 + 0.72\lambda^3 - 0.77\lambda^2 + 0.27\lambda - 0.011 \quad 6.2$$

## 6.2.3 Model of Permanent Magnet Synchronous Generator (PMSG)

The PMSG with the constant magnetic flux,  $\psi_{pm}$  has been modelled in the  $a-b-c$  coordinates,  $\alpha-\beta$  coordinates and as well as in  $d-q$  reference frame. The conversion from  $a-b-c$  coordinates to  $d-q$  reference frame was related through the Clarke and Park transformation (Ren et al., 2017). Figure 6.2 shows the model of PMSG in  $d-q$  reference frame for the modal analysis.



(a) d-axis model

(b) q-axis model

Figure 6.2 PMSG d-q reference frame modelling

By aligning the direction of the d-axis of the  $d-q$  reference frame with the flux linkage, the model of PMSG are given in Eq.(6.3) and Eq. (6.4).

$$V_{ds} = -R_s i_{ds} + \omega_e L_s i_{qs} - L_s \frac{di_{ds}}{dt} \quad 6.3$$

$$V_{qs} = -R_s i_{qs} + \omega_e L_s i_{ds} - L_s \frac{di_{qs}}{dt} + \omega_e \psi_{pm} \quad 6.4$$

where  $V_{ds}$  and  $V_{qs}$  represented the stator voltage in d and q component respectively,  $i_{ds}$  and  $i_{qs}$  were the stator current in d and q component respectively,  $R_s$  and  $L_s$  were the resistance and inductance of the stator winding respectively, and  $\omega_e$  was the generator electrical speed. Furthermore, the electromagnetic torque,  $T_e$  can be calculated by Eq.(6.5).

$$T_e = \frac{3}{2} n_p \psi_{pm} i_{qs} \quad 6.5$$

where  $n_p$  is the number of pole pairs. Eq. (6.5) indicates that the  $T_e$  can be controlled by controlling the q-axis current directly.

#### 6.2.4 Model of Drive Train

The turbine and PMSG were connected directly without a gearbox system. This is due to the capability of the PMSG to operate at the same speed of the turbine blades (Sarkar & Khule, 2016). Hence, the mechanical system has been modelled using the one-mass model as in Eq.(6.6).

$$\tau_j \frac{d\omega}{dt} = T_m - T_e \quad 6.6$$

where,  $\omega$  was the mechanical speed, which is equal to turbine speed,  $\tau_j$  was the equivalent inertia time constant of the whole drive train.  $T_m$  and  $T_e$  are the mechanical and electromagnetic torque, respectively.

#### 6.2.5 Model of the Converter

The PMSG was linked to the grid system through full scale back-to-back converter with DC-link system, as shown in Figure 6.1. The simplified diagram of converter model for modal analysis is shown in Figure 6.3. By assuming the input power and the output power are balanced without any losses, hence the power balanced equation can be written by Eq. (6.7).

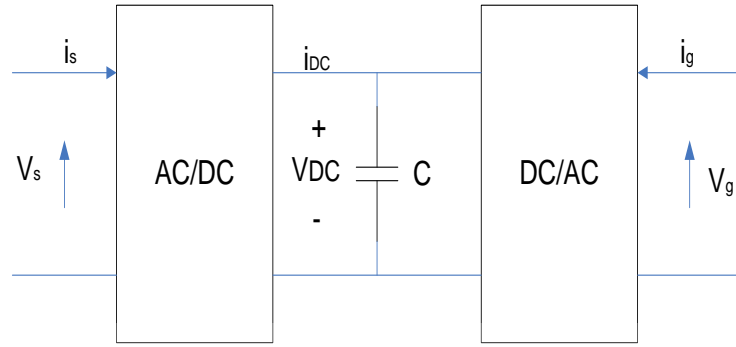


Figure 6.3 Model of back-to-back converter for modal analysis

$$P_{DC} = P_g - P_s \quad 6.7$$

where,  $P_{DC}$  is the active power at the DC-Link,  $P_g$  and  $P_s$  are the active power at the grid and PMSG respectively. The details derivation are given in Eq.(6.8)-Eq.(6.11).

$$P_{DC} = i_{DC}V_{DC} = CV_{DC} \frac{dV_{DC}}{dt} \quad 6.8$$

where,  $V_{DC}$  is a capacitor terminal voltage,  $C$  is the capacitor and  $i_{DC}$  is the current of the capacitor. Subsequently, the active power at the grid is given by Eq. (6.9).

$$P_g = V_{Dg}i_{Dg} + V_{Qg}i_{Qg} \quad 6.9$$

where,  $V_{Dg}$  and  $V_{Qg}$ , are the d and q axis voltage at the GSC respectively,  $i_{Dg}$  and  $i_{Qg}$  are the d and q axis current of the GSC respectively. On the other hand, the active power at the PMSG is given by Eq.(6.10).

$$P_s = V_{ds}i_{ds} + V_{qs}i_{qs} \quad 6.10$$

where,  $V_{ds}$  and  $V_{qs}$  represented the stator voltage in d and q component respectively,  $i_{ds}$  and  $i_{qs}$  are the stator current in d and q component respectively. Hence, the model of the converter and DC-link can be derived as given in Eq.(6.11)

$$CV_{DC} \frac{dV_{DC}}{dt} = V_{Dg}i_{Dg} + V_{Qg}i_{Qg} - (V_{ds}i_{ds} + V_{qs}i_{qs}) \quad 6.11$$

### 6.2.6 Model of Power Grid

By considering the single machine with the infinite bus as shown in Figure 6.3, the grid network voltage can be modelled as given by Eq. (6.12).

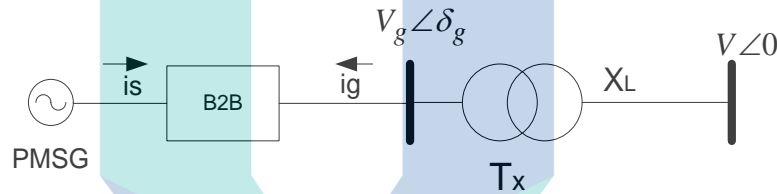


Figure 6.4 Model of grid network

$$V_g \angle \delta_g = V \angle 0 + jX_{TL}i_g \quad 6.12$$

where,  $V \angle 0$  is an infinite bus voltage,  $V_g \angle \delta_g$  is a voltage at the grid and  $X_{TL}$  is a reactance of the transformer and transmission line. The network equation can be represented in d-q reference frame. After simplifying, the corresponding transformation is given in Eq.(6.13) and Eq.(6.14) respectively (Wu, Zhang, & Ju, 2009).

$$i_{Dg} = \frac{V_{Dg} - V \sin \delta_g}{X_{TL}} \quad 6.13$$

where  $i_{Dg}$  and  $i_{Qg}$  are the d and q axis current of the GSC respectively.

$$i_{Qg} = \frac{V_{Qg} - V \cos \delta_g}{X_{TL}} \quad 6.14$$

where  $V_{Dg}$  and  $V_{Qg}$ , are the d and q axis voltage at the GSC respectively.

### 6.3 Control Strategies for Grid-Connected Hydrokinetic System

In this section, the proposed control strategy for grid-connected hydrokinetic energy harnessing is presented and followed by the implementation of PI controller at the RSC and GSC, respectively. Subsequently, the linearising process of non-linear equations around the equilibrium point is described.

#### 6.3.1 Proposed PI Controller with Eigenvalues Trajectory Tracing Method

The PI controller has been proposed because of the robustness and ability to improve the system stability by shifting the poles towards the left s-plane (Aly & El-Hawary, 2011; Omkar et al., 2019). In addition, the PI controller is the universal controller, and the gains ( $K_P$  and  $K_I$ ) can be tuned with available optimisation techniques such as Gravitational Search Algorithm (GSA), (Assareh & Biglari, 2015), Biogeography-Based-Optimisation (Abdul et al., 2014) and Ant Colony Optimisation (ACO) (Mokhtari & Rekioua, 2018).

The proposed control system for grid-connected hydrokinetic energy harnessing is based on the PI controller with the eigenvalues trajectory tracing method. Whereas the PI controller parameters,  $K_P$  and  $K_I$  have been tuned based on traces of eigenvalues. The eigenvalues tracing method provided a fast convergence process since only one eigenvalue is computed during the iteration (Wen & Ajarapu, 2006).



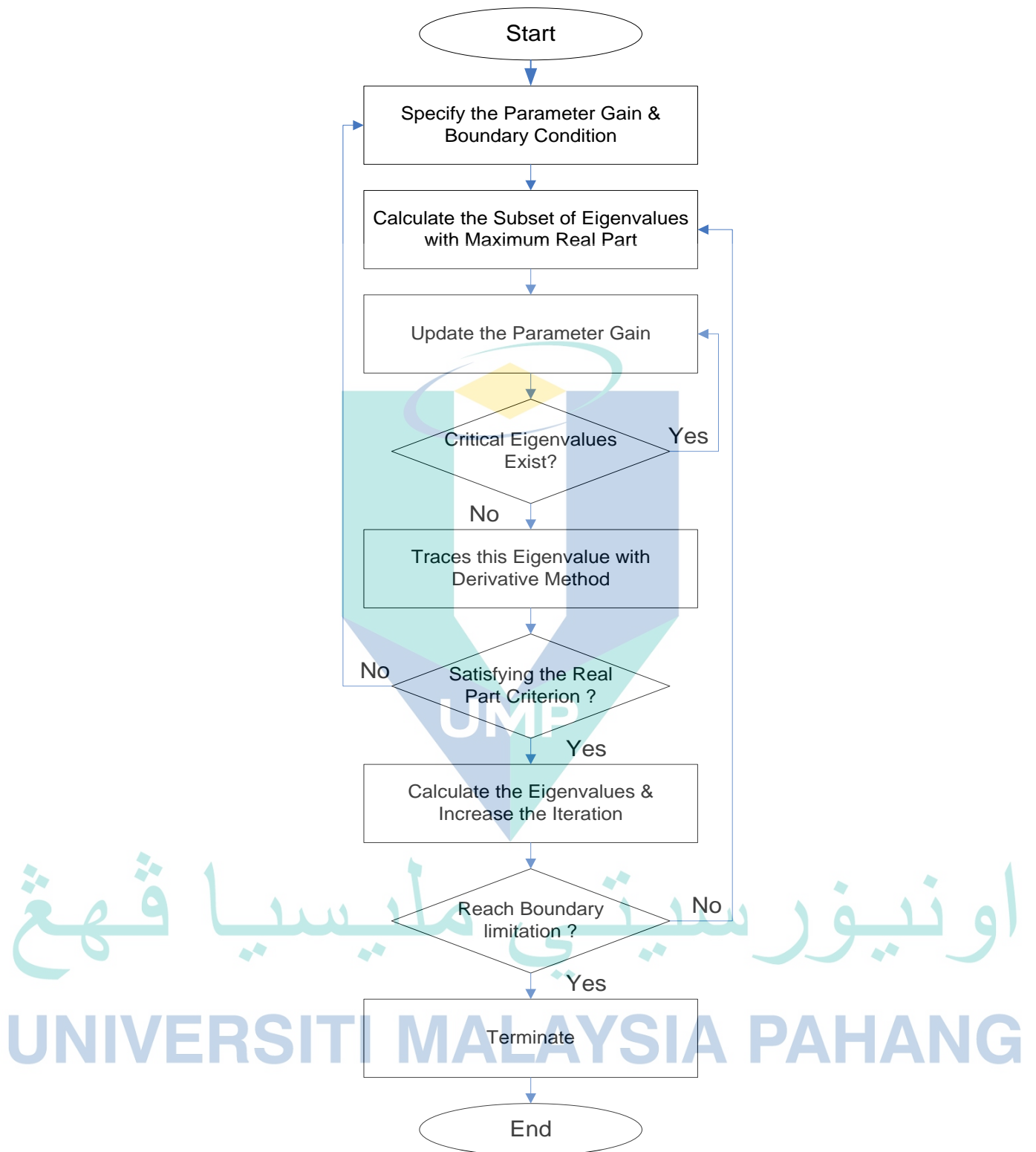


Figure 6.5 Eigenvalues Trajectory Tracing Method

Figure 6.5 shows the flow chart of the proposed controller using the eigenvalue tracing method. At first, the parameter gain and boundary condition need to be specified. In this work, the gain increment and boundary conditions are shown in Table 6.1. Then, compute the eigenvalues with the rightmost eigenvalues as well as the maximum real part at the equilibrium point. Subsequently, updated the parameter gain for the next tracing of eigenvalues by checking the eigenvalues moving direction during the parameter increments.

Table 6.1 The Parameter gain and boundary condition

Parameter	Gain Increment	Boundary Condition ( $\epsilon$ )
$K_{P1}$	0.1	$0.05 < \epsilon < 3.00$
$K_{I1}$	$K_{P1}/0.025$	$3.33 < \epsilon < 200$
$K_{P2}$	0.1	$0.05 < \epsilon < 3.00$
$K_{I2}$	$K_{P2}/0.025$	$3.33 < \epsilon < 200$
$K_{P3}$	0.1	$0.05 < \epsilon < 3.00$
$K_{I3}$	$K_{P3}/0.025$	$3.33 < \epsilon < 200$
$K_{P4}$	0.1	$0.1 < \epsilon < 1.5$
$K_{I4}$	$K_{P4}/0.025$	$0.83 < \epsilon < 50$
$K_{P5}$	0.1	$0.05 < \epsilon < 3.00$
$K_{I5}$	$K_{P5}/0.025$	$0.25 < \epsilon < 100$

The next sequence is to check the condition for critical eigenvalues. If the eigenvalue is positive and moving towards the left s-plane, it represents the uninstabilise condition of the system. Hence, the tracing process needs to stop and start to calculate another subset of eigenvalues with a new gain increment. Otherwise, the negative eigenvalues will be traced until it will cross the imaginary axis.

After that, if the eigenvalue is satisfied the criterion with real large part and lower imaginary part, then save the traced of eigenvalue and ready for the next iteration circle. Otherwise, the parameter and boundary need to setup again to achieve system stability.

The tracing of the eigenvalue for the real part is continuous and repeatable until it will reach the boundary and terminate the process.

Finally, based on the eigenvalues tracing method, the gain controller for PI control can be determined. The traces of eigenvalue that will produce the real large part and small imaginary part need to be chosen as a gain for proportional and integral, respectively.

### 6.3.2 Rotor Side Controller (RSC)

The purpose of RSC was to control the active power of the PMSG. The stator current at direct-axis, ( $i_{ds}$ ) was set to zero. The quadrature-axis stator current, ( $i_{qs}$ ) was controlled to track the maximum output power from the fluctuation of the river current. The control block diagram of RSC is shown in Figure 6.6.

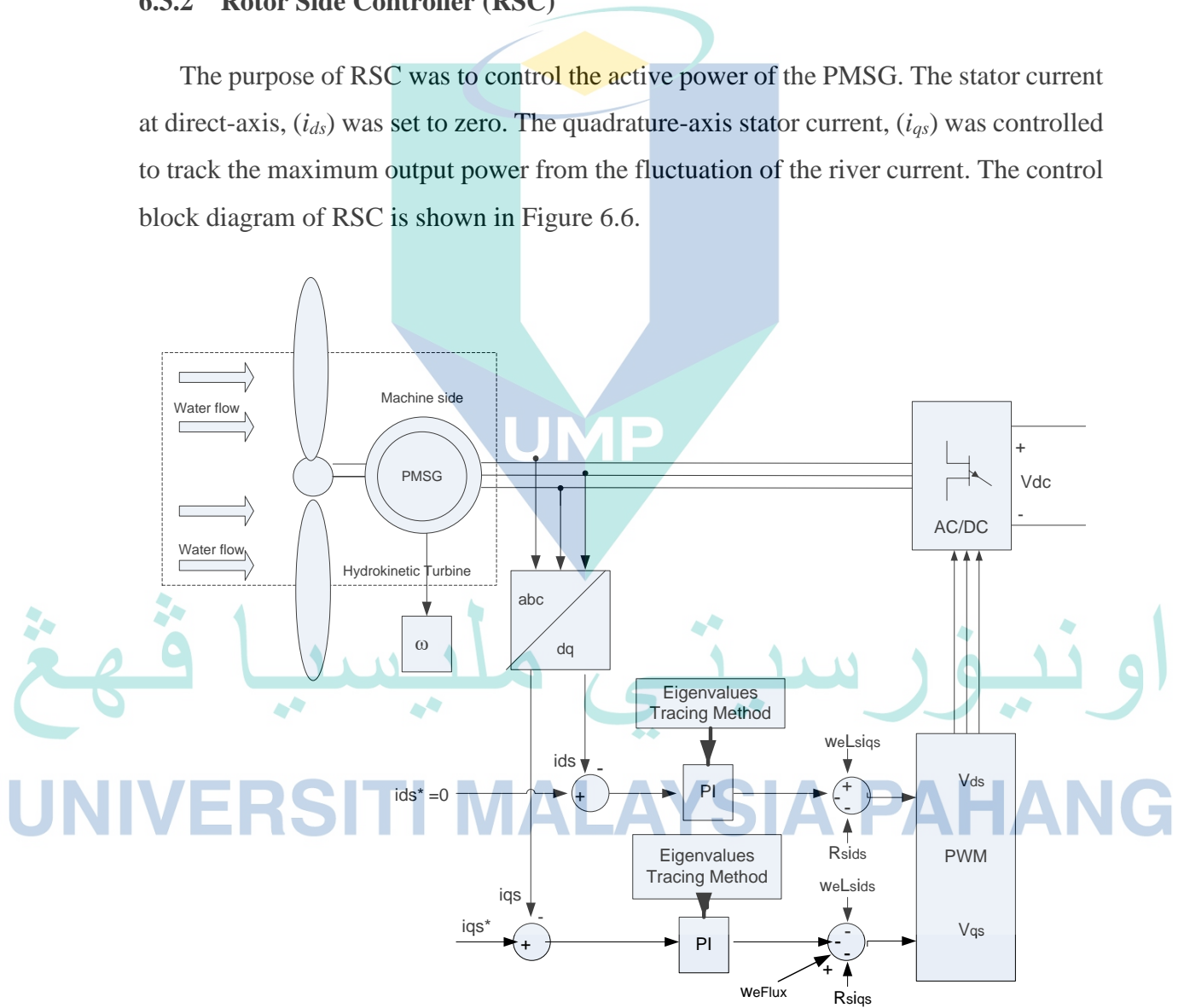


Figure 6.6 The block diagram of rotor side controller

As can be seen in Figure 6.5, the stator current,  $I_d$  and  $I_q$  need to be measured from the generator. Then, both current need to be compared with their reference values  $I_d^{\text{ref}}$  and  $I_q^{\text{ref}}$ . The respective output later is tuned by PI-controllers with eigenvalues tracing method.. The resulting stator voltages  $V_d$  and  $V_q$  are transformed back to the phase voltages (a, b, c). Besides, the rotor speed also is measured, and the speed will be compared to the speed reference values  $\omega(\Omega^{\text{ref}})$ . Due to generator torque is determined by the  $I_q$ , the PI controller will calculate the reference between the generator speed ( $\Omega$ ) and reference speed ( $\Omega^{\text{ref}}$ ).

The control equations of the RSC are given by Eq.(6.15)-Eq.(6.21).

$$i_{ds}^* = 0 \quad 6.15$$

where  $i_{ds}^*$  is a reference of direct-axis stator current.

$$\frac{dx_1}{dt} = i_{ds}^* - i_{ds} \quad 6.16$$

where,  $x_1$  is a intermediate state variables

$$V_{ds}^* = -K_{P1}(i_{ds}^* - i_{ds}) - K_{I1}x_1 + \omega_e L_s i_{qs} - R_s i_{ds} \quad 6.17$$

where,  $V_{ds}^*$  is a reference of direct axis stator voltage,  $R_s$  and  $L_s$  were the resistance and inductance of the stator winding respectively, and  $\omega_e$  was the generator electrical speed.  $K_P$  and  $K_I$  were the proportional and integrating gains of the RSC.

$$i_{qs}^* = \frac{2T_e}{3n_p \psi_{pm}} \quad 6.18$$

where  $i_{qs}^*$  is a reference of stator current in quadrature component,  $n_p$  is a number of pole pairs and  $T_e$  is an electromagnetic torque.

$$T_e = \frac{1}{2\lambda} \rho A R V^2 C_p \quad 6.19$$

$$\frac{dx_2}{dt} = i_{qs}^* - i_{qs} \quad 6.20$$

where,  $x_2$  is a intermediate state variables

$$V_{qs} = -K_{P2}(i_{qs}^* - i_{qs}) - K_{I2}x_2 - \omega_e L_s i_{ds} - R_s i_{qs} \quad 6.21$$

where,  $V_{qs}$  represented the stator voltage in quadrature component.

### 6.3.3 Grid Side Controller (GSC)

The GSC aims to sustain the DC-link voltage, hence controlling the active and reactive power of the grid. Based on aligned vector voltage,  $V_g$  to the direction of Q-axis as shown in Figure 6.7, the  $V_{Dg}$  is equal to zero and the active power  $P_g = V_{Qg}i_{Qg}$ .

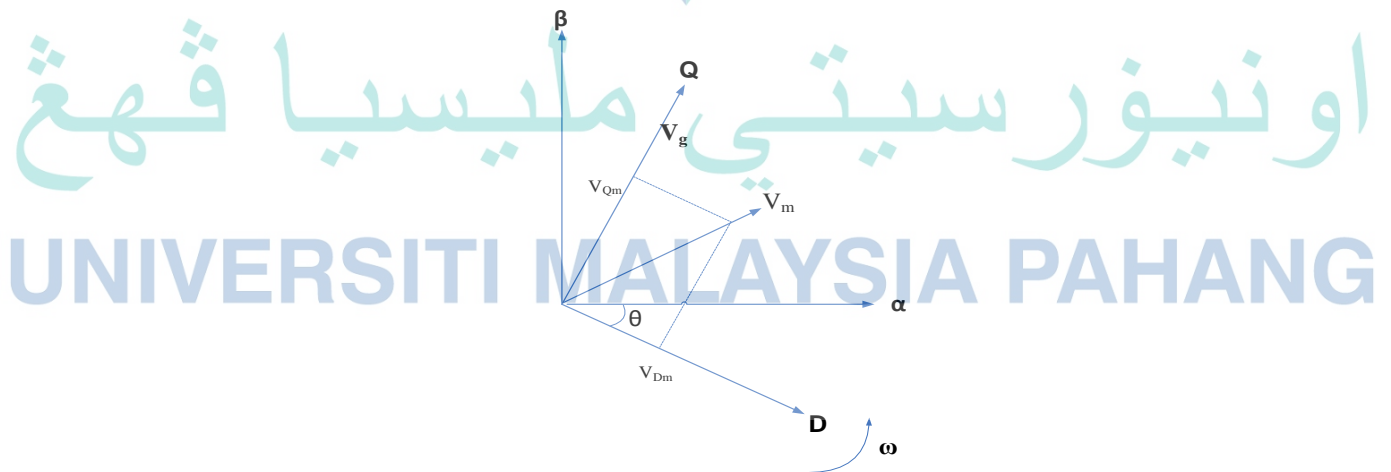


Figure 6.7 The vector diagram of GSC in  $\alpha$ - $\beta$  and  $d$ - $q$  reference frame.

The D-axis of grid current was controlled to zero, ( $i_{Dg}=0$ ) to obtain the reactive power at the grid equal to zero, ( $Q_G=0$ ). Hence, the stability of the DC voltage can be preserved by controlling the Q-axis grid current,  $i_{Qg}$ . The equation of grid side voltage source converter are given by Eq.(6.22) and Eq.(6.23).

$$L \frac{di_{Dg}}{dt} = V_{Dg} - V_{Dm} + \omega Li_{Qg} \quad 6.22$$

where  $i_{Dg}$  and  $i_{Qg}$  are the direct and quadrature axis grid current respectively,  $\omega$  is the electrical angular velocity at grid voltage.

$$L \frac{di_{Qg}}{dt} = V_{Qg} - V_{Qm} + \omega Li_{Dg} \quad 6.23$$

where  $i_{Qg}$  is a quadrature-axis grid current. Subsequently, the control equation are given by Eq.(6.24)-Eq.(6.30).

$$i_{Dg}^* = 0 \quad 6.24$$

where  $i_{Dg}^*$  is the reference of direct axis grid current.

$$\frac{dx_3}{dt} = i_{Dg}^* - i_{Dg} \quad 6.25$$

UNIVERSITI MALAYSIA PAHANG

where  $x_3$  is the intermediate state variable.

$$V_{Dm}^* = -K_{P3} (i_{Dg}^* - i_{Dg}) - K_{I3} x_3 + \omega Li_{Qg} - V_{Dg} \quad 6.26$$



where  $i_{Dg}$  and  $i_{Qg}$  are the  $d$ - $q$  axis grid current respectively and  $V_{Dg}$  is the  $d$ -axis grid voltages.

$$\frac{dx_4}{dt} = V_{DC}^* - V_{DC} \quad 6.27$$

where  $V_{DC}^*$  and  $V_{DC}$  are the reference and terminal voltage of capacitor, respectively.

$$i_{Qg}^* = K_{P4}(V_{DC}^* - V_{DC}) + K_{I4}x_4 \quad 6.28$$

where  $i_{Qg}^*$  is the reference of  $q$ -axis grid current.

$$\frac{dx_5}{dt} = i_{Qg}^* - i_{Qg} \quad 6.29$$

where  $x_5$  is the intermediate state variable.

$$V_{Qm} = -K_{P5}(i_{Qg}^* - i_{Qg}) - K_{I5}x_5 - \omega L i_{Dg} + V_{Qg} \quad 6.30$$

where the intermediate state variable was represented by  $x_5$ ,  $i_{Qg}$  is the  $q$ -axis grid current,  $V_{Qg}$  is the  $q$ -axis grid voltages,  $K_P$  and  $K_I$  were the proportional and integral controller constants respectively. The schematic diagram of the GSC is shown in Figure 6.8.

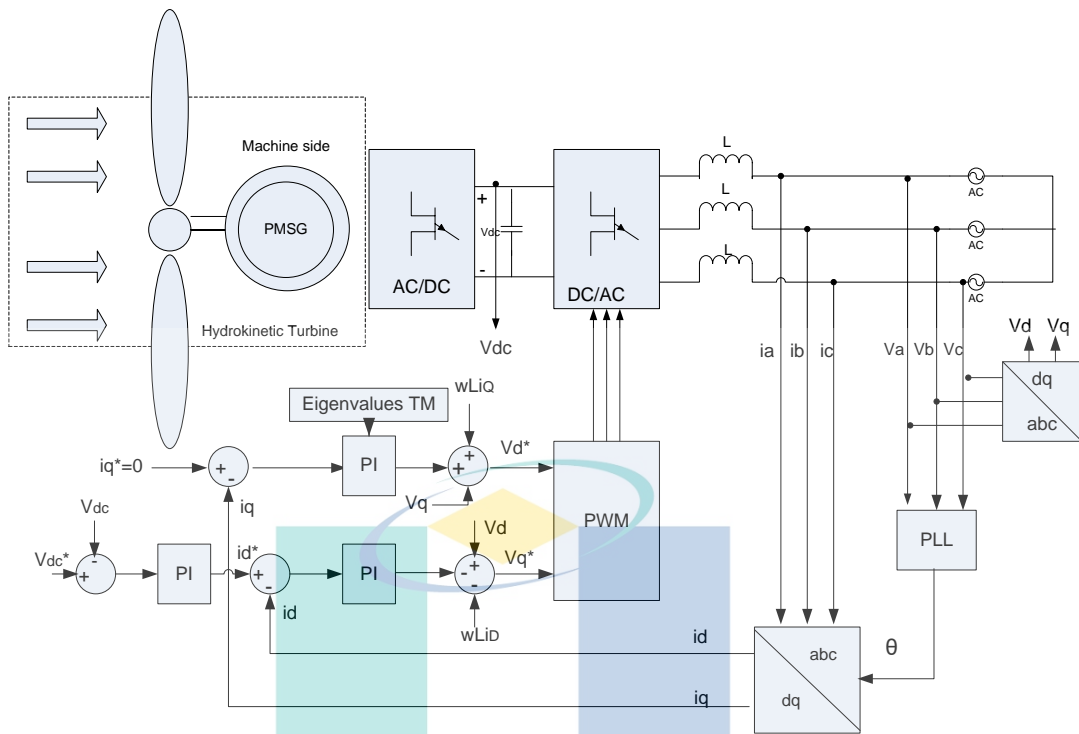


Figure 6.8 The schematic diagram of the grid side controller

It is observed, the different value between the reference of DC-link voltage and measurement of DC-link voltage is fed into the PI controller as an outer loop control as shown in Figure 6.8. Subsequently, the output from the PI controller is compared to the measurement of the d-axis current and is fed into the PI controller as an inner loop control. A feed-forward term ( $V_d$ ) is added to the system to improve the system response (Michas, 2018). On the contrary, the reference q-axis current is set to zero and has been compared to the measurement of the q-axis current. The output is fed into the PI controller and produced the voltage command signal ( $V_d^*$ ). Both resulting command signal ( $V_d^*$  and  $V_q^*$ ) are transformed from the d-q reference frame to the instantaneous voltage values. Ultimately, the instantaneous voltage signal is used to generate a PWM signal to activate the power converter.

On the other hand, the function of Phase Loop Lock (PLL) is to obtain the frequency and phase for the transformation of the current in the d-q reference frame (Ali et al., 2018). Therefore, the active power can be controlled by the d-axis of the converter

current, ( $i_d$ ), whereas, the reactive power can be controlled through the q-axis of the converter current, ( $i_q$ ).

#### 6.3.4 Linearising of The Hydrokinetic Model

Linear analysis technique is used to study the dynamic response stability of the control system (Mcgrath, 2018). According to Bianchi et al. (2007), the non-linear equation can be linearised around the equilibrium or operating point. The Taylor Series and Jacobian formulation can be used to linearise the non-linear equation for dynamic analysis (Goodwin, Graebe, & Salgado, 2000). The details of linearised equation for hydrodynamic model of hydrokinetic energy harnessing can be referred to the Appendix D.

The model of the hydrokinetic energy harnessing connected to the grid-network is described as follows: The model of PMSG is expressed by Eq. (6.3) and Eq. (6.4), whereas Eq. (6.6) is realised the mechanical dynamics of the turbine. Consequently, the DC-link model is represented by Eq. (6.11), whereas Eq. (6.15)-Eq. (6.21) and Eq. (6.24)-Eq. (6.30) are represented the dynamic model of the controller design at RSC and GSC respectively. Lastly, the dynamic model of the electric grid system is given by Eq. (6.23) and Eq. (6.24).

Subsequently, by applying linearising principle to all non-linear equation as stated above, the small-signal model with eleven state-space variables and an input are given by Eq. (6.31).

$$\frac{d\Delta x}{dt} = A\Delta x + B\Delta u \quad 6.31$$

where, the  $\Delta$  is represented a small-signal dynamic perturbation at the operating point, whereas  $x$  and  $u$  is given by Eq. (6.32).

$$x = \left[ \omega \ i_{ds} \ i_{qs} \ x_1 \ x_2 \ x_3 \ x_4 \ x_5 \ i_{Dg} \ i_{Qg} \ V_{dc} \right]^T \quad 6.32$$

$$u = V_w$$

On the other hand, the values matrix  $A$  and  $B$  are given by Eq. (6.33) and Eq. (6.34), respectively.

$$A = \begin{pmatrix} a_{11} & 0 & a_{13} & 0 & 0 & 0 & 0 & 0 & 0 & 0 & 0 \\ 0 & a_{22} & 0 & a_{24} & 0 & 0 & 0 & 0 & 0 & 0 & 0 \\ 0 & 0 & a_{33} & 0 & a_{35} & 0 & 0 & 0 & 0 & 0 & 0 \\ 0 & a_{42} & 0 & 0 & 0 & 0 & 0 & 0 & 0 & 0 & 0 \\ 0 & 0 & a_{53} & 0 & 0 & 0 & 0 & 0 & 0 & 0 & 0 \\ 0 & 0 & 0 & 0 & 0 & 0 & 0 & 0 & a_{69} & 0 & 0 \\ 0 & 0 & 0 & 0 & 0 & 0 & 0 & 0 & 0 & 0 & a_{711} \\ 0 & 0 & 0 & 0 & 0 & 0 & a_{87} & 0 & 0 & a_{810} & a_{811} \\ 0 & 0 & 0 & 0 & 0 & a_{96} & 0 & 0 & a_{99} & 0 & 0 \\ 0 & 0 & 0 & 0 & 0 & 0 & a_{107} & a_{108} & 0 & a_{1010} & a_{1011} \\ a_{111} & a_{112} & a_{113} & a_{114} & a_{115} & 0 & 0 & 0 & a_{119} & a_{1110} & a_{1111} \end{pmatrix} \quad 6.33$$

$$B = (b_1 \ b_2 \ b_3 \ b_4 \ b_5 \ b_6 \ b_7 \ b_8 \ b_9 \ b_{10} \ b_{11}) \quad 6.34$$

where,  $A$  was the  $[11 \times 11]$  state matrix,  $\Delta x$  was a vector of state variables, and  $\Delta u$  was a vector state variable of the input. The state variable ( $a$ ) and ( $b$ ) were given by Eq. (6.35) and Eq. (6.36), respectively.

$$a_{11} = \frac{1}{\tau j} \left( \frac{-0.055\rho AR^6 \omega_o^5}{V_o^3} + \frac{0.08\rho AR^5 \omega_o^3}{V_o^2} - \frac{0.39\rho AR^4 \omega_o^2}{V_o} + \frac{0.72\rho AR^3 \omega_o - 0.385\rho AR^2 V_o + \frac{0.0055\rho AV_o^3}{\omega_o^2}}{\omega_o^2} \right)$$

$$a_{13} = -\frac{\psi_{pm}}{\tau j}$$

$$a_{22} = -\frac{K_{P1}}{L_s}, a_{24} = \frac{K_{I1}}{L_s}$$

$$a_{33} = -\frac{K_{P2}}{L_s}, a_{35} = \frac{K_{I2}}{L_s}$$

$$a_{42} = -1, a_{53} = -1, a_{69} = -1, a_{711} = -1,$$

$$a_{87} = K_{I4}, a_{810} = -1, a_{811} = -K_{P4}$$

$$a_{96} = \frac{K_{I3}}{L}, a_{99} = \frac{K_{P3}}{L}$$

$$a_{107} = \frac{K_{P5}K_{I4}}{L}, a_{108} = \frac{K_{I5}}{L}, a_{1010} = -\frac{K_{P5}}{L}, a_{1011} = -\frac{K_{P5}K_{P4}}{L}$$

$$a_{111} = \frac{i_{qs}\psi_{pm}}{CV_{dc0}}, a_{112} = \frac{1}{CV_{dc}} [V_{ds0} + i_{ds0}(K_{P1} - R_s) - i_{qs0}L_s\omega_o]$$

$$a_{113} = \frac{1}{CV_{dc}} [V_{ds0} + i_{ds0}(K_{P2} - R_s) + i_{ds0}L_s\omega_o]$$

$$a_{114} = -\frac{K_{I1}i_{ds0}}{CV_{dc0}}, a_{115} = -\frac{K_{I2}i_{qs0}}{CV_{dc0}}, a_{119} = -\frac{i_{Qg0}x_{TL}}{CV_{dc0}}$$

$$a_{1110} = \frac{1}{CV_{dc0}} \left( -\frac{x_{TL}^2 i_{Qg0}^2}{V_{Qg0} + i_{Dg0}x_{TL}} + V_{Qg0} \right)$$

$$a_{1111} = \frac{1}{CV_{dc0}^2} (-V_{Qg0}i_{Qg0} - i_{ds0}V_{ds0} - i_{qs0}V_{qs0})$$

اونیورسیتی ملیسیا قهق

UNIVERSITI MALAYSIA PAHANG

$$b_1 = \frac{1}{\tau j} \left( \frac{0.033\rho AR^6 \omega_o^5}{V_o^4} - \frac{0.04\rho AR^5 \omega_o^4}{V_o^3} + \frac{0.13\rho AR^4 \omega_o^3}{V_o^2} - 0.385\rho AR^2 \omega_o + 0.27\rho AR V_o - \frac{0.0165\rho AV_o^2}{\omega_o} \right) \quad 6.36$$

$$b_3 = \frac{K_{P2} C_{p \max} \rho a R V}{L_s \psi_{pm} \lambda_{opt}}$$

$$b_5 = \frac{C_{p \max} \rho a R V}{\psi_{pm} \lambda_{opt}}$$

$$b_{11} = -\frac{K_{P2} i_{qs0} C_{p \max} \rho a R V}{C V_{dc} \psi_{pm} \lambda_{opt}}$$

According to Mcgrath (2018), the state-space model can be assessed by different operating points using analytical techniques such as pole-zero maps, eigenvalue analysis, and frequency response. The modelling of the hydrokinetic system is derived to study the system stability after small disturbance due to water fluctuation using the analysis of the eigenvalues. Besides that, the analysis of the small-signal model is essential in designing the controller's parameter of the system.

#### 6.4 Results & Discussions

In this section, the analysis of the eigenvalues to evaluate the stability and controller design as part of the control strategies for the hydrokinetic system is presented. The simulation was carried by specifying the parameter gain and boundary condition for proportional gain ( $K_{P1}$  to  $K_{P5}$ ) and Integral gain ( $K_{I1}$  to  $K_{I5}$ ). Subsequently, the effect of each parameter gain to the state variable is evaluated in term of controller stability. Then, the PI controller parameter is determined using the trace of eigenvalues is described. Lastly, the validation through the Simulink model is discussed at the end of the section.

### 6.4.1 Controller Stability Analysis

The small-signal stability analysis for the small-scale hydrokinetic energy harnessing was investigated to analyse the system stability due the disturbance. The data of PMSG from DVE Technologies Aps with 300 AC, 5 kW and 28 poles have been used in this studied. Table 6.2 shows the detailed parameter of the studied case.

On the other hand, Table 6.3 presents the results of controller stability without the proposed eigenvalues tracing method. The eigenvalues, oscillation frequency and damping factor for matrix A which consists of eleven states variables are evaluated . The stator current ( $i_{ds}$  and  $i_{qs}$ ) and DC-link voltage show high oscillation frequency. It is observed that, all the eigenvalues have a negative real part; hence, proves that the system is in a stable condition even after suffering small disturbance. The system consists of three evanescent modes for states  $\lambda_1$ ,  $\lambda_6$  and  $\lambda_7$ , whereas, four states are listed in oscillation modes as follows,  $\lambda_{2,3}$ ,  $\lambda_{4,5}$ ,  $\lambda_{8,9}$  and  $\lambda_{10,11}$ .

Table 6.2 Parameter of hydrokinetic system under study

Parameter	Value
<b>Hydrokinetic Turbine</b>	
Water density, $\rho$	1000 kg/m <sup>3</sup>
Radius	0.3 m
$C_{Pmax}$	0.45
$\lambda_{opt}$	2.54
Number of blades	3
<b>PMSG Parameter</b>	
$n_p$	28
$R_s$	1.74 $\Omega$
$L_s$	36.2mH
$\Psi_{pm}$	2.32 Wb



Table 6.2 Continued.

Parameter	Value
<b>Drive train parameter</b>	
$\tau_j$	5s
<b>Converter parameter</b>	
L	0.17 pu
C	0.21 pu
<b>Controller Parameter</b>	
$K_{P1}$	0.5 pu
$K_{I1}$	20/s
$K_{P2}$	1 pu
$K_{I2}$	100/s
$K_{P3}$	0.5 pu
$K_{I3}$	20/s
$K_{P4}$	0.5 pu
$K_{I4}$	20/s
$K_{P5}$	0.5 pu
$K_{I5}$	20/s

Table 6.3 State variable of Matrix A without the proposed controller

No.	Eigenvalues	Oscillation Frequency, (Hz)	Damping ratio
$\lambda_1$	-8.14	0	1
$\lambda_{2,3}$	$-53.18 \pm 37.77i$	6.01	0.815
$\lambda_{4,5}$	$-106.36 \pm 99.80i$	15.88	0.73
$\lambda_6$	-278.65	0	1
$\lambda_7$	-46.70	0	1
$\lambda_{8,9}$	$-21.40 \pm 4.74i$	0.754	0.976
$\lambda_{10,11}$	$-492.47 \pm 204.30i$	32.51	0.923

The eigenvalues placement of Matrix A is shown in Figure 6.9. It should be noted, all the eigenvalues have a negative real part. Hence proves the system is in a stable condition even after suffering small disturbance. The system consists of three evanescent modes and four oscillation modes. Nevertheless, the dynamic system performance can be improved by selecting the appropriate value for the controller's parameter to eliminate the oscillation modes in the system.

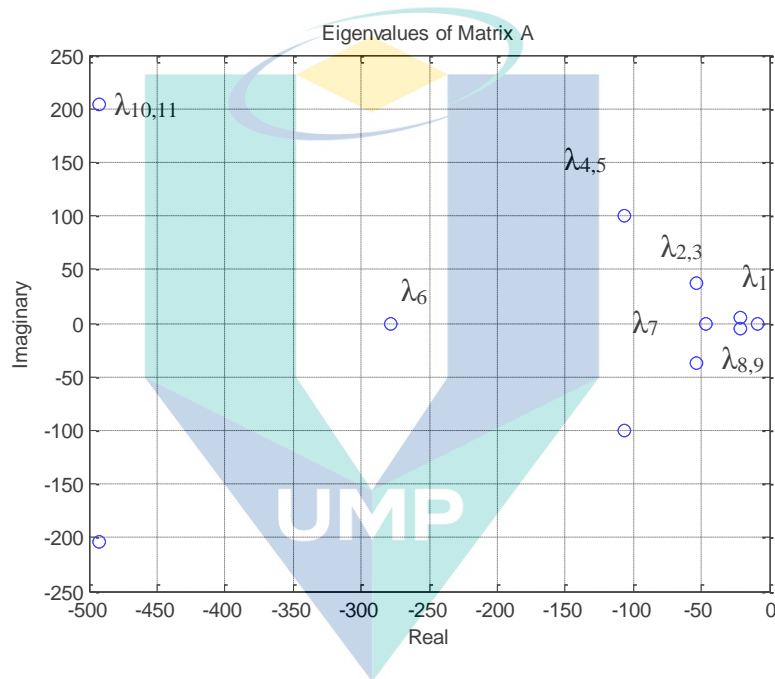


Figure 6.9 The eigenvalues placement of the Matrix A without the proposed controller

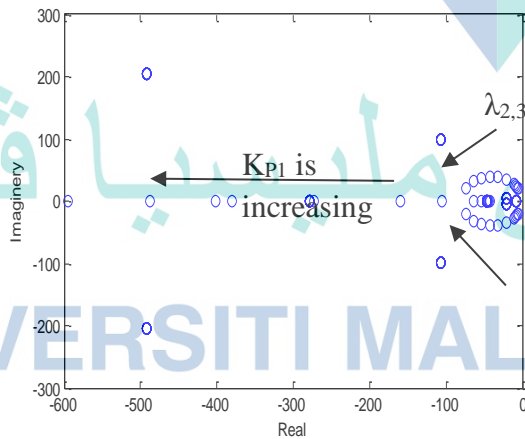
#### 6.4.2 PI Controller Gain by Eigenvalues Tracing Method

In this work, the heuristic method based on the traces of eigenvalues were used to determine the PI controller's parameter, to eliminate the oscillation modes. The controller consists of five proportional coefficient ( $K_P$ ) and integral coefficient ( $K_I$ ) respectively, which are the  $K_{P1}$  to  $K_{P5}$  and  $K_{I1}$  to  $K_{I5}$ . The gain values of  $K_P$  and  $K_I$  will be tuned to the best using the eigenvalues tracing method as the state of eigenvalues will change accordingly. Figure 6.10(a)–(j) show the traces of eigenvalues as a function of  $K_P$  and  $K_I$ .

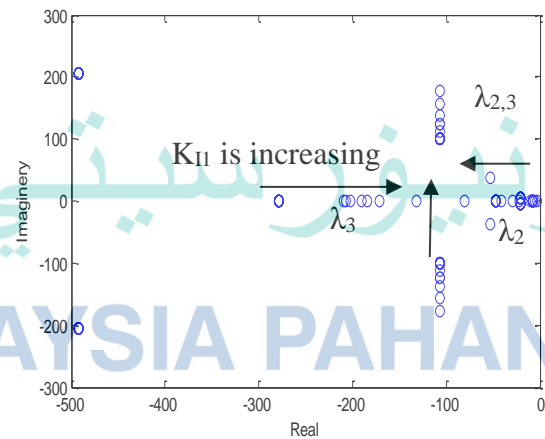
Figure 6.10 (a) and (b) show that, when the values of  $K_{P1}$  and  $K_{I1}$  are changed, the eigenvalues  $\lambda_2$  and  $\lambda_3$  are changed accordingly. It can be observed that,  $\lambda_{2,3}$  moves towards the stable region and become evanescent modes when  $K_{P1}$  is increasing. On the other hand, when the  $K_{I1}$  value is increased,  $\lambda_2$  and  $\lambda_3$  moves towards the stable and unstable region respectively and become conjugated roots with large imaginary parts as shown in Figure 6.6 (b).

As noted by Mao & Wang (2012), when the real part of eigenvalues is higher, the system's disturbance will be removed and eliminated. Conversely, the system disturbance such as the oscillation frequency will be higher when the imaginary part of eigenvalues is bigger. Consequently, this will be affected to the efficiency and dynamic system performance. Therefore, the values of  $K_P$  and  $K_I$  must be chosen to make  $\lambda_{2,3}$  conjugated roots with a large real part and small imaginary part.

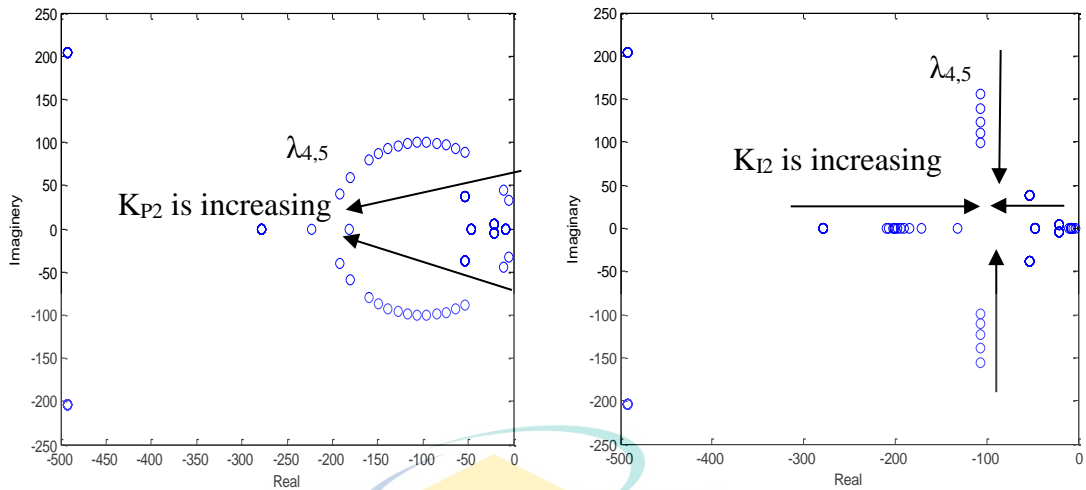
Figure 6.10 (c) and (d) show the effect on the traces of eigenvalues when the  $K_{P2}$  and  $K_{I2}$  are changed. It can be observed that, only  $\lambda_4$  and  $\lambda_5$  are changes and the trend are similar to the  $\lambda_{2,3}$  as shown in Figure 6.10 (a) and (b). Therefore, the best selection for the  $K_{P2}$  and  $K_{I2}$  must be eigenvalues with the large real part and small imaginary part respectively.



(a)  $0.05 \leq K_{P1} \leq 3$  at  $T = 0.025$



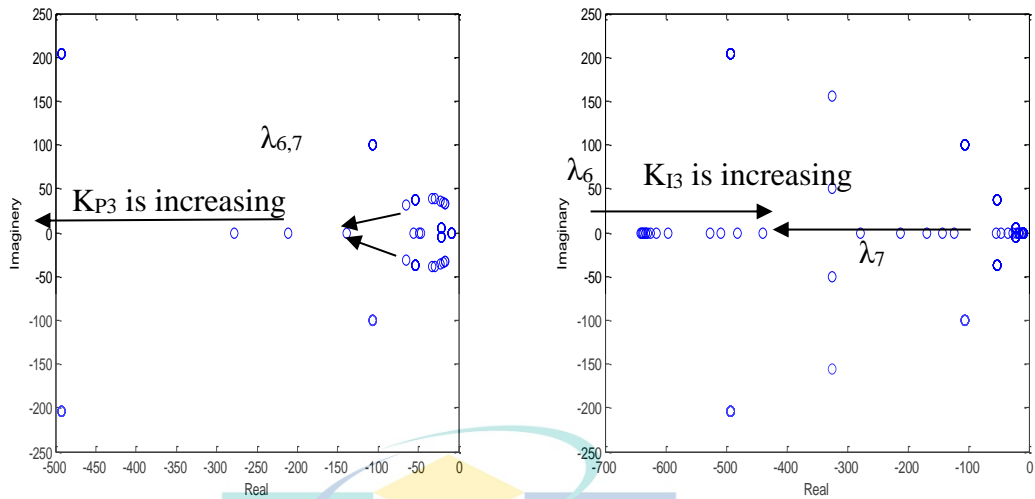
(b)  $3.33 \leq K_{I1} \leq 200$  at  $K_{P1} = 1$



(c)  $0.05 \leq K_{P2} \leq 3$  at  $T = 0.025$

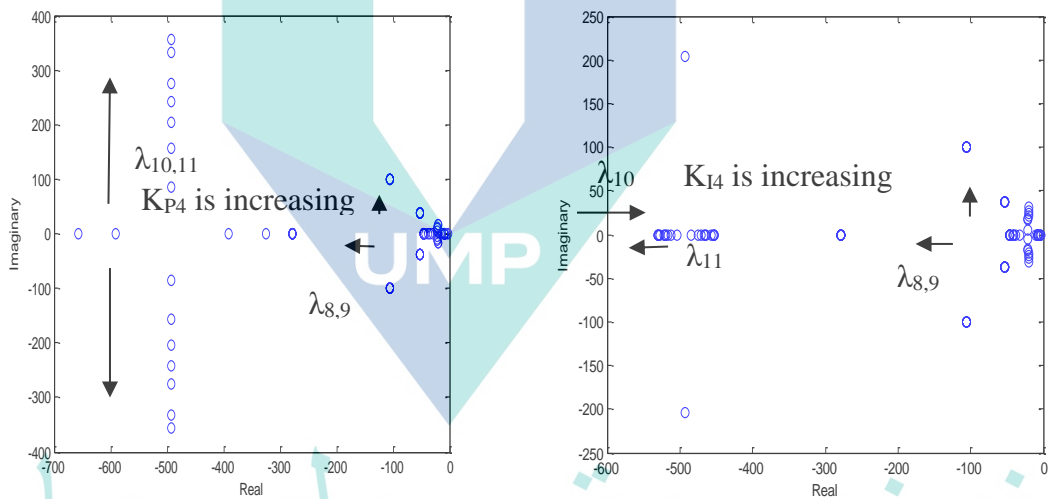
(d)  $3.33 \leq K_{I2} \leq 200$  at  $K_{P2} = 1$

Figure 6.10 (e) and (f) show the traces of eigenvalues as a function of  $K_{P3}$  and  $K_{I3}$ . In this case, the  $\lambda_6$  and  $\lambda_7$  are changing accordingly. It can be observed that, the traces of eigenvalues  $\lambda_{6,7}$  moves toward the stable region and become evanescent modes when  $K_{P3}$  is increases. On the other hand, when the  $K_{I3}$  is increased,  $\lambda_6$  and  $\lambda_7$  become a conjugated roots with a large imaginaryy part respectively. Conversely, if the  $K_{I3}$  is decreased,  $\lambda_6$  become evenescent mode and moves toward the stable region. Whereas  $\lambda_7$  moves toward to unstable region. Therefore, the value of  $K_{P3}$  and  $K_{I3}$  must be chosen in the middle of traces to make  $\lambda_{6,7}$  conjugated roots with large real parts and small imaginary parts.



(e)  $0.05 \leq K_{P3} \leq 3$  at  $T = 0.025$

(f)  $03.33 \leq K_{I3} \leq 200$  at  $K_{P3} = 1$



(g)  $0.1 \leq K_{P4} \leq 1.5$  at  $T = 0.025$

(h)  $0.83 \leq K_{I4} \leq 50$  at  $K_{P4} = 0.25$

Figure 6.10 (g) and (h) show the traces of eigenvalues when  $K_{P4}$  and  $K_{I4}$  are changed. In this case, four state consists of  $\lambda_{8,9}$  and  $\lambda_{10,11}$  are change accordingly. It is observed that, when  $K_{P4}$  is increased, the  $\lambda_{10,11}$  and  $\lambda_{8,9}$  value become a conjugated roots with large imaginary parts respectively. This will increase the oscillation and fluctuation on the output voltage and current at the grid side converter. On the other hand, when the  $K_{I4}$  value is increased,  $\lambda_{10}$  and  $\lambda_{11}$  are maintained as evanescent modes and moves along in a

stable region. Nevertheless, the traces of  $\lambda_8$  and  $\lambda_9$  are changed from the evanescent modes to conjugated roots respectively when the  $K_{I4}$  is increased as shown in Figure 6.10 (h).

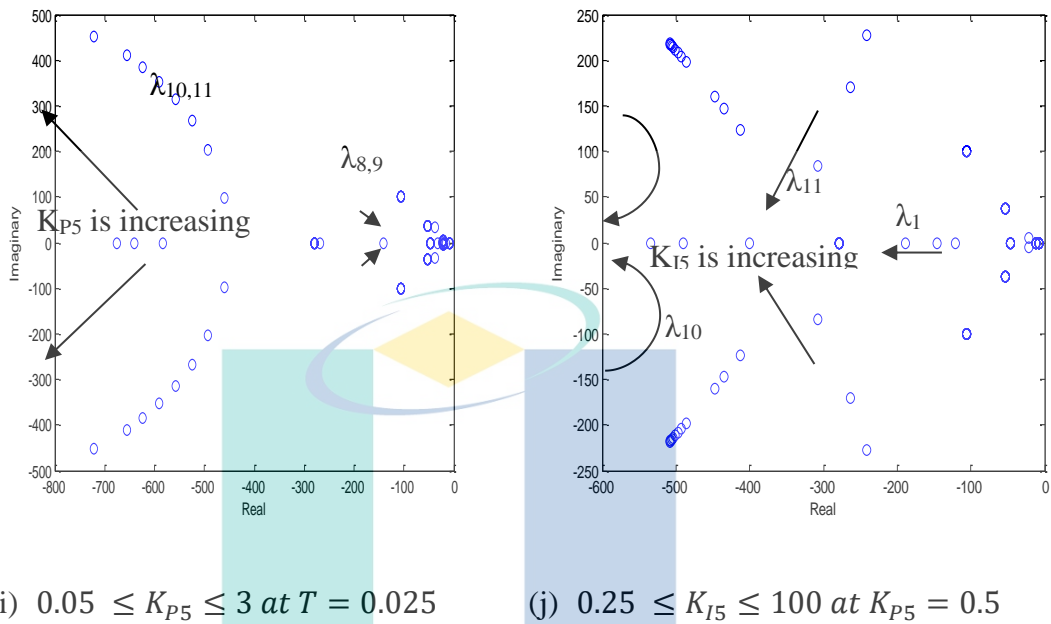


Figure 6.10 The traces of the eigenvalues as a function of  $K_P$  and  $K_I$ .

Figure 6.10 (i) shows the traces of eigenvalues of the  $\lambda_{8,9,10,11}$  states when  $K_{P5}$  is changed. It can be observed that, when  $K_{P5}$  is increased, the  $\lambda_{8,9}$  are conjugates roots and moves toward unstable region. Whereas,  $\lambda_{10,11}$  is varies to a conjugated roots with higher imaginary parts. On the other hand, when  $K_{I5}$  is increased,  $\lambda_{10}$  and  $\lambda_{11}$  varies from high imaginary conjugated roots to evanescent modes and maintain in a stable region. Conversely,  $\lambda_1$  varies from evanescent modes to conjugated roots at the unstable region. Therefore, the values of  $K_{P5}$  and  $K_{I5}$  must be chosen between the middle of Figure 6.10 (i) and (j), respectively to reduce the oscillation at the grid current and DC-Link voltage.

A set of reasonable values of  $K_P$  and  $K_I$  was chosen based on the traces of eigenvalues analysis. Table 6.4 shows that, the value of the controller's parameter ( $K_P$  and  $K_I$ ) play significant roles in determining the dynamic performance of the hydrokinetic system. On the other hand, Table 6.5 shows the improvement of states after the analysis of eigenvalues. It can be observed that, there are seven evanescent modes and two

conjugated roots. The oscillation frequency reduced significantly from 6.01 Hz to 3.57 Hz and from 15.88 Hz to 6.06 Hz for  $\lambda_{2,3}$  and  $\lambda_{4,5}$  respectively. In addition, the oscillation frequency has been eliminated for  $\lambda_{8,9,10,11}$  with the large real parts at the stable region. The spectrum of improvement of eigenvalues for Matrix A is shown in Figure 6.11.

Table 6.4 The values of the controller parameter

Controller Parameter	Value
$K_{P1}$	1
$K_{I1}$	55.55
$K_{P2}$	1
$K_{I2}$	60
$K_{P3}$	1
$K_{I3}$	111.11
$K_{P4}$	0.25
$K_{I4}$	10
$K_{P5}$	0.5
$K_{I5}$	25

Through the analysis of the eigenvalues, the stability of Matrix A improves up to 63.63 % by eliminating the imaginary part of the eigenvalues. The elimination of disturbances at the state  $\lambda_{8,9,10,11}$  gives a high impact on the efficiency and stability of the system. This is due to the real parts are larger, and the poles are maintained at the stable region. The state  $\lambda_{8,9,10,11}$  are represented the intermediate state variable ( $x_5$ ),  $i_{Dg}$ ,  $i_{Qg}$  and  $V_{dc}$  respectively. On the other hand, the state  $\lambda_{2,3}$  have represented the  $I_{ds}$  and  $I_{qs}$ , respectively. The controller can reduce the disturbances up to 40.1 % by decreasing the oscillation frequency. The small-signal stability analysis proves that the proper gain for  $K_P$  and  $K_I$  can be chosen based on the traces of eigenvalues; hence, the PI controller is sufficient to control at the RSC and GSC, respectively. Other researchers commonly use this method in designing the PI controller's gain especially in WECS (Mao & Wang,



2012; Wu, Zhang, Godfrey, & Ju, 2007; Wu et al., 2009) and also in tidal current turbine (Aly & El-Hawary, 2011; Li, Hu, Hu, & Chen, 2018).

Table 6.5 Eigenvalues of State Matrix A with the proposed controller

No.	Eigenvalues	Oscillation Frequency (Hz)	Damping
$\lambda_1$	-8.14	0	1
$\lambda_{2,3}$	$-106.36 \pm 22.44i$	3.57	0.978
$\lambda_{4,5}$	$-106.36 \pm 38.08i$	6.06	0.941
$\lambda_6$	-508.53	0	1
$\lambda_7$	-142.17	0	1
$\lambda_8$	-7.40	0	1
$\lambda_9$	-49.79	0	1
$\lambda_{10}$	-547.66	0	1
$\lambda_{11}$	-492.47	0	1

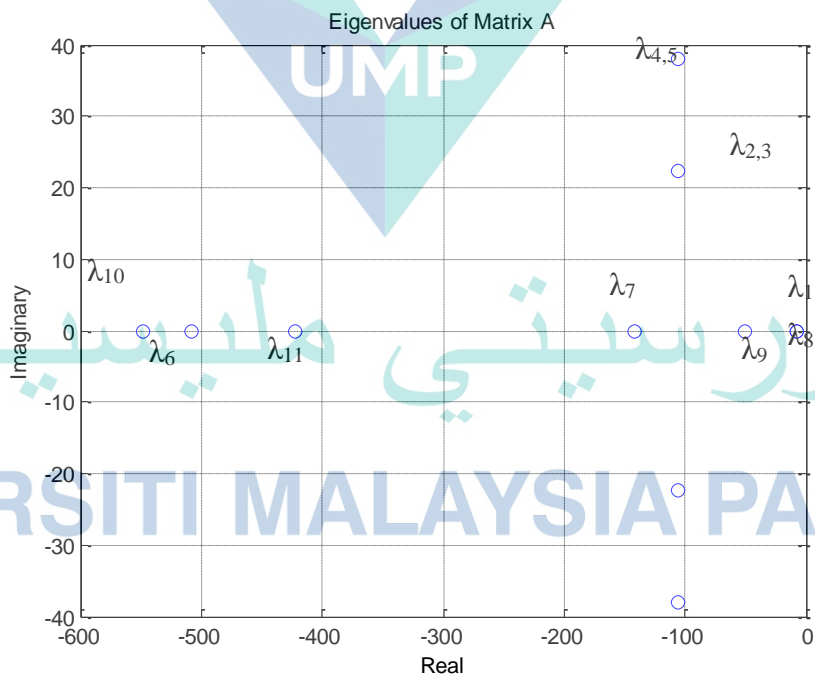
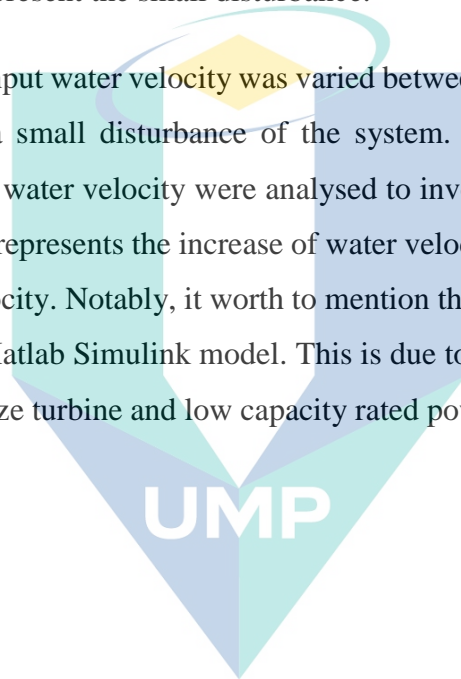


Figure 6.11 The eigenvalues placement of Matrix A with the proposed controller

### 6.4.3 Matlab Simulink Simulation Model

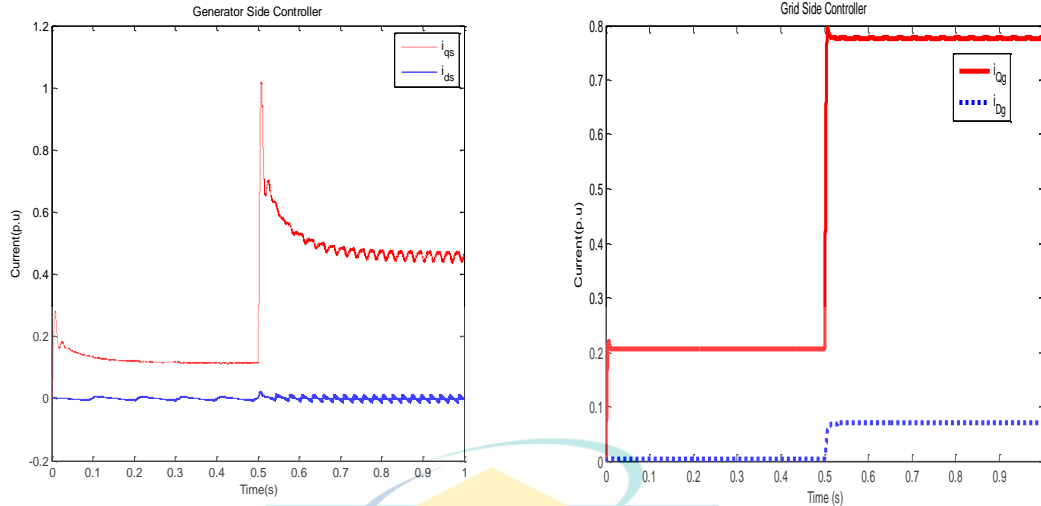
The hydrokinetic system with back-to-back converter has been developed by Matlab/Simulink to validate the small-signal analysis model. The complete Matlab/Simulink diagram can be referred in the Appendix D. As noted by Mao & Wang (2012), an instant variation of wind speed in short of time (i.e. one second) was chosen to represent the small disturbances in their analysis. Other similar work by Wu et al. (2009) was applied three-phase ground fault with clearance within 0.05 s at the transmission line terminal voltage to represent the small disturbance.

In this work, the input water velocity was varied between  $0.5 \text{ ms}^{-1}$  and  $1.2 \text{ ms}^{-1}$  in one second to represent a small disturbance of the system. Two case studies during the increase and decrease water velocity were analysed to investigate the dynamic response of the system. Case 1 represents the increase of water velocity, and Case 2 represents the decrease of water velocity. Notably, it worth to mention the turbine and generator inertia are neglected in the Matlab Simulink model. This is due to the turbine and generator are considered as small size turbine and low capacity rated power, respectively.



اونيورسيتي مليسيا قهغ

UNIVERSITI MALAYSIA PAHANG



(a) Direct current ( $I_{ds}$ ) and Quadrature Current ( $I_{qs}$ ) of the generator at the RSC

(b) Direct current ( $I_{Dg}$ ) and Quadrature Current ( $I_{Qg}$ ) at the GSC

Figure 6.12 The dynamic response of the direct and quadrature current at the RSC and GSC respectively during Case 1.

Figure 6.12 (a) and (b) show the dynamic response of the system during Case 1, whereas the water velocity was increased from  $0.5 \text{ ms}^{-1}$  to  $1.2 \text{ ms}^{-1}$ . It is observed that, the system experienced a small disturbance at the generator's stator current. Based on the RSC design in Section 6.4.1, the  $I_{ds}$  value was set to zero, whereas  $I_{qs}$  was used to control the generator for the maximum energy extraction. In the small-signal stability analysis, the state  $\lambda_{2,3}$  represented  $I_{ds}$  and  $I_{qs}$ , respectively. As can be seen in Table 6.5, the oscillation frequency or disturbances occur on state  $\lambda_{2,3}$ . It can be observed that, the oscillation occurs at  $I_{ds}$  and  $I_{qs}$  as shown in Figure 6.12 (a).  $I_{ds}$  was approached to be zero with small oscillations during the disturbance. Meanwhile,  $I_{qs}$  was used to control the generator speed when the water velocity is increased. As can be seen, the oscillation occurs and  $I_{qs}$  increases from 0.2 p.u to 0.5 p.u due to the disturbance.

On the other hand, at the GSC,  $I_{Dg}$  was set to be zero, whereas  $I_{Qg}$  was used to stabilise the DC-link system and active power at the grid side. Based on the small-signal analysis, the oscillation frequency at the state  $\lambda_{9,10}$ , was eliminated, as shown in Table 6.4. This state represents  $I_{Dg}$  and  $I_{Qg}$ , respectively. Besides, the Simulink model proves that the

graph is smooth without the oscillation, as shown in Figure 6.12 (b). Nevertheless, the  $I_{Qg}$  was controlled to maintain the output power at the grid with 0.21 p.u up to 0.78 p.u during increased of water velocity.

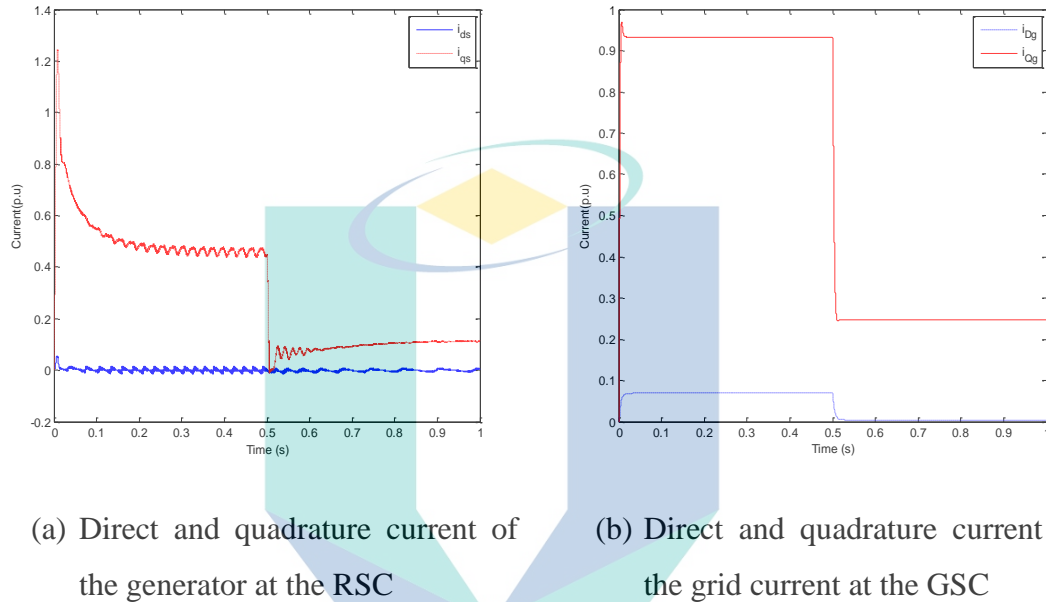


Figure 6.13 The dynamic response of the direct and quadrature current at the RSC and GSC respectively during the Case 2.

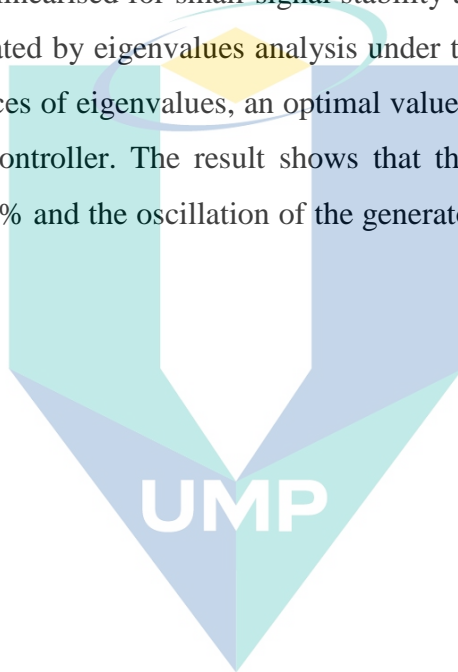
Conversely, Case 2 represents the water velocity decrease from  $1.2 \text{ ms}^{-1}$  to  $0.5 \text{ ms}^{-1}$  in one second. The dynamic response of the stator current and grid current during Case 2 is shown in Figure 6.13 (a) and (b), respectively. The trend of  $I_{ds}$ ,  $I_{qs}$ ,  $I_{Dg}$  and  $I_{Qg}$  are similar to Case 1. Nevertheless, both the output current either at the RSC and GSC are contradicted to Case 1.

The simulation results indicated that the oscillation frequency occurs in the generator stator current but eliminates at the grid site converter. Consequently, this result is in agreement with the result obtained from the small-signal analysis. Therefore, the validation of the small-signal model and analysis can be verified accurately. Other similar

work regarding the comparison between small-signal analysis and Simulink model has also been discussed by (Chouket & Krichen, 2015; Rahimi, 2017).

## 6.5 Summary

In this chapter, the modelling of the hydrokinetic for grid-connected energy harnessing system are presented. First, the complete model of the hydrokinetic system has been derived and linearised for small-signal stability analysis. Then, the stability of the system was evaluated by eigenvalues analysis under the small disturbance of water velocity. By using traces of eigenvalues, an optimal value of  $K_P$  and  $K_I$  was determined in designing the PI controller. The result shows that the stability of the system has increased up to 63.63 % and the oscillation of the generator stator current is reduced up to 40.1 % at the RSC.



اونيورسيتي ملايسيا قهغ

UNIVERSITI MALAYSIA PAHANG

## CHAPTER 7

### CONCLUSION

#### 7.1 Chapter Overview

This chapter presents the conclusion of the hydrokinetic research and recommendation for the future work.

#### 7.2 Concluding Remarks

Based on the research, it is worth to mention that this work presented the design consideration and modelling of generalised power equation for the hydrokinetic turbine based on the Malaysia river's characteristics. Three types of vertical axis turbines consist of H-Darrieus, Darrieus, and Gorlov, with twelve different hydrofoils blades profiles, which were designed and simulated using QBlade and Matlab software. Since hydrokinetic energy harnessing is a new field of research in Malaysia, there is no specific information in which turbines are most practical and suitable to be implemented that match the river's characteristics in Malaysia. Therefore the simulation studies were conducted to analyse the effect of symmetrical and non-symmetrical hydrofoils, thickness, and solidity on the hydrokinetic turbine. Based on the analysis, the turbine with the higher power coefficient ( $C_P$ ) and torque coefficient ( $C_M$ ) was chosen as the best option for the energy extraction in water. The findings showed that the vertical axis H-Darrieus turbine with NACA 0018 hydrofoil profile is one of the best turbines that match the river characteristics in Malaysia. Subsequently, the generalised turbine model was proposed based on the H-Darrieus turbine characteristic curve.

Besides this work presented the control strategy for off-grid connected using the maximum power point tracking (MPPT) algorithm. The MPPT algorithm provided the maximum energy extraction under fluctuation of water velocity. The establish circuit

topologies for the MPPT control is based on the uncontrolled rectifier and boost converter circuit. Since the MPPT in hydrokinetic technology is scarcely mentioned in the literature, the presented MPPT algorithm is inspired by the wind energy conversion system. In this work, the proposed MPPT algorithm is the combination of the Fuzzy Logic Controller (FLC) and Hill-Climbing Search (HCS) Algorithm. The HCS algorithm is based on a heuristic optimisation strategy by locating the local maximum point of the function given. The FLC will determine the suitable step-size according to the changes in water velocity with respect to the operating point position. The findings indicated that, the proposed MPPT algorithm offered high tracking accuracy, fast-tracking response, and reduce the steady-state oscillation near the maximum power point.

Last but not least, this work presented the modelling of the hydrokinetic energy harnessing connected to the grid-network. A completed system consists of dynamic model of the H-Darrieus turbine, PMSG, drive train, back-to-back converter and grid model were linearised at equilibrium operating point or around steady state values. Subsequently, the system stability or small-signal stability analysis (SSSA) can be assessed through eigenvalues analysis method. In this work, the PI control strategy was applied to field oriented control and voltage source control at rotor side controller (RSC) and grid side controller (GSC) respectively. The proportional and integral gain of PI controller were tuned using the eigenvalues tracing method to solve the oscillation at generator stator current and grid current due to disturbance. The findings indicated the stability of the hydrokinetic system was improved under the small disturbance and reduced the oscillation frequency at the stator and grid current, respectively.

### 7.3 Recommendation for the Future Work

1. The current study was used the QBlade software to analyse the blade element momentum (BEM) and double multiple stream tube (DMS), respectively, for exploration of the pressure distribution on the turbine blades. Although the QBlade software is sufficient to analyse the design of the blades, nevertheless, the computational fluid dynamic (CFD) by Ansys is preferable in fluid dynamic analysis to analyse the turbine



performance. This is due to the pressure distribution on the turbine blades that can be visualised nicely.

2. The current work focused on the control strategies of the MPPT algorithm for an off-grid system. Since the MPPT algorithm is scarce for the stand-alone hydrokinetic energy harnessing, the MPPT algorithm was inspired by WECS and solar PV. Nevertheless, the MPPT of WECS is preferable due to the concept and hardware similarity in the hydrokinetic system. Notably, for the small-scale system, the circuit topology is based on an uncontrolled rectifier with the boost converter as a control circuit. Besides, the turbine and generator inertia were also neglected in these simulation studies. Therefore it is recommended to apply the circuit topology based on active rectifier control for better MPPT energy extraction.

3. The current work is focused on modelling of direct drive permanent magnet synchronous generator (PMSG). This type of topology is suitable for small-scale energy harnessing. Applying a different generator or implementation of drive train with the gearbox for large output capacity is recommended. Additionally, improving control strategies, such as a robust control and adaptive control for the RSC and GSC, are recommended to improve the dynamic performance of the hydrokinetic system.

اونيورسيتي مليسيا قهغ

UNIVERSITI MALAYSIA PAHANG

## REFERENCES

- Aashoor, F. A. O. (2015). *Maximum Power Point Tracking Techniques for Solar Water Pumping Systems. PhD Thesis*. University of Bath.
- Abazari, A., Dozein, M. G., & Monsef, H. (2018). An optimal Fuzzy-logic based frequency control strategy in a high wind penetrated power system. *Journal of the Franklin Institute*, 355(14), 6262–6285. <https://doi.org/10.1016/j.jfranklin.2018.06.012>
- Abdul, M., Shafei, R., Ibrahim, D. K., & El-Zahab, E. E. A. (2014). Biogeography-Based Optimization Technique for Maximum Power Tracking of Hydrokinetic Turbines. In *3rd International Conference on Renewable Energy Research and Applications (ICRERA 2014)* (pp. 789–794). Milwaukee, USA.
- Abdullah, M. A., Yatim, A. H. M., Tan, C. W., & Saidur, R. (2012). A review of maximum power point tracking algorithms for wind energy systems. *Renewable and Sustainable Energy Reviews*, 16(5), 3220–3227.
- Abdullah, Majid A, Yatim, A. H. M., & Chee Wei Tan. (2011). A Study of Maximum Power Point Tracking Algorithms for Wind Energy System. In *2011 IEEE Conference on Clean Energy and Technology (CET 2011)* (pp. 321–326). Kuala Lumpur, Malaysia.
- Ahmed, E. M., Shoyam, M., & Dousoky, G. M. (2012). On the Behaviour of Marine and Tidal Current Converters with DC-DC Boost Converter. In *2012 IEEE 7th International Power Electronics and Motion Control Conference-ECCE Asia* (Vol. 3, pp. 2250–2254). Harbin, China.
- Ali, Z., Christofides, N., Hadjidemetriou, L., Kyriakides, E., Yang, Y., & Blaabjerg, F. (2018). Three-phase phase-locked loop synchronization algorithms for grid-connected renewable energy systems: A review. *Renewable and Sustainable Energy Reviews*, 90(2018), 434–452.
- Alvarez Alvarez, E., Rico-Secades, M., Corominas, E. L., Huerta-Medina, N., & Soler Guitart, J. (2018). Design and control strategies for a modular hydroKinetic smart grid. *International Journal of Electrical Power and Energy Systems*, 95, 137–145.
- Aly, H. H. H., & El-Hawary, M. E. (2011). Small signal Stability Analysis of Tidal Current Turbine using DDPMSG with and without Controller. In *2011 IEEE Electrical Power and Energy Conference (EPEC 2011)* (pp. 239–243). Winnipeg, Canada.
- Anderson, A., & Rezaie, B. (2019). Geothermal technology: Trends and potential role in a sustainable future. *Applied Energy*, 248(2019), 18–34.

- Aner, M. (2014). *Improved MPPT Dynamics for Starting and Power Extraction of a Small Wind Turbine Employing a PMSG and a VSMC*. PhD Thesis. University of Calgary, Alberta.
- Ani, S. O., Polinder, H., & Ferreira, J. A. (2013). Comparison of Energy Yield of Small Wind Turbines in Low Wind Speed Areas. *IEEE Transactions on Sustainable Energy*, 4(1), 42–49.
- Anyi, M., & Kirke, B. (2010). Evaluation of small axial flow hydrokinetic turbines for remote communities. *Energy for Sustainable Development*, 14(2), 110–116.
- Anyi, M., & Kirke, B. (2011). Hydrokinetic turbine blades: Design and local construction techniques for remote communities. *Energy for Sustainable Development*, 15(3), 223–230.
- Arani, M. F. M., & Mohamed, Y. A. R. I. (2015). Analysis and Impacts of Implementing Droop Control in DFIG-Based Wind Turbines on Microgrid/Weak-Grid Stability. *IEEE Transactions on Power Systems*, 30(1), 385–396.
- Arkel, R. Van, Owen, L., Allison, S., Tryfonas, T., Winter, A., Entwistle, R., ... Parr, J. (2011). Design and preliminary testing of a novel concept low depth hydropower device. In *2011 IEEE OCEANS* (Vol. 5, pp. 1–10). Santander, Spain.
- Ashourianjozdani, M. H., Lopes, L. A. C., & Pillay, P. (2017). Power Control Strategy For Fixed-Pitch PMSG-Based Hydrokinetic Turbine. In *IEEE International Conference on Power Electronics, Drives and Energy Systems, (PEDES 2016)* (pp. 1–6). Trivandrum, India.
- Assareh, E., & Biglari, M. (2015). A novel approach to capture the maximum power from variable speed wind turbines using PI controller, RBF neural network and GSA evolutionary algorithm. *Renewable and Sustainable Energy Reviews*, 51, 1023–1037.
- Atlantis Resources Corporation. (2019). Retrieved July 18, 2019, from <http://www.emec.org.uk/about-us/our-tidal-clients/atlantis-resources-corporation-2/>
- Bachant, P., & Wosnik, M. (2015). Performance measurements of cylindrical- and spherical-helical cross-flow marine hydrokinetic turbines, with estimates of exergy efficiency. *Renewable Energy*, 74, 318–325.
- Bahaj, A. S., & Myers, L. E. (2003). Fundamentals applicable to the utilisation of marine current turbines for energy production. *Renewable Energy*, 28(14), 2205–2211.
- Barber, D. (2018). The Four Forces That Influence Wind Speed & Wind Direction. Retrieved August 3, 2019, from <https://sciencing.com/hadley-cell-effects-8550966.html>

- Baroudi, J. A., Dinavahi, V., & Knight, A. M. (2007). A review of power converter topologies for wind generators. *Renewable Energy*, 32(14), 2369–2385.
- Baruah, D. C., & Enweremadu, C. C. (2019). Prospects of decentralized renewable energy to improve energy access: A resource-inventory-based analysis of South Africa. *Renewable and Sustainable Energy Reviews*, 103(3), 328–341.
- Beddar, A., Bouzekri, H., Babes, B., & Afghoul, H. (2016). Experimental enhancement of fuzzy fractional order PI+I controller of grid connected variable speed wind energy conversion system. *Energy Conversion and Management*, 123, 569–580. <https://doi.org/10.1016/j.enconman.2016.06.070>
- Behrouzi, F., Nakisa, M., Maimun, A., & Ahmed, Y. M. (2016). Global renewable energy and its potential in Malaysia: A review of Hydrokinetic turbine technology. *Renewable and Sustainable Energy Reviews*, 62, 1270–1281.
- Belhadji, L., Bacha, S., Munteanu, I., Rumeau, A., & Roye, D. (2013). Adaptive MPPT Applied to Variable-Speed Microhydropower Plant. *IEEE Transactions on Energy Conversion*, 28(1), 34–43.
- Belhassan, K. (2011). Relationship between River Flow , Rainfall and Groundwater pumpage in Mikkes Basin, Morocco. *Iranian Journal of Earth Sciences*, 3(2011), 98–107.
- Belmokhtar, K., Doumbia, M. L., & Agbossou, K. (2014). Novel fuzzy logic based sensorless maximum power point tracking strategy for wind turbine systems driven DFIG (doubly-fed induction generator). *Energy*, 76, 679–693. <https://doi.org/10.1016/j.energy.2014.08.066>
- Bevrani, H., & Daneshmand, P. R. (2012). Fuzzy Logic-Based Load-Frequency Control Concerning High Penetration of Wind Turbines. *IEEE Systems Journal*, 6(1), 173–180.
- Bevrani, Hassan, & Daneshmand, P. R. (2012). Fuzzy logic-based load-frequency control concerning high penetration of wind turbines. *IEEE Systems Journal*, 6(1), 173–180. <https://doi.org/10.1109/JSYST.2011.2163028>
- Bianchi, F. D., Battista, H. De, & Mantz, R. J. (2007). *Wind Turbine Control Systems-Principles, Modelling and Gain Scheduling Design*. Argentina: Springer-Verlag London Limited.
- Birjandi, A. H., Woods, J., & Bibeau, E. L. (2012). Investigation of macro-turbulent flow structures interaction with a vertical hydrokinetic river turbine. *Renewable Energy*, 48, 183–192.
- Borhanazad, H., Mekhilef, S., Saidur, R., & Boroumandjazi, G. (2013). Potential application of renewable energy for rural electrification in Malaysia. *Renewable Energy*, 59, 210–219.

- Bracke, X. (2014). *Maximum Power Point Tracking of Small Wind Turbines with a Full Active Rectifier. Master Thesis*. Universiteit Gent.
- Camera, F. La. (2019). People , Planet and Prosperity. Raising Climate Ambitions Through Renewables. Retrieved August 20, 2019, from <https://www.irena.org/publications/2019/Jul/People-Planet-and-Prosperity>
- Canadian Hydraulics Centre (National Research Council of Canada). (2010). Assessment of Canada's Hydrokinetic Power Potential (Phase I Report, Methodology and Data Review).
- Cavagnaro, R. J. (2016). *Performance Evaluation , Emulation , and Control of Cross-Flow Hydrokinetic Turbines. PhD Thesis*. University of Washington.
- Chabane, Y., & Hellal, A. (2013). Critical eigenvalues tracing for small signal stability analysis using Krylov subspaces. In *2013 3rd International Conference on Systems and Control, ICSC 2013* (pp. 303–307). IEEE. <https://doi.org/10.1109/ICoSC.2013.6750875>
- Chen, B., Su, S., Viola, I. M., & Greated, C. A. (2018). Numerical investigation of vertical-axis tidal turbines with sinusoidal pitching blades. *Ocean Engineering*, *155*(1), 75–87.
- Chen, H., Chen, X., & Xie, W. (2018). Fractional-Order PI Controller for DFIG-Based Marine Tidal Current Applications. In *Proceedings - 2018 IEEE International Power Electronics and Application Conference and Exposition, (PEAC 2018)* (pp. 1–6). Shenzhen, China.
- Chen, H., Tang, T., Ait-Ahmed, N., Benbouzid, M. E. H., MacHmoum, M., & Zaim, M. E. H. (2018). Attraction, Challenge and Current Status of Marine Current Energy. *IEEE Access*, *6*, 12665–12685.
- Chen, J., Lin, T., Wen, C., & Song, Y. (2016). Design of a Unified Power Controller for Variable-Speed Fixed-Pitch Wind Energy Conversion System. *IEEE Transactions on Industrial Electronics*, *63*(8), 4899–4908. <https://doi.org/10.1109/TIE.2016.2547365>
- Chen, Z., Chi, S., Li, M., & Wang, J. (2015). Design and Implementation of The Pitch Control System for Horizontal Axis Tidal turbines. In *Proceedings of the 2015 IEEE 27th Chinese Control and Decision Conference, CCDC 2015* (pp. 4078–4082). Qindao, China.
- Chong, H. Y., & Lam, W. H. (2013). Ocean renewable energy in Malaysia: The potential of the Straits of Malacca. *Renewable and Sustainable Energy Reviews*, *23*, 169–178.
- Chouket, M., & Krichen, L. (2015). Small Signal Modeling and Stability Analysis of Wind Turbine with PMSG Connected to The Grid. In *2015 IEEE 12th International Multi-Conference on Systems, Signals and Devices* (Vol. 2, pp. 1–8). Sfax, Tunisia.



- Chowdhury, M. M. (2014). *Modelling and Control of Direct Drive Variable Speed Wind Turbine with Interior Permanent Magnet Synchronous Generator*. PhD Thesis. University of Tasmania.
- Comello, S., Reichelstein, S., & Sahoo, A. (2018). The road ahead for solar PV power. *Renewable and Sustainable Energy Reviews*, 92(5), 744–756.
- D. Phil Turnipseed, & Sauer, V. B. (2010). *Discharge Measurements at Gaging Stations*. U.S Geological Survey. Virginia.
- Daili, Y., Gaubert, J. P., & Rahmani, L. (2015). Implementation of a new maximum power point tracking control strategy for small wind energy conversion systems without mechanical sensors. *Energy Conversion and Management*, 97, 298–306. <https://doi.org/10.1016/j.enconman.2015.03.062>
- Dalala, Z. M., Zahid, Z. U., Yu, W., Cho, Y., & Lai, J. S. (2013). Design and analysis of an MPPT technique for small-scale wind energy conversion systems. *IEEE Transactions on Energy Conversion*, 28(3), 756–767.
- Daniel Zammit, Cyril Spiteri Staines, Alexander Micallef, Maurice Apap, J. L. (2017). Incremental Current Based MPPT for a PMSG Micro Wind Turbine in a Grid-Connected DC Microgrid. In *9th International Conference on Applied Energy, ICAE2017* (Vol. 142, pp. 2284–2294). Cardiff, UK.
- Davis, B. . (1989). Vertical Axis Hydro Turbines for Off Grid Installations. In *International Conference on Hydropower Niagara Falls, New York, United States*.
- De Freitas, T. R. S., Menegáz, P. J. M., & Simonetti, D. S. L. (2016). Rectifier topologies for permanent magnet synchronous generator on wind energy conversion systems: A review. *Renewable and Sustainable Energy Reviews*, 54, 1334–1344.
- Domenech, J., Eveleigh, T., & Tanju, B. (2018). Marine Hydrokinetic (MHK) systems: Using systems thinking in resource characterization and estimating costs for the practical harvest of electricity from tidal currents. *Renewable and Sustainable Energy Reviews*, 81, 723–730.
- Donald, R. Mac, ELS, R. H. van, & Brasil Junior, A. C. (2017). Maximum Power Point Tracking strategy for energy conversion in a hydrokinetic turbine. In *12th Conference on Sustainable Development Energy Water and Environmental System (SDEWES 2017)* (pp. 1–14). Dubrovnik, Croatia.
- Eddine, Seif Elghali, B., El, Mohamed Benbouzid, H., Ahmed-ali, T., & Charpentier, J. F. (2010). High-Order Sliding Mode Control of a Marine Current Turbine Driven Doubly-Fed Induction Generator. *IEEE Journal of Oceanic Engineering*, 35(2), 402–411.
- EIA. (2018). *Annual Energy Outlook 2018 with projections to 2050*. U.S Energy Information Administration (Vol. Feb).

- Elbatran, A. H., Yaakob, O. B., Ahmed, Y. M., & Jalal, M. R. (2015). Novel approach of bidirectional diffuser-augmented channels system for enhancing hydrokinetic power generation in channels. *Renewable Energy*, *83*, 809–819.
- Elliott, D. (2013). *Renewables: A Review of Sustainable Energy Supply Options*. IOP Publishing, Bristol, UK.
- Els, R. H. Van, & Junior, A. C. P. B. (2015). The Brazilian Experience with Hydrokinetic Turbines. In *The 7th International Conference on Applied Energy – ICAE2015* (Vol. 75, pp. 259–264). Abu Dhabi, UAE: Energy Procedia.
- Eltamaly, A. M., & Farh, H. M. (2013). Maximum power extraction from wind energy system based on fuzzy logic control. *Electric Power Systems Research*, *97*, 144–150.
- Energy, B. (2018). BP Energy Outlook: 2018 Edition. Retrieved July 18, 2019, from <https://www.bp.com/content/dam/bp/en/corporate/pdf/energy-economics/energy-outlook/bp-energy-outlook-2018.pdf>
- Erdiwansyah, Mahidin, Mamat, R., Sani, M. S. M., Khoerunnisa, F., & Kadarohman, A. (2019). Target and demand for renewable energy across 10 ASEAN countries by 2040. *The Electricity Journal*, *32*(10), 1–12.
- Exxon Mobil. (2018). *2018 Outlook for Energy: A view to 2040*. Retrieved from <https://cdn.exxonmobil.com/~media/global/files/outlook-for-energy/2018/2018-outlook-for-energy.pdf>
- Foo, K. Y. (2015). A vision on the opportunities, policies and coping strategies for the energy security and green energy development in Malaysia. *Renewable and Sustainable Energy Reviews*, *51*, 1477–1498.
- Forbush, D., Cavagnaro, R. J., Donegan, J., McEntee, J., & Polagye, B. (2017). International Journal of Marine Energy Multi-mode evaluation of power-maximizing cross-flow turbine controllers. *International Journal of Marine Energy*. <https://doi.org/10.1016/j.ijome.2017.09.001>
- Forbush, D., Cavagnaro, R. J., Donegan, J., McEntee, J., & Polagye, B. (2017). Multi-mode evaluation of power-maximizing cross-flow turbine controllers. *International Journal of Marine Energy*, *20*, 80–96.
- Fraenkel, P. (2004). Marine Current Turbines: An Emerging Technology. In *Paper for Scottish Hydraulics Study Group Seminar in Glasgow on 19 March 2004 Renewable Energy – Hydraulic Applications – Theory and Practice* (pp. 1–10).
- Frick, W. F., Baerwald, E. F., Pollock, J. F., Barclay, R. M. R., Szymanski, J. A., Weller, T. J., ... McGuire, L. P. (2017). Fatalities at wind turbines may threaten population viability of a migratory bat. *Biological Conservation*, *209*, 172–177.



- Ganjefar, S., Ghassemi, A. A., & Ahmadi, M. M. (2014). Improving efficiency of two-type maximum power point tracking methods of tip-speed ratio and optimum torque in wind turbine system using a quantum neural network. *Energy*, 67, 444–453.
- García, E., Pizá, R., Benavides, X., Quiles, E., Correcher, A., & Morant, F. (2014). Mechanical augmentation channel design for turbine current generators. *Advances in Mechanical Engineering*, 2014.
- Gasim, Muhamad Barzani, Toriman, M. E., Idris, M., Lun, P. I., Kamarudin, M. K. A., Nor Azlina, A. A., ... Mastura, S. A. S. (2013). River flow conditions and dynamic state analysis of Pahang river. *American Journal of Applied Sciences*, 10(1), 42–57.
- Gasim, Muhammad Barzani, Sultan, U., Abidin, Z., & Rahim, S. A. (2011). Hydrological Pattern Of Pahang River Basin And Their Relation To Flood Historical Event. *Jurnal E-Bangi*, 6(1), 1–10.
- Gasim, Muhammad Barzani, Toriman, M. E., Rahim, S. A., Islam, M. S., Chek, T. C., & Juahir, H. (2006). Hydrology and Water Quality and Land-use Assessment of Tasik Chini's Feeder Rivers, Pahang Malaysia. *Geografia*, 3(3), 1–16.
- Ghefiri, K., Bouallègue, S., Haggège, J., Garrido, I., & Garrido, A. J. (2018). Firefly Algorithm based-Pitch Angle Control of a Tidal Stream Generator for Power Limitation Mode. In *2018 IEEE International Conference on Advanced Systems and Electric Technologies* (Vol. 1, pp. 387–392). Hammamet, Tunisia.
- Ghefiri, K., Garrido, I., Garrido, A. J., Bouallegue, S., & Haggège, J. (2018). Fuzzy Gain Scheduling of a Rotational Speed Control for a Tidal Stream Generator. In *SPEEDAM 2018 - Proceedings: IEEE International Symposium on Power Electronics, Electrical Drives, Automation and Motion* (pp. 1271–1277). Amalfi, Italy.
- Ginter, V. J., & Pieper, J. K. (2011). Robust gain scheduled control of a hydrokinetic turbine. *IEEE Transactions on Control Systems Technology*, 19(4), 805–817.
- Goodwin, G. C., Graebe, S. F., & Salgado, M. E. (2000). *Control Systems Design*. Pearson, Valparaiso. <https://doi.org/10.1002/9780470432754.ch13>
- Google, M. (2019). Riverbank Pebbles Picnic Area (Perkelahan Pasir Kubur). Retrieved November 28, 2019, from [https://www.google.com/maps/place/River+Bank+Pebbles+Picnic+Area+\(Perkelahan+Pasir+Kubur\)/@3.9385086,103.0490936,18z/data=!4m8!1m2!2m1!1spasir+kubur+river+sungai+leming!3m4!1s0x31c8c2437d8e5fcb:0x25dcdd8ae17c61ba!8m2!3d3.9399258!4d103.0496186](https://www.google.com/maps/place/River+Bank+Pebbles+Picnic+Area+(Perkelahan+Pasir+Kubur)/@3.9385086,103.0490936,18z/data=!4m8!1m2!2m1!1spasir+kubur+river+sungai+leming!3m4!1s0x31c8c2437d8e5fcb:0x25dcdd8ae17c61ba!8m2!3d3.9399258!4d103.0496186)
- Grabbe, M., Yuen, K., Goude, A., Lalander, E., & Leijon, M. (2009). Design of An Experimental Setup for Hydro-kinetic Energy Conversion. *The International Journal on Hydropower and Dams*, 16(5), 112–116.

- Güney, M. S., & Kaygusuz, K. (2010). Hydrokinetic energy conversion systems: A technology status review. *Renewable and Sustainable Energy Reviews*, 14(9), 2996–3004.
- Gupta, H., & Roy, S. (2008). The Energy Outlook. In *Geothermal Energy* (Vol. 2, pp. 1–13).
- GWEC. (2019). *Global Wind Report 2018*. Retrieved from <https://gwec.net/wp-content/uploads/2019/04/GWEC-Global-Wind-Report-2018.pdf>
- Hamta, A., Birjandi, A. H., & Bibeau, E. L. (2013). Influence of Turbulent Flow Field on Power Generation. In *2013 IEEE Oceans - San Diego* (pp. 1–6).
- Hansen, K., Breyer, C., & Lund, H. (2019). Status and perspectives on 100 % renewable energy systems. *Energy*, 175, 471–480.
- Harrag, A., & Messalti, S. (2015). Variable step size modified P&O MPPT algorithm using GA-based hybrid offline/online PID controller. *Renewable and Sustainable Energy Reviews*, 49, 1247–1260.
- He, L., Li, Y., & Harley, R. G. (2013). Adaptive multi-mode power control of a direct-drive PM wind generation system in a microgrid. *IEEE Journal of Emerging and Selected Topics in Power Electronics*, 1(4), 217–225.
- Heliciel. (2020). Propeller & Wing: Air foils Blades Profile. Retrieved January 15, 2020, from [https://www.heliciel.com/en/aerodynamique-hydrodynamique/profils\\_aile\\_profil\\_pale.htm](https://www.heliciel.com/en/aerodynamique-hydrodynamique/profils_aile_profil_pale.htm)
- Hong, C. M., Chen, C. H., & Tu, C. S. (2013). Maximum power point tracking-based control algorithm for PMSG wind generation system without mechanical sensors. *Energy Conversion and Management*, 69, 58–67. <https://doi.org/10.1016/j.enconman.2012.12.012>
- Hu, J., Huang, Y., Wang, D., Yuan, H., & Yuan, X. (2015). Modeling of Grid-Connected DFIG-Based Wind Turbines for DC-Link Voltage Stability Analysis. *IEEE Transactions on Sustainable Energy*, 6(4), 1325–1336.
- Hu, J., Wang, B., Wang, W., Tang, H., Chi, Y., & Hu, Q. (2017). Small Signal Dynamics of DFIG-Based Wind Turbines during Riding Through Symmetrical Faults in Weak AC Grid. *IEEE Transactions on Energy Conversion*, 32(2), 720–730.
- Hui, J. (2008). *An Adaptive Control Algorithm for Maximum Power Point Tracking for Wind Energy*. Master Thesis. Queen's University Kingston, Ontario, Canada.
- Hui, J. C. Y., Bakhshai, A., & Jain, P. K. (2015). A Sensorless Adaptive Maximum Power Point Extraction Method With Voltage Feedback Control for Small Wind Turbines in Off-Grid Applications. *IEEE Journal of Emerging and Selected Topics in Power Electronics*, 3(3), 817–828.

- Hui, J. C. Y., Bakhshai, A., & Jain, P. K. (2016). An Energy Management Scheme with Power Limit Capability and an Adaptive Maximum Power Point Tracking for Small Standalone PMSG Wind Energy Systems. *IEEE Transactions on Power Electronics*, 31(7), 4861–4875.
- Hussain, A., Arif, S. M., & Aslam, M. (2017). Emerging renewable and sustainable energy technologies: State of the art. *Renewable and Sustainable Energy Reviews*, 71, 12–28.
- Hussain, J. (2016). Adaptive Maximum Power Point Tracking Control Algorithm for Wind Energy Conversion Systems. *IEEE Transactions on Energy Conversion*, Vol. 31, No. 2, June 2016, 31(2), 697–705.
- Hussein, I., & Raman, N. (2010). Reconnaissance studies of micro hydro potential in Malaysia. In *2010 International Conference on Energy and Sustainable Development: Issues and Strategies (ESD)* (pp. 1–10). Chiang Mai, Thailand.
- Ibrahim, W. I., Ismail, R. M. T. R., & Mohamed, M. R. (2018). Hydrokinetic energy harnessing for river application. *Journal of Telecommunication, Electronic and Computer Engineering*, 10(1–3), 133–138.
- IEA. (2018). World Energy Outlook 2018: The Future is Electrifying. Retrieved August 10, 2019, from <https://www.iea.org/workshops/world-energy-outlook-2018-the-future-is-electrifying.html>
- Islam, R., Bashar, L. Bin, Saha, D. K., & Rafi, N. (2019). Comparison and Selection of Airfoils for Small Wind Turbine between NACA and NREL 's S series Airfoil Families. *International Journal of Research in Electrical, Electronics and Communication Engineering*, 4(2), 1–11.
- Izadyar, N., Ong, H. C., Chong, W. T., Mojumder, J. C., & Leong, K. Y. (2016). Investigation of potential hybrid renewable energy at various rural areas in Malaysia. *Journal of Cleaner Production*, 139, 61–73.
- Jafari, M., Razavi, A., & Mirhosseini, M. (2018). Effect of airfoil profile on aerodynamic performance and economic assessment of H-rotor vertical axis wind turbines. *Energy*, 165, 792–810. <https://doi.org/10.1016/j.energy.2018.09.124>
- Jahangir, K., Tariq, I., & Quaiocoe, J. (2015). Evaluation of maximum power point tracking in hydrokinetic energy conversion systems. *The Journal of Engineering*, (11), 331–338.
- Jain, B., Jain, S., & Nema, R. K. (2015). Control strategies of grid interfaced wind energy conversion system: An overview. *Renewable and Sustainable Energy Reviews*, 47, 983–996.

- Johnson, J. B., & Pride, D. J. (2010). River, tidal and ocean current hydrokinetic energy technologies: Status and future opportunities in Alaska. *Alaska Center for Energy and Power*. Retrieved from [http://www.uaf.edu/files/acep/2010\\_11\\_1\\_State\\_of\\_the\\_Art\\_Hydrokinetic\\_Final.pdf](http://www.uaf.edu/files/acep/2010_11_1_State_of_the_Art_Hydrokinetic_Final.pdf)
- José, A. L. J., Rogério, P. V. J., Luiz, A. M. A., Luiz, A. M. A., & José, C. B. C. (2015). An Approach for the Dynamic Behavior of Hydrokinetic Turbines. In *The 7th International Conference on Applied Energy – ICAE2015* (Vol. 75, pp. 271–276). Abu Dhabi, UAE: Energy Procedia.
- K, K., Babu, R., & K.R, P. (2017). Design and Analysis of Modified Single P& O MPPT Control Algorithm for a Standalone Hybrid Solar and Wind Energy Conversion System. *Gazi University Journal of Science*, 30(4), 296–312.
- Kadier, A., Sahaid, M., Pudukudy, M., Abu, H., Mohamed, A., & Abdul, A. (2018). Pico hydropower ( PHP ) development in Malaysia : Potential , present status , barriers and future perspectives. *Renewable and Sustainable Energy Reviews*, 81, 2796–2805.
- Kaltschmitt, M., & Thrän, D. (2019). Bioenergy. In *Managing Global Warming. An Interface of Technology and Human Issues* (pp. 346–351). Academic Press.
- Kamal, T., Arifoğlu, U., & Hassan, S. Z. (2018). Buck-boost converter small signal model: Dynamic analysis under system uncertainties. *Journal of Electrical Systems*, 14(2), 165–178.
- Kamarudin, M. K. A., Sulaiman, N. H., Abd Wahab, N., Toriman, M. E., Hanafiah, M. M., Umar, R., ... Harith, H. (2019). Impact of Malaysia major flood to river geomorphology changes and totalsuspended solid using GIS technique. *Desalination and Water Treatment*, 149, 242–257. <https://doi.org/10.5004/dwt.2019.23837>
- Kamsani, N. (2018). Dua lelaki dikhuatiri lemas di kawasan perkelahan Sungai Lembang. Retrieved August 19, 2018, from <http://www.astroawani.com/berita-malaysia/dua-lelaki-dikhuatiri-lemas-di-kawasan-perkelahan-sungai-lembing-171868>
- Kani, J. S., Dasan, S. G. B., Ravichandran, S., & Devi, R. P. K. (2014). Small signal stability analysis of PMSG based WECS with coordinated controller tuning. In *Proceeding of the 2014 IEEE International Conference on Green Computing, Communication and Electrical Engineering* (pp. 1–6).
- Karbasian, H. R., Esfahani, J. A., & Barati, E. (2016). The power extraction by flapping foil hydrokinetic turbine in swing arm mode. *Renewable Energy*, 88, 130–142.
- Karbasian, Hamid Reza. (2019). Wind Turbine Aerodynamic. Retrieved October 11, 2019, from <https://sites.google.com/site/mysitepagehamid/wind-turbines>



- Karimian, S. M. H., & Abdolahifar, A. (2019). Performance investigation of a new Darrieus Vertical Axis Wind Turbine. *Energy*. <https://doi.org/10.1016/J.ENERGY.2019.116551>
- Karin, J. (2019). Hydropower from vortex induced vibrations. Retrieved August 19, 2019, from <https://thefutureofthings.com/3889-hydropower-from-vortex-induced-vibrations/>
- Kaunda, C. S., Kimambo, C. Z., & Nielsen, T. K. (2014). A technical discussion on microhydropower technology and its turbines. *Renewable and Sustainable Energy Reviews*, 35, 445–459.
- Kaw, A., & Paul, J. (2019). Spline Interpolation Method. Retrieved December 16, 2019, from [http://mathforcollege.com/nm/mws/gen/05inp/mws\\_gen\\_inp\\_ppt\\_spline.pdf](http://mathforcollege.com/nm/mws/gen/05inp/mws_gen_inp_ppt_spline.pdf)
- Khaigh, A., & Onar, O. C. (2010). *Energy Harvesting Solar, Wind and Ocean Energy Conversion Systems*. CRC Press, Taylor & Francis Group New York.
- Khalid, S. S., Liang, Z., & Shah, N. (2013). Harnessing tidal energy using vertical axis tidal turbine. *Research Journal of Applied Sciences, Engineering and Technology*, 5(1), 239–252.
- Khan, M. J., Bhuyan, G., Iqbal, M. T., & Quaicoe, J. E. (2009). Hydrokinetic energy conversion systems and assessment of horizontal and vertical axis turbines for river and tidal applications: A technology status review. *Applied Energy*, 86(10), 1823–1835.
- Khan, M. J., Iqbal, M. T., & Quaicoe, J. E. (2006). Design considerations of a straight bladed darrieus rotor for river current turbines. In *IEEE International Symposium on Industrial Electronics (ISIE 2006)* (Vol. 3, pp. 1750–1755). Montreal, Quebec, Canada.
- Khan, M. J., Iqbal, M. T., & Quaicoe, J. E. (2008). River current energy conversion systems: Progress, prospects and challenges. *Renewable and Sustainable Energy Reviews*, 12(8), 2177–2193.
- Khan, M. J., Iqbal, M. T., & Quaicoe, J. E. (2010). Dynamics of a vertical axis hydrokinetic energy conversion system with a rectifier coupled multi-pole permanent magnet generator. *IET Renewable Power Generation*, 4(2), 116.
- Khan, M. J., Iqbal, M. T., & Quaicoe, J. E. (2011). Effects of efficiency nonlinearity on the overall power extraction: A case study of hydrokinetic-energy-conversion systems. *IEEE Transactions on Energy Conversion*, 26(3), 911–922.
- Khan, M. N. I. (2015). *Modelling, Design and Control of a Small Marine Current Energy Conversion System*. PhD Thesis. Memorial University of Newfoundland.

- Kilcher, L., & Kilcher, L. (2016). *Marine Hydrokinetic Energy Site Identification and Ranking Methodology Part I: Wave Energy Marine Hydrokinetic Energy Site Identification*.
- Kim, K., Van, T. L., Lee, D., Song, S., & Kim, E. (2013). Maximum Output Power Tracking Control in Variable-Speed Wind Turbine Systems Considering Rotor Inertial Power. *IEEE Transaction on Industrial Electronics*, 60(8), 3207–3217.
- Kim, S. K., & Kim, E. S. (2007). PSCAD/EMTDC-based modeling and analysis of a gearless variable speed wind turbine. *IEEE Transactions on Energy Conversion*, 22(2), 421–430. <https://doi.org/10.1109/TEC.2005.858063>
- Kinsey, T., & Dumas, G. (2017). Impact of channel blockage on the performance of axial and cross-flow hydrokinetic turbines. *Renewable Energy*, 103, 239–254. <https://doi.org/10.1016/j.renene.2016.11.021>
- Kirke, B. (2019). Hydrokinetic and ultra-low head turbines in rivers: A reality check. *Energy for Sustainable Development*, 52, 1–10.
- Knüppel, T., Nielsen, J. N., Jensen, K. H., Dixon, A., & Ostergaard, J. (2012). Small-signal stability of wind power system with full-load converter interfaced wind turbines. *IET Renewable Power Generation*, 6(2), 79.
- Koko, S. P., Kusakana, K., & Vermaak, H. J. (2017). Optimal energy management of a grid-connected micro-hydrokinetic with pumped hydro storage system. *Journal of Energy Storage*, 14, 8–15.
- Koko, Sandile Phillip, Kusakana, K., & Vermaak, H. J. (2015). Micro-hydrokinetic river system modelling and analysis as compared to wind system for remote rural electrification. *Electric Power Systems Research*, 126, 38–44.
- Koutroulis, E., & Kalaitzakis, K. (2006). Design of a maximum power tracking system for wind-energy-conversion applications. *IEEE Transactions on Industrial Electronics*, 53(2), 486–494. <https://doi.org/10.1109/TIE.2006.870658>
- Kumar, A., & Saini, R. P. (2017). Performance analysis of a single stage modified Savonius hydrokinetic turbine having twisted blades. *Renewable Energy*, 113, 461–478.
- Kumar, Dinesh, & Sarkar, S. (2016). A review on the technology, performance, design optimization, reliability, techno-economics and environmental impacts of hydrokinetic energy conversion systems. *Renewable and Sustainable Energy Reviews*.
- Kumar, Dipesh, & Chatterjee, K. (2016). A review of conventional and advanced MPPT algorithms for wind energy systems. *Renewable and Sustainable Energy Reviews*, 55, 957–970.

- Ladokun, L. L., Sule, B. F., Ajao, K. R., & Adeogun, A. G. (2018). Resource assessment and feasibility study for the generation of hydrokinetic power in the tailwaters of selected hydropower stations in Nigeria. *Water Science*, (2017).
- Lago, L. I., Ponta, F. L., & Chen, L. (2010). Advances and trends in hydrokinetic turbine systems. *Energy for Sustainable Development*, 14(4), 287–296.
- Lalander, E., & Leijon, M. (2009). Numerical modeling of a river site for in-stream energy converters. In *8th European Wave and Tidal Energy Conference*.
- Laws, N. D., & Epps, B. P. (2016). Hydrokinetic energy conversion: Technology, research, and outlook. *Renewable and Sustainable Energy Reviews*, 57, 1245–1259.
- Lee, J. H., Xiros, N., & Bernitsas, M. M. (2011). Virtual damperspring system for VIV experiments and hydrokinetic energy conversion. *Ocean Engineering*, 38(5–6), 732–747.
- Lee, J., & Kim, Y.-S. (2016). Sensorless fuzzy-logic-based maximum power point tracking control for a small-scale wind power generation systems with a switched-mode rectifier. *IET Renewable Power Generation*, 10(2), 194–202.
- Lei Wang. (2012). *Advanced Control of Variable Speed Wind Turbine based on Doubly-Fed Induction Generator. PhD Thesis*. The University of Liverpool.
- Levy, D. (1995). Power from natural flow at zero static head. *International Power Generation*, 18(1).
- Li, P., Hu, W., Hu, R., & Chen, Z. (2018). Stability Analysis for Primary Frequency Regulation from DFIG Tidal Turbines. In *Proceedings - 2018 IEEE PES Innovative Smart Grid Technologies Conference Europe, (ISGT-Europe 2018)* (pp. 1–6). Sarajevo, Bosnia and Herzegovina.
- Liu, J., Gao, Y., Geng, S., & Wu, L. (2017). Nonlinear Control of Variable Speed Wind Turbines via Fuzzy Techniques. *IEEE Access*, 5, 27–34.
- Lopez, H. E. M. (2007). *Maximum Power Tracking Control Scheme for Wind Generator. Master Thesis*. Texas A & M University.
- Magagna, D., & Uihlein, A. (2015). Ocean energy development in Europe: Current status and future perspectives. *International Journal of Marine Energy*, 11, 84–104. <https://doi.org/1>
- Maizi, M., Mohamed, M. H., Dizene, R., & Mihoubi, M. C. (2018). Noise reduction of a horizontal wind turbine using different blade shapes. *Renewable Energy*, 117, 242–256.
- Malipeddi, A. R., & Chatterjee, D. (2012). Influence of duct geometry on the performance of Darrieus hydro turbine. *Renewable Energy*, 43, 292–300.



- Mansour, M., Mansouri, M. N., & Mimouni, M. F. (2011). Comparative Study affixed Speed and Variable Speed Wind Generator with Pitch Angle Control Mohamed. In *2011 IEEE International Conference on Communications, Computing and Control Applications* (pp. 1–7). Hammamet, Tunisia.
- Mao, H. H. C., & Wang, J. L. D. (2012). Small-signal modelling and analysis of wind turbine with direct drive permanent magnet synchronous generator connected to power grid. *IET Renewable Power Generation*, 6(1), 48–58.
- Marine Renewables Canada. (2018). *2018 State of the Sector Report*. Canada. Retrieved from [www.marinerenewables.ca](http://www.marinerenewables.ca)
- Marten, D., & Wendler, J. (2013). QBLADE: an open source tool for design and simulation of horizontal and vertical axis wind turbines. *International Journal of Emerging Technology and Advanced Engineering*, 3(3), 264–269.
- Mathias Maehlum. (2019). Wind Energy Pros and Cons. Retrieved August 7, 2019, from <https://energyinformative.org/wind-energy-pros-and-cons/>
- McCormick, B. W. (1998). *Aerodynamics of V/STOL flight*. Dover Publications.
- Mcgrath, B. P. (2018). Small Signal Dynamic Model of a Self-Synchronising Current Regulated Rectifier for a Permanent Magnet Wind Energy Conversion System ( WECS ). *2018 IEEE Energy Conversion Congress and Exposition (ECCE)*, 5521–5528.
- Melts, I., Ivask, M., Geetha, M., Takeuchi, K., & Heinsoo, K. (2019). Combining bioenergy and nature conservation: An example in wetlands. *Renewable and Sustainable Energy Reviews*, 111, 293–302.
- Messalti, S., Harrag, A., & Loukriz, A. (2017). A new variable step size neural networks MPPT controller: Review, simulation and hardware implementation. *Renewable and Sustainable Energy Reviews*, 68, 221–233.
- Michas, M. (2018). *Control of Turbine-Based Energy Conversion Systems*. PhD Thesis. Cardiff University, Wales, UK.
- Michas, M., Ugalde-Loo, C. E., Ming, W., Jenkins, N., & Runge, S. (2019). Maximum power extraction from a hydrokinetic energy conversion system. *IET Renewable Power Generation*, 1411–1419.
- Miller, N. W., Price, W. W., & Sanchez-Gasca, J. J. (2003). *Dynamic modeling of GE 1.5 and 3.6 wind turbine-generators*. *GE-Power systems energy consulting* (Vol. 3).
- Mishra, M. K., Khare, N., & Agrawal, A. B. (2015). Small hydro power in India: Current status and future perspectives. *Renewable and Sustainable Energy Reviews*, 51, 101–115.

- Mohamed, A. Z., Eskander, M. N., & Ghali, F. A. (2001). Fuzzy logic control based maximum power tracking of a wind energy system. *Renewable Energy*, 23(2), 235–245. [https://doi.org/10.1016/S0960-1481\(00\)00099-9](https://doi.org/10.1016/S0960-1481(00)00099-9)
- Mohamed, M. H. (2012). Performance investigation of H-rotor Darrieus turbine with new airfoil shapes. *Energy*, 47(1), 522–530. <https://doi.org/10.1016/j.energy.2012.08.044>
- Mohamed, M. H., Dessoky, A., & Alqurashi, F. (2019). Blade shape effect on the behavior of the H-rotor Darrieus wind turbine: Performance investigation and force analysis. *Energy*, 179, 1217–1234. <https://doi.org/10.1016/j.energy.2019.05.069>
- Mokhtari, Y., & Rekioua, D. (2018). High performance of Maximum Power Point Tracking Using Ant Colony algorithm in wind turbine. *Renewable Energy*, 126, 1055–1063.
- Mousa, H. H. H., Youssef, A., & Mohamed, E. E. M. (2019). Electrical Power and Energy Systems Variable step size P & O MPPT algorithm for optimal power extraction of multi-phase PMSG based wind generation system. *Electrical Power and Energy Systems*, 108, 218–231.
- Mukherji, S. (2010). *Design and critical performance evaluation of horizontal axis hydrokinetic turbines. Master Thesis.* Missouri University of Science & Technology.
- Muljadi, E., Wright, A., Gevorgian, V., Donegan, J., Marnagh, C., & McEntee, J. (2016). Turbine control of tidal and river power generator. In *2016 IEEE North American Power Symposium (NAPS)* (pp. 1–5).
- Muljadi, Eduard, Gevorgian, V., Wright, A., Donegan, J., & Marnagh, C. (2016). *Electrical Power Conversion of a River and Tidal Power Generator. National Renewable Energy Laboratory.*
- Musunuri, S., & Ginn, H. L. (2011). A Fast Maximum Power Extraction Algorithm For Wind Energy Systems. In *2011 IEEE Power and Energy Society General Meeting* (Vol. 2, pp. 1–7). Detroit, Michigan, USA.
- Nasiri, M., Milimonfared, J., & Fathi, S. H. (2014). Modeling , analysis and comparison of TSR and OTC methods for MPPT and power smoothing in permanent magnet synchronous generator-based wind turbines. *Energy Conversion and Management*, 86, 892–900.
- Niebuhr, C. M., van Dijk, M., Neary, V. S., & Bhagwan, J. N. (2019). A review of hydrokinetic turbines and enhancement techniques for canal installations: Technology, applicability and potential. *Renewable and Sustainable Energy Reviews*, 113.

- Nordqvist, E. (2016). *A pilot study on the coupling potential for a hydrokinetic turbine within the Amazon basin - Optimization from an energy perspective*. Master Thesis. Karlstads Universitet.
- Novaes Menezes, E. J., Araújo, A. M., & Bouchonneau da Silva, N. S. (2018). A review on wind turbine control and its associated methods. *Journal of Cleaner Production*, 174, 945–953.
- Odedele, N., Olmi, C., & Charpentier, J. F. (2014). Power Extraction Strategy of a Robust kW Range Marine Tidal Turbine Based on Permanent Magnet Synchronous Generators and Passive Rectifiers. In *IET Conference Publications* (Vol. 2014, pp. 1–6).
- Official Page: Department of Irrigation & Drainage. (2018). Retrieved August 20, 2018, from <https://www.water.gov.my/index.php/pages/view/349?mid=220>
- Omkar, K., Karthikeyan, K. B., Srimathi, R., Venkatesan, N., Avital, E. J., Samad, A., & Rhee, S. H. (2019). A performance analysis of tidal turbine conversion system based on control strategies. In *2nd International Conference on Energy and Power, ICEP2018* (Vol. 160, pp. 526–533). Sydney, Australia: Energy Procedia.
- ORPC. (2019). Utility Grid. Retrieved August 13, 2019, from <http://www.orpc.co/markets/utility-grids>
- Othman, Z. A. (2005). The Future of Hydropower in Malaysia. *Buletin Jurutera*, (May), 32–33.
- Paduani, V., Kabalan, M., & Singh, P. (2019). Small-Signal Stability of Islanded-Microgrids with DC Side Dynamics of Inverters and Saturation of Current Controllers. In *IEEE Power and Energy Society General Meeting* (Vol. 2019-Augus). <https://doi.org/10.1109/PESGM40551.2019.8974017>
- Papathanassiou, S. A., & Boulaxis, N. G. (2006). Power limitations and energy yield evaluation for wind farms operating in island systems. *Renewable Energy*, 31(4), 457–479.
- Paredes-Sánchez, J. P., López-Ochoa, L. M., López-González, L. M., Las-Heras-Casas, J., & Xiberta-Bernat, J. (2019). Evolution and perspectives of the bioenergy applications in Spain. *Journal of Cleaner Production*, 213, 553–568.
- Patel, V., Eldho, T. I., & Prabhu, S. V. (2017a). Experimental investigations on Darrieus straight blade turbine for tidal current application and parametric optimization for hydro farm arrangement. *International Journal of Marine Energy*, 17, 110–135.
- Patel, V., Eldho, T. I., & Prabhu, S. V. (2017b). Experimental investigations on Darrieus straight blade turbine for tidal current application and parametric optimization for hydro farm arrangement. *International Journal of Marine Energy*, 17, 110–135. <https://doi.org/10.1016/j.ijome.2017.01.007>

- Peter Garman. (1986). Water current turbines: A fieldworker's guide. *Intermediate Technology Publishing*, (ISBN: 0946688273).
- Petinrin, J. O., & Shaaban, M. (2015). Renewable energy for continuous energy sustainability in Malaysia. *Renewable and Sustainable Energy Reviews*, 50, 967–981.
- Petrie, J., Diplas, P., Gutierrez, M., & Nam, S. (2014). Characterizing the mean flow field in rivers for resource and environmental impact assessments of hydrokinetic energy generation sites. *Renewable Energy*, 69, 393–401.
- Pierre, T., René, W., Mohand, O., Andy, T. T., & Gabriel, E. (2015). A new approach for modeling darrieus-type vertical axis wind turbine rotors using electrical equivalent circuit analogy: Basis of theoretical formulations and model development. *Energies*, 8(10), 10684–10717.
- Pobering, S., & Schwesinger, N. (2004). A Novel Hydropower Harvesting Device. In *2004 IEEE International Conference on MEMS, NANO and Smart Systems (ICMENS'04)* (pp. 480–485). Banff, AB, Canada.
- Pongduang, S., Kayankannavee, C., & Tiaple, Y. (2015). Experimental Investigation of Helical Tidal Turbine Characteristics with Different Twists. In *Energy Procedia* (Vol. 79, pp. 409–414). Elsevier B.V. <https://doi.org/10.1016/j.egypro.2015.11.511>
- Ponta, F., & Dutt, G. S. (2000). An improved vertical-axis water-current turbine incorporating a channelling device. *Renewable Energy*, 20(2000), 223–241.
- Prakashkumar, V., & Tamilselvi, A. (2010). A Control Strategy for a Variable-Speed Wind Turbine with a Permanent-Magnet Synchronous Generator. *IEEE Transaction on Industry Application*, 46(1), 331–339.
- Rahimi, M. (2017). Electrical Power and Energy Systems Modeling , control and stability analysis of grid connected PMSG based wind turbine assisted with diode rectifier and boost converter. *International Journal of Electrical Power and Energy Systems*, 93, 84–96.
- Raman, N., Hussein, I., & Palanisamy, K. (2009). Micro hydro potential in West Malaysia. In *Proceeding of ICEE 2009 IEEE 3rd International Conference on Energy and Environment* (pp. 348–359). Malacca, malaysia.
- Raza Kazmi, S. M., Goto, H., Guo, H.-J., & Ichinokura, O. (2011). A Novel Algorithm for Fast and Efficient Speed-Sensorless Maximum Power Point Tracking in Wind Energy Conversion Systems. *Industrial Electronics, IEEE Transactions On*, 58(1), 29–36.
- Ren, B., Wang, Y., & Zhong, Q. C. (2017). UDE-based control of variable-speed wind turbine systems. *International Journal of Control*, 90(1), 121–136.



- RL, R., & BD, H. (1981). Definition of cost effective river turbine designs. Retrieved November 27, 2019, from <https://www.osti.gov/biblio/5358098>
- Romero-Gomez, P., & Richmond, M. C. (2014). Simulating blade-strike on fish passing through marine hydrokinetic turbines. *Renewable Energy*, 71, 401–413.
- Sadollah, A. (2018). Introductory Chapter: Which Membership Function is Appropriate in Fuzzy System? In *Fuzzy Logic Based in Optimization Methods and Control Systems and its Applications* (pp. 3–6). <https://doi.org/10.5772/intechopen.79552>
- Salter, S. (2005). Pitch–Control for Vertical-Axis, Marine-Current Generator. In *World Renewable Energy Conference Aberdeen 2005* (pp. 1–6).
- Sarauskiene, D. (2017). Assessment of hydrokinetic resources of small and medium-size rivers : The Lithuanian Case. *Baltica*, 30(1), 23–30.
- Sarkar, J., & Khule, S. S. (2016). A study of MPPT schemes in PMSG based wind turbine system. In *International Conference on Electrical, Electronics, and Optimization Techniques, ICEEOT 2016* (pp. 100–105).
- Sarma, N. K., Biswas, A., & Misra, R. D. (2014). Experimental and computational evaluation of Savonius hydrokinetic turbine for low velocity condition with comparison to Savonius wind turbine at the same input power. *Energy Conversion and Management*, 83(2014), 88–98.
- Sasi, M. A. (2017). *Fuzzy Logic Control of MPPT Controller for PV Systems*. Memorial University of Newfoundland, Canada.
- Scarlat, N., & Dallemand, J.-F. (2018). Future Role of Bioenergy. In *The Role of Bioenergy in the Bioeconomy* (pp. 435–547). Retrieved from <http://dx.doi.org/10.1016/B978-0-12-813056-8.00010-8>
- Schleicher, W. C., Riglin, J. D., & Oztekin, A. (2015). Numerical characterization of a preliminary portable micro-hydrokinetic turbine rotor design. *Renewable Energy*, 76, 234–241.
- Schramm, M. P., Bevelhimer, M., & Scherelis, C. (2017). Effects of hydrokinetic turbine sound on the behavior of four species of fish within an experimental mesocosm. *Fisheries Research*, 190, 1–14.
- Sefidgar, H., & Asghar Gholamian, S. (2014). Fuzzy Logic Control of Wind Turbine System Connection to PM Synchronous Generator for Maximum Power Point Tracking. *International Journal of Intelligent Systems and Applications*, 6(7), 29–35. <https://doi.org/10.5815/ijisa.2014.07.04>
- Shafei, M. A. R., Ibrahim, D. K., Ali, A. M., Younes, M. A. A., & El-Zahab, E. E. D. A. (2015). Novel approach for hydrokinetic turbine applications. *Energy for Sustainable Development*, 27(2015), 120–126.

- Shahsavarifard, M., Bibeau, E. L., & Birjandi, A. H. (2013). Performance gain of a horizontal axis hydrokinetic turbine using shroud. In *2013 IEEE Oceans - San Diego* (pp. 1–5).
- Shahsavarifard, M., Bibeau, E. L., & Chatoorgoon, V. (2015). Effect of shroud on the performance of horizontal axis hydrokinetic turbines. *Ocean Engineering*, *96*, 215–225.
- Silva, P. A. S. F. Da, Shinomiya, L. D., Oliveira, T. F. De, Vaz, J. R. P., Mesquita, A. L. A., & Junior, A. C. P. B. (2015). Design of Hydrokinetic Turbine Blades Considering Cavitation. In *The 7th International Conference on Applied Energy – ICAE2015* (Vol. 75, pp. 277–282). Abu Dhabi, United Arab Emirates: Energy Procedia.
- Simões, M. G., Bose, B. K., & Spiegel, R. J. (1997). Design and performance evaluation of a fuzzy-logic-based variable-speed wind generation system. *IEEE Transactions on Industry Applications*, *33*(4), 956–965. <https://doi.org/10.1109/28.605737>
- Sira-Ramireza, H., & Silva-Ortigoza, R. (2006). Modelling of DC-to-DC Power Converters. *Control Design Techniques in Power Electronics Devices*, XVIII, 424. <https://doi.org/10.1007/1-84628-459-7>
- Siti Waznah, A., Kamaruzzaman, B. Y., Ong, M. C., Rina, S. Z., & Mohd Zahir, S. (2010). Spatial and temporal bottom sediment characteristics of Pahang River-Estuary, Pahang, Malaysia. *Oriental Journal of Chemistry*, *26*(1), 39–44.
- Slootweg, J. G., De Haan, S. W. H., Polinder, H., & Kling, W. L. (2002). General Model for Representing Variable-Speed Wind Turbines in Power System Dynamics Simulations. *IEEE Power Engineering Review*, *22*(11), 56. <https://doi.org/10.1109/MPER.2002.4311816>
- Smart Hydro Power. (2019). Retrieved September 10, 2019, from <https://www.smart-hydro.de/>
- Soheil Ahmadzadeh, G. A. M. (2017). Incremental Conductance Based MPPT Using A High Step-Up V-Source DC-DC Converter. In *IEEE 8th Power Electronics, Drive Systems & Technologies Conference (PEDSTC 2017)* (pp. 1–6). Mashhad, Iran.
- Sornes, K. (2010). *Small-scale Water Current Turbines for River Applications*. Zero Emission Resource Organization.
- Sovacool, B. K., & Bulan, L. C. (2012). Energy security and hydropower development in Malaysia : The drivers and challenges facing the Sarawak Corridor of Renewable Energy ( SCORE ). *Renewable Energy*, *40*(2012), 113–129.
- Stehly, T., Heimiller, D., & Scott, G. (2016). *2016 Cost of Wind Energy Review*. Retrieved from <https://www.nrel.gov/docs/fy18osti/70363.pdf>



- Subbottin, Y. N. (2011). Spline Interpolation. Retrieved December 16, 2019, from [https://www.encyclopediaofmath.org/index.php/Spline\\_interpolation](https://www.encyclopediaofmath.org/index.php/Spline_interpolation)
- Subramanian, A., Yogesh, S. A., Sivanandan, H., Giri, A., Vasudevan, M., Mugundhan, V., & Velamati, R. K. (2017). Effect of airfoil and solidity on performance of small scale vertical axis wind turbine using three dimensional CFD model. *Energy*, *133*, 179–190. <https://doi.org/10.1016/j.energy.2017.05.118>
- Takagi, K., Suyama, Y., & Kagaya, K. (2011). An attempt to control the motion of floating current turbine by the pitch control. In *2011 IEEE OCEANS* (pp. 1–6). Santander, Spain.
- Tanier-Gesner, F., Stillinger, C., Bond, A., Egan, P., & Perry, J. (2014). Design, build and testing of a hydrokinetic H-Darrieus turbine for developing countries. In *IEEE Power and Energy Society General Meeting* (Vol. 2014, pp. 1–5). National Harbour, Washington DC.
- Tekolla, A. W. (2010). Rainfall and Flood Frequency Analysis in Pahang River Basin, Malaysia. *Master of Science Thesis in Water Resources Engineering*, 1–80.
- Thongam, J. S., Bouchard, P., Ezzaidi, H., & Ouhrouche, M. (2009). Wind Speed Sensorless Maximum Power Point Tracking Control of Variable Speed Wind Energy Conversion Systems. In *IEEE Int. Conf. on Elect. Mach. & Drives (IEMDC 2009)* (pp. 1832–1837). Miami, FL, USA.
- TidGen Power Generation. (2017). Retrieved July 23, 2019, from [http://www.orpc.co/orpcpowersystem\\_tidgenpowersystem.aspx](http://www.orpc.co/orpcpowersystem_tidgenpowersystem.aspx)
- Tiwari, R., & Babu, N. R. (2016a). Fuzzy logic based MPPT for permanent magnet synchronous generator in wind energy conversion system. *International Federation of Automatic Control (IFAC-PapersOnLine)*, *49*(1), 462–467. <https://doi.org/10.1016/j.ifacol.2016.03.097>
- Tiwari, R., & Babu, N. R. (2016b). Recent developments of control strategies for wind energy conversion system. *Renewable and Sustainable Energy Reviews*, *66*, 268–285.
- Ugalde-loo, C. E., Ekanayake, J. B., & Jenkins, N. (2013). State-Space Modeling of Wind Turbine Generators for Power System Studies. *IEEE Transactions on Industry Applications*, *49*(1), 223–232.
- VanZwieten, J. H., Pyakurel, P., Ngo, T., Sultan, C., & Xiros, N. I. (2016). An assessment of using variable blade pitch for moored ocean current turbine flight control. *International Journal of Marine Energy*, *13*(2016), 16–26.
- Vennell, R., Funke, S. W., Draper, S., Stevens, C., & Divett, T. (2015). Designing Large Arrays of Tidal Turbines: A synthesis and review. *Renewable and Sustainable Energy Reviews*, *41*, 454–472.

- Vermaak, H. J., Kusakana, K., & Koko, S. P. (2014). Status of micro-hydrokinetic river technology in rural applications: A review of literature. *Renewable and Sustainable Energy Reviews*, 29, 625–633.
- Wai, R. ., Lin, C. ., & Chang, Y. . (2007). Novel maximum-power-extraction algorithm for PMSG wind generation system. *IET Electric Power Applications*, 1(1), 275–283. <https://doi.org/10.1049/iet-epa>
- Wang, Y., Shen, S., Li, G., Huang, D., & Zheng, Z. (2018). Investigation on aerodynamic performance of vertical axis wind turbine with different series airfoil shapes. *Renewable Energy*, 126, 801–818. <https://doi.org/10.1016/j.renene.2018.02.095>
- Water, G. (2009). *FP111-FP211-FP311 Global Water Flow Probe User ' s Manual*. Global Water Instrumentation Inc. Retrieved from [www.globalw.com](http://www.globalw.com)
- Wei, Z., Wei, D., Liu, S. M., Yang, M. L., Pan, S. B., Zhu, X. W., & Pan, Z. G. (2014). Probabilistic Small Signal Stability Analysis of Power System with Large Scale Wind Power. In *IEEE Transportation Electrification Conference and Expo (ITEC Asia-Pacific 2014 )* (pp. 1–4). Beijing, China.
- Wen, X., & Ajarapu, V. (2004). Critical eigenvalue trajectory tracing for power system oscillatory stability assessment. In *2004 IEEE Power Engineering Society General Meeting* (Vol. 2, pp. 1883–1889). IEEE. <https://doi.org/10.1109/pes.2004.1373205>
- Wen, X., & Ajarapu, V. (2006). Application of a Novel Eigenvalue Trajectory Tracing Method to Identify Both Oscillatory Stability Margin and Damping Margin. *IEEE Transactions on Power Systems*, 21(2), 817–824. <https://doi.org/10.1109/TPWRS.2006.873111>
- Whei-Min Lin, C.-M. H. (2010). Maximum power point tracking control strategy for variable speed wind turbine generation system. *Energy*, 35(2010), 2440–2447.
- Wikiversity. (2019). Cubic Spline Interpolation. Retrieved December 16, 2019, from [https://en.wikiversity.org/wiki/Cubic\\_Spline\\_Interpolation](https://en.wikiversity.org/wiki/Cubic_Spline_Interpolation)
- Wu, F., Zhang, X., Godfrey, K., & Ju, P. (2007). Small signal stability analysis and optimal control of a wind turbine with doubly fed induction generator. *IET Generation Transmission Distribution*, 1(5), 1–10.
- Wu, F., Zhang, X. P., & Ju, P. (2009). Small signal stability analysis and control of the wind turbine with the direct-drive permanent magnet generator integrated to the grid. *Electric Power Systems Research*, 79(12), 1661–1667.
- Xia, Y., Ahmed, K. H., & Williams, B. W. (2013). Wind Turbine Power Coefficient Analysis of a New Maximum Power Point Tracking Technique. *IEEE Transaction on Industrial Electronics*, 60(3), 1122–1132.

- Xue-wei, Z., Shu-qi, W., Feng, W., Liang, Z., & Qi-hu, S. (2012). The Hydrodynamic Characteristics of Free variable-Pitch Vertical Axis Tidal Turbine. *Journal of Hydrodynamics*, 24(6), 834–839.
- Yaakoubi, A. El, Asselman, A., Djebli, A., & Aroudam, E. H. (2016). A MPPT Strategy Based on Fuzzy Control for a Wind Energy Conversion System. In *Procedia Technology* (Vol. 22, pp. 697–704). Tirgu-Mures, Romania: Elsevier. <https://doi.org/10.1016/j.protcy.2016.01.145>
- Yah, N. F., Oumer, A. N., & Idris, M. S. (2017). Small scale hydro-power as a source of renewable energy in Malaysia: A review. *Renewable and Sustainable Energy Reviews*, 72(2017), 228–239.
- Yang, D., & Ajarapu, V. (2005). Tracing of Critical Eigenvalues for Power System Analysis via Continuation of Invariant Subspaces and Projected Arnoldi Method. In *2005 IEEE Power Engineering Society General Meeting* (Vol. 2, pp. 1630–1636). IEEE. <https://doi.org/10.1109/pes.2005.1489334>
- Yavuz, T., Kilkis, B., Akpınar, H., & Erol, O. (2011). Performance analysis of a hydrofoil with and without leading edge slat. In *Proceedings - 10th IEEE International Conference on Machine Learning and Applications, ICMLA 2011* (Vol. 2, pp. 281–285). Honolulu, Hawaii USA.
- Yazici, İ., & Yaylaci, E. K. (2017). Maximum power point tracking for the permanent magnet synchronous generator-based WECS by using the discrete-time integral sliding mode controller with a chattering-free reaching law. *IET Power Electronics*, 10(13), 1751–1758.
- Yin, M., Li, W., Zhou, L., Chen, Z., & Zou, Y. (2017). Optimal torque control based on effective tracking range for maximum power point tracking of wind turbines under varying wind conditions. *IET Renewable Power Generation*, 11(4), 501–510.
- Yin, X., & Zhao, X. (2019). Sensor-less Maximum Power Extraction Control of a Hydrostatic Tidal Turbine Based on Adaptive Extreme Learning Machine. *IEEE Transactions on Sustainable Energy*. <https://doi.org/10.1109/tste.2019.2894064>
- Yuce, M. I., & Muratoglu, A. (2015). Hydrokinetic energy conversion systems: A technology status review. *Renewable and Sustainable Energy Reviews*, 43, 72–82.
- Zammit, D., Zammit, D., Staines, C. S., Micallef, A., & Apap, M. (2017). MPPT with Current Control for a PMSG Small Wind Turbine in a Grid-Connected DC Microgrid MPPT with Current Control for a PMSG Small Wind Turbine in a. *Energy Procedia*, 142(June), 2284–2294. <https://doi.org/10.1016/j.egypro.2017.12.631>
- Zhang, H.-B., Fletcher, J., Greeves, N., Finney, S. J., & Williams, B. W. (2011). One-power-point operation for variable speed wind/tidal stream turbines with synchronous generators. *IET Renewable Power Generation*, 5(1), 99–108.

Zhou, H. (2012). *Maximum Power Point Tracking Control of Hydrokinetic Turbine and Low-Speed High-Thrust Permanent Magnet Generator Design*. Master Thesis. Missouri University of Science & Technology.

Zhu, W., Shang, L., Li, P., & Guo, H. (2018). Modified hill climbing MPPT algorithm with reduced steady-state oscillation and improved tracking efficiency. *The Journal of Engineering*, 2018(17), 1878–1883.

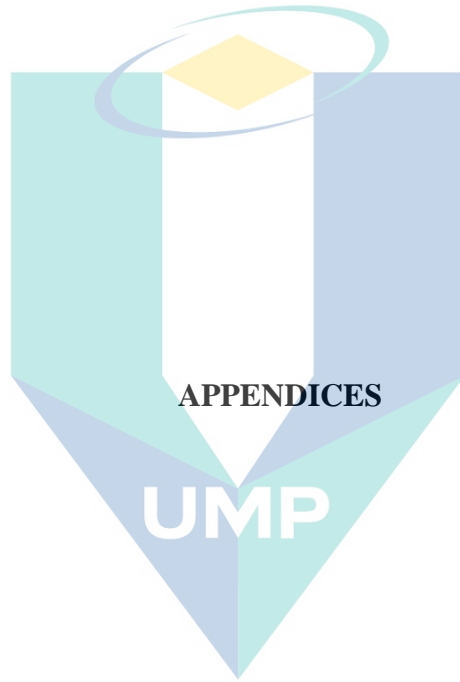
Zupone, G. Lo, Amelio, M., Barbarelli, S., Florio, G., Scornaienchi, N. M., & Cutrupi, A. (2015). Levelized Cost of Energy: A First Evaluation for a Self Balancing Kinetic Turbine. *Energy Procedia*, 75(2015), 283–293.

Zwaan, B. Van Der, & Longa, F. D. (2019). Integrated assessment projections for global geothermal energy use. *Geothermics*, 82(2019), 203–211.



اونيورسيتي ملايسيا قهغ

UNIVERSITI MALAYSIA PAHANG



اونيورسيتي مليسيا قهغ

UNIVERSITI MALAYSIA PAHANG

## Appendix A: Analysis of DID Data

### A1. Velocity Measurement at Pasir Kubur River

The reconnaissance study and hydrological sampling were carried out in April 2018. The river velocity at Pasir Kubur Sungai Lembing was between  $0.4 \text{ ms}^{-1}$  and  $1.3 \text{ ms}^{-1}$  as shown in Figure 7.1. The trend of velocity from Station 1 to Station 2 slightly increased but gradually decreased at Station 3.

Twelve sampling measurement data were recorded during the one-hour session at each station. Based on the study, Station 2 has the potential for hydrokinetic turbine placement due to high water velocity with an average of  $1.1 \text{ ms}^{-1}$ . The velocity at Station 2 can also achieve  $1.3 \text{ ms}^{-1}$  maximum with  $1.0 \text{ ms}^{-1}$  minimum water speed. The depth at the Station 2 also ranges between 1.15 m and 5 m which is suitable for the horizontal and vertical axis hydrokinetic turbine. In contrast, Station 1 and Station 3 are not ideal for hydrokinetic deployment due to its shallow water depth, even though the water velocity at Station 1 is in an acceptable range.

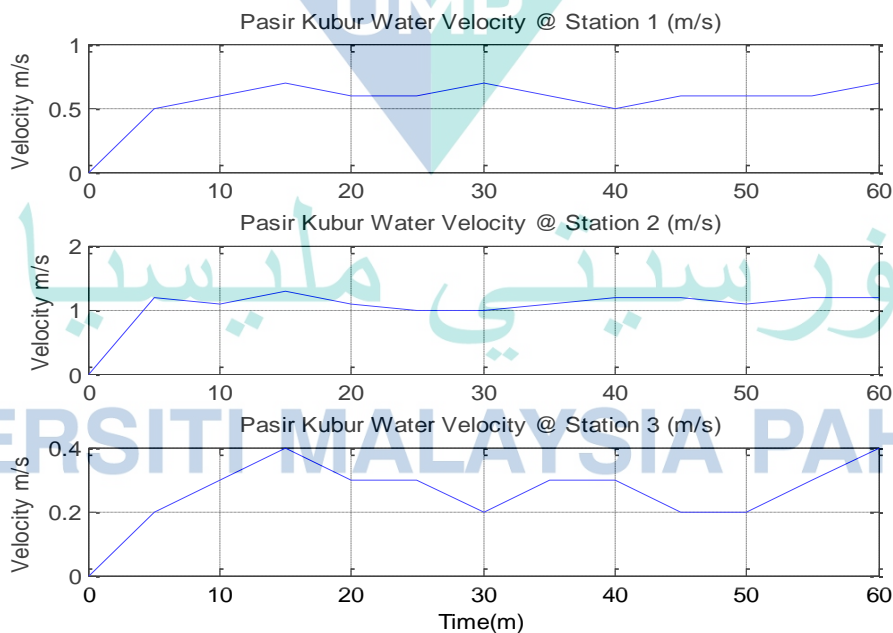




Figure 7.1 The water velocity at sampling station. Three sampling stations were setup to measure the water velocity.

Figure 7.2 shows the water velocity at Station 2 in 60 minutes. The Matlab fitting tool was used to generate the spline-interpolation curve. Based on the Matlab fitting function, the spline-interpolation gives an interpolating polynomial with the smooth and less error compared to other fitting methods such as Lagrange polynomial (Subbottin, 2011; Wikiversity, 2019). This method is able to prevent Runge's phenomenon, which the oscillation occurred between the point due to a higher order of polynomial (Kaw & Paul, 2019). Therefore the spline-interpolation method is sufficient to represent the actual input of water velocity under fluctuation.

As can be seen, the graph shows the comparison between the sampling measurement and the spline interpolant method. It is observed, the fluctuation was occurred and became the main challenge in hydrokinetic energy harnessing. Therefore, the maximum power point tracking (MPPT) algorithm was employed for optimal energy extraction in the hydrokinetic system (Ginter and Pieper, 2011).

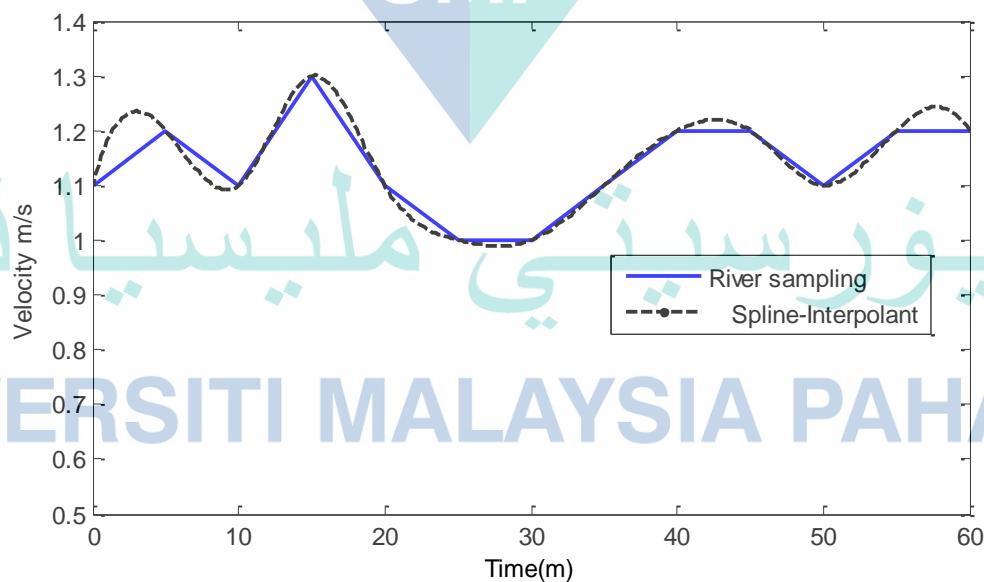
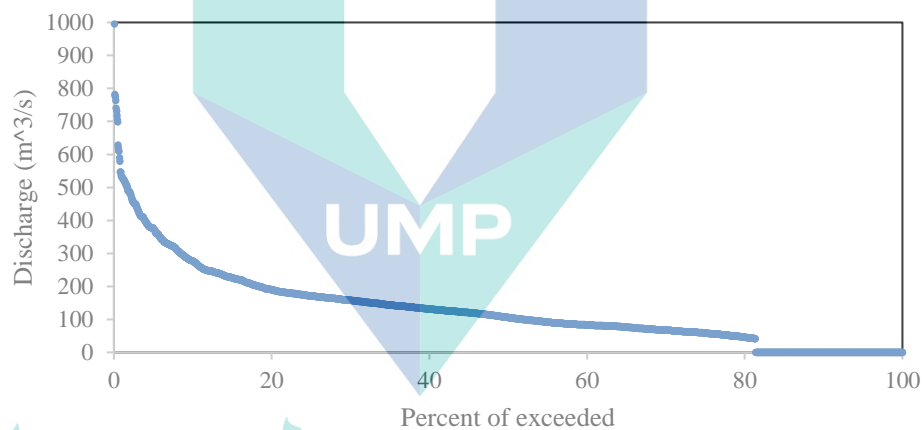


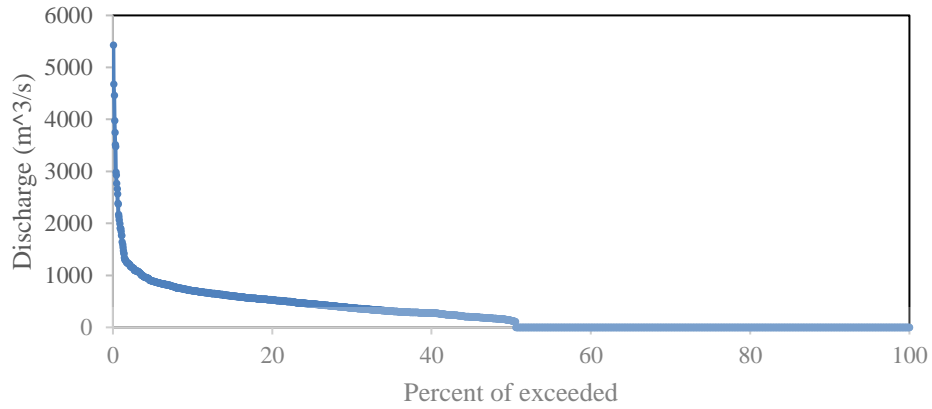
Figure 7.2 The water variation at Station 2. The River Sampling represent the measurement of river data whereas the Spline-Interpolant represent the mathematical interpolation technique.

## A1. Flow Duration Curve

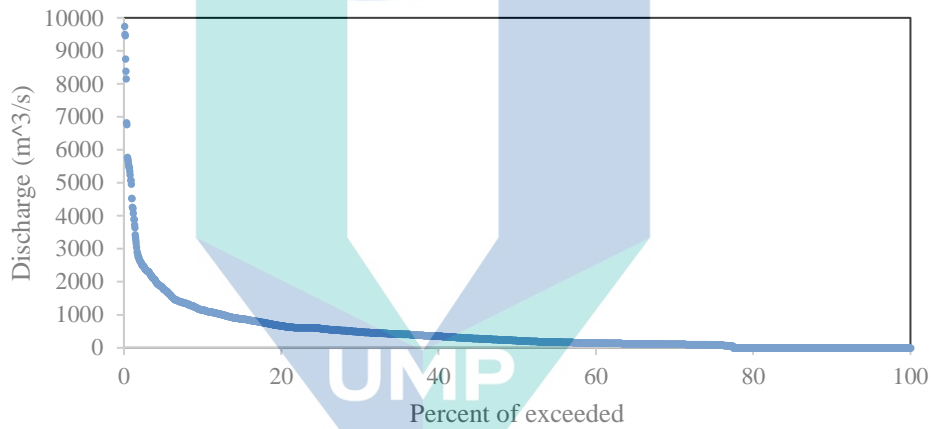
Figure (a)–(d) shows the FDC of four selected sites at the upstream, middle and downstream of the Pahang River. The FDC provides the information of annual streamflow and the percentage of how many days in a year a particular flow is exceeded (Kaunda, Kimambo, and Nielsen, 2014). The upper and the lower regions of FDC are essential in evaluating the river's characteristics. The upper shape represents the river discharge during the flood, whereas the lower region represents the ability of the river to sustain low flow during the dry season (Tekolla, 2010).



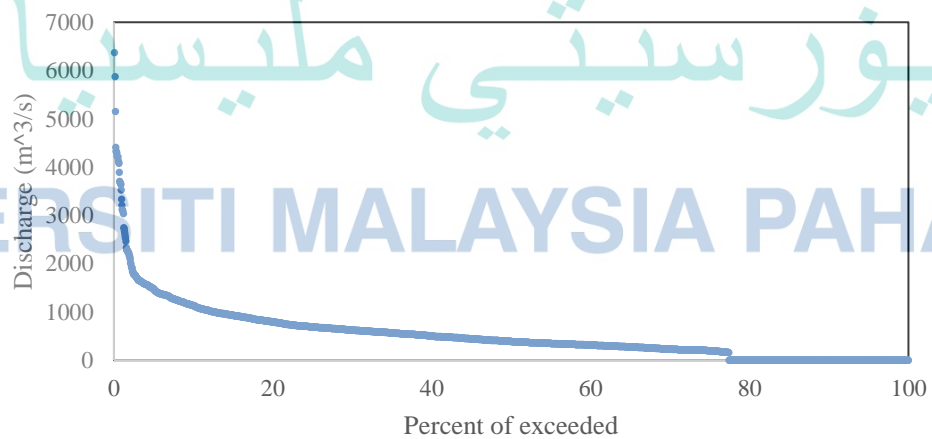
(a) FDC of Pahang River at Sungai Tembeling from 2012 to 2017



(b) FDC of Pahang River at Sungai Yap from 2012 to 2017



(c) FDC of Pahang River at Temerloh from 2012 to 2017



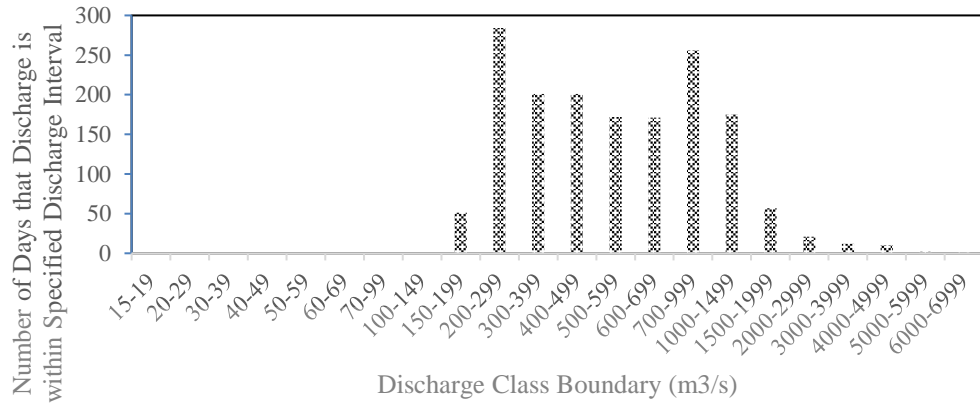
(d) FDC of Pahang River at Lubuk Paku from 2012 to 2017

The flow duration curve of the four rivers along Pahang River.

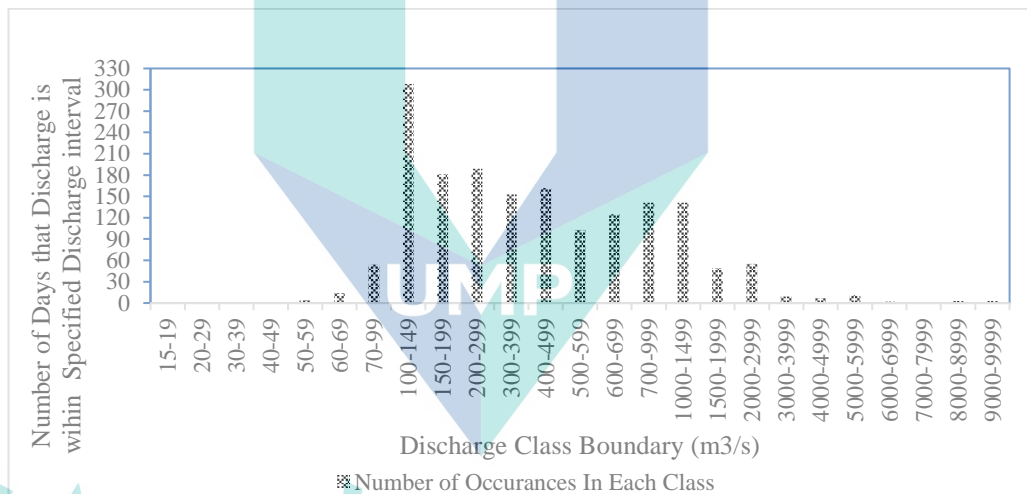
As can be seen, the highest flowrate was recorded by Pahang River at Temerloh with the data being more than 9500 m<sup>3</sup>/s, followed by Pahang River at Lubuk Paku with more than 6000 m<sup>3</sup>/s and Pahang River at Sg. Yap with more than 4000 m<sup>3</sup>/s. Meanwhile, the data on Sg. Tembeling achieved below 1000 m<sup>3</sup>/s even though the river's location is at the upstream of the Pahang River. The base-flow can be identified by taking the median-flow (Q50), which is equal to 50 % of the central time of the graph. Based on FDC, the median-flow for the Pahang River at Lubuk Paku was 436 m<sup>3</sup>/s, followed by the Pahang River at Temerloh at 220.9 m<sup>3</sup>/s of median-flow. Meanwhile, the Q50 Pahang River at Sg. Yap and Sg. Tembeling only showed 127.5 m<sup>3</sup>/s and 105.22 m<sup>3</sup>/s, respectively. This indicator means that the curve flow below the median (Q50) was considered as a low-flow condition.

## A2. Frequency Distribution Analysis

Pahang River at Temerloh and Pahang River at Lubuk Paku were chosen for the frequency distribution analysis. Although the Pahang River at Temerloh recorded the highest discharge with 9745 m<sup>3</sup>/s on 30 November 2014, however, the Pahang River at Lubuk Paku had higher potential compared to the Pahang River at Temerloh due to the Q50 median-flow and base-flow. This can be proven by the frequency distribution graph of the Pahang River at Lubuk Paku, as shown in (a). The frequency distribution graph represents the number of days that the discharge happened within the specified discharge interval along the particular duration.



(a) Frequency distribution for log cycle class intervals for Pahang River at Lubuk Paku



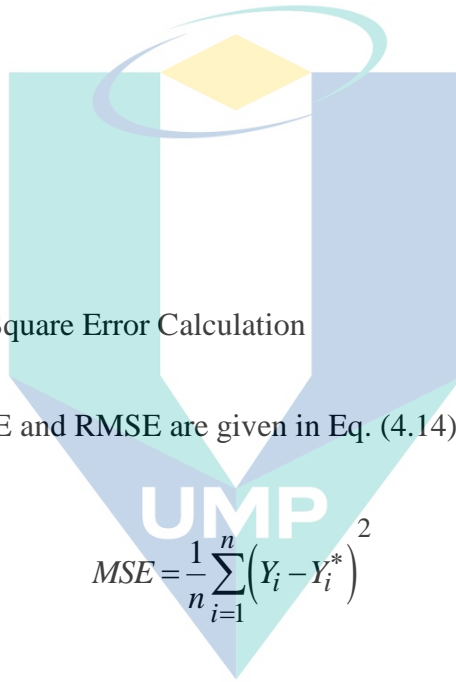
(b) Frequency distribution for log cycle class intervals for Pahang River at Temerloh

### Frequency distribution analysis for Pahang River

As can be seen, the discharge in the class boundary between 150 to 199 m<sup>3</sup>/s occurred for only fifty days at Lubuk Paku between 2012-2017. The frequency of the highest discharge was also minimal and only occurred during the raining monsoon. Most of the time, Sg. Pahang at Lubuk Paku flows continuously between 300 m<sup>3</sup>/s to 700 m<sup>3</sup>/s. This

result is in agreement with the median-flow and mean annual discharge of Pahang River at Lubuk Paku by 436 m<sup>3</sup>/s and 733.08 m<sup>3</sup>/s respectively.

On the other hand, more than 300 days of discharge occurred in the class boundary between 100-149 m<sup>3</sup>/s for the Pahang River at Temerloh. However, based on the FDC analysis, the Q50 or median flow was recorded as 220.9 m<sup>3</sup>/s. This result is also in agreement with the frequency distribution graph, as shown in Figure (b). In addition, the mean annual discharge for this river was recorded at 509 m<sup>3</sup>/s between 2012-2017.



#### Appendix B: Mean Square Error Calculation

The equations for MSE and RMSE are given in Eq. (4.14) and Eq.(4.15) respectively.

$$MSE = \frac{1}{n} \sum_{i=1}^n (Y_i - Y_i^*)^2 \quad 7.1$$

$$RMSE = \sqrt{\frac{1}{n} \sum_{i=1}^n (Y_i - Y_i^*)^2} \quad 7.2$$

**UNIVERSITI MALAYSIA PAHANG**

where  $n$  is the prediction sample of data point,  $Y_i$  is the observed values of a variable being predicted,  $Y_i^*$  is the predicted values.



n	Actual(Yi)	4th Poly (Yi*)	Errors	Square Error
1.00000e-02	0.000146008	0.05504289	-0.054896882	0.003013668
6.00000e-02	0.000848184	0.036524349	-0.035676165	0.001272789
1.10000e-01	0.00150677	0.02005782	-0.01855105	0.000344141
1.60000e-01	0.00212148	0.005562945	-0.003441465	1.18437E-05
2.10000e-01	0.0026906	-0.007039374	0.009729974	9.46724E-05
2.60000e-01	0.00321691	-0.017826974	0.021043884	0.000442845
3.10000e-01	0.00370831	-0.026876434	0.030584744	0.000935427
3.60000e-01	0.00416752	-0.034263072	0.038430592	0.00147691
4.10000e-01	0.00460521	-0.040060946	0.044666156	0.001995065
4.60000e-01	0.00504044	-0.044342854	0.049383294	0.00243871
5.10000e-01	0.0055013	-0.047180333	0.052681633	0.002775354
5.60000e-01	0.00599391	-0.048643662	0.054637572	0.002985264
6.10000e-01	0.00649718	-0.048801859	0.055299039	0.003057984
6.60000e-01	0.00703233	-0.047722682	0.054755012	0.002998111
7.10000e-01	0.00767921	-0.045472629	0.053151839	0.002825118
7.60000e-01	0.00851532	-0.042116937	0.050632257	0.002563625
8.10000e-01	0.00957712	-0.037719585	0.047296705	0.002236978
8.60000e-01	0.0109067	-0.032343291	0.043249991	0.001870562
9.10000e-01	0.0126859	-0.026049513	0.038735413	0.001500432
9.60000e-01	0.0150115	-0.018898449	0.033909949	0.001149885
1.01000e+00	0.0179017	-0.010949036	0.028850736	0.000832365
1.06000e+00	0.0214528	-0.002258954	0.023711754	0.000562247
1.11000e+00	0.0259267	0.007115381	0.018811319	0.000353866
1.16000e+00	0.031698	0.017118811	0.014579189	0.000212553
1.21000e+00	0.0387545	0.027697436	0.011057064	0.000122259
1.26000e+00	0.0471001	0.03879862	0.00830148	6.89146E-05
1.31000e+00	0.0562323	0.050370983	0.005861317	3.4355E-05
1.36000e+00	0.066893	0.062364409	0.004528591	2.05081E-05
1.41000e+00	0.0794901	0.07473004	0.00476006	2.26582E-05
1.46000e+00	0.0937967	0.087420276	0.006376424	4.06588E-05
1.51000e+00	0.10996	0.10038878	0.00957122	9.16082E-05
1.56000e+00	0.127207	0.113590475	0.013616525	0.00018541
1.61000e+00	0.146952	0.126981542	0.019970458	0.000398819
1.66000e+00	0.169602	0.140519423	0.029082577	0.000845796
1.71000e+00	0.193167	0.154162821	0.039004179	0.001521326
1.76000e+00	0.219718	0.167871696	0.051846304	0.002688039
1.81000e+00	0.24889	0.181607272	0.067282728	0.004526965
1.86000e+00	0.28074	0.19533203	0.08540797	0.007294521
1.91000e+00	0.315796	0.209009712	0.106786288	0.011403311
1.96000e+00	0.354744	0.222605321	0.132138679	0.017460631
2.01000e+00	0.399304	0.236085117	0.163218883	0.026640404

2.06000e+00	0.439451	0.249416624	0.190034376	0.036113064
2.11000e+00	0.452018	0.262568623	0.189449377	0.035891066
2.16000e+00	0.464107	0.275511156	0.188595844	0.035568392
2.21000e+00	0.476177	0.288215526	0.187961474	0.035329516
2.26000e+00	0.482592	0.300654293	0.181937707	0.033101329
2.31000e+00	0.483524	0.312801281	0.170722719	0.029146247
2.36000e+00	0.484866	0.324631571	0.160234429	0.025675072
2.41000e+00	0.485352	0.336121505	0.149230495	0.022269741
2.46000e+00	0.485955	0.347248686	0.138706314	0.019239442
2.51000e+00	0.484218	0.357991974	0.126226026	0.01593301
2.56000e+00	0.480865	0.368331493	0.112533507	0.01266379
2.61000e+00	0.476889	0.378248624	0.098640376	0.009729924
2.66000e+00	0.474633	0.387726009	0.086906991	0.007552825
2.71000e+00	0.471975	0.39674755	0.07522745	0.005659169
2.76000e+00	0.470019	0.40529841	0.06472059	0.004188755
2.81000e+00	0.469048	0.41336501	0.05568299	0.003100595
2.86000e+00	0.464813	0.420935032	0.043877968	0.001925276
2.91000e+00	0.460527	0.427997418	0.032529582	0.001058174
2.96000e+00	0.456552	0.43454237	0.02200963	0.000484424
3.01000e+00	0.451477	0.440561351	0.010915649	0.000119151
3.06000e+00	0.444624	0.446047082	-0.001423082	2.02516E-06
3.11000e+00	0.437963	0.450993545	-0.013030545	0.000169795
3.16000e+00	0.429744	0.455395982	-0.025651982	0.000658024
3.21000e+00	0.422766	0.459250895	-0.036484895	0.001331148
3.26000e+00	0.415546	0.462556047	-0.047010047	0.002209944
3.31000e+00	0.410186	0.465310459	-0.055124459	0.003038706
3.36000e+00	0.404285	0.467514413	-0.063229413	0.003997959
3.41000e+00	0.398777	0.469169451	-0.070392451	0.004955097
3.46000e+00	0.394892	0.470278375	-0.075386375	0.005683106
3.51000e+00	0.389959	0.470845248	-0.080886248	0.006542585
3.56000e+00	0.385285	0.47087539	-0.08559039	0.007325715
3.61000e+00	0.382038	0.470375385	-0.088337385	0.007803494
3.66000e+00	0.377797	0.469353075	-0.091556075	0.008382515
3.71000e+00	0.373563	0.46781756	-0.09425456	0.008883922
3.76000e+00	0.371652	0.465779204	-0.094127204	0.00885993
3.81000e+00	0.365774	0.463249627	-0.097475627	0.009501498
3.86000e+00	0.363431	0.460241713	-0.096810713	0.009372314
3.91000e+00	0.359845	0.456769604	-0.096924604	0.009394379
3.96000e+00	0.356417	0.4528487	-0.0964317	0.009299073
4.01000e+00	0.353009	0.448495664	-0.095486664	0.009117703
4.06000e+00	0.34968	0.443728419	-0.094048419	0.008845105
4.11000e+00	0.34643	0.438566146	-0.092136146	0.008489069

4.16000e+00	0.344333	0.433029287	-0.088696287	0.007867031
4.21000e+00	0.341123	0.427139545	-0.086016545	0.007398846
4.26000e+00	0.337888	0.42091988	-0.08303188	0.006894293
4.31000e+00	0.334692	0.414394516	-0.079702516	0.006352491
4.36000e+00	0.331458	0.407588934	-0.076130934	0.005795919
4.41000e+00	0.32826	0.400529876	-0.072269876	0.005222935
4.46000e+00	0.326151	0.393245345	-0.067094345	0.004501651
4.51000e+00	0.322737	0.385764601	-0.063027601	0.003972479
4.56000e+00	0.319274	0.378118168	-0.058844168	0.003462636
4.61000e+00	0.315806	0.370337827	-0.054531827	0.00297372
4.66000e+00	0.312209	0.36245662	-0.05024762	0.002524823
4.71000e+00	0.308516	0.35450885	-0.04599285	0.002115342
4.76000e+00	0.304825	0.346530077	-0.041705077	0.001739313
4.81000e+00	0.3022	0.338557125	-0.036357125	0.001321841
4.86000e+00	0.29812	0.330628075	-0.032508075	0.001056775
4.91000e+00	0.293904	0.322782269	-0.028878269	0.000833954
4.96000e+00	0.289531	0.31506031	-0.02552931	0.000651746
5.01000e+00	0.285029	0.307504058	-0.022475058	0.000505128
5.06000e+00	0.280404	0.300156637	-0.019752637	0.000390167
5.11000e+00	0.2757	0.293062428	-0.017362428	0.000301454
5.16000e+00	0.270793	0.286267073	-0.015474073	0.000239447
5.21000e+00	0.266509	0.279817474	-0.013308474	0.000177115
5.26000e+00	0.260624	0.273761794	-0.0113137794	0.000172602
5.31000e+00	0.256611	0.268149454	-0.011538454	0.000133136
5.36000e+00	0.251035	0.263031136	-0.011996136	0.000143907
5.41000e+00	0.245266	0.258458782	-0.013192782	0.000174049
5.46000e+00	0.239365	0.254485594	-0.015120594	0.000228632
5.51000e+00	0.233229	0.251166035	-0.017937035	0.000321737
5.56000e+00	0.226925	0.248555826	-0.021630826	0.000467893
5.61000e+00	0.22045	0.246711949	-0.026261949	0.00068969
5.66000e+00	0.216873	0.245692646	-0.028819646	0.000830572
5.71000e+00	0.206949	0.245557419	-0.038608419	0.00149061
5.76000e+00	0.203063	0.246367031	-0.043304031	0.001875239
5.81000e+00	0.192743	0.248183503	-0.055440503	0.003073649
5.86000e+00	0.185294	0.251070117	-0.065776117	0.004326498
5.91000e+00	0.177714	0.255091415	-0.077377415	0.005987264
5.96000e+00	0.17135	0.260313199	-0.088963199	0.007914451
6.01000e+00	0.163221	0.266802532	-0.103581532	0.010729134
6.06000e+00	0.154882	0.274627734	-0.119745734	0.014339041
6.11000e+00	0.146334	0.283858389	-0.137524389	0.018912958
6.16000e+00	0.137563	0.294565339	-0.157002339	0.024649734
6.21000e+00	0.128575	0.306820684	-0.178245684	0.031771524

6.26000e+00	0.11936	0.320697788	-0.201337788	0.040536905
6.31000e+00	0.109958	0.336271271	-0.226313271	0.051217697
6.36000e+00	0.100344	0.353617017	-0.253273017	0.064147221
6.41000e+00	0.0904348	0.372812168	-0.282377368	0.079736978
6.46000e+00	0.0802961	0.393935124	-0.313639024	0.098369437
6.51000e+00	0.0699239	0.417065548	-0.347141648	0.120507324
6.56000e+00	0.0593133	0.442284363	-0.382971063	0.146666835
6.61000e+00	0.0484443	0.46967375	-0.42122945	0.17743425
6.66000e+00	0.0373288	0.499317151	-0.461988351	0.213433237
6.71000e+00	0.026018	0.531299269	-0.505281269	0.255309161
6.76000e+00	0.0143744	0.565706064	-0.551331664	0.303966604
6.81000e+00	0.00253649	0.60262476	-0.60008827	0.360105932
6.86000e+00	-7.96842e-03	0.642143838	-0.650112258	0.422645948
6.91000e+00	-2.04428e-02	0.68435304	-0.70479584	0.496737177
6.96000e+00	-3.31739e-02	0.729343369	-0.762517269	0.581432585
Sum Error				4.186707387
MSE				0.030120197
RMSE				0.173551713

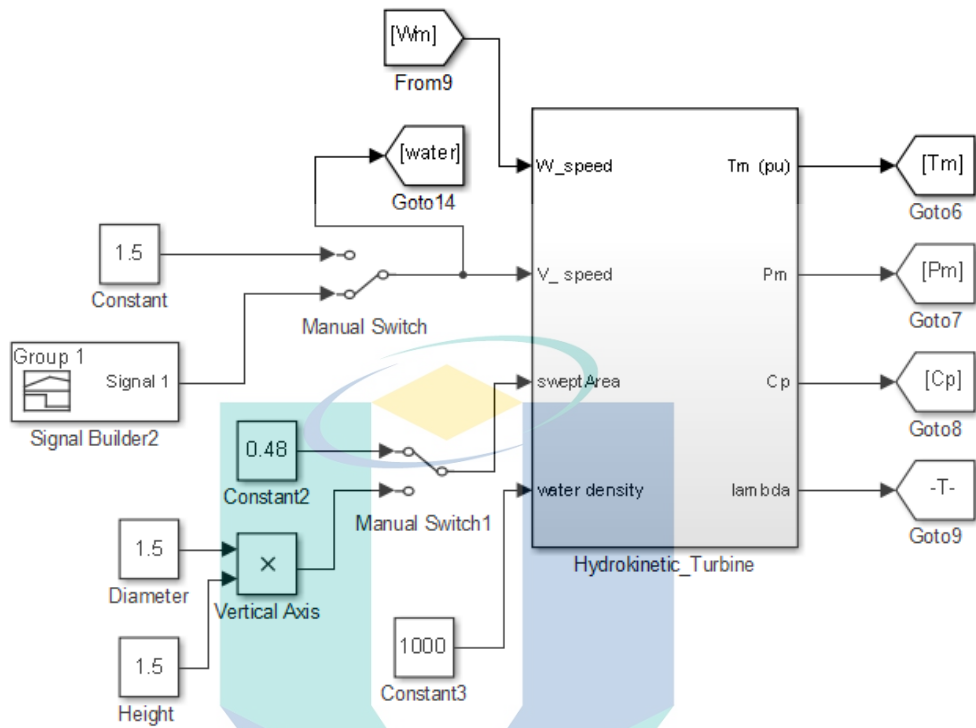
UMP

اونيورسيتي ملايسيا قهغ

UNIVERSITI MALAYSIA PAHANG

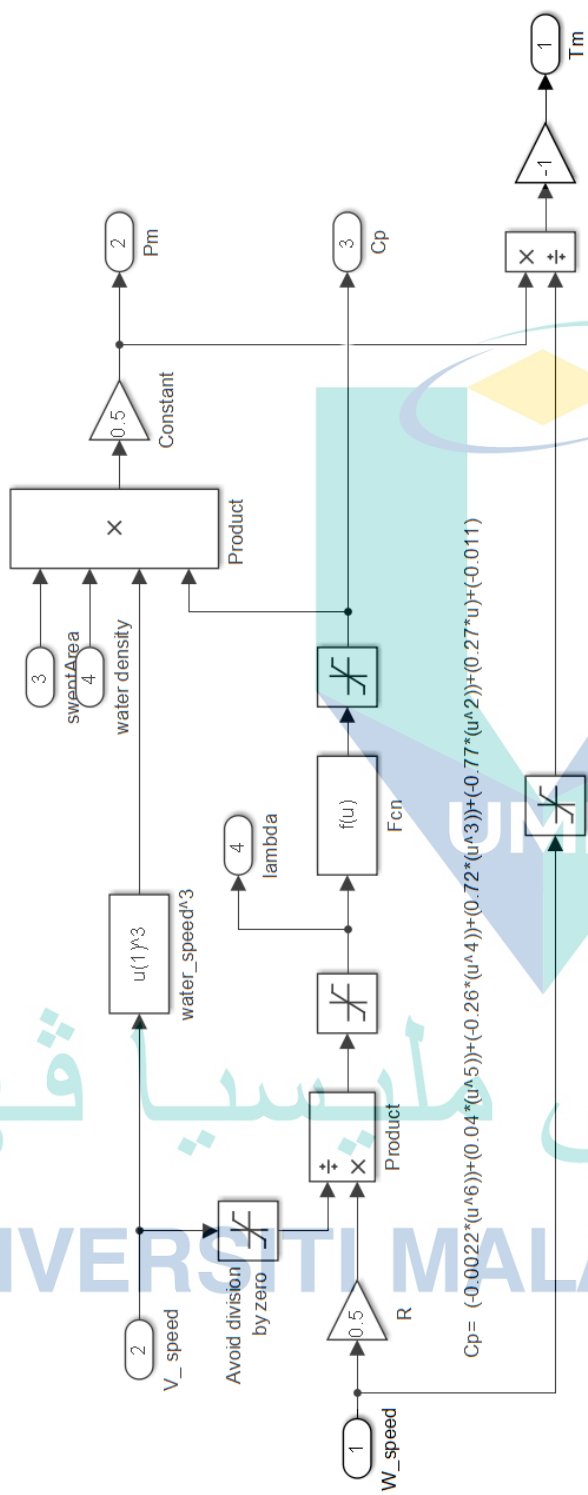
Appendix C: MPPT Circuit Topology-Uncontrolled Rectifier with DC Boost Converter

## C1.Turbine Block Diagram



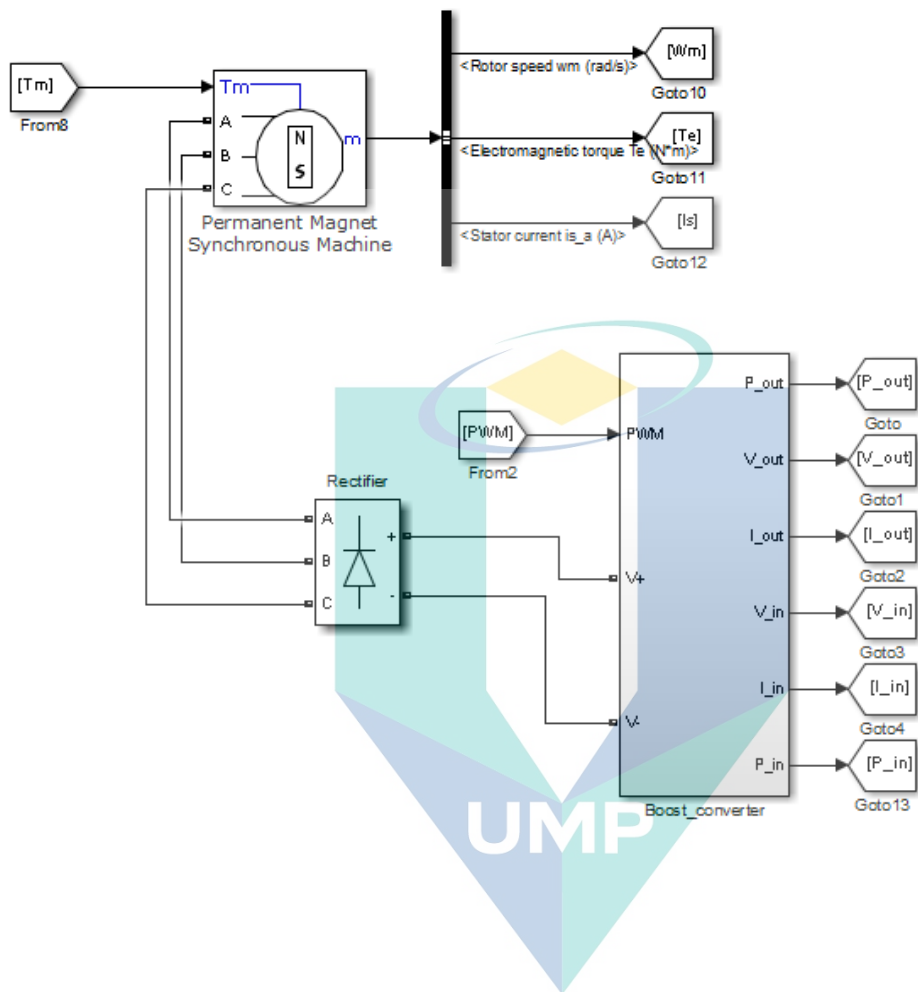
اونيورسيتي مليسيا قهغ  
UNIVERSITI MALAYSIA PAHANG

## C2. Hydrokinetic Turbine Subsystem





### C3.PMSG & Uncontrolled Rectifier and Boost Converter

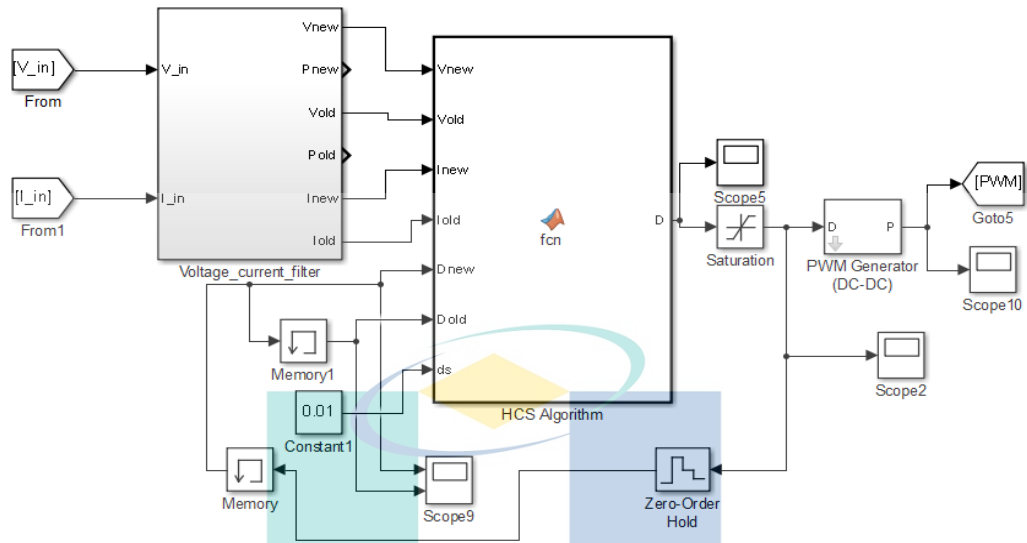


اونیورسیتی ملیسیا قهق  
 UNIVERSITI MALAYSIA PAHANG

C4. Boost Converter Circuit-Subsystem



## C5. MPPT Algorithm and PWM Generator



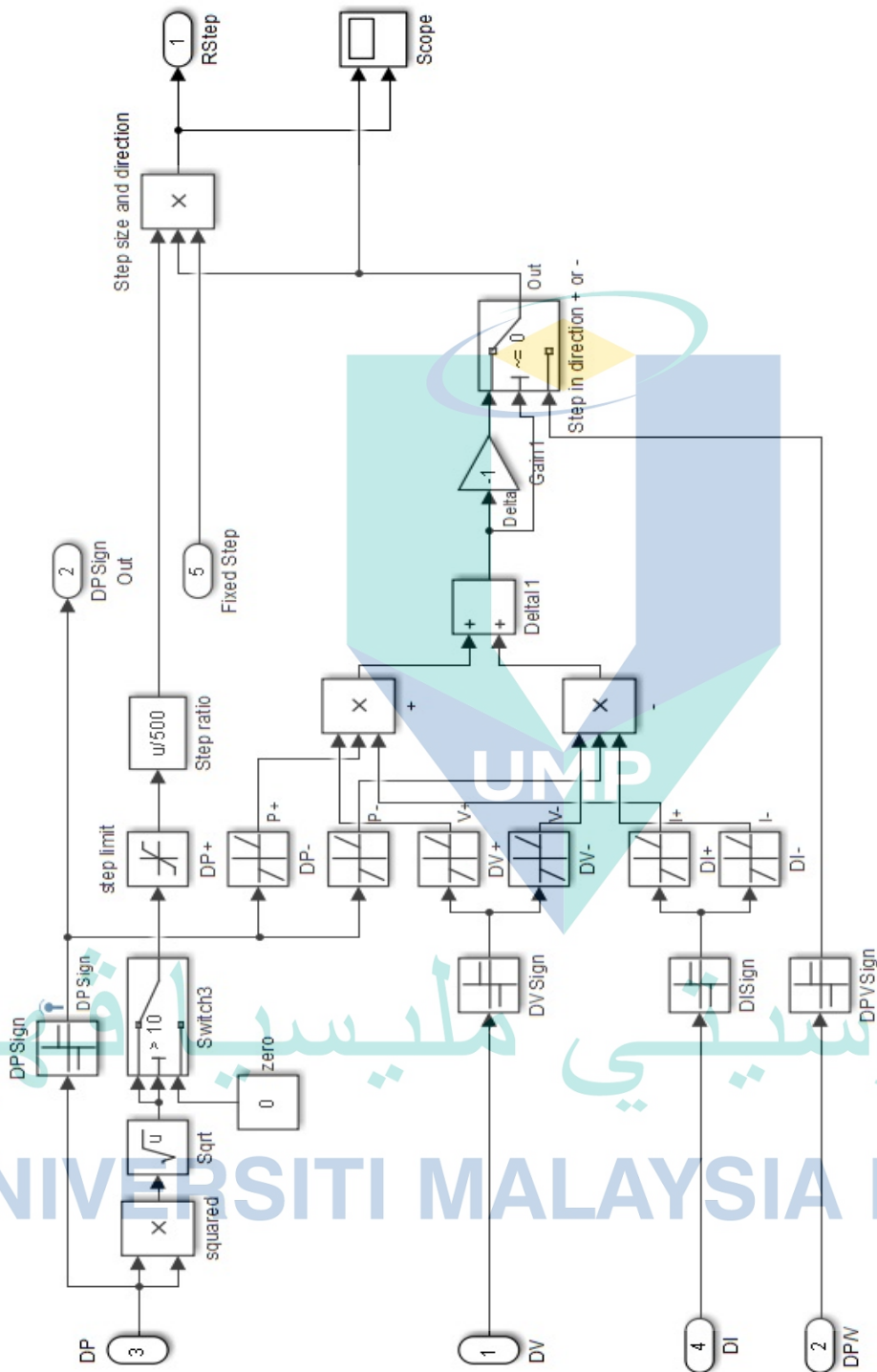
(a) SS-HCS and LS-HCS MPPT Algorithm- Matlab Function Code

UMP

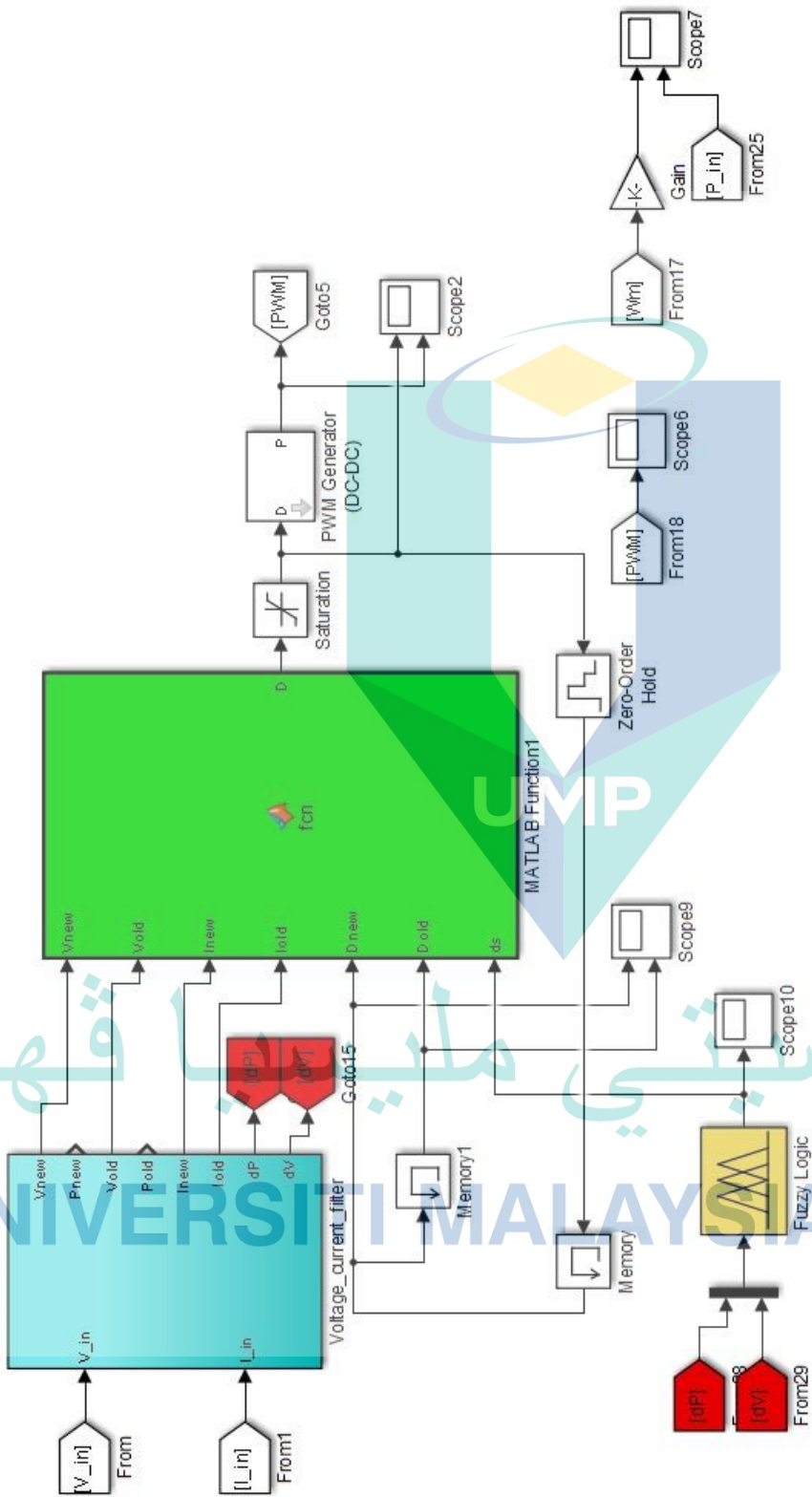
اونيورسيٲي ملايسيا قهغ

UNIVERSITI MALAYSIA PAHANG

### C6. Ramsey MPPT Algorithm



### C7. Fuzzy HCS MPPT Algorithm



## Appendix D: Derivation of Matrix A for Small-signal Stability Analysis

By combining the Equations (6.1), (6.2), (6.5), and (6.6), and subsequently linearising at the steady state, the linear equation is obtained by Eq. (7.3).

$$\tau j\Delta\omega = K_1\Delta\omega + K_2\Delta V - \Delta T_e \quad 7.3$$

where ,  $K_1$  and  $K_2$  are given in Eq. (7.2)

$$K_1 = 0.5\rho A \left( \begin{array}{c} \frac{5C_1R^6\omega_o^5}{V_o^3} + \frac{4C_2R^5\omega_o^3}{V_o^2} + \frac{3C_3R^4\omega_o^2}{V_o} + \\ 2C_4R^3\omega_o + C_5R^2V_o - \frac{C_7V_o^3}{\omega_o^2} \end{array} \right) \Delta\omega \quad 7.4$$

$$K_2 = 0.5\rho A \left( \begin{array}{c} -\frac{3C_1R^6\omega_o^5}{V_o^4} - \frac{2C_2R^5\omega_o^4}{V_o^3} - \frac{C_3R^4\omega_o^3}{V_o^2} \\ -C_4R^2\omega_o + 2C_5V_o + \frac{3C_7V_o^2}{\omega_o} \end{array} \right) \Delta V$$

$$C_1 = -0.022, C_2 = 0.04, C_3 = -0.26, \\ C_4 = 0.72, C_5 = -0.77, C_6 = 0.27, C_7 = -0.011$$

By replacing the values of  $C_1$ - $C_7$ , the dynamic model of turbine is given by Eq.(7.3).

اونيور سيني مليسيا قهغ  
UNIVERSITI MALAYSIA PAHANG



$$\frac{d\Delta\omega}{dt} = \frac{1}{\tau_j} \left[ \begin{array}{l} \left( \frac{-0.055\rho AR^6 \omega_o^5}{V_o^3} + \frac{0.08\rho AR^5 \omega_o^3}{V_o^2} \right) \\ - \frac{0.39\rho AR^4 \omega_o^2}{V_o} + 0.72\rho AR^3 \omega_o \\ - 0.385\rho AR^2 V_o + \frac{0.0055\rho AV_o^3}{\omega_o^2} \end{array} \right] \Delta\omega + \left[ \begin{array}{l} \left( \frac{0.033\rho AR^6 \omega_o^5}{V_o^4} - \frac{0.04\rho AR^5 \omega_o^4}{V_o^3} \right) \\ + \frac{0.13\rho AR^4 \omega_o^3}{V_o^2} - 0.385\rho AR^2 \omega_o \\ + 0.27\rho AR V_o - \frac{0.0165\rho AV_o^2}{\omega_o} \end{array} \right] \Delta V - \frac{3}{2} n_p \psi_{pm} \Delta i_{qs} \quad 7.5$$

The model of PMSG by Equation 6.3 and 6.4 can be combined with the control equation of the RSC (from Equation 6.15-6.21) to represent the Eq. (7.4) and Eq. (7.5)

$$L_s \frac{di_{ds}}{dt} = K_{P1}(0 - i_{ds}) + K_{I1}x1 \quad 7.6$$

$$L_s \frac{di_{qs}}{dt} = K_{P2} \left( \frac{2 \times 0.5 \rho AR V^2 C_{p \max} / \lambda}{3 n_p \psi_{pm}} - i_{ds} \right) + K_{I2}x2 \quad 7.7$$

Subsequently, the Eq. (7.6) and Eq. (7.7) are produced by linearising the Eq.(7.4) and Eq. (7.5) to the dynamic steady state.

$$\frac{d\Delta i_{ds}}{dt} = \frac{1}{L_s t_B} [-K_{P1}\Delta i_{ds} + K_{I1}\Delta x_1] \quad 7.8$$

$$\frac{d\Delta i_{qs}}{dt} = \frac{1}{L_s t_B} \left[ \frac{K_{P2}\rho ARV}{3n_p\psi_{pm}\lambda} \Delta V - K_{P2}\Delta i_{qs} + K_{I2}\Delta x_2 \right] \quad 7.9$$

Additionally, part of control equation from Equation 6.16 and 6.20 can be represented by Eq. (7.8) and Eq. (7.9).

$$\frac{dx_1}{dt} = 0 - i_{ds} \quad 7.10$$

$$\frac{dx_2}{dt} = \frac{2 \times 0.5 \rho ARV^2 C_{p \max} / \lambda}{3n_p\psi_{pm}} - i_{qs} \quad 7.11$$

Subsequently, the Eq.(7.10) and Eq. (7.11) are produced by linearising the Eq. (7.8) and Eq.(7.9).

$$\frac{d\Delta x_1}{dt} = -\Delta i_{ds} \quad 7.12$$

$$\frac{d\Delta x_2}{dt} = \frac{\rho AR C_{p \max} V}{3n_p\psi_{pm}\lambda} \Delta V - \Delta i_{qs} \quad 7.13$$

The model of grid side controller, from Eq.(6.25), (6.27), and (6.29) can be linearised as given by Equation 6.42-6.44.

$$\frac{d\Delta x_3}{dt} = -\Delta i_{Dg} \quad 7.14$$

$$\frac{d\Delta x_4}{dt} = -\Delta V_{dc} \quad 7.15$$

$$\frac{d\Delta x_5}{dt} = -K_{P4}\Delta V_{dc} + K_{I4}\Delta x_4 - \Delta i_{Qg} \quad 7.16$$

Additionally the GSC model from Eq. (6.22), (6.23) and (6.28) can be linearised as given by Equation 6.45 and 6.46.

$$\frac{d\Delta i_{Dg}}{dt} = \frac{1}{L} \left[ -K_{P3}\Delta i_{Dg} + K_{I3}\Delta x_3 \right] \quad 7.17$$

$$\frac{d\Delta i_{Qg}}{dt} = \frac{1}{L} \left[ -K_{P5}K_{P4}\Delta V_{dc} + K_{P5}K_{I4}\Delta x_4 - K_{P5}\Delta i_{Qg} + K_{I5}\Delta x_5 \right] \quad 7.18$$

The model of DC-link in Eq. (6.11) can be linearised as given by Eq. (6.47).

$$\frac{d\Delta V_{dc}}{dt} = \frac{3}{2CV_{dc}} \left[ V_{ds}\Delta i_{ds} + i_{ds}\Delta V_{ds} + V_{qs}\Delta i_{qs} + i_{qs}\Delta V_{qs} + V_{Qg}\Delta i_{Qg} + i_{Qg}\Delta V_{Qg} \right] \quad 7.19$$

On the other hand, the model of the grid network in Eq. (6.13) and (6.14) can be linearised as given by Eq. (7.18).

$$\frac{d\Delta V_{Qg}}{dt} = -\frac{x_{TL}^2 i_{Qg}}{V_{Qg} + i_{Dg} x_{TL}} \Delta i_{Qg} - x_{TL} \Delta i_{Dg} \quad 7.20$$

## Appendix E: Matlab M-File Code for Small Signal Stability Analysis

```
%Small-signal Modelling & Analysis of The Hydrokinetic with direct
drive
%permanent magnet synchronous generator connected to power grid.

clear;
clc;
% water turbine parameter
rho=1000;
Rw=0.3;
Cpmax=0.48;
lambda=2.53;
pi=3.142;
A=0.48;

%Pmsg Parameter
%DVTech PMG0-5K-260
np=28; % number of poles
Fn=30.33; % 120*f/np
Rs= 0.070; %1.74ohm
Ls= 0.52; %0.0362H
flux=1.05;
fluxpm=2.32;

% Drive train parameter
J=5;

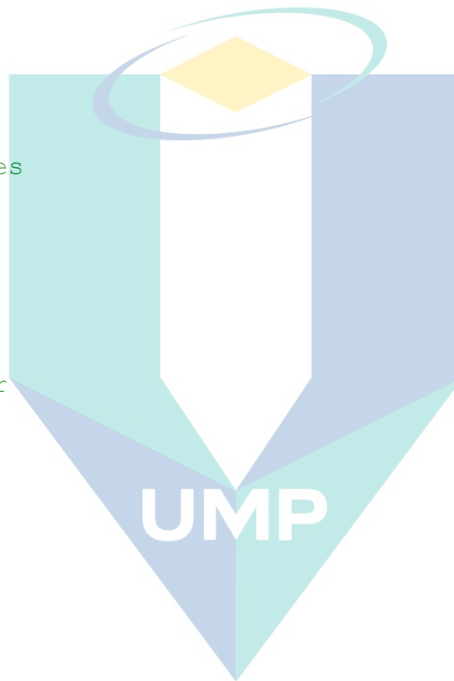
%Converter parameter
C=0.21;
L=0.17;

% Controller parameter
KP_1=1;
KI_1=55.55;
KP_2=1;
KI_2=60;
KP_3=1;
KI_3=111.11;
KP_4=0.25;
KI_4=10;
KP_5=0.5;
KI_5=25;

%power grid parameter
Xt=0.061;
Xl=0.014;

%Matrix Equation

c1=(0.055*rho*pi*A*Rw^6*omega0^5)/(Vw0^3);
c2=(0.08*rho*pi*A*Rw^5*omega0^3)/(Vw0^2);
c3=(0.39*rho*pi*A*Rw^4*omega0^2)/(Vw0);
c4=(0.72*rho*pi*A*Rw^3);
c5=(0.385*rho*pi*A*Rw^2*1.4);
```



اونیورسیتی ملیسیا قوچ  
UNIVERSITI MALAYSIA PAHANG

```

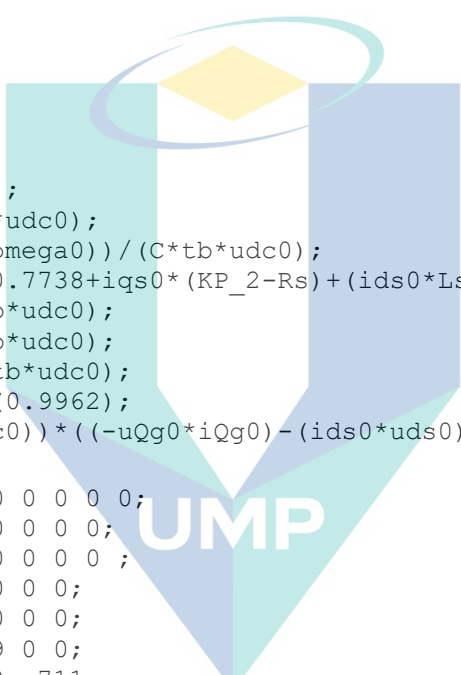
c6=(0.0055*rho*A*1.728)/omega0^2;

a11=(-c1+c2-c3+c4-c5+c6)/J;
a13=-fluxpm/J;
a22=-KP_1/(Ls*tb);
a24=KI_1/(Ls*tb);
a33=-KP_2/(Ls*tb);
a35=KI_2/(Ls*tb);
a42=-1;
a53=-1;
a69=-1;
a711=-1;
a87=KI_4;
a810=-1;
a811=-KP_4;
a96=KI_3/(L*tb);
a99=-KP_3/(L*tb);
a107=KP_5*KP_4/(L*tb);
a108=KI_5/(L*tb);
a1010=-KP_5/(L*tb);
a1011=-KP_5*KP_4/(L*tb);
a111=iqs0*fluxpm/(C*tb*udc0);
a112=((uds0)-(iqs0*Ls*omega0))/(C*tb*udc0);
a113=(1/(C*tb*udc0))*(0.7738+iqs0*(KP_2-Rs)+(ids0*Ls*omega0));
a114=- (KI_1*ids0)/(C*tb*udc0);
a115=- (KI_2*iqs0)/(C*tb*udc0);
a119=- (iQg0*0.075)/(C*tb*udc0);
a1110=(1/(C*tb*udc0))*(0.9962);
a1111=(1/(C*tb*udc0*udc0))*((-uQg0*iQg0)-(ids0*uds0)-(iqs0*uqs0));

A=[a11 0 a13 0 0 0 0 0 0 0 0;
0 a22 0 a24 0 0 0 0 0 0 0;
0 0 a33 0 a35 0 0 0 0 0 0;
0 a42 0 0 0 0 0 0 0 0 0;
0 0 a53 0 0 0 0 0 0 0 0;
0 0 0 0 0 0 0 0 a69 0 0;
0 0 0 0 0 0 0 0 0 0 a711;
0 0 0 0 0 a87 0 0 a810 a811;
0 0 0 0 0 a96 0 0 a99 0 0;
0 0 0 0 0 a107 a108 0 a1010 a1011;
a111 a112 a113 a114 a115 0 0 0 a119 a1110 a1111];

e=eig(A)

```

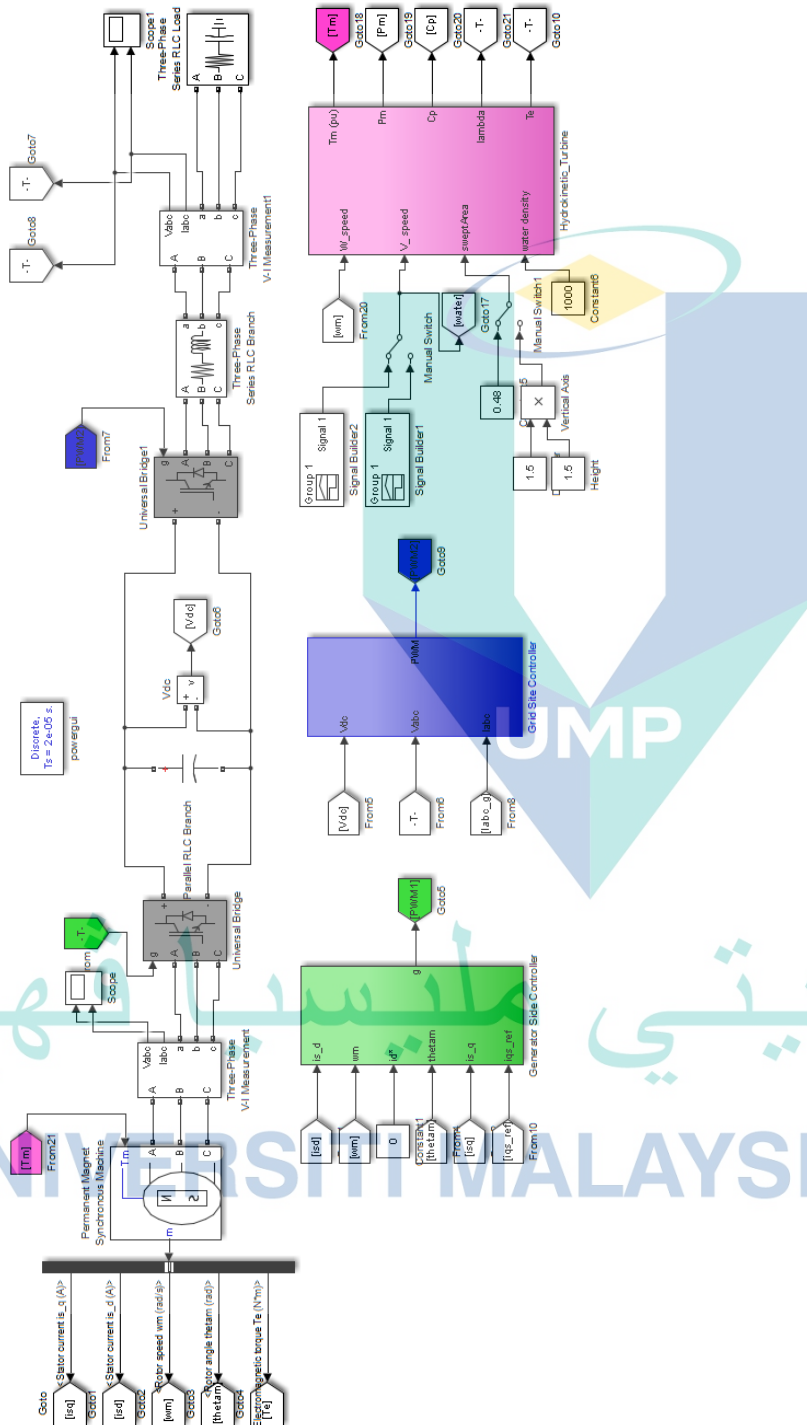


اونيور سيطي ماليزيا افهغ

UNIVERSITI MALAYSIA PAHANG

# Appendix F: Matlab/Simulink Program -Back-to-back Converter

## F1. Complete System





## F2. Generator Side Controller

